Optimising Nitrogen-Vacancy based widefield imaging for broadband applications

Von der Fakultät 8 Mathematik und Physik der Universität Stuttgart
zur Erlangung der Würde eines Doktors der Naturwissenschaften
(Dr. rer. nat.) genehmigte Abhandlung

Vorgelegt von

Marwa Garsi

aus Cagnes-sur-Mer, Frankreich

Hauptberichter:	Prof. Dr. Jörg Wrachtrup
Mitberichter:	Prof. Dr. Stefanie Barz
Prüfungsvorsitzender:	Prof. Dr. Christian Holm

Tag der mündlichen Prüfung: 5. Dezember 2022

Universität Stuttgart

3. Physikalisches Institut der Universität Stuttgart

2023

"The wonder is, not that the field of the stars is so vast, but that man has measured it."

– Anatole France

Contents

List of Figures

List of Tables

List of Abbreviations

a.u.	arbitrary units
AC	alternating current, used in the sense of 'oscillating' or 'varying'
AFM	atomic force microscopy
AL	active layer
AOM	acousto-optic modulator
APD	avalanche photo diode
ATP	adenosine triphosphate
BEOL	back-end-of-line
$\mathbf{B}$	magnetic field
CCD	charge coupled device
CMOS	complementary metal–oxide–semiconductor
CVD	chemical vapour depostion
cw	continuous wave
DC	direct current, used in the sense of 'constant' or 'static/quasi-static'
DO	dissolved oxygen
ECM	extracellular matrix
$\mathbf{E}$	electric field
ESR	electron-spin resonance
f	radiation frequency
FFT	fast Fourier transformation
FID	free induction decay
FOV	field of view
γ	gyromagnetic ratio
GMR	giant magneto-resistance
$\hat{\mathcal{H}}$	Hamiltonian operator

HPHT	high-pressure high-temperature
hwhm	half width at half maximum
IC	integratd circuit
I_n	nuclear spin
IR	infrared
ISC	intersystem crossing
k_B	Boltzmann constant
MCI	magnetic current imaging
MRI	magnetic resonance imaging
μ_0	magnetic permeability
MW	microwave
NA	numerical aperture
NMR	nuclear magnetic resonance
NV	nitrogen-vacancy
NV axis	nitrogen-vacancy centre's symmetry axis
NVs	nitrogen-vacancy centres
ODMR	optically detected magnetic resonance
Ω	rabi frequency
PBS	phosphate-buffered saline
PCB	printed circuit board
PDMS	polydimethylsiloxane
PEG	polyethylene glycol
ϕ, θ	angles in spherical coordinates
PL	photoluminescence
ppm	parts per million
PSB	phonon side band
qubit	quantum bit
RF	radiofrequency
RGD	Arg-Gly-Asp
rms	root mean square

ROI	region of interest
S	electron spin
SC	semiconductor
SEM	scanning electron microscopy
sinc	sinus cardinal
SNR	signal-to-noise ratio
SQUID	superconducting quantum interference device
STED	stimulated-emission-depletion
STORM	stochastic optical reconstruction microscopy
T_1	longitudinal spin relaxation time
$T_2{}^*$	inhomogeneous relaxation time
T_2	transversal spin relaxation time
τ	free evolution interval time
T	temperature
TIR	total internal reflection
TSV	through-silicon via
UV	ultraviolet
WLC	worm-like chain
ZFS	zero-field splitting
zp	zero padding
ZPL	zero-phonon line

Summary

Our understanding of the world and intrinsically scientific advances rely on our ability to see ever further, far beyond the limits of our vision. Whether we are trying to observe single molecules or distant objects in the sky, the fundamental problem is the same: we need highly accurate and precise tools.

Since the study *Micrographia* published by Robert Hooke in 1665 [1], the visualisation of structures smaller than the eye can distinguish has been a driving force in scientific research and led to many discoveries that founded our modern world. For example, Louis Pasteur revolutionised medicine in the 19th century by proving that microorganisms could cause disease and developed the germ theory, which changed the process of identifying, treating and preventing infectious diseases. Since then, advanced imaging techniques have been developed to allow us to see beyond optical limits, i.e. the diffraction limit, and explore the nanoscopic world [2, 3].

Despite the development of cutting-edge technologies in recent decades, fundamental questions remain open across many scientific fields [4]: *How did life begin? Where do we put all the carbon? Can computers keep getting faster?* The challenge in answering these questions lies in dissecting the helpful information from complex environments, such as cell systems or modern microelectronic devices. Two criteria are crucial to seek information about such systems: **sensors with outstanding capabilities** and **an efficient way to control them**.

In this respect, the interaction of light and matter has driven some of the most successful experimental techniques and technological advances in the modern era. For example, half of the 2018 Nobel Prize in Physics was awarded to Arthur Ashkin for the development of optical tweezers [5], which enabled breakthroughs in the field of biology [6–9]. In particular, optical tweezers were used to measure the force-extension relationships of individual DNA molecules scaling in the pN range [10], which will be discussed later in this manuscript. Another

example of these achievements is the 2012 Nobel Prize in Physics awarded to Serge Haroche and David J. Wineland [11] for the optical measurement and manipulation of single quantum systems while maintaining their quantum state. These experiments have enabled advances in both the understanding of quantum mechanics and the development of new technologies that take advantage of these quantum properties. However, because of the complexity of atom-based experiments, *artificial atoms* in the solid state have been intensively studied for the development of quantum technologies [12].

Among these systems, the nitrogen-vacancy (NV) centre in diamond has attracted much attention in the last decades and will form the central part of this manuscript. The NV centre is a defect in the diamond lattice in which two unpaired electrons form a spin triplet $S = 1$. Deep inside the diamond lattice, the NV centre is shielded from many environmental influences and stands out as a suitable quantum bit (qubit) for which spin lifetimes on the order of milliseconds have been observed, even at room temperature [13, 14]. With these properties, the NV centre has been established as a room temperature platform for quantum information processing, where entanglement between electron spins led to the realisation of a loophole-free Bell test [15].

Another key application of the NV centres is in the field of quantum sensing, which is the cornerstone of this manuscript. When brought close to external fields, quantum mechanical interactions with the spin state of the defect take place, giving the ability to the NV centre to sense various fields from its environment [16–20]. In particular, the atom-like magnetic Zeeman sensitivity combined with the optical readout of the NV centre enables the association of magnetic resonance spectroscopy with microscopy. As illustrated in figure 1, a microscope based on NV centres can transduce a magnetic signal into an optical signal to produce an image that quantifies magnetic fields.

In addition, the NV centre is stable down to a distance of about 2 nm from the diamond surface, allowing sensor-sample distances of only a few nanometres and, thus, nanoscale spatial resolution. Building on these properties, the first experimental demonstration of nanoscale magnetic field imaging using an NV

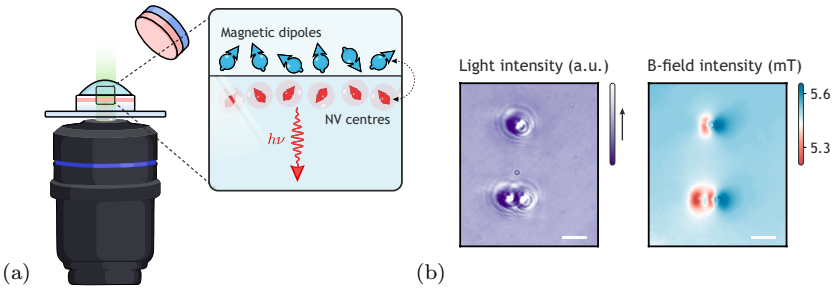

Figure 1: **The NV centre: a magnetic field transducer.**
a) Schematic illustration of the NV-based microscope, where the NV centres interact with magnetic spins and transduce the signal into an optical signal. b) Example showing the imaging of magnetic beads. *Left:* Bright illumination image of three magnetic beads on a diamond with NV centres and with an additional external magnetic field of about 5.5 mT. *Right:* Corresponding magnetic field magnitude sensed by the NV centres, recorded by a scientific camera. The scale bars are 10 µm wide.

centre was achieved in 2008 [21–23]. Many experiments followed in order to explore the properties of the NV centre [24–28] and to develop new measurement techniques to improve the tuning capabilities of the NV centre [29–32]. In particular, these improvements enabled the detection of subpicotesla fields [33, 34].

These advances have established the NV centre as one of the leading platforms for solid-state sensors, and the concepts are now being adopted for real-world applications. Notable achievements include the study of Johnson noise in metals [35], the detection of electric fields associated with surface band bending in diamond [36], and the mapping of current density with a spatial resolution down to 22 nm [37]. In summary, the NV centre is a versatile sensor with which science and engineering can be combined to provide the best possible results in a wide range of applications.

Accordingly, the question that can now be asked is:

Can NV-based technologies help to bridge gaps across multiple disciplines?

To this end, the device must be **practical, accessible, and provide high throughput and new solutions to existing problems**. One promising configuration that combines these features is the widefield microscope, in which a dense layer of NV centres near the surface of a diamond can be interrogated to produce spatially resolved maps of local quantities. While the first implementation of an on-chip widefield microscope was demonstrated in 2019 [38], recent studies discuss the pathway to realise a handy and practical microscope while optimising its performances [39, 40].

In this context, the aim of this thesis is to use the widefield microscope to sketch new pathways to solve current problems in microelectronics and bio-applications.

This manuscript is divided into four parts, organised as follows:

(1) Part I - *The NV-based widefield imager* - consists of two chapters introducing the NV-based widefield microscope used in this thesis. Chapter 1 introduces the physical properties of the NV centre and the basic schemes for conducting sensing experiments. Chapter 2 presents the experimental implementation of the NV-based widefield microscope.

(2) Part II - *Probing arbitrarily shaped microelectronics' activity* - consists of three chapters discussing several aspects of imaging current activity in microelectronic devices. Chapter 3 presents an optimised method for mapping vectorial magnetic fields, such as Oersted fields generated by current sources. Chapter 4 describes the method for reconstructing current densities using the associated magnetic field images. Finally, chapter 5 tackles the challenge of mapping current densities in a modern integrated circuit with three-dimensional architecture.

(3) Part III - *Probing life* - consists of two chapters that exploit the properties of the NV centre for bio-applications. Chapter 6 examines the

mechanocommunication channels of a cell, which are not yet well understood, although they are involved in many life processes. Chapter 7 is dedicated to inferring the dissolved oxygen levels in water, which has the potential to identify the harm that humankind's activities present to the ocean.

(4) Finally, the part IV concludes this manuscript with an outlook on the continuation of the work presented here.

Zusammenfassung

Unser Verständnis der Welt und auch jeglicher naturwissenschaftliche Fortschritt beruht auf unserer Fähigkeit die Grenzen unserer Wahrnehmung weit über das menschliche Sehvermögen hinaus zu erweitern. Ob wir versuchen einzelne Moleküle zu beobachten oder weit entfernte Objekte am Himmel zu untersuchen, das grundlegende Problem ist immer das gleiche: wir benötigen Werkzeuge mit hoher Genauigkeit und Präzision.

Seit der Studie *Micrographia* veröffentlicht von Robert Hooke im Jahr 1665 [1], ist die Visualisierung von Strukturen, die kleiner sind, als das Auge unterscheiden kann, eine treibende Kraft in der wissenschaftlichen Forschung und führte zu vielen Entdeckungen, die unsere moderne Welt begründen. Ludwig Pasteur beispielsweise revolutionierte im 19. Jahrhundert die Medizin, indem er bewies, dass Mikroorganismen Krankheiten verursachen können und indem er die Keimtheorie entwickelte, veränderte er den Prozess der Identifizierung, Behandlung und Vorbeugung von Infektionskrankheiten. Seitdem wurden zahlreiche fortschrittliche bildgebende Verfahren entwickelt, die es uns ermöglichen, über optische Grenzen, d.h. die Beugungsgrenze, hinauszusehen und die nanoskalige Welt zu erkunden [2, 3].

Trotz der Entwicklung von Spitzentechnologien in den letzten Jahrzehnten bleiben in vielen Bereichen der Wissenschaft Fragen offen [4]: *Wie hat das Leben begonnen? Wohin mit dem ganzen Kohlenstoff? Können Computer immer schneller werden?* Die Herausforderung bei der Beantwortung dieser Fragen liegt darin, hilfreiche Informationen aus komplexen Umgebungen, wie Zellsystemen oder modernen mikroelektronischen Geräten herauszusezieren. Zwei Voraussetzungen sind entscheidend, um Informationen über solche Systeme zu erhalten: **Sensoren mit herausragenden Fähigkeiten** und eine **effiziente Art diese zu beherrschen**.

In dieser Hinsicht hat das Verständnis der Wechselwirkung von Licht und Materie einige der erfolgreichsten experimentellen Techniken hervorgerufen und

zahlreiche technologische Fortschritte der Neuzeit ermöglicht. So ging beispielsweise die Hälfte des Nobelpreises für Physik 2018 an Arthur Ashkin für die Entwicklung optischer Pinzetten [5], die Durchbrüche auf dem Gebiet der Biologie ermöglichten [6–9]. Insbesondere wurden optische Pinzetten verwendet, um die Kraft zu messen die nötig ist, um einzelne DNA-Moleküle auseinanderzuziehen. Diese Kräfte sind typischerweise im pN-Bereich [10], und werden später in dieser Arbeit im Detail besprochen. Ein weiteres Beispiel für diese Errungenschaften ist der Nobelpreis für Physik 2012, der Serge Haroche und David J. Wineland [11] für die optische Messung und Manipulation einzelner Quantensysteme unter Beibehaltung ihres Quantenzustands verliehen wurde. Diese Experimente haben Fortschritte sowohl beim Verständnis der Quantenmechanik als auch bei der Entwicklung neuer Technologien ermöglicht, die sich diese Quanteneigenschaften zunutze machen. Wegen der Komplexität atombasierter Experimente, wurden jedoch auch *künstliche Atome* in Festkörpersystemen intensiv für die Entwicklung von Quantentechnologien untersucht [12].

Unter diesen Systemen hat das Stickstoff-Fehlstellen-Zentrum (NV) in Diamanten in den letzten Jahrzenten viel Aufmerksamkeit auf sich gezogen und wird den zentralen Teil dieser Arbeit bilden. Das NV-Zentrum ist ein Defekt im Diamantgitter, in dem zwei ungepaarte Elektronen ein Spin-Triplett bilden $S = 1$. Im Diamantgitter ist das NV-Zentrum von vielen Umwelteinflüssen abgeschirmt und zeichnet sich als ein vielversprechendes Quantenbit (Qubit) aus, für das sogar bei Raumtemperatur Spinlebensdauern in der Größenordnung von Millisekunden beobachtet wurden [13, 14]. Aufgrund dieser Eigenschaften hat sich das NV-Zentrum als Raumtemperaturplattform zur Quanteninformationsverarbeitung etabliert, bei der die Verschränkung von Elektronenspins dazu führte, einen lückenlosen Bell-Test zu realisieren [15].

Eine weitere wichtige Anwendung von NV-Zentren ist das Gebiet der Quantensensorik, was gleichzeitig einen Eckpfeiler dieser Arbeit bildet. Die Fähigkeit des NV-Zentrums, eine Vielzahl von äußeren Feldern in seiner Umgebung wahrzunehmen, basiert auf den quantenmechanischen Wechselwirkungen der Spin-Zustände dieses Defekts [16–20]. Insbesondere ermöglicht die Kombination aus

atomarer magnetischer Zeeman-Empfindlichkeit und der optischen Adressierbarkeit des NV-Zentrums die Verbindung von magnetischer Resonanzspektroskopie mit optischer Mikroskopie. Wie in Abbildung 1 dargestellt, kann ein auf NV-Zentren basierendes Mikroskop magnetische Messgrößen in optische Signale umwandeln, um so Bilder zu erzeugen welche lokale Magnetfelder darstellen.

Außerdem ist das NV-Zentrum bereits ab einer Tiefe von nur 2 nm unter Diamantenoberfläche stabil, was Sensor-Proben-Abstände von nur wenigen Nanometern und damit eine ebenso hohe räumliche Auflösung ermöglicht. Aufbauend auf diesen Eigenschaften erfolgte die erste experimentelle Visualisierung von Magnetfeldern im Nanometermaßstab unter Verwendung eines NV-Zentrums bereits 2008 [21–23]. Viele Experimente folgten, um die Eigenschaften der NV-Zentren weiter zu erforschen [24–28] und um neue Messtechniken zu entwickeln, welche die Sensitivität der NV-Zentren verbesserte [29–32], was wiederum die Detektion von Subpicotesla-Feldern ermöglichte [33, 34].

Diese Fortschritte haben das NV-Zentrum zu einer der führenden Plattformen für Festkörpersensoren gemacht, und die Messkonzepte werden nun für reale Anwendungen übernommen. Bemerkenswerte Erfolge umfassen die Untersuchung von Johnson-Rauschen in Metallen [35], das Beobachten von elektrischen Feldern, die im Zusammenhang mit der Veränderung der Bandstruktur an der Diamantoberfläche stehen [36], und die Abbildung von Stromdichten mit einer Ortsauflösung bis von zu 22 nm [37]. Schlussendlich ist das NV-Zentrum ein vielseitiger Sensor, bei dem Wissenschaft und Ingenieurstechnik kombiniert werden können, um für eine Vielfalt von Anwendungen die bestmögliche Lösung zu finden. Dementsprechend stellt sich nun die Frage:

Können NV-basierte Technologien dazu beitragen, technologische Lücken zwischen verschiedenen Disziplinen zu schließen?

Zu diesem Zweck muss das Gerät **praktisch und zugänglich sein, mit einem hohen Durchsatz und neue Lösungen für bestehende Probleme bieten**. Eine vielversprechende Konfiguration, die diese Merkmale kombiniert, ist das Weitfeldmikroskop, bei dem eine dichte Schicht von NV-Zentren nahe der

Oberfläche eines Diamanten ausgelesen werden kann, um so ortsaufgelöste Karten von lokalen Messgrößen zu erstellen. Während die erste Implementierung eines solchen On-Chip-Weitfeldmikroskops im Jahr 2019 demonstriert wurde [38], zeigen neuere Studien den Weg zur Realisierung eines handlichen und praktischen Mikroskops bei gleichzeitiger Optimierung seiner Leistungsparameter auf [39, 40].

In diesem Zusammenhang ist es das Ziel dieser Arbeit, mit Verfahren der Weitfeldmikroskopie neue Wege zur Lösung aktueller Probleme in der Mikroelektronik und in Bioanwendungen zu skizzieren.

Diese Arbeit ist in vier Teile gegliedert, die wie folgt organisiert sind:

(1) Teil I - *Die NV-basierte Weitfeld-Bildgebung* - besteht aus zwei Kapiteln, in denen das in dieser Arbeit verwendete NV-basierte Weitfeldmikroskop vorgestellt wird. Kapitel 1 stellt die physikalischen Eigenschaften des NV-Zentrums und die grundlegenden Schemata für die Durchführung von Messanwendungen vor. Kapitel 2 stellt die experimentelle Implementierung des NV-basierten Weitfeldmikroskops vor.

(2) Teil II - *Messung willkürlich gearteter Mikroelektroniksignale* - besteht aus drei Kapiteln, in denen verschiedene Aspekte zur Abbildung von Strömen in mikroelektronischen Bauteilen diskutiert werden. Kapitel 3 stellt eine optimierte Methode zur Darstellung vektorieller Magnetfelder vor, wie z. B. von Stromquellen erzeugte Oersted-Felder. Kapitel 4 beschreibt eine Methode zur Rekonstruktion von Stromdichten aus den zugehörigen Magnetfeldabbildungen. Schließlich befasst sich Kapitel 5 mit der Herausforderung, Stromdichten in einem modernen integrierten Schaltkreis mit dreidimensionaler Architektur abzubilden.

(3) Teil III - *Das Leben erforschen* - besteht aus zwei Kapiteln, welche die Eigenschaften des NV-Zentrums für Bioanwendungen nutzen. Kapitel 6 untersucht die mechanischen Kommunikationskanäle einer Zelle, die noch nicht gut verstanden sind, obwohl sie an vielen Bioprozessen beteiligt sind.

Kapitel 7 widmet sich der Bestimmung des Gehalts an gelöstem Sauerstoff in Wasser, was das Potenzial hat, den Schaden zu erkennen, den die Aktivitäten der Menschheit auf die Ozeane hat.

(4) Abschließend schließt Teil IV dieser Arbeit mit einem Ausblick auf die Fortführung der hier vorgestellten Arbeit ab.

Abbildung 1: **Das NV-Zentrum: ein Magnetfeldwandler.** a) Schematische Darstellung des NV-basierten Mikroskops, bei dem die NV-Zentren mit magnetischen Spins interagieren und dies in ein optisches Signal umwandeln. b) Beispiel Anhand der Abbildung magnetischer Partikel. *Links:* Hellfeldbild von drei magnetischen Kügelchen auf einem Diamanten mit NV-Zentren und mit einem zusätzlichen externen Magnetfeld von etwa 5,5 mT. *Rechts:* Entsprechende Magnetfeldstärke, die von den NV-Zentren erfasst wird und durch eine geeignete Kamera aufgezeichnet wird. Die Maßstabsbalken sind 10 µm breit.

Part I

The NV-based widefield imager

The ability of the so-called nitrogen-vacancy (NV) centre in diamond to operate under a wide span of external parameters, including ambient conditions, combined with the atom-like magnetic Zeeman sensitivity, has led to its intensive investigation [18, 32, 41]. These characteristics have triggered substantial activities in the field of quantum sensing [16, 17, 42] and quantum computing [43–45].

A wide scope of NV-based sensing modalities have been developed, ranging from scanning probe microscopy enabling nanoscale spatial resolution [46] to ensemble magnetometry providing $\mathrm{pT}/\sqrt{\mathrm{Hz}}$ sensitivity [33, 34]. Among these methods, the widefield microscope enables a trade-off between high spatial resolution and high sensitivity. Typical NV-based widefield microscopes enable spatial resolution at the optical limit, i.e. about $200 - 400\,\mathrm{nm}$, with sensitivity about a few tens of $\mathrm{nT}/\sqrt{\mathrm{Hz}}$ [40, 47]. Besides, the multiplexed readout of the widefield microscope using a scientific camera enables real-time video recording [48–50]. Finally, the simple configuration of the widefield microscopy setup enables a highly integrated system [38], particularly engaging for real-world applications.

The first part of this dissertation introduces NV-based imaging using the widefield approach. In the first chapter, a brief review of the physical properties of the NV centre and the basic schemes to manipulate the NV centre are presented. The second chapter presents the experimental implementation of the NV-based widefield microscope used throughout this work.

Chapter 1

Sensing using the nitrogen-vacancy centre in diamond

Diamond crystal defects have emerged as unique objects for various applications granted by their stability in the diamond matrix and their interesting optical properties. One fascinating defect is the NV centre in diamond, which enables local detection of a large panel of physical quantities, such as magnetic [16, 18–20, 42, 51, 52] and electric [53–55] fields, temperature [56–61] and strain [26, 62–64].

This chapter introduces the NV centre in diamond and the features relevant to the work presented in this manuscript. The chapter is organised as follows:

(1) Section 1.1 gives a brief overview of the general material's properties of the diamond host and the growth techniques.

(2) Section 1.2 introduces the properties of the NV centre as its geometric features and electronic structure.

(3) Section 1.3 discusses the basic measurement mechanisms and schemes for sensing magnetic fields with NV centres.

(4) Finally, section 1.4 reviews the different processes for engineering NV centres in diamond.

1.1 The diamond host material

1.1.1 Structure and basic properties of the diamond crystal

Diamond is an allotrope of carbon where the atoms are covalently bound in a tetrahedral geometry. As depicted in figure 1.1a, the crystal structure of a diamond is a face-centred cubic (fcc) lattice having eight atoms per unit cell and with a lattice constant of $a_0 = 3.567\,\text{Å}$ at room temperature [65]. The carbon atoms are interconnected with high bonding forces resulting from the sp^3-hybridisation [66, 67], represented in figure 1.1b. The combination of such bonds with the low mass of the lattice constituents makes the diamond the solid-state material with the highest hardness known in any natural material [68]. Another consequence of such bonds is the diamond's high Debye temperature of 1860 K resulting in a low phonon density even at room temperature [69]. Additionally, diamond features a high thermal conductivity of $22\,\text{W}\,\text{cm}^{-1}\,\text{K}^{-1}$, surpassing the thermal conductivity of most metals [70].

The electronic band structure of the diamond classifies it as a semiconductor (SC) with a wide bandgap of 5.48 eV at 300 K [71], giving the diamond insulator-like properties and optical transparency in the visible spectrum at ambient conditions.

Finally, the chemical inertness of the diamond and its low cytotoxicity makes the diamond a bio-compatible material, allowing applications in very close proximity to living entities [72].

1.1.2 Colour centres in diamond

Colour centres in diamonds have been intensively studied for decades, as they are responsible for the typical colouration of diamond gemstones. They are fluorescent lattice defects that consist of one or several impurity atoms or vacant lattice sites in a crystal. Such defects in the diamond lattice can lead to localised states within the bandgap, making light absorption and fluorescence possible, resulting in uniquely identifiable spectra.

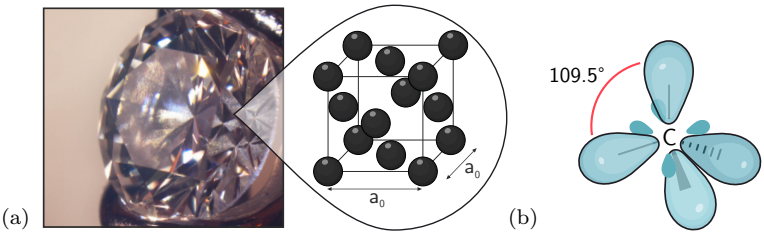

Figure 1.1: **The diamond structure.** a) Photograph of a natural diamond and representation of the diamond lattice with fcc geometry. All atoms form bonds to four neighbours in tetrahedral angles. b) Representation of four sp^3 orbitals in diamond, adapted from [73].

Several hundred defects have been identified to date [74–76]. Despite the diversity of colour centres, the diamond crystal structure allows only a few atoms to penetrate the lattice. Amongst them, the most common impurities are the atoms next to the carbon atom (C) in the periodic table of elements: the nitrogen atom (N) and the boron atom (B). Diamonds are classified into several categories depending on these impurities concentrations [77] as summarised in table 1.1.

Finally, the carbon atom composing the basic diamond lattice has two stable isotopes, the spin-free ^{12}C and the ^{13}C with a nuclear spin I_n[1] $= 1/2$. Since the natural abundance of ^{13}C is of only 1.1 %, the diamond lattice contains a low density of spins, ensuring a low magnetic noise environment. As such, the diamond crystal is a favourable environment for the coherence properties of colour centres. In addition, the diamond lattice can be enriched with ^{12}C and further engineered to reduce the environmental magnetic noise [13, 80, 81].

[1] Conventionally, the nuclear spin operator is represented by I. Here, the symbol I_n is used instead to avoid confusion with the current amplitude I used in part II of this manuscript.

Type I high nitrogen amount 5 ppm $<$ N $\lesssim$ 3000 ppm		**Type II** low nitrogen amount N $<$ 5 ppm	
$>$ 98 % of natural diamond		Most CVD diamond	Very rare in nature
Type Ia aggregated nitrogen	**Type Ib** single paramagnetic nitrogen atoms (P1 centres)	**Type IIa** nitrogen as major impurity (unless doped)	**Type IIb** boron as major impurity $\rightarrow$ p-type SC
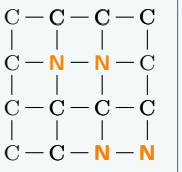	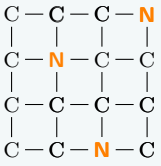	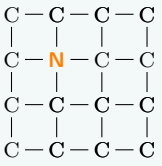	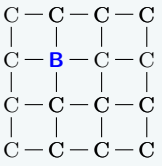

Table 1.1: **Classification of diamonds.** The density of nitrogen impurities in a diamond, expressed in parts per million (ppm), differentiates the classes of diamonds. The bottom line shows diamond lattice representations. Adapted from [76, 78, 79].

1.1.3 Diamond growth

Natural diamond stones can be used for scientific experiments, but the control over the lattice parameters is limited. In this regard, artificial diamond growth allows a high degree of control over the lattice constitution. In particular, isotopically purified diamonds can be grown, which further improves colour centres properties [82].

There are two main methods that enable the creation of artificial diamonds: the high-pressure high-temperature (HPHT) [83] process and the chemical vapour depostion (CVD) one [70]. HPHT imitates the natural process of diamond formation where graphite is transformed into diamond by applying temperatures above 1800 °C and pressures above 70 kbar. CVD growth is a homoepitaxial technique where a diamond seed is placed in a reactive methane

plasma with a temperature $\sim 800\,^{\circ}\mathrm{C}$ and a pressure of $\sim 30\,\mathrm{mbar}$. The carbon atoms from the methane molecules bind to the activated diamond surface and thus grow layer by layer. The composition of the growth gas, plasma energy, temperature and the crystal direction influence the growth and can be tuned to engineer the crystal lattice with high precision. All the diamonds used in this thesis were grown via CVD (see appendix A) as it offers better control over the crystal composition and its surface properties.

1.2 Properties of the negatively charged nitrogen-vacancy centre

The first reports about the NV centre date from 1976, when Davies and Hamer published their optical studies about a diamond defect emitting at 1.945 eV, corresponding to a zero-phonon line (ZPL) at 637 nm [84]. After the identification of its ground state electronic structure and the possible application of electron-spin resonance (ESR) [85], pioneering experiments were conducted by Eric van Oort and published in the early 90s [86, 87]. Finally, the first detection of a single NV was reported in 1997 [88], initiating a new era of research in the field of quantum sensing and quantum computing. In this section, the structure of the NV centre and its basic properties are briefly reviewed.

1.2.1 Geometrical features and charge state of the NV centre

The NV centre consists of a substitutional nitrogen atom and an adjacent carbon vacancy, forming four molecular orbitals with C_{3v} symmetry [28, 89]. This configuration, depicted in figure 1.2a, gives the NV centre a well-defined orientation within the diamond lattice, along with one of the four directions of the crystal's tetrahedral structure.

Depending on the number of electrons occupying the molecular orbitals, NV centres have been observed in three charge states: neutral for the NV^0, positive for the NV^+ and negative for the NV^- [90, 91]. The electronic structure of the NV^- centre includes two electrons from the nitrogen atom, three electrons from

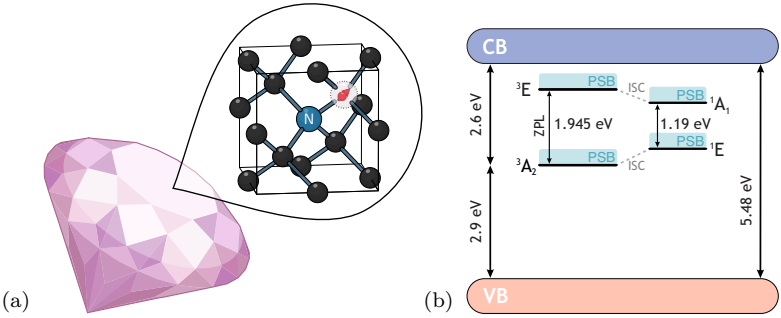

Figure 1.2: **Structure of the NV centre.** a) An NV centre in the diamond lattice. Carbon atoms are shown in grey, the nitrogen atom in blue and the vacancy is transparent with a red arrow representing the NV spin. b) Simplified electronic structure of the NV centre within the diamond band-gap. Solid arrows indicate radiative transitions between the states ^{3}E and ^{3}A$_2$ and between the states ^{1}A$_1$ and ^{1}E. Dotted lines indicate non-radiative decays. The fine structure of these electronic states is further developed in section 1.2.2 and figure 1.3.

the carbon's dangling bonds and another one from a donor in the lattice. This configuration makes the NV centre paramagnetic and hence sensitive to other spins. As such, the NV$^-$ centre is the cornerstone of most sensing experiments carried out with NV centres and throughout this work. For these reasons, the NV centre will refer to the NV$^-$ state in the following text.

1.2.2 Electronic level structure of the NV centre

NV centres are embedded in the diamond's bandgap, as depicted in figure 1.2b, away from both the valence and the conduction bands (VB and CB, respectively). The NV centre is thus a deep-level defect, and its optical transitions are protected from thermal fluctuations at room temperature.

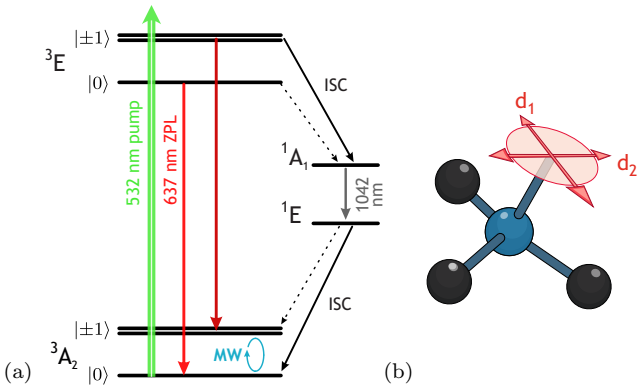

Figure 1.3: **Optical transitions of the NV centre.** a) Electronic level structure of the NV centre. Plain arrows represent optical transitions, while dotted arrows represent non-radiative decays. b) Optical dipoles (d_1, d_2) of the NV centre, in the plane orthogonal to the N-V symmetry axis.

The electronic level structure of the NV centre is shown in figure 1.3a. The two unpaired electrons of the NV centre form a spin triplet ($S = 1$) and thus a triplet ground state $^3A_2$ and a triplet excited state ^3E. The spin-spin interaction between the unpaired electrons leads to a partial lifting of the degeneracy of these triplet states by a zero-field splitting (ZFS), which separates the sublevel $m_s = 0$ from the sublevels $m_s = \pm 1$. The latter two remain degenerate if no external field is applied. In addition, the NV centre has two intermediate state singlets ^1A and ^1E [28].

The diamond host's transparency to the visible spectrum allows optical access to the NV centre in its entire colour spectrum using a pump laser. At room temperature, a blue-shifted excitation down to 500 nm can be used due to the presence of vibronic levels [84, 92, 93]. As depicted in figure 1.3b, there are two possible transition dipoles, here denoted (d_1, d_2), to optically excite the NV centre [94–96]. Both dipoles are perpendicular to the N-V symmetry axis,

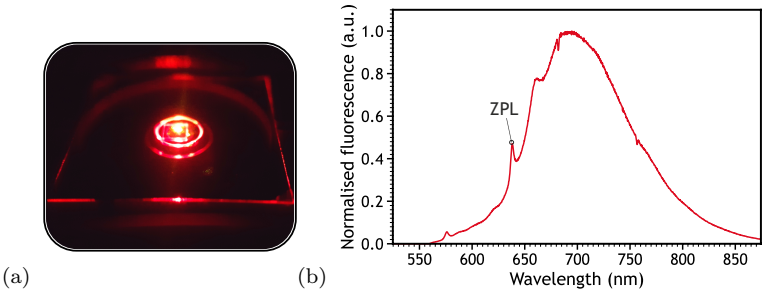

Figure 1.4: **NV centres' emission spectrum.** a) Photograph of a bulk diamond containing a high density of NV centres (∼1 ppm), excited with a 532 nm laser and emitting a bright red light. b) Spectrum of an ensemble of NV centres at room temperature. A sufficiently sharp ZPL can be noted, although a broad PSB composes the spectrum. Data courtesy of Alastair Marshall.

defined as the bond between the nitrogen and the vacancy site, and the dipoles are perpendicular to each other. Optical transitions must preserve the total intrinsic spin and only occur between levels with the same total spin number. Therefore, excitation by a 532 nm-pump laser results in a far-red fluorescence stemming from the $^3E \rightarrow {}^3A_2$ transition. This emission typically spans over $600 - 850$ nm due to the vibronic sublevels leading to a large phonon side band (PSB), as shown in figure 1.4. Finally, the $^3E \rightarrow {}^1A_1$ and $^1E \rightarrow {}^3A_2$ transitions are non-radiative, while $^1A_1 \rightarrow {}^1E$ has both a non-radiative and an infrared decay path.

However, it is worth noting that optical excitation can lead to the photoionisation of the NV centre through the Auger process, whereby an electron from the NV centre is excited to the diamond's conduction band, converting the NV centre into its neutral state NV^0. This spin-to-charge conversion can be exploited for electrical readout [97–99], and for super-resolution techniques [100]. However, for most applications based on NV centres, the NV^0 centres generate spurious fluorescence, particularly in the case of shallow NV centres. With a

ZPL located at 575 nm, the NV^0 signal is partially filtered out in this work using a long-pass filter at 650 nm (see section 2.2.2).

1.3 Sensing with NV centres in diamond

Due to its electron spin, the NV centre is highly susceptible to magnetic fields. In addition, the NV centre is affected by temperature, electric field and strain variations through the crystal field of the diamond host. Understanding and identifying the various sources of interaction with the NV centre is the key to performing sensing experiments. This section looks at the basic schemes for operating the NV centre to detect magnetic fields.

1.3.1 The NV centre's Hamiltonian

The capacity of the NV centre to sense its environment is based on the quantum mechanical interactions of the defect's spin state. To understand these mechanisms, it is important to describe the Hamiltonian governing the coupling of the NV centre with its environment. The sublevels of the electron spin associated with the NV centre can be described by the Hamiltonian $\hat{\mathcal{H}}_0$, given by:

$$\hat{\mathcal{H}}_0 = \hat{\mathcal{H}}_{\mathrm{ZFS}} + \hat{\mathcal{H}}_{\mathrm{EZ}} + \hat{\mathcal{H}}_{\mathrm{nuclear}}. \tag{1.1}$$

At low magnetic fields (defined such as $\mathcal{H}_{\mathrm{ZFS}} \gg \mathcal{H}_{\mathrm{EZ}}$), as used in this work and most typical sensing experiments, the NV centre's quantisation axis coincides with the N-V bond defined by the crystal geometry, shown in figure 1.5a. In the following, the description of the NV spin Hamiltonian terms is, thus, given in a basis where the symmetry axis of the NV centre defines the z-axis. The associated spin basis is given by:

$$\hat{S}_x = \frac{\hbar}{\sqrt{2}} \begin{pmatrix} 0 & 1 & 0 \\ 1 & 0 & 1 \\ 0 & 1 & 0 \end{pmatrix} \quad \hat{S}_y = \frac{i\hbar}{\sqrt{2}} \begin{pmatrix} 0 & -1 & 0 \\ 1 & 0 & -1 \\ 0 & 1 & 0 \end{pmatrix} \quad \hat{S}_z = \hbar \begin{pmatrix} 1 & 0 & 0 \\ 0 & 0 & 0 \\ 0 & 0 & -1 \end{pmatrix}, \tag{1.2}$$

where $\hbar$ is the reduced Planck constant.

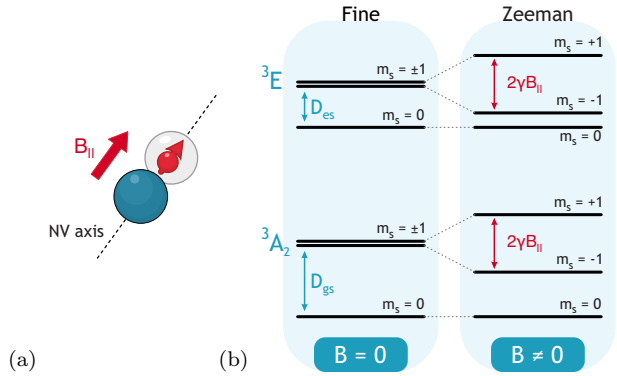

Figure 1.5: **Fine structure and Zeeman splitting of the NV centre.** a) Schematic representation of a magnetic field $B_{\|}$ aligned with the NV quantisation axis coinciding with the symmetry axis of the NV centre at low magnetic fields and ambient conditions. b) *Left*: Fine structure of the ground state of the NV centre without magnetic field; *Right*: Zeeman splitting induced by a magnetic field $B_{\|}$ along the quantisation axis of the NV centre. A description of the hyperfine splitting due to the intrinsic nitrogen atom can be found in [20].

Also, $\mathcal{H}_0$ is dominated by the ZFS term $\mathcal{H}_{\mathrm{ZFS}}$, arising from the dipole-dipole interaction of the unpaired electrons and mediated by the crystal field. For the ground state manifold, $\hat{\mathcal{H}}_{\mathrm{ZFS}}$ is given by:

$$\frac{\hat{\mathcal{H}}_{\mathrm{ZFS}}}{h} = D_{\mathrm{gs}}\left[\hat{S}_z^2 - \frac{2}{3}\right] + \varepsilon_{\mathrm{gs}}\left(\hat{S}_x^2 - \hat{S}_y^2\right), \tag{1.3}$$

where D_{gs} is the axial component of the NV ground state magnetic dipole-dipole interaction, $\varepsilon_{\mathrm{gs}}$ the transverse component and h the Planck constant. The resulting fine structure is depicted in figure 1.5b. At room temperature, $D_{\mathrm{gs}} = 2.87\,\mathrm{GHz}$ and separates the ground state $|0\rangle$ from the degenerate state $|\pm 1\rangle$. The $\varepsilon_{\mathrm{gs}}$ term results from the anisotropy within the crystal, which can

arise from strain or electric field acting on $\hat{S}_x$ or $\hat{S}_y$. For NV centres in bulk diamonds, $\varepsilon_{\mathrm{gs}}$ is about 100 kHz and is usually neglected. For diamond crystals that have incurred mechanical strain, such as thinned diamond plates, it can increase to a few MHz and up to tens of MHz in the case of nanodiamonds.

The second largest term in the presence of a static magnetic field is the $\mathcal{H}_{\mathrm{EZ}}$ term, representing the electronic Zeeman interaction with the magnetic field. With a static magnetic field $\vec{B_0} = (B_{0x}, B_{0y}, B_{0z})^\intercal$, the term becomes:

$$\frac{\hat{\mathcal{H}}_{\mathrm{EZ}}}{h} = \gamma_{\mathrm{NV}} \vec{B_0} \cdot \hat{\vec{S}} = \gamma_{\mathrm{NV}} \left[B_{0x}\hat{S}_x + B_{0y}\hat{S}_y + B_{0z}\hat{S}_z \right], \tag{1.4}$$

where γ_{NV} is the gyromagnetic ratio of the NV centre given by $\gamma_{\mathrm{NV}} = \mathrm{g}_{\mathrm{NV}}\mu_B\hbar = 28\,\mathrm{MHz/mT}$ for which $\mathrm{g}_{\mathrm{NV}} = 2.0028$ is the electron g-factor of the NV centre [75], and μ_B the Bohr magneton. The term $\hat{\vec{S}} = \left(\hat{S}_x, \hat{S}_y, \hat{S}_z\right)^\intercal$ represents the spin operators. The resulting Zeeman splitting is depicted in figure 1.5b.

Since both stable isotopes of nitrogen, ^{14}N and ^{15}N, carry a nuclear spin, nuclear interactions contribute to the NV centre spin state. The spin Hamiltonian $\hat{\mathcal{H}}_{\mathrm{nuclear}}$ including these terms, is given by:

$$\hat{\mathcal{H}}_{\mathrm{nuclear}} = \hat{\mathcal{H}}_{\mathrm{HF}} + \hat{\mathcal{H}}_{\mathrm{NZ}} + \left[\hat{\mathcal{H}}_{\mathrm{NQ}}\right], \tag{1.5}$$

leading to equation (1.6):

$$\frac{\hat{\mathcal{H}}_{\mathrm{nuclear}}}{h} = \hat{\vec{S}}\mathcal{A}\hat{\vec{I_n}} - \gamma_{\mathrm{N}}\vec{B_0} \cdot \hat{\vec{I_n}} + \left[\mathcal{Q}\hat{I}_{nz}^2\right], \tag{1.6}$$

where $\hat{\vec{I_n}} = \left(\hat{I}_{nx}, \hat{I}_{ny}, \hat{I}_{nz}\right)^\intercal$ represents the spin operators for the nuclear spin associated with the intrinsic nitrogen atom of the NV centre (with either $I_n = 1$ or $I_n = 1/2$ for intrinsic ^{14}N and ^{15}N respectively). The first term on the right-hand side of the equation (1.6) represents the hyperfine interaction between the electron spin and the nuclear spin, where $\mathcal{A}$ is the hyperfine coupling tensor. The following term represents the nuclear Zeeman interaction, where γ_{N} is the gyromagnetic ratio associated with the nitrogen nuclear spin. Finally,

the last term appears in the case of ^{14}N and represents the nuclear quadrupolar interaction $\mathcal{H}_{\mathrm{NQ}}$ [101], where $\mathcal{Q}$ represents the quadrupole splitting. In addition to these terms, the hyperfine signature of the ^{13}C isotope with a nuclear spin $I_n = 1/2$ can also be observed in crystals with a natural abundance of 1.1 % [102].

All the ensemble measurements shown in this work were obtained with NV centres consisting of a ^{15}N nuclear spin. However, splittings caused by the interaction with nuclear spins were generally not resolved in this work and, therefore, only given here for reference. Finally, further terms can be added to the NV spin Hamiltonian and are described in chapter 3.

1.3.2 Spin state manipulation

Electron spins are easy and fast to control because they interact strongly with both electric and magnetic fields, and their energies are in the microwave frequency regime [103]. Optical manipulation enables initialisation of the spin and readout, while microwaves (MWs) enable manipulation of the spin in the ground state manifold.

1.3.2.1 Optical initialisation

At low external fields and in thermal equilibrium, all sublevels of the ground state manifold are almost uniformly populated due to their small energy differences, as given by the Boltzmann distribution. The combination of spin-preserving optical transitions $^3A_2 \rightarrow {}^3E$ with spin-selective intersystem crossing (ISC) to the singlet state $^1A_1$ provides a high degree of electron spin polarisation in the sublevel $m_\mathrm{s} = 0$.

Such spin polarisation can be illustrated by the 7-level model described in appendix B. The time evolution of the system, illustrated in figure 1.6, depends on the intrinsic rates of the NV centres and the optical pumping. Here, the fluorescence signal with an initial spin state $m_\mathrm{s} = 0$ (red curve) shows a high initial fluorescence which decays back to a steady state after about 1200 ns. The fluorescence signal with an initial spin state $m_\mathrm{s} = \pm 1$ (orange curve) shows a

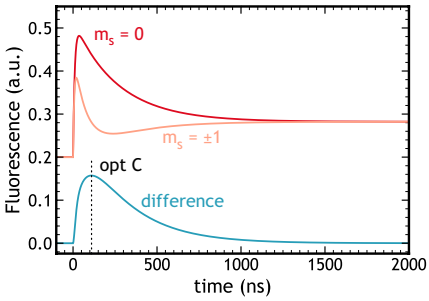

Figure 1.6: **Simulation of an NV centre emission in the time domain.** The red curve represents the fluorescence emitted by an NV centre with initial state $m_s = 0$, the orange curve for an initial state $m_s = \pm 1$ and the blue curve represents the difference. The pumping induced by the laser starts at t=0.

lower initial fluorescence that decays fast to the singlet state due to a high ISC rate. Since the singlet state mainly relaxes to the spin ground state $m_s = 0$, the fluorescence increases until reaching the steady state.

The time-resolved contrast between the states (blue curve) reveals a maximum fluorescence contrast (here at about 110 ns), which is generally used for confocal/avalanche photo diode (APD) detection. After 1200 ns of laser excitation, the NV is repolarised to the $m_s = 0$ state and prepared for the next measurement. The time needed to repolarise the NV centre depends on the pumping rate induced by the laser.

1.3.2.2 Microwave manipulation and Rabi oscillations

In the following, a static magnetic field, aligned with the NV axis such as $\vec{B}_{\parallel} = (0, 0, B_{0z})^{\intercal}$ is considered. Thus, the degeneracy of the $|\pm 1\rangle$ is lifted, allowing us to consider the ground state as a pseudo-2-level system, since the $|0\rangle \rightarrow |1\rangle$ transition can be isolated. Likewise, the transition $|0\rangle \rightarrow |-1\rangle$ could instead be considered.

Driving the spin transitions within the ground state manifold of the NV centre can be achieved by coupling the states to an additional magnetic field $\vec{B}_1(t)$ oscillating in the microwave range and perpendicular to the z-axis, such as

$$\vec{B}_1(t) = \vec{B}_1 \cos(2\pi\omega t)\,. \tag{1.7}$$

For a simple interpretation of the effect of $\vec{B}_1(t)$ on the NV-associated spin, the system is transferred into the rotating frame, spinning around the z- axis at the frequency ω. Using the rotating-wave approximation [104], $\vec{B}_1(t)$ results in an effective magnetic field of the form:

$$\vec{B}_{1,\text{eff}} = -\frac{\omega}{\gamma_{\text{NV}}}\hat{e}_z + B_1\hat{e}_x, \tag{1.8}$$

where the oscillating field is assumed to be polarised in the x- direction without loss of generality. The first term on the right-hand side of the equation (1.8) is along the z-direction and stems from the transformation. The second term reveals that $\vec{B}_1$ is constantly pointing along the x-axis.

The action of the microwave field on the NV centre can be illustrated using the so-called Bloch sphere, shown in figure 1.7. The north and south poles represent the eigenstates of the system. All points on the surface represent pure states, while the points inside the sphere represent mixed states. The trajectories in the Bloch sphere represent the interactions of the system with the environment, where the MW drives the system from one state to another.

When applying $\vec{B}_1(t)$ to the NV centre with a resonant frequency $\omega = D_{\text{gs}} + \gamma_{\text{NV}} B_{\parallel}$, the associated spin Hamiltonian becomes time-dependent, leading to Rabi nutations [105, 106] between the spins states. This resonant driving of the population between the spin states $|0\rangle$ and $|1\rangle$ yields a periodic oscillation in fluorescence as shown in figure 1.8 and is known as the Rabi cycle. The frequency Ω of the Rabi oscillations is given by:

$$\Omega = \gamma_{\text{NV}} B_1. \tag{1.9}$$

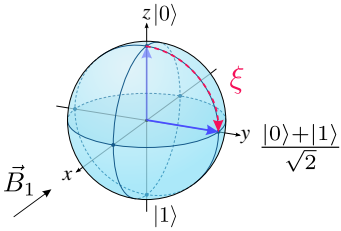

Figure 1.7: **Bloch sphere representation for the effective two-level system of $|0\rangle$ and $|1\rangle$.** The north and south poles correspond to the pure states $|0\rangle$ and $|1\rangle$, respectively.

The spin manipulation of the NV centre by MW drive brings one spin state to another, resulting in rotations on the Bloch sphere. The rotation angle ξ, as shown in figure 1.7, depends on the MW pulse strength, i.e. Ω, and its duration t_{pulse}, such as:

$$\xi = \Omega \cdot t_{\text{pulse}}. \tag{1.10}$$

For example, applying transverse microwaves in the x direction results in a precession in the yz-plane. When such a precession with an angle $\xi = \frac{\pi}{2}$ is applied to an initial state $|0\rangle$, the MW pulse brings the spin state to the equator, representing the superposition of states $\frac{|0\rangle+|1\rangle}{\sqrt{2}}$, as shown in figure 1.8. Analogously, if an angle $\xi = \pi$ is applied, the population is transferred from $|0\rangle$ to $|1\rangle$. Such pulses are named after the angle ξ they induce on the Bloch sphere, resulting here in the $\frac{\pi}{2}$-pulse and the π-pulse.

Finally, as reported in [64], another way to control the NV-associated spin would be to replace the oscillating magnetic field with an oscillating strain or an oscillating electric field. Such control has the potential to offer lower power requirements, faster spin control, and local addressability of electronic spin qubits.

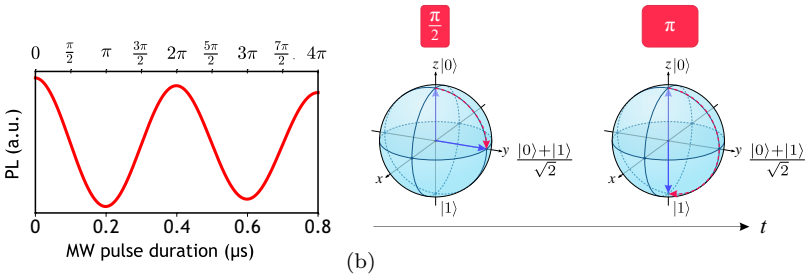

Figure 1.8: **Rabi Oscillation.** a) Fluorescence pattern and corresponding angle ξ (top axis). b) Schematic view of the action of a $\frac{\pi}{2}$-pulse (left) and a π-pulse (right) on the Bloch sphere.

1.3.3 Static and quasi-static magnetic fields sensing

Static and quasi-static magnetic fields, also denoted as direct current (DC) magnetic field, used in the sense of 'constant' field, can be measured by probing the Zeeman interaction of the NV centre, given by the equation (1.4). Gauging the Zeeman effect with NV centres can be performed with optically detected magnetic resonance (ODMR) or free induction decay (FID). In the following, the ODMR sensing method is described since it serves as the basis for the measurements performed in chapters 3 and 5. The FID acquisition scheme is briefly introduced in 1.3.4 and its comparison with the ODMR method can be found in [32].

1.3.3.1 Continuous optically detected magnetic resonance (cw-ODMR)

ODMR is the optical detection of electron resonance lines, analogous to the traditional ESR spectroscopy [107], as it allows the study of defect centres spectra [108]. The particular feature of ODMR is that the absorption of electromagnetic radiation is monitored by recording the emitted fluorescence of the defect centre. The first ODMR spectra associated with the NV centre were recorded

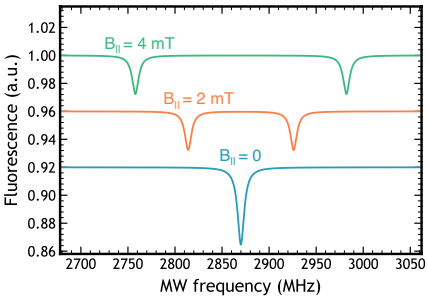

Figure 1.9: **Examples of ODMR spectra.** A magnetic field $B_{\parallel}$ applied along the NV axis results in a symmetric splitting proportional to the magnetic field strength. When the hyperfine splitting is resolved, the ODMR spectrum of an NV centre shows a two-fold hyperfine splitting, indicating coupling with the ^{15}N-nucleus (with $I_n = 1/2$). In contrast, NV centres formed with ^{14}N show a three-fold splitting caused by the ^{14}N nuclear spin ($I_n = 1$). The traces are separated by an offset for better visibility.

in 1988 [85] with an ensemble at low temperature and in 1997 [88] with a single NV centre at ambient conditions.

The acquisition of an ODMR spectrum can be done via the continuous wave (cw) method and the pulsed one. For both techniques, the measurement consists of recording the fluorescence intensity of the NV centre as a function of an applied MW frequency while scanning MW ranges comprising the resonant values.

With the cw regime, the NV centre is permanently irradiated by a 532 nm laser, which leads to its spin polarisation into the $m_s = 0$ sublevel. At the same time, MWs are applied to the NV centres while varying the MW frequency. When the MW hits the resonant frequency, the population shifts towards the $m_s = \pm 1$ sublevels, leading to a lower emission due to a higher rate through the ISC. Because of the large ZFS with $D_{gs} \simeq 2.87$ GHz at room temperature, ODMR can be performed without magnetic fields. Thus, a single dip can be

observed, as shown in figure 1.9. Applying a magnetic field $B_{\parallel}$ splits the resonance lines due to the Zeeman interaction, as discussed in section 1.3.1. Thus, measuring the frequency shift $\Delta\nu$ of the resonant lines $\nu_{\pm}$, provides direct access to the magnetic field amplitude $B_{\parallel}$. Without additional strain or electric field, the frequency shift is given by:

$$\nu_{\pm} = D_{\mathrm{gs}} \pm \Delta\nu = D_{\mathrm{gs}} \pm \gamma_{\mathrm{NV}} B_{\parallel}, \tag{1.11}$$

enabling magnetometry of static fields using NV centres [21]. Finally, the presence of off-axial components in the magnetic field leads to non-symmetric splitting. This feature can be explored to measure vectorial magnetic fields using an ensemble of NV centres, as further discussed in chapter 3.

1.3.3.2 Pulsed ODMR

The continuous laser pumping with simultaneous MW drive of the NV spins during the cw-ODMR measurement results in competing processes of spin-state initialisation and transitions driving. The sensitivity of the cw-ODMR measurement is thus limited since the contrast between the on-resonance and the off-resonance signals is reduced (see section 2.2.1).

An alternative method is to use a pulsed scheme such as pulsed-ODMR [109] or FID. Pulsed-ODMR first requires a short laser pulse to polarise the NV centre into $|0\rangle$, followed by a π-pulse driving the $|0\rangle \rightarrow |\pm 1\rangle$ transition. Since both processes are separated, the contrast can be maximised, and the sensitivity optimised to the system's limit, which is given here by the inhomogeneous relaxation time ($T_2{}^*$) [32].

However, for large ensembles of NV centres, pulsed schemes require both high optical and microwave power. In schemes such as pulsed ODMR, where the duty cycle is high, it can give rise to repetitive heat bursts and be invasive to the sample to probe. For these reasons, only cw-ODMR was employed throughout this work.

1.3.4 Spin echo and nuclear spins sensing

Recent advances in controlling the electron spin associated with the NV centre have enabled sensing, imaging, and control of individual nuclear spins [13, 110], leading to nuclear magnetic resonance (NMR) spectroscopy [111], and its imaging variant, magnetic resonance imaging (MRI) [112]. While conventional NMR/MRI is a powerful analytical technique to reveal soft matter composition in chemistry, biology, and medicine [113], the method is limited to the mesoscale. NV centres leverage NMR/MRI on the nanoscale and at ambient conditions, enabling the probing of signals within a single protein [114–116].

These sensing schemes exploit the relative phase that the coherent superposition of states $|0\rangle$ and $|1\rangle$ can acquire when subjected to a varying magnetic field, also conventionally denoted as alternating current (AC) field. The principle is detailed in the following and can be pictured using the Bloch sphere shown in figure 1.7.

Firstly, the NV centre is polarised into the state $|0\rangle$, and a $\frac{\pi}{2}$-pulse brings it to an equal superposition of state between $|0\rangle$ and $|1\rangle$:

$$|\psi\rangle = \frac{1}{\sqrt{2}}\left(|0\rangle + e^{i\varphi}\,|1\rangle\right). \tag{1.12}$$

Subsequently, the spin state collects a phase $\Delta\varphi$ during a free evolution interval time (τ), given by [13, 29]:

$$\Delta\varphi = \gamma_{\mathrm{NV}} \int_0^{\tau} B(t)dt. \tag{1.13}$$

Thus, by inferring the phase acquired by the sensor, a magnetic field $B(t)$ can be measured.

However, when spins are brought out of equilibrium, fluctuating magnetic fields[2] interact with the spin. The transverse component of this interaction with the NV centre causes the spin to pass the Larmor precession at different

[2] e.g. induced by neighbouring ^{13}C nuclei or spin impurities in the diamond lattice.

rates for each measurement run[3] and leads to the fanning out of the accumulated phase, meaning that the system loses its coherence.

However, the coherence of the system can be extended using spin echo techniques, borrowed from conventional NMR sequences. The simplest protocol is the so-called Hahn-echo technique [117], described in figure 1.10. After the free evolution time of duration τ, a $\pi-$pulse is applied to flip all spins by 180 °C with respect to the x-axis. This action inverts the dynamics of the system which refocuses again after a second period of free evolution time. The collected phase $\Delta\varphi_{\text{Hahn}}$ is thus given by:

$$\Delta\varphi_{\text{Hahn}} = \gamma_{\text{NV}} \left[\int_0^{\tau} B(t)dt - \int_{\tau}^{2\tau} B(t)dt \right]. \tag{1.14}$$

Finally, a $\frac{\pi}{2}$-pulse is applied to encode the phase into a population difference, enabling readout of the signal with optical detection. Using such spin echo techniques enables the NV spin coherence time extension from the abovementioned ${T_2}^*$ to the transversal spin relaxation time (T_2).

Interestingly, $B(t)$ becomes negative when the $\pi-$ pulse is synchronised with an AC field such as a sine wave of frequency $\left(\frac{1}{2\tau}\right)$. Thus, the two terms on the right-hand side of the equation (1.14) sum up. Since the term *resonance* in NMR implies tuning a sensor to the natural frequency of the magnetic system, such a protocol can be used to perform NMR by synchronising the phase acquired by an NV centre to the Larmor frequency of a nucleus [23]. Finally, to maximise the sensitivity to this field and shield it from noise, the sequence can be extended to maximise the total phase acquisition, such as:

$$\Delta\varphi = \gamma_{\text{NV}} \left(\int_0^{t_1} - \int_{t_1}^{t_2} + \ldots + (-1)^m \int_{t_m}^{\tau} \right) B(t)dt. \tag{1.15}$$

An example of such sequence is given in figure 1.11, depicting the $XY8$ protocol, widely used for NMR sensing using NV centres. The total number of

[3] or for each spin in an ensemble of NV centres.

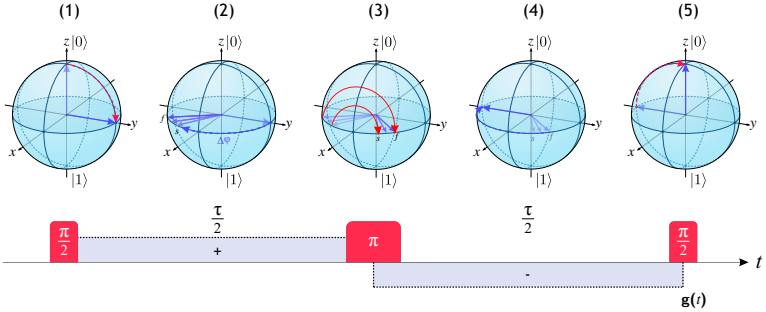

Figure 1.10: **Hahn echo sequence: a refocusing mechanism.** *Top*: Bloch spheres showing the spin state evolution during the Hahn echo sequence. The sequence is as follows: (1) A $\frac{\pi}{2}$-pulse is applied to bring the NV spin state to a superposition of $|0\rangle$ and $|1\rangle$. (2) First half of the free evolution time. The spin state undergoes a slightly different Larmor frequency for each measurement run. Slow components are denoted with the letter *s* and fast components with the letter *f*. (3) A π-pulse is applied, flipping the spin states by 180 °C. (4) Second half of the free evolution time. For each run, the same phase is picked up as in the first half of the evolution time. The inversion induced by the π-pulse refocuses the different states. (5) A final $\frac{\pi}{2}$-pulse is applied to transfer the spin state into a population difference. *Bottom*: Corresponding sensitivity function g(t), in the time domain and sequence of the applied microwave pulses. The function g(t) is positive (+) in the first half of the evolution time and is inverted due to the $\pi-$pulse in the second half (-).

pulses is limited by two factors: the coherence time the system can achieve when shielding it from environmental noise and the robustness of the pulses. Further developments, such as sequences optimisation using Hamiltonian engineering [118], optimal control [47] and deep learning [119] to extend nuclear spin imaging of large and complex spin samples have been developed.

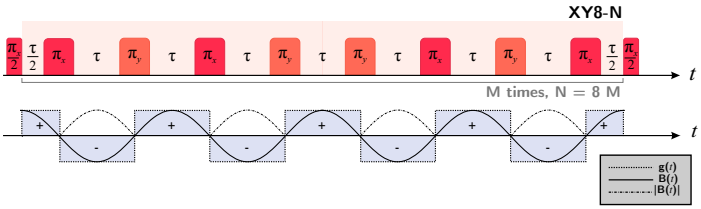

Figure 1.11: **XY8-N protocol.** *Top*: MW pulse sequence, where N is total number of π-pulses (obtained by repeating the sequence several times). π_x corresponds to a π-pulse around the x-axis, and π_y corresponds to a π-pulse around the y-axis *Bottom*: Phase signal accumulation. The plain line corresponds to the oscillating magnetic field $B(t)$, and the dotted line shows the effective field sensed by the NV centre when the sensitivity function $g(t)$ is negative.

1.3.5 Relaxometry

As mentioned above, the qubit NV centre is prone to decoherence since it couples to the environment. Albeit such coupling limits the coherence time of the sensor, it also gives a way to probe the environment.

So far, the transverse coherence time $T_2{}^*$ and its extension T_2 have been discussed. The longitudinal relaxation time, referred to as T_1, is the characteristic time for which the system returns to its thermal equilibrium after a perturbation and also sets the upper limit for T_2. At room temperature (T), the thermal energy k_BT (where k_B is the Boltzmann constant) is much larger than the energy differences of the NV ground states and leads to an equal distribution of the triplet states, as defined by the Boltzmann distribution.

Several mechanisms can lead the NV centre to relax back to its thermal equilibrium. At room temperature and under a weak external magnetic field, the longitudinal relaxation is governed by phonon-assisted processes in the lattice.

The decay into the thermal equilibrium can also be induced by magnetic noise with a frequency component around D_{gs}, i.e. the transition frequency between

the spin states of the NV at low magnetic fields. Such noise can be generated by paramagnetic impurities in the vicinity of the NV centre [120]. Subsequently, the NV relaxation rate T_1^{-1} can be decomposed into an intrinsic diamond term and an environmental term, such as:

$$T_1^{-1} = T_{1,int}^{-1} + T_{1,env}^{-1}. \tag{1.16}$$

$T_{1,int}^{-1}$ describes the relaxation rate induced by spin-lattice interactions [121] and the diamond intrinsic spin bath while $T_{1,env}^{-1}$ takes into account the external environment, such as spins at the surface of the diamond. Thus, measuring T_1 gives information about the system and its environment. The decaying process is shown with the Bloch sphere in figure 1.12.

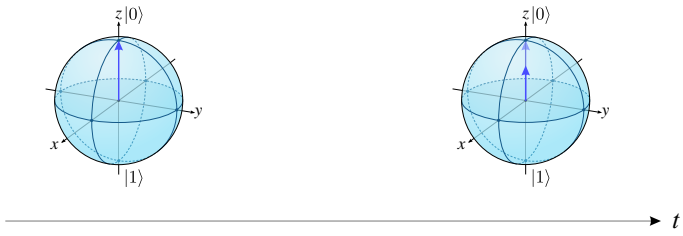

Figure 1.12: **The T_1-relaxation process on the Bloch sphere.** After polarising the NV centre into the $m_s = 0$ sublevel, the system relaxes back to thermal equilibrium after a time corresponding to T_1.

Since the longitudinal relaxation directly affects the spin population, the T_1 relaxation time of the NV centre can be evaluated with an all-optical scheme. First, the NV centre is polarised into the $|0\rangle$ ground state by applying a short 532 nm-laser pulse. Then, the system evolves during a given dark time τ, and the signal is read out by applying a second laser pulse. The sequence is repeated for different values of τ, and the acquired signal is given by:

$$S(\tau) = A \exp -\frac{\tau}{T_1} + o, \tag{1.17}$$

where A is the amplitude of the signal and o is an offset value. To obtain a better contrast of the signal, a complementary measurement including a π-pulse to invert the population can be performed.

During the dark time, flip-flop processes of the spin due to paramagnetic species can occur, inducing a faster relaxation of the NV spin state as described by equation (1.16). Such processes result from the dipole-dipole interaction between the NV centre and the spin impurities of the environment. The corresponding interaction Hamiltonian is given by:

$$\hat{\mathcal{H}}_{\text{env}} = \frac{\mu_0 \gamma_{\text{NV}} \gamma_{\text{env}}}{4\pi} \left(\frac{\hat{\vec{S}}_{\text{NV}} \hat{\vec{S}}_{\text{env}}}{|\vec{r}|^3} - \frac{3\left(\hat{\vec{S}}_{\text{NV}} \cdot \vec{r}\right)\left(\hat{\vec{S}}_{\text{env}} \cdot \vec{r}\right)}{|\vec{r}|^5} \right), \tag{1.18}$$

where $\vec{r}$ is the separation vector of the two spins, and $|\vec{r}|$ is the corresponding magnitude.

Finally, the measurement of T_1 is a way to investigate the interaction Hamiltonian given by the equation (1.18), and thus to sense fluctuating spins, as performed in [122, 123] and in the part III of this manuscript.

1.3.6 A broadband magnetic field sensor

The various techniques for measuring magnetic fields have been discussed so far in the time domain and can be expressed using a Fourier transform in their associated spectral domain. Such a transformation enables the visualisation of each experiment as a filter that shields the NV centre from sources of interactions outside the window. The narrower the window, the more selective the filter and the more sensitive the measurement.

The sensing sequences expressed in the Fourier domain result in the following filter functions [124]:

$$F_{\mathrm{ODMR/FID}}(f,\tau) = \frac{2}{\tau}\frac{\sin^2(\pi f\tau)}{(f\tau)^2} \tag{1.19a}$$

$$F_{\mathrm{Hahn}}(f,\tau) = \frac{8}{\tau}\frac{\sin^4\left(\frac{\pi f\tau}{2}\right)}{(f\tau)^2} \tag{1.19b}$$

$$F_{\mathrm{XY8}}(f,\tau,N) = \frac{8}{N\tau}\left[\frac{\sin(\pi fN\tau)}{f\tau}\frac{\sin^2\left(\frac{\pi f\tau}{2}\right)}{\cos(\pi f\tau)}\right]^2 \tag{1.19c}$$

$$F_{\mathrm{Relax}}(f,T_2^*) = \sum_{f_{\mathrm{res}}}\frac{1}{\pi}\frac{1/T_2^*}{(1/T_2^*)^2+(f-f_{\mathrm{res}})^2}. \tag{1.19d}$$

In the above equations, f is the frequency, τ is the waiting time as defined in the respective pulse sequences, and N is the total number of π-pulses used for the XY8 sequence. For an overview, these filter functions are plotted in figure 1.13 with normalised amplitudes.

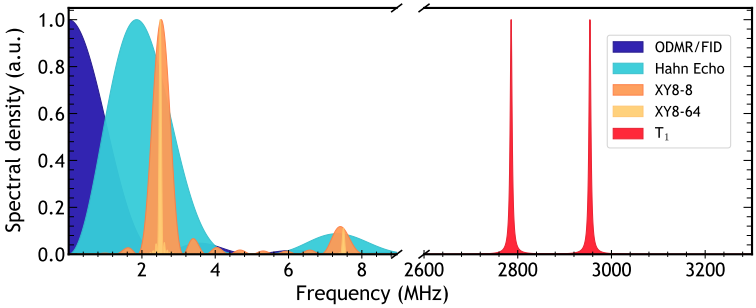

Figure 1.13: **Filter functions.** Frequency-domain filter functions for the different measurement schemes. All graphs were normalised to one for easier comparison. The following parameters were used to generate the diagrams: for the FID and Hahn echo filter function, a total evolution time of $\tau = 400\,\mathrm{ns}$ was chosen. For the XY8-8 and XY8-64 a value of $\tau = 200\,\mathrm{ns}$ was used. The splitting of the two transition lines in T_1 corresponds to the two NV transitions split induced by an offset field $B_0 = 3\,\mathrm{mT}$ along the NV axis.

The coherence times set the achievable sensitivity of the measurement, as discussed in the previous sections. Broad resonance lines in the spectrum shown in figure 1.13 underline sensing schemes limited by short relaxation times. Since the NV centre has long coherence times even at room temperature (typically a few ms for T_1 [14]), precise measurements can be performed at ambient conditions, whereas most defect centres only perform well at low temperatures. This property distinguishes the NV centre from other systems since it can be operated under a wide range of external conditions. NV centres can be employed from cryogenic temperatures [125, 126] to nearly 1000 K [127], and under extreme conditions [128]. As shown in figure 1.13, the NV centre also provides access to a high dynamic range, from quasi-static fields to gigahertz fields [16, 18, 32] and shows sensitivity down to subpicotelsa [33, 34]. Finally, it enables sensor-sample distances of only a few nanometres and, thus, spatial resolution on the nanoscale. Accordingly, the NV centre is a broadband sensor that can be tuned to various sources of magnetic fields with high sensitivity.

1.4 Engineering NV centres in diamond

1.4.1 NV centres synthesis

NV centres exist in natural diamonds, but they can be synthesised in a more controllable fashion, allowing us to tune the density of NV centres, their depth and their lateral position. There are several ways to generate NV centres in diamond.

In ultrapure diamonds such as type IIa, NV centres can be generated following two major steps, as illustrated in figure 1.14 and summarised as follows:

1. Nitrogen ions ($^{14}N^+$ or $^{15}N^+$) are implanted into the crystal, creating damages along the way in the lattice and hence, vacancies.

2. Both ingredients, nitrogen atoms and vacancies, now present inside the crystal lattice, need to be combined. Such combination is usually done using annealing with a temperature above 600 °C, for which the vacancies

migrate stochastically until meeting nitrogen atoms, thus creating NV centres.

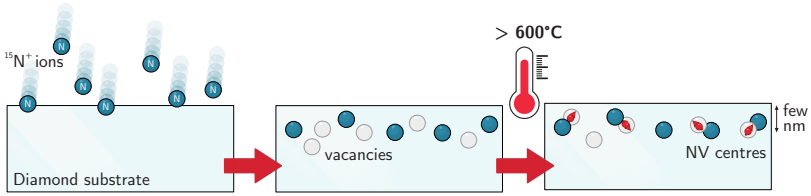

Figure 1.14: **Ion implantation process to create NV centres.** Nitrogen ions (blue spheres) are accelerated towards the diamond sample. When they penetrate the surface, they scatter inside the crystal lattice and take stochastic paths. The lateral and axial distributions of ion stopping positions depend on the ion energy, which allows us to control the depth of the NV defects. Annealing makes the vacancies mobile inside the crystal while the energy is insufficient to affect the position of the nitrogen atoms. Some vacancies migrate erratically towards a nitrogen atom, creating thus an NV centre.

The advantage of this technique is that the implantation energy is tuneable, granting control over the depth of the NV centres for which higher energies result in deeper NV centres. Additionally, NV centres can be created with a high lateral positioning accuracy as the distribution can be constrained by blocking the ion beam with masks [129]. Besides, high NV densities can be created (up to about $1000\,\mathrm{NVs}/\mu\mathrm{m}^2$), which is essential for sensing applications where the number of sensors enhances the sensitivity (see section 2.2.1). However, the depth dispersion is large even at relatively low acceleration energies due to ion straggling and channelling effects [130].

In type Ib diamonds, the procedure is similar. As the material already contains a high density of nitrogen, NV centres can be generated by creating vacancies with subsequent annealing. In such a process, vacancies are generally

created by irradiating the crystal with high-energy particles using either focused electron beams [131] or focused ion beams [132].

Another promising way to generate NV centres is to introduce nitrogen atoms into the lattice during the diamond growth [129, 133]. The most common process is delta doping, in which ultra-pure diamond containing a nanometric layer of NV centres is developed using plasma-enhanced chemical vapour deposition (PECVD) [134]. First, an ultra-pure diamond substrate is grown using methane gas, followed by the introduction of an N_2 gas, creating a nitrogen-doped layer. The nitrogen gas release is then stopped, and another layer of pure diamond is overgrown. Finally, NV centres are formed separately from the nitrogen incorporation by creating vacancies with *ex-situ* electron irradiation and subsequent annealing. The advantage of this technique is the nanometre-scale depth control on the layer's thicknesses, enabling sharp axial NV centres density profiles. Additionally, far less damage in the nitrogen-doped layer is created compared to ion implantation techniques as only electrons are damaging the lattice [135]. Hence, the NV centres' coherence times are generally better than those obtained by ions implantation [134]. However, the lateral density of NV centres is low compared to implantation processes where about 10^3 denser samples can be prepared. Furthermore, clusters of lone nitrogen atoms, also known as P1 centres, can be prominent, creating spurious interactions with the NV centres.

Alternatively, NV centres can be generated *in situ* using laser writing. A single laser pulse (the "seed pulse") is applied to a diamond sample containing nitrogen atoms. The seed pulse generates an ensemble of vacancies, and a subsequent 1 kHz stream of pulses ("annealing pulses") is applied to irradiate the same region, inducing the diffusion of vacancies. The fluorescence in this region is monitored during the annealing pulse stream until a signal indicating the creation of an NV centre is recorded. The NV centres can be positioned with high precision, with a lateral positioning accuracy of about 33 nm and near-unity yield [136]. If delta-doped diamonds are used, the axial position accuracy can reach the nanometre precision.

Several other methods aim to obtain NV centres with a preferential alignment along one direction [137, 138]. Such diamond samples are relevant for applications where the alignment homogeneity of the NV centres is essential such as for an NV quantum spin register [139]. Another application concerns ensemble-based magnetometry for which the sensitivity is greatly enhanced as more NV centres can be simultaneously addressed to contribute to the signal [140].

Within this work, all the diamond samples were engineered using $^{15}N^{+}$ implantation at low energy. The resulting high density of NV centres using this approach outweighs the increase in coherence times obtained by other methods for the applications discussed in this dissertation. Further details about the implantation parameters can be found in appendix A.

1.4.2 Setup configurations

Depending on the targeted application, different configurations of the NV centre implantation can be considered as depicted in figure 1.15. A single NV centre can be used to gain local precision, such as in a scanning-probe device [22, 141] or to address a single electron spin as for quantum information processing applications [43, 45, 142]. An ensemble of NV centres can be used to gain in sensitivity (see section 2.2.1), image large areas, or to gain in vectorial information (see chapter 3). Several configurations with ensembles are possible: a thin layer of NV centres close to the surface is optimal to image proximal magnetic sources and avoid background noise, whereas a volume sensor is favourable to sense magnetic fields away from the sensor, such as with gradiometers [34]. Nanodiamonds can serve to track temperature since the contact surface is minimised or to track local chemical events in bio environments [143–146]. Finally, diamonds can be engineered to optimise the collection efficiency of the signal, *e.g* by using an array of NV centres in nanopillars [147].

A close-up of the configuration employed in this work is given in figure 1.16. A two-dimensional layer of NV centres is obtained by nitrogen implantation,

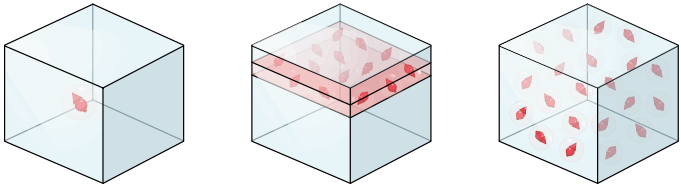

Figure 1.15: **NV centres configurations.** *Left:* A single NV defect in an ultra-pure diamond. *Middle:* A 2D layer of an ensemble of NV centres parallel to the diamond surface. This geometry was used throughout this work. *Right:* A 3D ensemble of NV centres homogeneously distributed within the diamond sample.

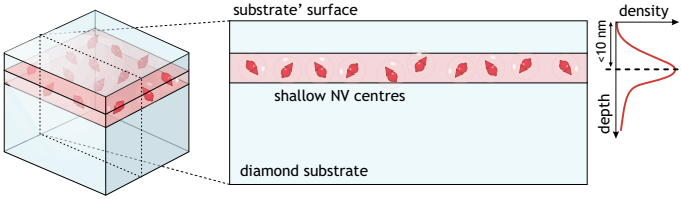

Figure 1.16: **Shallow NV ensemble.** The experimental configuration used in this work. Diamond membranes are implanted using nitrogen ion beams with low energy. A cross-section through the diamond substrate shows that a shallow two-dimensional ensemble of NV defects is located within a few nm below the surface, depending on the implantation energy. An implantation energy of 2.5 keV results in a median depth of the NV centres below 10 nm.

resulting in an NV centres' depth distribution spanning several nanometres. For spins sensing applications, it is crucial to place the NV centres close to the diamond surface, within the interaction range of an external sample containing electron or nuclear spins [148, 149]. Typical implantation energies to obtain shallow NV centres are below 20 keV. However, photoionisation is particularly

relevant for proximal NV centres, where impurities and surface termination influence the band structure [36, 150, 151]. As such, implantation energies used in this work were kept above 2.5 keV, resulting in a median NV depth below 10 nm. Additionally, the implantation process was followed by an oxygen-termination treatment. Such implantation ensures stable defects but is still close enough to the surface to interact with external spins (see appendix A). Nitrogen fluences used for the implantation of shallow ensembles used in this work are given in appendix A.

Chapter 2

NV-based widefield microscopy

With a rich history spanning hundreds of years, microscopes [152, 153] are indispensable tools in many areas of scientific research, enabling the visualisation and capture of images at various scales. One of the prevailing microscopy techniques is light microscopy with a *widefield* approach since it is within reach of a broad scientific community. Such accessibility is an essential prerequisite for scientific advances across several research fields.

In this chapter, the NV-based version of the widefield microscope is presented. The chapter is structured as follows:

(1) Section 2.1 gives an introduction to widefield microscopy. It also introduces the Fourier analysis as a basis for understanding the analytical tools used in chapter 4.

(2) Section 2.2 gives a brief overview of the combination of NV-based sensing with widefield microscopy.

2.1 Widefield microscopy

2.1.1 Standard light microscopy

Since the first studies conducted by Robert Hooke using a microscope [1], the instrument has enabled many discoveries that have led to our modern world.

Standard light microscopes consist of two subsystems: an illumination system that irradiates the sample and an imaging system that produces a magnified image of the light that has interacted with the sample. Various configurations are possible for the construction of a microscope. For light microscopy, widefield and confocal microscopes can be employed. The configurations are depicted in figure 2.1.

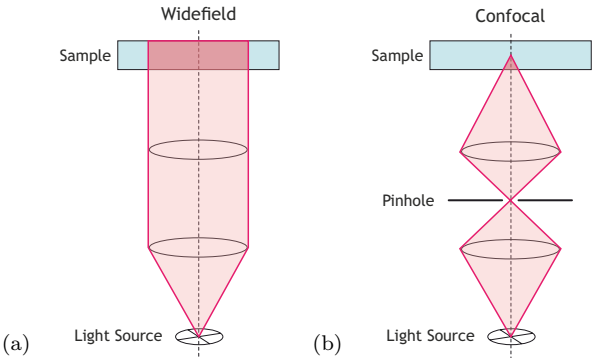

Figure 2.1: **Widefield vs confocal illumination.** a) With the widefield configuration, the light coming from the source is collimated and the whole sample is illuminated. b) With the confocal configuration, the light coming from the source is focused through a pinhole and subsequently to the sample. Adapted from [154].

With widefield microscopes, the object or specimen of interest is irradiated with a light source over the entire area to image. The resulting image is either viewed directly through an eyepiece or captured by a multi-array sensor such as a charge coupled device (CCD) or a complementary metal–oxide–semiconductor (CMOS) camera [155]. The choice of camera is crucial because it determines the experiment's performance [49]. For example, lock-in cameras enable acquisitions with high temporal resolution [156], while CCD cameras aim to be highly sensitive to the signals [157].

With confocal microscopes [158], the object or sample of interest is illuminated by a light source at only one focal point at a time. A pinhole eliminates out-of-focus and background fluorescence, allowing the acquisition of sharper images. However, image acquisition with a confocal microscope often requires more time, as a longer exposure time is needed to collect a sufficient amount of in-focus light to generate images [159].

Finally, when objects or specimens are photosensitive, the use of light to seek their properties can be invasive and alter their behaviour. This is the case with most living specimens, which are subject to phototoxicity [160]. One advantage of the widefield microscope is that it offers a high degree of freedom with regard to the incident light. The angle of incidence can be chosen so that the light hits the sample at the critical angle that allows total reflection at the interface between the coverslip and the specimen. Such configuration thus limits the spurious light exposure of the sample [161].

2.1.2 Spatial resolution

In imaging techniques, spatial resolution is an essential parameter to characterise as it defines the power to resolve nearby objects in real-space. For optical imaging instruments, the spatial resolution is fundamentally limited by the diffraction of light [162]. For a microscope with a circular aperture of diameter D, the diffraction pattern has a radial symmetry given by the Airy pattern shown in figure 2.2.

According to the Rayleigh criterion [163], it is only possible to distinguish a pair of light sources if the central peaks of the two diffraction patterns are not closer than the radius of the Airy disc, as depicted in figure 2.3. The lateral spatial resolution xy of an optical microscope is thus defined by the Airy radius r_{Airy} given by:

$$r_{\text{Airy}} = \frac{1.22\lambda}{2\text{NA}}, \tag{2.1}$$

where λ is the wavelength of the illuminating light and NA is the numerical aperture of the microscope's objective.

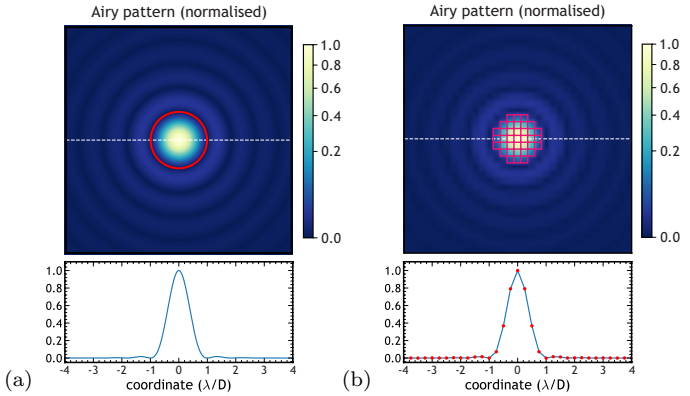

Figure 2.2: **Airy pattern.** a) *Top*: Diffraction pattern (Airy disc) produced by the fluorescence emission of a single point source. *Bottom*: profile of the Airy pattern taken along the dashed line. b) *Top*: Discretised Airy pattern. *Bottom*: profile of the discretised Airy pattern taken along the dashed line. Red dots indicate the position of the data points.

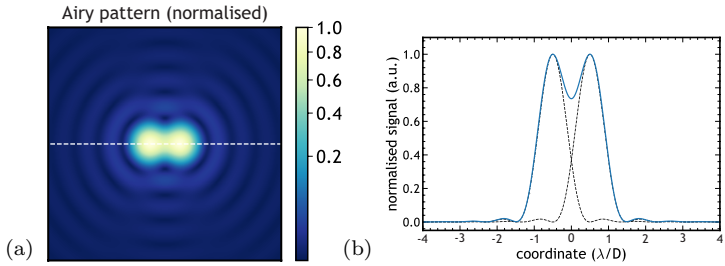

Figure 2.3: **Rayleigh criterion.** a) Two Airy patterns separated according to the Rayleigh criterion. b) Profile of the pattern taken along the dashed line. The solid blue line corresponds to the total signal amplitude, and the dashed lines to each single Airy disk.

In the case of a signal recorded with a camera, the signal is discretised as shown in figure 2.2b. Therefore, it is important to define the pixel size according to the airy disc to preserve the spatial resolution of the microscope.

Finally, superresolution techniques such as stimulated-emission-depletion (STED) microscopy [164, 165] or stochastic optical reconstruction microscopy (STORM) [166] can be employed to improve the spatial resolution beyond the diffraction limit.

2.1.3 Fourier space imaging

The Fourier transform is an important image processing tool which is used in a wide range of applications such as image analysis, image filtering, image reconstruction and image compression. All the principles developed in this part will serve as the basis for the current distribution reconstruction described in chapter 4.

Derived from Huygens' principle where the optical signal is considered as a sum of several oscillations, the Fourier transform decomposes an image into sine and cosine components. The output of the transformation represents the image in the Fourier space or frequency domain, while the input image corresponds to the spatial domain. In the Fourier domain image, each point represents a particular frequency contained in the spatial domain image.

The 2D Fourier transform is given by:

$$F(k_x, k_y) = \int\int f(x, y)\, e^{-j2\pi\left(k_x x + k_y y\right)} dxdy, \tag{2.2}$$

where (x, y) are the real space components and (k_x, k_y) the Fourier space components, as defined in figure 2.4. In order to grasp the meaning of the Fourier space, figure 2.5 shows components of the k-space and their translation to the real space.

To illustrate image processing using the Fourier space, the photo, shown in figure 2.6, will serve as an example. An image is a matrix of PxS pixels

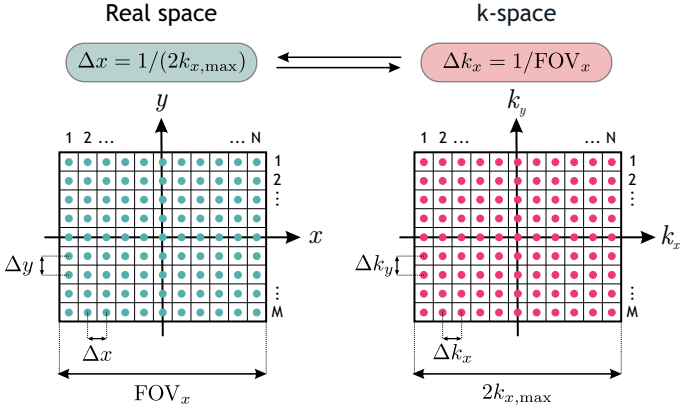

Figure 2.4: **Real space and k-space structures.** The frame size of the real space image defines the frequency resolution of the k-space, and vice versa.

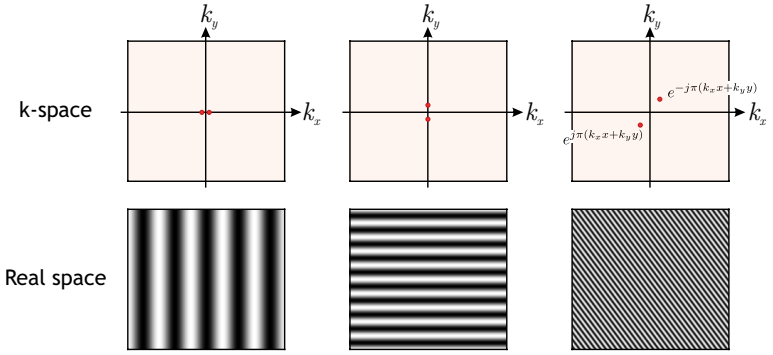

Figure 2.5: **k-space components and their translation to real space.** Low frequencies in k-space result in a sinusoidal signal with a large period in real space, while high frequencies in k-space result in a sinusoidal signal with a small period. Furthermore, the vectors (k_x, k_y) define the orientation of the oscillations.

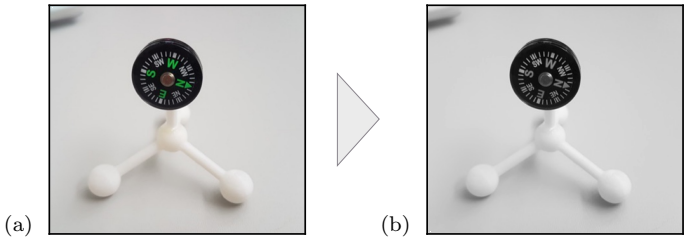

Figure 2.6: **Photograph to analyse.** a) Photograph encoded with RGB values. b) Photograph translated to grey scale.

encoding light intensity. For a coloured image, the matrix is of size CxPxS where C=3 encodes the light intensity for red, green and blue values, generating RGB encoding. Although many entry-level cameras can produce coloured images, a large portion of scientific research, including the one used in this work, is carried out with monochrome cameras. Hence, for the sake of simplicity and without loss of generality, the photo shown in figure 2.6a is translated into grey scale. To execute the Fourier transformation into an RGB encoded picture, required in fields such as histology where tissues are stained with bright colours, the process must be repeated for the three RGB matrices.

The amplitude of the Fourier transform of the image is shown in figure 2.7, where the pattern is too complex to understand the meaning of the individual contributions.One way to understand the Fourier image is to filter the frequencies and apply the inverse Fourier transform to recreate the image to see the changes. For this purpose, the Hanning window [167] shown in figure 2.8 serves as a filter. When a positive Hanning window is applied to the image in the Fourier space, the high-frequency components are filtered out. This removes all the fine details of the image in real space and blurs the image as shown in figure 2.9. On the contrary, when a negative Hanning window is applied to the image in the Fourier space, the low-frequency components are filtered out. This leaves only the fine details of the image in real space, as shown in figure 2.9.

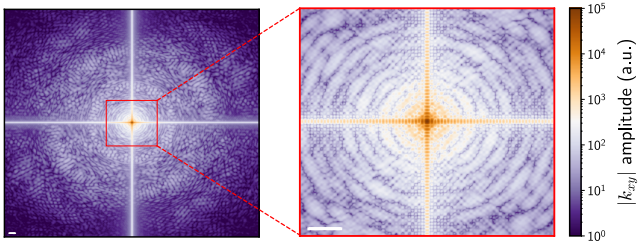

Figure 2.7: **Photograph's k-space.** The left-hand side panel shows the entire k-space attributed to the photograph, and the right-hand side shows a zoom-in of the central part, outlined by a red box. Scale bars represent 10 unit values.

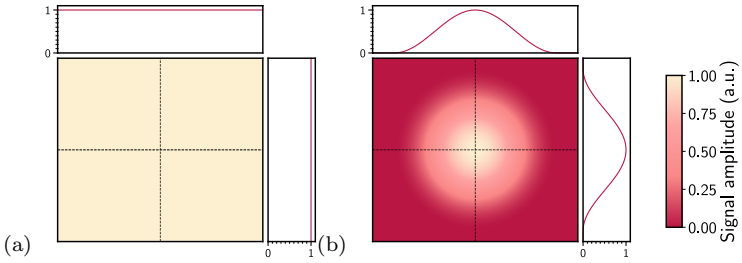

Figure 2.8: **Hanning window.** a) All-ones matrix before applying a filter function. b) Resulting matrix after convolution with a Hanning window with parameter $= 40 * k$.

Finally, it is important to point out that the Hanning window is an interesting filter because it smoothly excludes the values of k-space without producing artefacts like sharp filters. Therefore, this is the filter used in chapter 5 to remove high-frequency noise components from the Fourier images used for the reconstruction of the current distributions.

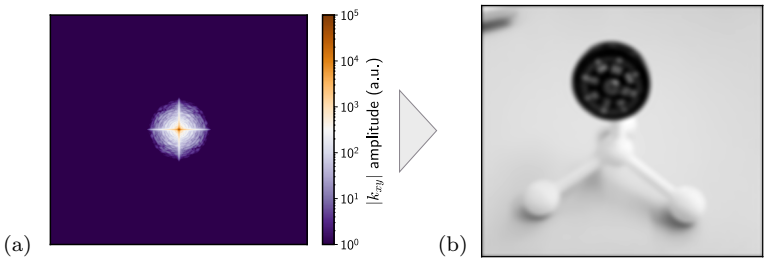

Figure 2.9: **k-space low frequencies selection.** a) Photograph's k-space convoluted with a Hanning window with parameter $= 250 * k$. b) Resulting real-space image where only the large features appear.

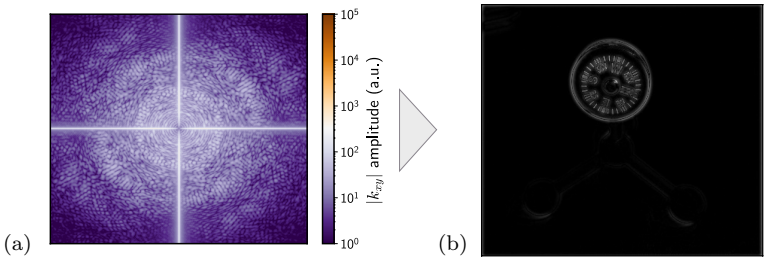

Figure 2.10: **k-space high frequencies selection.** a) Photograph's k-space convoluted with a negative Hanning window with parameter $= 250 * k$. b) Resulting real-space image where all the fine details appear.

2.2 NV-based widefield microscope: a magneto-optical imaging system

Since the first experimental realisation of the widefield NV microscope in 2010 [168], the technology has seen rapid development and demonstration of applications in various areas across condensed matter physics, technology and biology [47, 122, 169–173].

2.2.1 NV ensemble measurements

Employing several sensors simultaneously amplifies the detected signal and inherently improves the magnetic sensitivity which scales with $\frac{1}{\sqrt{N_{\mathrm{NV}}}}$, where N_{NV} is the number of interrogated NV centres [16]. The minimum detectable magnetic field δB_{min} is proportional to the following terms [174, 175]:

$$\delta B_{\mathrm{min}} \propto \frac{1}{\gamma_{\mathrm{NV}}} \cdot \frac{1}{\sqrt{N_{\mathrm{NV}} \cdot T_{\mathrm{relax}}}} \cdot \frac{1}{C\sqrt{\zeta}} \cdot \frac{1}{\sqrt{t_{\mathrm{m}}}}. \tag{2.3}$$

The first term in the right-hand side of equation (2.3) is given by the electron of the NV centre. The first term highlights that employing electron spins for sensing is advantageous compared to their analogue nuclear spin, since $\gamma_{\mathrm{NV}} \propto \mu_B \gg \mu_N$, where μ_N is the nuclear magneton. The second term is the one of interest in this section since it highlights that employing an ensemble of NV centres enhances the sensitivity. However, the density of NV centres is intrinsically connected to the maximum interrogation time of the system given by T_{relax}. For example, for NV centres obtained by nitrogen implantation as discussed in chapter 1, the higher the density of NV centres, the higher the number of lone nitrogen atoms and damages in the lattice, leading to shorter dephasing times T_{relax}. Therefore, engineering diamonds with a high density of NV centres while preserving their coherence time is one of the key strategies to improve the sensitivity of NV centres. The third term accounts for optical detection where C represents the signal's contrast and ζ the detection efficiency. Finally, the last term takes into account the total measurement time t_{m} during which the sensing protocol is repeated several times to improve the signal.

In order to compare different sensing schemes, it is common to use the sensitivity η, corresponding to the minimum detectable field normalised to the corresponding measurement time, such as:

$$\eta = \delta B_{\mathrm{min}} \cdot \sqrt{t_{\mathrm{m}}}, \tag{2.4}$$

where η is thus given in units of $\mathrm{T}/\sqrt{\mathrm{Hz}}$.

2.2.2 Experimental Setup

The custom-built wide-field fluorescence microscope is depicted in figure 2.11. The experimental setup consists of an air objective[1] (Olympus MPLAPON 50×, NA = 0.95), a 650 nm long-pass filter (Omega), a 300 nm tube lens and a Cascade II:512 CCD camera (512 × 512 pixels, Photometrics), resulting in an effective pixel width of about 192 nm on the object side.

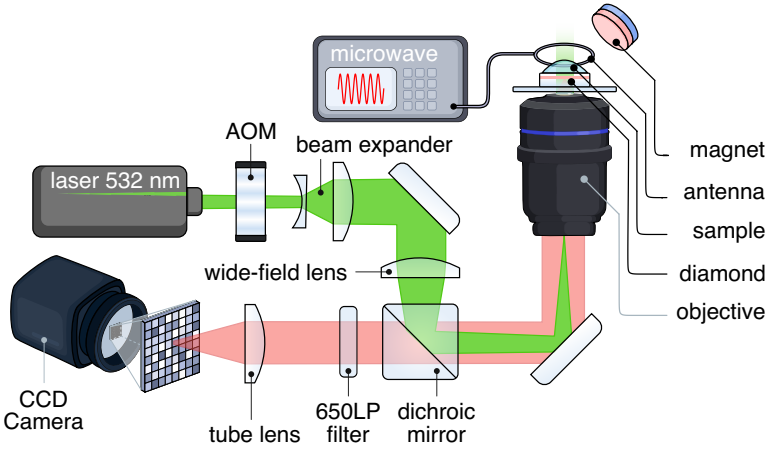

Figure 2.11: **Widefield experimental setup.** Three main ingredients enable optically detected magnetic resonance measurements with NV centres: 1) the optical excitation for polarisation and readout of the spin state, 2) MW spin control and 3) detection of the NV fluorescence.

Experimental realisation of the measurement protocols was achieved by exciting NV centres with a 532 nm laser (Coherent) gated with an acousto-optic modulator (AOM) (Crystal Technology, Model 3250) and coupled into the optical path with a dichroic mirror (Semrock). Simultaneously, microwave radiations were generated using an MW source (Rhode&Schwarz SMBV100A) and amplified (100S1G4, Amplifier Research) before being sent to a microwave an-

[1] In chapter 6, an oil objective (Olympus PlanAPO N, 60×, NA = 1.49)) is employed.

tenna (e.g. a 50 µm-thick copper wire). Finally, in order to limit the acquisition of the NV^0 emission [176], which does not contribute to the measurement signal, a 650 nm longpass (LP) filter was used in this work.

2.2.3 Widefield workflow

The slow detection of the CCD camera, does not enable gating the detection to maximise the measurement contrast, as defined in figure 1.6. Instead, the signal is integrated until the NV centres are polarised, as shown in figure 2.12.

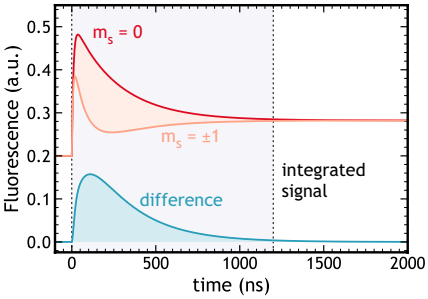

Figure 2.12: **Integrated signal for slow detectors.** The CCD camera's gating being too slow to resolve the fluorescence in the nanosecond time domain, the signal is integrated over time, until the steady-state is reached (here at 1200 ns). The integration of the signal results in an overall reduced contrast, which is then compensated by the use of an ensemble of NV centres to keep a high sensitivity.

As such, a fluorescence averaging scheme is used in which the camera is continuously exposed to fluorescence while the pulse sequence is repeated several times. The principle is depicted in figure 2.13. For a given experiment, there is a set of K-independent parameters over which the sequence runs. In the case of a T_1 measurement, these are K different periods of dark time τ. The sequence with a given parameter is repeated R times for one image to collect a sufficient amount of photons, and the image is transferred to the computer running the

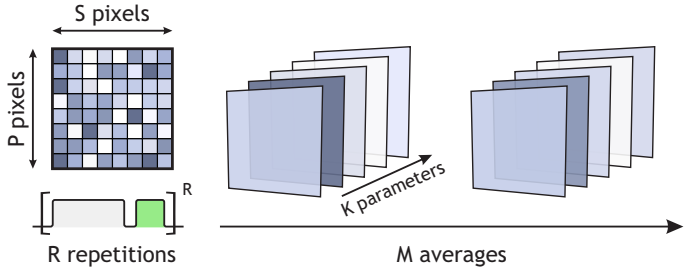

Figure 2.13: **Experimental workflow with CCD readout.** (i) Frames are captured by repeating the measurement sequence R times while exposing the camera to maximise the acquired fluorescence signal. (ii) The measurement iterates over the K combinations of the experimental parameters. (iii) M averages of each image can be acquired for further averaging. The final dataset contains K × M frames.

measurement software. The sequence then continues with the next parameter K for the second exposure. After all parameters have been run through, a new series of images can be acquired for further averaging. After M measurement runs, M × K frames have been collected. For background correction, a second sequence is usually performed so that a total of 2 × M × K frames are acquired.

Part II

Probing arbitrarily shaped microelectronics' activity

The continuous scaling of semiconductor-based technologies to micron and sub-micron regimes has resulted in higher device density and lower power dissipation. Many physical phenomena, such as self-heating or current leakage, become significant at such scales. Thus, developing sensors able to **map current densities revealing these features is decisive for the development of modern electronics.**

An efficient way to visualise such charge transport is to **image the associated magnetic fields** that pass unaffected through the materials used in semiconductor devices. However, advanced non-invasive technologies offer either low sensitivity or poor spatial resolution and are limited to the two-dimensional spatial realm only.

In part II of this dissertation, chapter 3 describes the optimisation process to analyse the NV centres signal and retrieve the vectorial magnetic field synchronously with temperature gradients and other parameters affecting the diamond crystal lattice. This procedure enables an excellent signal-to-noise ratio (SNR) of the magnetic fields, enabling mapping of the associated vector currents with high spatial resolution and precision, as described in chapter 4. Finally, chapter 5 demonstrates three-dimensional current density imaging within an integrated circuit in pre-development.

The long-term goal of such developments is to build a user-friendly and versatile device with minimal overhead to bridge gaps in multidisciplinary fields. Such an instrument will benefit both the semiconductor industry by enabling failure analysis of 3D devices and the spintronic community by enabling the analysis of three-dimensional signals in multi-layered devices.

Chapter 3

Optimisation of vectorial magnetic field imaging

Detecting weak magnetic fields with nanoscale resolution is essential in fundamental physics [177], material sciences [178, 179], medicine [180–182], and modern technologies (see chapter 5). The unique ability of NV centres to detect vectorial fields on the nanoscale, offers a new perspective in these disciplines as it enables current density [37, 170, 183] and stray magnetic field imaging [42, 141, 171, 184, 185] on the nanoscale. Advancements in vector fields imaging using NV centres already enabled remarkable achievements such as revealing spin waves [186] and electric fields associated with surface band bending in diamond [36], probing Johnson noise in metals [35], and imaging current density with spatial resolution down to 22 nm [37].

In this chapter, an optimised technique is developed to synchronously determine a magnetic field with its absolute orientation, temperature gradients and strain/electric fields affecting the crystal field of the diamond host. This technique will help to enhance imaging of current density, as demonstrated in chapter 5 and to image various parameters in a single measurement, particularly relevant for seeking new phases of matter [187–189].

The chapter is structured as follows:

(1) Section 3.1 introduces quasi-static vectorial fields measurements using NV centres in diamond.

(2) Section 3.2 discusses how to reconstruct vectorial fields in the lab frame using the measurements collected in the NV frame and how to optimise the process.

(3) Section 3.3 demonstrates imaging of current-associated magnetic fields produced by a complex microstructure.

(4) Finally, in section 3.4, the conclusions and outlook of the chapter are discussed.

3.1 Probing the NV centre's Hamiltonian for quasi-static vectorial field imaging

3.1.1 Vector magnetic field imaging

A large panel of magnetometers has been developed over the past few decades. They fall into two major categories: scalar magnetometers and vector magnetometers.

The sensing element of a scalar magnetometer tends to align along with the magnetic field. Hence, they sense the entire magnetic field and can be highly sensitive, as demonstrated with vapour cell magnetometers [174]. However, the sensor can sense the magnitude only and not the direction.

In contrast, superconducting quantum interference devices (SQUIDs), Hall probes, fluxgate magnetometers, and NV sensors are vector magnetometers. In this case, the sensing element is fixed in space and does not align along the magnetic field's direction. Therefore, such devices sense the field projection along with the sensing element [190]. The advantage of the NV sensor among

the vector magnetometers is that NV centres present up to four symmetry axes, forming a basis spanning the three-dimensional space within a single device on the atomic scale. Therefore, NV centres can be used to determine the three-dimensional vector information reliably [21, 168].

In the following, the vector field sensing ability of NV centres will be described.

3.1.2 Probing the quasi-static Hamiltonian of a single NV centre

As described in chapter 1, a single NV centre (see figure 3.1) possesses an electron spin $S = 1$ causing interactions with surrounding electromagnetic fields. Besides, fields such as strain and temperature mediated through the crystal lattice also affect the NV centre. All these parameters can be captured in the Hamiltonian associated with the NV centre.

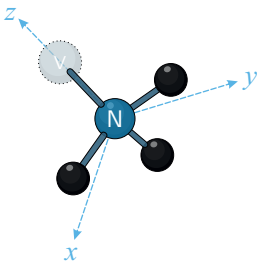

Figure 3.1: **Chosen frame for a single NV centre.** By convention, the NV centre's main axis coincides with the z-axis of an arbitrarily chosen xyz frame.

The Hamiltonian for the NV ground state spin in the presence of a bias magnetic field $\boldsymbol{B} = \{B_x, B_y, B_z\}$, an electric field $\boldsymbol{E} = \{E_x, E_y, E_z\}$, and intrinsic crystal strain $\boldsymbol{M} = \{M_x, M_y, M_z\}$ is given by equation (3.1) [64, 191]:

$$\frac{\hat{\mathcal{H}}_{NV}}{h} = D_{\mathrm{gs}}\left[\hat{S}_z^2 - \frac{2}{3}\right] + \varepsilon_{\mathrm{gs}}\left(\hat{S}_x^2 - \hat{S}_y^2\right) \tag{3.1a}$$

$$+ \gamma_{NV}\left[B_x\hat{S}_x + B_y\hat{S}_y + B_z\hat{S}_z\right] \tag{3.1b}$$

$$+ d_{\parallel}E_z\left[\hat{S}_z^2 - \frac{2}{3}\right] - d_{\perp}E_x\left(\hat{S}_x^2 - \hat{S}_y^2\right) + d_{\perp}E_y\left(\hat{S}_x\hat{S}_y - \hat{S}_y\hat{S}_x\right) \tag{3.1c}$$

$$+ M_z\left[\hat{S}_z^2 - \frac{2}{3}\right] + M_x\left(\hat{S}_x^2 - \hat{S}_y^2\right) + M_y\left(\hat{S}_x\hat{S}_y - \hat{S}_y\hat{S}_x\right). \tag{3.1d}$$

By convention, the Hamiltonian is written such that the z-axis coincides with the NV centre's quantisation axis (see section 1.3.3). Interactions such as hyperfine coupling have been disregarded for simplicity. The coupling terms and typical sensitivity parameters can be found in table 3.1.

The right-hand side terms of equation (3.1a) express the ZFS, described in section 1.3.1. As mentioned in section 1.3.1, the ZFS term is the dominant interaction for all experiments presented in this manuscript and most typical experiments. Both ZFS components depend on the temperature T and pressure P, yet transversal variations are small and usually neglected. The dependence of D_{gs} with T and P is expressed in table 3.1. Additionally, the inhomogeneous spin lifetime T_2^* is temperature independent up to at least 625 K, suggesting that single NV centres can serve as nanoscale thermometers over a broad temperature range [192].

The terms expressed in equations (3.1b) and (3.1c) represent the Zeeman and Stark effects due to nearby magnetic and electric fields, respectively. The vectorial dependence of these fields enables monitoring changes in both magnitude and orientation. Thus, the NV centre can serve to probe vectorial electromagnetic fields. However, the coupling parameters show that the magnetic interaction is significantly larger than the electric one. Accordingly, the NV centre is mainly used as a magnetometer. Measuring electric fields with a single NV centre requires suppression of the magnetic field interaction to achieve a good sensitivity [193].

Finally, the last part of the Hamiltonian (3.1d) represents the strain mediated by the diamond lattice through spin-orbit coupling. The interactions act as pseudo-electric field interactions.

Property	Coupling coefficient		Typical sensitivity[1]	Reference(s)
Magnetic field[2]	γ	28 GHz/T	$0.36\,\mu\mathrm{T}/\sqrt{\mathrm{Hz}}$	[21–23, 194]
Electric field[2]	$d_{\parallel}$	$0.17\,\mathrm{Hz}/(\mathrm{V/m})$	$5.8\,\mathrm{kV/cm}/\sqrt{\mathrm{Hz}}$	[87, 193]
Electric field[3]	$d_{\perp}$	$3.5 \times 10^{-3}\,\mathrm{Hz}/(\mathrm{V/m})$	$280\,\mathrm{kV/cm}/\sqrt{\mathrm{Hz}}$	[87, 193]
Strain[3]	$\sim d_{\perp}/p^4$	$\sim 10^{11}\mathrm{Hz}/(\delta l/l)$	$\sim 10^{-7}\,\sqrt{\mathrm{Hz}}$	[25]
Orientation[5]	γB	100 kHz/°	$0.1\,°/\sqrt{\mathrm{Hz}}$	[22, 143]
Temperature	$\partial D/\partial T$	−74 kHz/K	$0.13\,\mathrm{K}/\sqrt{\mathrm{Hz}}$	[56–58, 195]
Pressure	$\partial D/\partial P$	1.5 kHz/bar	$6.8\,\mathrm{bar}/\sqrt{\mathrm{Hz}}$	[196]

[1] Typical sensitivity for DC detection assuming a frequency resolution of $10\,\mathrm{kHz}/\sqrt{\mathrm{Hz}}$.
[2] Longitudinal ($\theta = 0°$), where θ is the angle between the NV axis and the electric field.
[3] Transverse ($\theta = 90°$).
[4] $p \approx 3 \times 10^{-13}\,(\mathrm{V/m})^{-1}$ is the local piezoelectric coupling coefficient [25].
[5] At a transverse magnetic field of 1 mT.

Table 3.1: **Coupling coefficients and typical sensitivities.** Table reported from [17].

In principle, the NV centre's ground state Hamiltonian terms are accessible experimentally, but measurements using the electron spin of a single NV centre give limited information. The electron spin associated with the NV centre interacts with an effective field corresponding to its projection on the NV axis. As such, the vectorial information is incomplete if no complementary experiments are done or if no prior knowledge about the vector field is available. Alternatively, probing NV centres on several crystal axes can be sufficient to infer vector fields.

3.1.3 Probing quasi-static Hamiltonian of an ensemble of NV centres

Probing the electron ground state Hamiltonian of an ensemble of NV centres enables inferring the complete vector information about a nearby field through

the relevant interaction term (e.g. the Zeeman term for magnetic field sensing [21, 168]). Due to the diamond geometry, four tetrahedral orientations of the NV bond are possible in a sample reference frame xyz, as depicted in figure 3.2, where the bonds are denoted by the letters $\{A, B, C, D\}$.

The ground state Hamiltonian $\mathcal{H}_{NVi}$ of an NV centre along an N-V$_i$ axis, with $i \in \{A, B, C, D\}$, can be rewritten as follows:

$$\frac{\mathcal{H}_{NVi}}{h} = (D_{\text{gs}} + \delta)\left[\left(\hat{u}_{NVi}\cdot\hat{S}_z\right)^2 - \frac{2}{3}\right] + \gamma_{\text{NV}}\vec{B}\cdot\vec{S} \tag{3.2a}$$

$$- \alpha\left[\left(\hat{u}_{NVi}\cdot\hat{S}_x\right)^2 - \left(\hat{u}_{NVi}\cdot\hat{S}_y\right)^2\right] \tag{3.2b}$$

$$+ \beta\left[\left(\hat{u}_{NVi}\cdot\hat{S}_x\right)\left(\hat{u}_{NVi}\cdot\hat{S}_y\right) + \left(\hat{u}_{NVi}\cdot\hat{S}_y\right)\left(\hat{u}_{NVi}\cdot\hat{S}_x\right)\right], \tag{3.2c}$$

where the four NV axes of a (100)-oriented crystal are defined in the lab frame xyz as follows:

$$\hat{u}_{NVA} = \pm\frac{1}{\sqrt{3}}\begin{pmatrix}-\sqrt{2} & 0 & 1\end{pmatrix} \tag{3.3}$$

$$\hat{u}_{NVB} = \pm\frac{1}{\sqrt{3}}\begin{pmatrix}\sqrt{2} & 0 & 1\end{pmatrix} \tag{3.4}$$

$$\hat{u}_{NVC} = \pm\frac{1}{\sqrt{3}}\begin{pmatrix}0 & -\sqrt{2} & 1\end{pmatrix} \tag{3.5}$$

$$\hat{u}_{NVD} = \pm\frac{1}{\sqrt{3}}\begin{pmatrix}0 & \sqrt{2} & 1\end{pmatrix}. \tag{3.6}$$

Since the crystal strain (due to external pressure or lattice imperfections) can be written as an effective electric field, coupling terms related to electric and strain fields have been expressed in common terms α, β, δ in $\mathcal{H}_{NVi}$. If vectorial Stark effects are relevant, e.g. to imaging high voltage currents, explicit expressions in the adopted coordinate system can be expressed as developed in [197, 198].

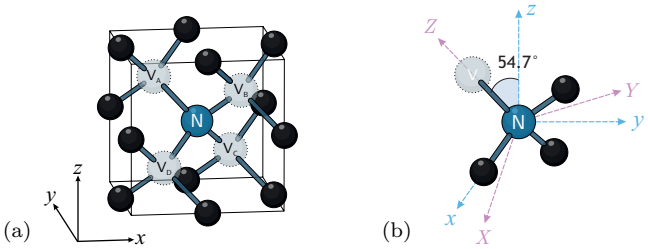

Figure 3.2: **Possible orientations of the NV centres in the diamond lattice.** a) Representation of the four possible tetrahedral orientations of the NV bond for a (100)-oriented crystal in the reference frame xyz. The four possible NV-associated axes are defined by the combination of the nitrogen atom labelled with the letter N with one of the vacancies labelled with the letters $\{A, B, C, D\}$. b) Representation of the tilt angle between the Z-axis defined as the quantisation axis of the NV centre and the z-axis of the lab frame, defined as the normal to the diamond surface. For a (100)-oriented crystal, this angle corresponds to 54.7°.

In the following, the focus will be on vectorial magnetic field imaging. As such, the essential terms are the ZFS and Zeeman terms, but considering the remaining ones can help to gain precision.

3.2 Vector field reconstruction: an optimisation problem

Probing quasi-static fields near NV centres can be done through ODMR or Ramsey experiments (see section 1.3.3.2). Tracking changes in the resonance lines enables isolating the effects of an external field. On a widefield setup, this information leads to imaging magnetic fields on a large area within a short time. However, the effects result from the projection of the field into the NV-based frames. In order to infer the vectorial fields in the three-dimensional lab frame, the field must be reconstructed. This section will discuss the NV centre Hamiltonian acquisition in the quasi-static regimes using ODMR measurements

and how to use optimisation tools for extracting multiple parameters from the NV spectrum to reconstruct the vectorial information.

3.2.1 Optimisation of the experimental settings

Several experimental parameters must be ensured to infer multiple quantities from the ODMR experiment optimally.

A carefully aligned magnetic field enables monitoring the resonance lines of each NV centre family and thus imaging the vector magnetic field and other effects. Therefore, a bias magnetic field B_0 must be applied to lift the eight otherwise degenerate electron spin resonances and identify the four crystallographic NV orientations. The amplitude of this bias field should satisfy $|B_I| \ll |B_0|$, where B_I is the magnetic field to infer, e.g. current-induced field as demonstrated in section 3.3. An example of such a bias field is shown in figure 3.3.

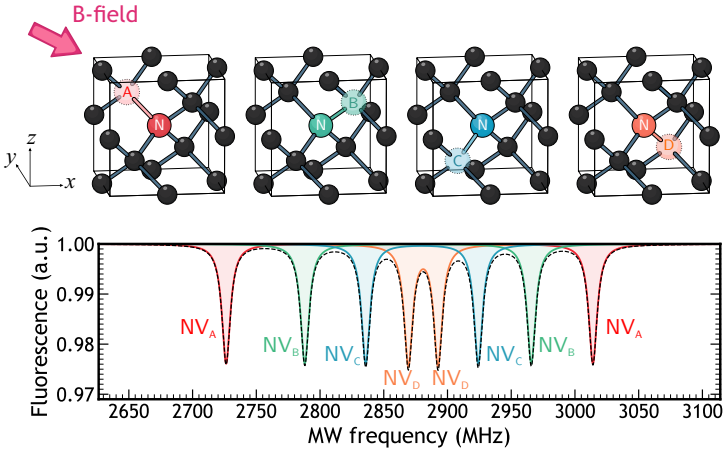

Figure 3.3: **ODMR spectrum of an ensemble of NV centres.** The ODMR spectrum shows the Zeeman splitting of the four crystallographic NV orientations with an arbitrarily chosen static magnetic field $\boldsymbol{B_0} = \{5.09, 0.72, 1.70\}\,\mathrm{mT}$.

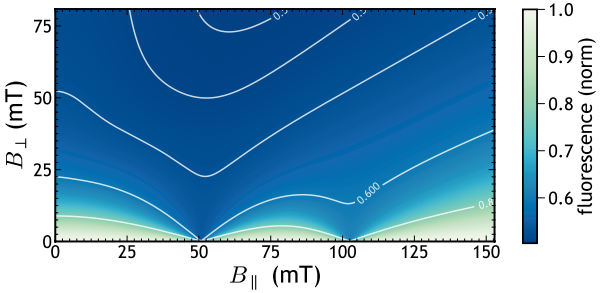

Figure 3.4: **Magnetic field dependence of a single NV centre fluorescence.** $B_\parallel$ represents the field aligned with the NV axis with $B_\parallel = B_z$ and $B_\perp$ represents the off-axis field with $B_\perp = \sqrt{B_x^2 + B_y^2}$ in the NV frame as defined in figure 3.1. Plain lines represent fluorescence isolines.

Although it is crucial to apply a magnetic field large enough to lift the degenerated states of the NV centres, the amplitude should be kept under boundaries to preserve the coherence of the system. Indeed, off-axis magnetic fields, denoted as $B_\perp$, can induce significant spin mixing. Thus, the optically induced spin polarisation and spin-dependent photoluminescence of the NV centre become inefficient, reducing the ODMR spectrum's contrast and hence limiting the sensitivity, as defined in [199].

In order to evaluate the optimal magnetic field alignment, the dependence of the NV centre's photodynamics with an applied magnetic field is evaluated. A 7-level system is simulated, following the procedure described in [200] for a single NV centre (see appendix B). The resulting map for a single NV is shown in figure 3.4. In order to minimise spin mixing, the magnetic field must be aligned along the NV axis and far from levels anticrossing (i.e. $B_\parallel \simeq 51.2\,\mathrm{mT}$ for the excited state and $B_\parallel \simeq 102.4\,\mathrm{mT}$ for the ground state at room temperature).

However, for an ensemble of NV centres with multiple axes involved, the magnetic field's projection can differ for each axis. As such, the simulation is repeated for each NV axis independently. The basis formed by the NV_A

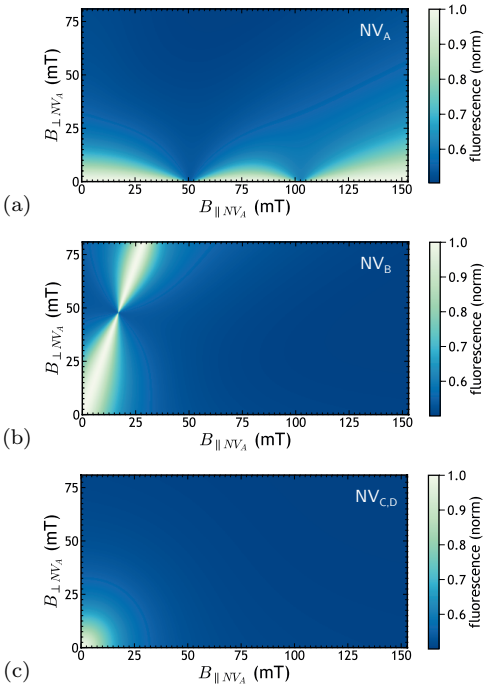

Figure 3.5: **Magnetic field dependence of NVs ensemble fluorescence for each NV axis independently.** $B_{\parallel A}$ represents the field aligned with the NV_A axis with $B_{\parallel A} = B_{Z,A}$ and $B_{\perp A}$ represents the off-axis field with $B_{\perp A} = \sqrt{B_{X,A}^2 + B_{Y,A}^2}$ in the NV frame as defined in figure 3.2. a) Resulting map for the NV_A family. Since the NV_A axis is the reference, the map is identical to the single NV centre. b) Resulting map for the NV_B family. $B_{\parallel A}$ partially acts as an off-axis field, resulting in spin-mixing for only a few mT applied fields. c) Resulting map for the NV_C, NV_D families. Only the projection on x and y differs, resulting in an equivalent dependence with $B_{\perp A}$. Here both $B_{\parallel A}$ and $B_{\perp A}$ rapidly reduce the fluorescence of the NV centres.

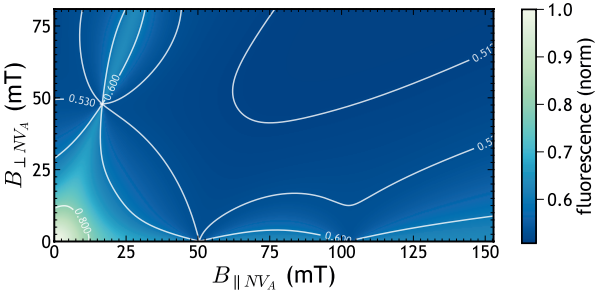

Figure 3.6: **Magnetic field dependence of NVs ensemble fluorescence.** The map represents the normalised sum of the fluorescence of each NV axis when varying the magnetic field $B_{\parallel A}$ and $B_{\perp A}$. Cross-relaxation effects are not modelled. Plain lines represent fluorescence isolines.

centres is arbitrarily taken for reference to varying the magnetic field without loss of generality. The resulting maps for each NV axis are shown in figure 3.5. Finally, the fluorescence emitted by each NV centre family is summed up and normalised, resulting in figure 3.6. It is worth noting that cross-relaxation effects between NVs families [201–204] are not modelled, but simulating each axis-dependant fluorescence is sufficient to grasp how to minimise spin-mixing. Here, it is clear that minimising the background magnetic field is essential to preserve the coherence of the ensemble system.

Although off-axis fields reduce the ODMR contrast, such fields can be applied to lower the Zeeman effect, resulting in noticeable Stark effects [193]. Hence, carefully engineering the background magnetic field helps to tune the sensitivity of the NV centres to a given parameter. Finally, all the control parameters (MW and optical fields) should be chosen to allow homogeneous driving of the ensembles.

3.2.2 Seeking multiple parameters

As described in section 3.1.3, several parameters influence the spectrum of an ensemble of NV centres. Once the background magnetic field B_0 is chosen and tuned for a given purpose, such as for magnetic field sensing, it is essential to assess the parameters that can be extracted from a single ODMR spectrum. To this end, the influence of the parameters on the ODMR spectrum of NV centres is evaluated.

First, the background magnetic field B_0, as defined in figure 3.3, is applied to the NV centres. Then, an additional magnetic field is applied to the NV centres, varying each component independently, as shown in figure 3.7. Due to the geometry of the crystal, the centres $\{NV_A, NV_B\}$ have a strong linear dependence on B_x (i.e. a slight change in B_x induces a noticeable shift of the resonance line). In turn, the $\{NV_C, NV_D\}$ centres show a strong linear dependence to B_y, and all NV centres have a similar sensitivity to B_z. Hence, each axis gives complementary information about the nearby magnetic field.

Secondly, the NV centre's spectrum's dependence on D_{gs} is assessed and shown in figure 3.8. Here, all the lines shift in the same direction. Such variations can be induced by temperature changes, allowing thermometry using NV centres in diamond [57, 58, 195, 205].

Finally, as shown in figure 3.9, the NV resonance lines show a symmetric evolution when varying the parameters α and β. With this configuration, both maps are similar and show disparency only at high fields for the NV_B and NV_C centres. Hence, exploring vectorial Stark effects is possible only for very high voltages or with an alternative experiment configuration (e.g. a different background magnetic field). However, insights into the lateral Stark effect (without distinction of the x and y components) can be extracted.Since the NV_D centres experience a $\boldsymbol{B_0}$ projection mainly perpendicular to the NV axis, the NV_D centres are more sensitive to the Stark effect. Such sensitivity is translated by larger shifts of the resonance lines induced by α/β for the NV_D centres compared to the other NVs orientations.

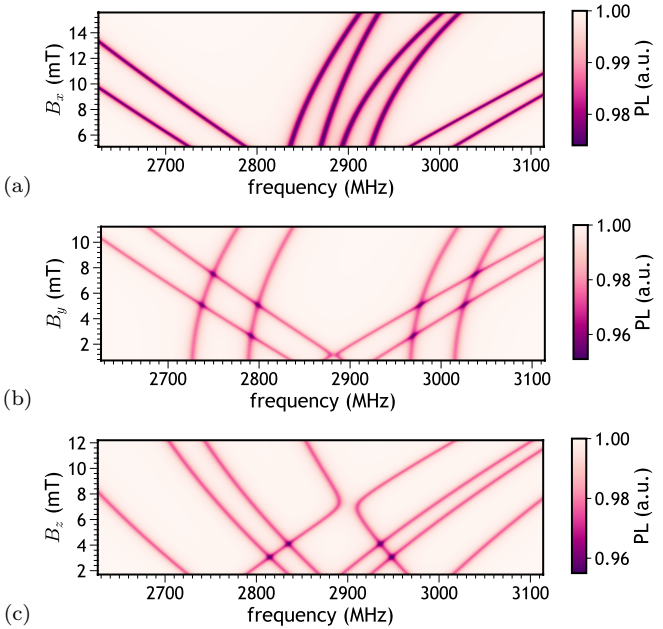

Figure 3.7: **Evolution of the ODMR lines with magnetic field variations.** a) Resonance lines with B_x variations. b) Resonance lines with B_y variations. c) Resonance lines with B_z variations.

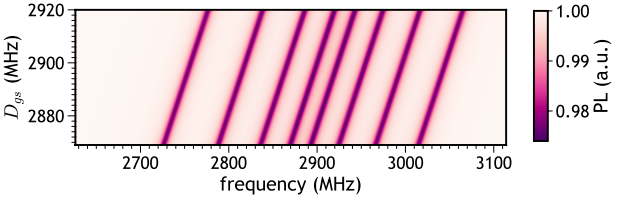

Figure 3.8: **Evolution of the ODMR lines with D_{gs} variations.**

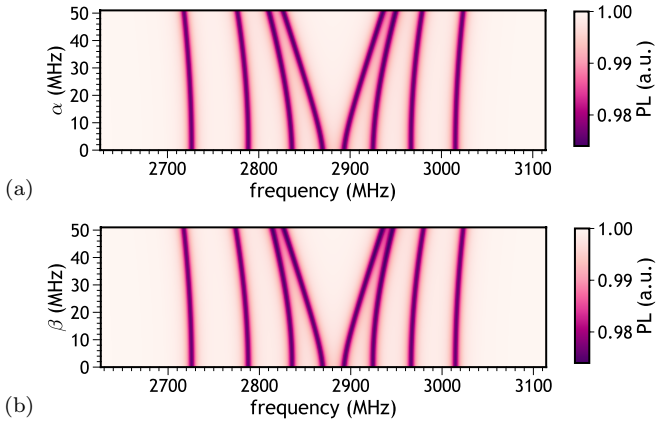

Figure 3.9: **Evolution of the ODMR lines with α and β variations.** a) Resonance lines with α variations. b) Resonance lines with β variations.

All the parameters have a distinct signature in the ODMR signal. However, all the effects sum up to form a single ODMR spectrum, and identifying and distinguishing several parameters is challenging. In order to determine each parameter contribution, it is crucial to solve multiple parameter problems efficiently and robustly. To this end, the following sections discuss optimisation processes to find the optimal Hamiltonian corresponding to the measured signal.

3.2.3 Choice of the solver

Many roads lead to solving an optimisation problem. Among them, gradient-based methods are the most widely used because of their robustness. However, a more advanced class of optimisation tools gives alternative assets such as faster convergence towards the optimal solution: the Newton-type algorithms.

Both procedures are iterative methods used to find the roots of a differentiable function f, where $f(\boldsymbol{x}) = 0$. In these procedures, the $\{k+1\}$-th parameter-set $\boldsymbol{x}_{k+1}$ is estimated using the previous iteration's parameter-set $\boldsymbol{x}_k$, and a

step $s(\boldsymbol{x}_k)$ is evaluated using the function's derivatives at the k-th point. The iteration can be expressed as follows:

$$\boldsymbol{x}_{k+1} = \boldsymbol{x}_k + s(\boldsymbol{x}_k). \tag{3.7}$$

The step $s(\boldsymbol{x}_k)$ includes the direction of the search and the step size between the k-th and the$\{k+1\}$-th point, influencing the convergence rate towards the optimal solution. The estimation of the step $s(\boldsymbol{x}_k)$ is performed according to the chosen optimisation algorithm as discussed in the following.

Gradient algorithms belong to the so-called Cauchy-type algorithms and are first-order methods. They use the gradient of the function $\nabla f(\boldsymbol{x}_k)$ and a learning rate α_k to estimate the step $s(\boldsymbol{x}_k)$. The iteration can be rewritten as follows:

$$\boldsymbol{x}_{k+1} = \boldsymbol{x}_k - \alpha_k \nabla f(\boldsymbol{x}_k). \tag{3.8}$$

The negative sign in equation (3.8) symbolises that the step's direction points towards the *steepest descent*, i.e. each iteration follows the direction where $f(\boldsymbol{x}_k)$ decreases the fastest. The learning rate α_k is a positive real number controlling the step size $s(\boldsymbol{x}_k)$ taken at each iteration. If the learning rate α_k is too large, the model diverges, but if α_k is too small, the model becomes unnecessarily slow to converge towards a minimum.

Newton-based algorithms are second-order methods derived from Taylor expansion and use second derivatives to determine the step's parameters. The model, at the $\{k+1\}$-th iteration, can be represented by equation (3.9):

$$\boldsymbol{x}_{k+1} = \boldsymbol{x}_k - \frac{\nabla f(\boldsymbol{x}_k)}{\nabla^2 f(\boldsymbol{x}_k)} \tag{3.9}$$

$$= \boldsymbol{x}_k - \boldsymbol{H}(\boldsymbol{x}_k)^{-1} \nabla f(\boldsymbol{x}_k), \tag{3.10}$$

where $\boldsymbol{H}(\boldsymbol{x}_k)$ is the Hessian of the function $f(x, y)$. For each iteration k, Newton's method approximates the function $f(x, y)$ at the point $\boldsymbol{x}_k$ with a

paraboloid. The step size is determined by the distance of $\boldsymbol{x}_k$ to the minimum of the fitted parabola at that point. This quadratic method increases the convergence rate, achieves a more general search strategy, and accelerates the overall optimisation procedures.

It is crucial to grasp the differences between the methods to choose the correct solver to image magnetic fields with NV centres. In summary, gradient-based algorithms have only a linear convergence rate, while Newton-based ones have a quadratic one. If it may appear appealing to use Newton-based methods because of their fast convergence, its use comes with a cost: the procedure is less stable than the gradient-based one. For example, Newton's methods can diverge if the initial condition is not well chosen or if the function is too noisy. To illustrate the difference between both methods, a minima search is applied to the Himmelblau function defined by equation (3.11):

$$f(x,y) = \left(x^2 + y - 11\right)^2 + \left(x + y^2 - 7\right)^2 . \tag{3.11}$$

The results are shown in figure 3.10 where Newton's method converges ten times faster than the gradient's when starting with a reasonable value (i.e. at the vicinity of the minimum). However, when starting from a saddle or a local maximum, as in figure 3.11, Newton's method diverges in the first iterations before converging back to a minimum. Despite the divergence, Newton's method is still about three times faster than the gradient-based one, but in more complex landscapes, the method can be trapped in local minima or saddles.

With such high convergence rates, it is natural to assume that Newton's methods are well adapted to optimise problems with many free parameters. However, another aspect is to be considered: the computation of the Hessian matrix.

For a n-parameters function, the Hessian matrix is defined as follows:

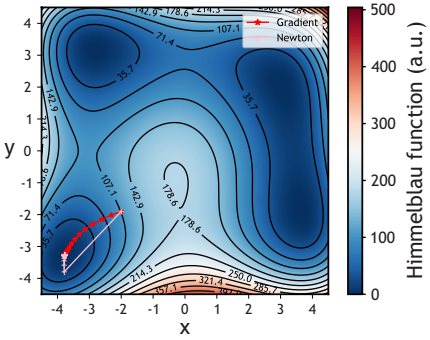

Figure 3.10: **Minimum search of the Himmelblau function: Gradient-based vs Newton-based methods.** The 2D map represents the Himmelblau function with four adjacent local minima, one central local maximum, and four saddles. With the initial point $[x, y] = [-2.0, -1.9]$, the gradient method (red marks) slowly slides to the minimum located at $[x, y] = [-3.8, -3.3]$ while the Newton method (pink marks), makes a leap towards the same optimum.

$$\boldsymbol{H}\left(\boldsymbol{x}_k\right) = \begin{bmatrix} \dfrac{\partial^2 f}{\partial x_1^2} & \dfrac{\partial^2 f}{\partial x_1\, \partial x_2} & \cdots & \dfrac{\partial^2 f}{\partial x_1\, \partial x_n} \\ \dfrac{\partial^2 f}{\partial x_2\, \partial x_1} & \dfrac{\partial^2 f}{\partial x_2^2} & \cdots & \dfrac{\partial^2 f}{\partial x_2\, \partial x_n} \\ \vdots & \vdots & \ddots & \vdots \\ \dfrac{\partial^2 f}{\partial x_n\, \partial x_1} & \dfrac{\partial^2 f}{\partial x_n\, \partial x_2} & \cdots & \dfrac{\partial^2 f}{\partial x_n^2} \end{bmatrix}, \tag{3.12}$$

Calculating and inverting such a Hessian matrix (equation (3.12)) is computationally very expensive.

To overcome such a cost, another class of algorithms has been developed: the *quasi-Newton methods* [206]. Quasi-Newton methods compute an approximate Hessian using a positive-definite matrix $\boldsymbol{M}$, updated at each iteration using

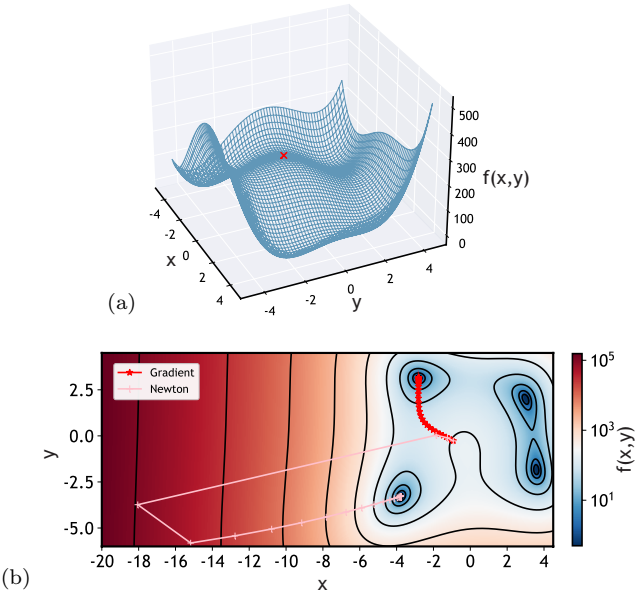

Figure 3.11: **Minimum search of the Himmelblau function: starting from a local maximum.** a) 3D representation of the Himmelblau function $f(x, y)$ where the red mark represents the initial point taken at the local maximum $[x, y] = [-0.27, -0.92]$. b) As for the previous example shown in figure 3.10, the gradient method (red marks) slowly slides to one of the minima, here located at $[x, y] = [-2.8, 3.1]$. The Newton method (pink marks), on the contrary, diverges in the first iterations before converging back to the minimum at $[x, y] = [-3.8, -3.3]$.

information extracted from previous steps. In a simplified manner, the matrix at an iteration $k+1$ can be written as follows:

$$M_{k+1}\left[\boldsymbol{x}_{k+1}-\boldsymbol{x}\right]=\nabla f\left(\boldsymbol{x}_{k+1}\right)-\nabla f\left(\boldsymbol{x}_{k}\right). \tag{3.13}$$

Hence, quasi-Newton methods use previously computed quantities and are therefore highly efficient. Finally, different quasi-Newton algorithms have been developed over the years, and they differ from the method used to approximate the Hessian. In this work, it is the BFGS method [207–210] named after its creators Broyden, Fletcher, Goldfarb, and Shanno, which is used. The BFGS method directly approximates the inverse Hessian $\boldsymbol{M}^{-1}$ to steer its search through variable space and enable the optimisation of several free parameters. More specifically, the variant "l-BFGS-b" of the algorithm is used in the next sections. With this variant, the memory is limited for efficient computation of the Hessian's invert, and constraints can be applied to fix boundaries.

3.3 Application to Oersted fields imaging

In order to unleash the full potential of magnetometry using an ensemble of NV centres, it is essential to optimise the procedure to take full advantage of the diamond geometry. In this last section, the optimisation tools discussed in section 3.2.3 are applied to a concrete case where the NV centres' signal is exploited to image current-induced magnetic fields.

3.3.1 Measuring Oersted fields using NV centres in diamond

The principle of the experiment is depicted in figure 3.12. Long-range magnetic fields, also known as Oersted fields [211], are created by static electrical current distributions according to the Biot-Savart law (equation (3.14)):

$$\mathbf{B}(\mathbf{r})=\frac{\mu_0}{4\pi}\iiint\frac{\boldsymbol{J}(\mathbf{r}')\times(\mathbf{r}-\mathbf{r}')}{|\mathbf{r}-\mathbf{r}'|^3}d^3\mathrm{r}, \tag{3.14}$$

where μ_0 is the vacuum permeability, $\mathbf{r}$ is the spatial coordinates at the observation point, and $\boldsymbol{J}(\mathbf{r}')$ is the current distribution in the source plane.

Magnetic field isolines in figure 3.12 show that magnetic field contributions merge with distance from the current source, resulting in blurry patterns. Hence, it is primordial to place a diamond homogeneously implanted with near-surface NV centres in the vicinity of the current flow. With such a setup, the electron spin of each NV centre is affected by the magnetic field via the Zeeman interaction $\mathcal{H}_{\mathrm{EZ}} = -\gamma_{\mathrm{NV}}\mathbf{B}\cdot\mathbf{S}$. Probing this Zeeman interaction on the multiple NV orientations (figure 3.3), is done here by performing cw-ODMR on the NV centres.

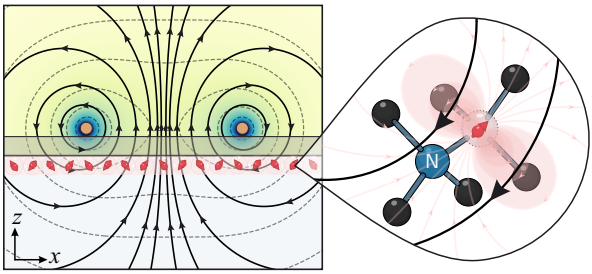

Figure 3.12: **Sensing Oersted fields with NV centres.** Representation of Oersted fields created by two counter-propagative wires. Solid lines with arrows represent the magnetic flux lines, and dashed lines represent magnetic field isolines. A diamond with near-surface NV centres is brought close to the wires to sense the Oersted fields with high resolution.

3.3.2 Complex structure: a challenging demonstration

Figure 3.13 shows the copper fabricated microstructure used for the experiment discussed in this section. In order to demonstrate the technique's robustness, the structure is designed with a shape featuring an eagle (figure 3.13), where the sharp edges and corners make the magnetic field reconstruction challenging.

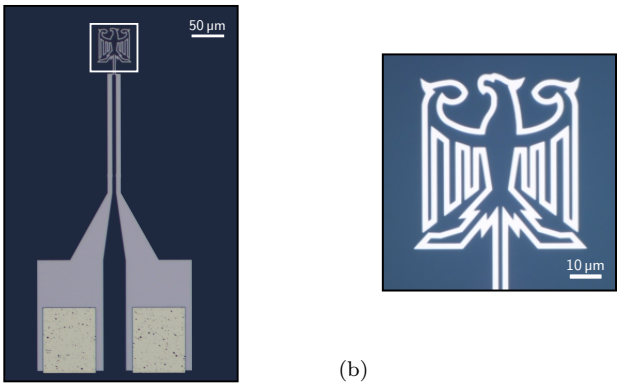

(a) (b)

Figure 3.13: **Eagle-shaped microstructure under bright illumination.** a) Full structure showing the pads that serve to connect the structure to an electronic source via wire bonding. b) Close-up on the region of interest (ROI).

As briefly discussed in section 3.3.1, the distance between the sensors and the current source plays a crucial role in defining the spatial resolution. Minimising this distance using a diamond microplate, as shown in figure 3.14, ensures preserving the spatial resolution defined by the sensor.

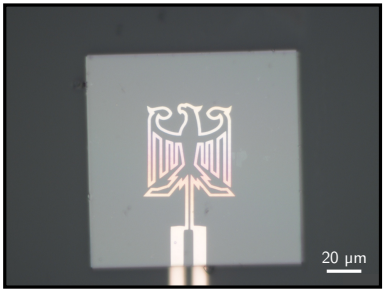

Figure 3.14: **Diamond plate glued on top of the eagle-shaped microstructure.**

3.3.3 Downstream analysis of the ODMR spectra

A voltage of 20 mV is applied to the structure, resulting in a current of about 600 µA. In order to image the resulting Oersted field, the NV-based widefield microscope described in chapter 2 is employed to perform cw-ODMR over a region of about 90 µm × 90 µm, capturing the entire eagle-shaped structure.

In order to suppress background illumination and fluctuations of the ODMR baseline, the ODMR signal is acquired with microwave ON, labelled as $\mathrm{PL_{ON}}$, and with microwave OFF, labelled as $\mathrm{PL_{OFF}}$. The signals $\mathrm{PL_{ON}}$ and $\mathrm{PL_{OFF}}$ are then used to compute the Michelson contrast [212] of the ODMR signal, defined as:

$$\text{Michelson contrast} = \frac{\mathrm{PL_{ON}} - \mathrm{PL_{OFF}}}{\mathrm{PL_{ON}} + \mathrm{PL_{OFF}}}. \tag{3.15}$$

The strategy for extracting the full vector information from the ODMR spectrum for each pixel follows the procedure developed in [168].

First, the data are analysed using nonlinear least-squares numerical minimisation to fit the ODMR spectrum at each pixel, as depicted in figure 3.15. The model for fitting the spectra is the sum of eight Lorentzian functions, defined as:

$$L(\omega; A, \omega^{\mathrm{exp}}, \sigma) = y_0 + \sum_{i=1}^{4} \sum_{j=\pm} \frac{A_{i,j}}{\pi} \left[\frac{\sigma_{i,j}}{\left(\omega - \omega_{i,j}^{\mathrm{exp}}\right)^2 + \sigma_{i,j}^2} \right], \tag{3.16}$$

where the resonance frequencies $\omega_{i,j}^{\mathrm{exp}}$, linewidths $2\sigma_{i,j}$, amplitudes $A_{i,j}$ and the offset y_0 are all free parameters. The indices i, j identify the resonance frequencies where $i \in [A, B, C, D]$ is associated to the NV centre's orientation as illustrated in figure 3.3 and $j \in [-, +]$ is associated to the spin states $m_s = -1$ and $m_s = +1$, respectively.

For a robust analysis, the fitting procedure is based on the Levenberg-Marquardt algorithm [213, 214]. The Levenberg-Marquardt algorithm reduces

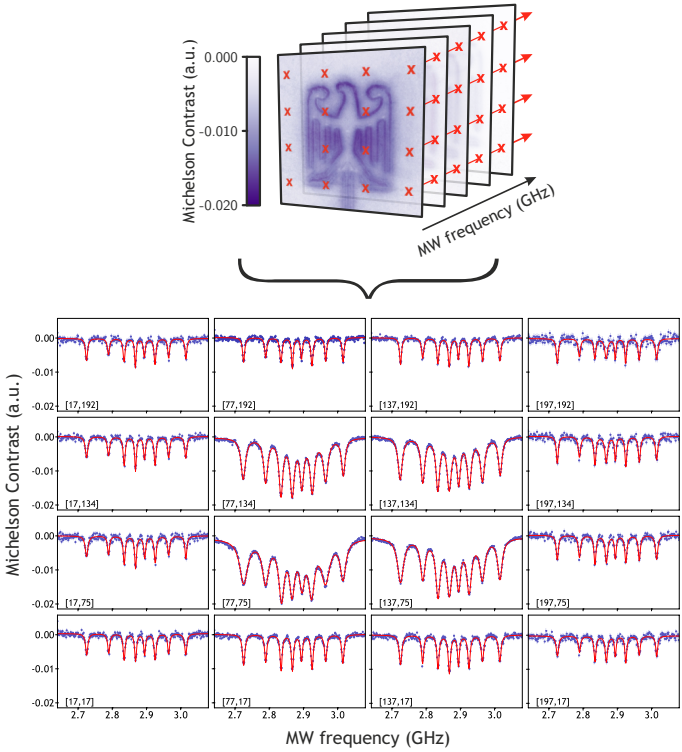

Figure 3.15: **Multi-lines ODMR fitting procedure.** Each pixel contains an ODMR spectrum fitted using the Levenberg-Marquardt algorithm for a robust analysis across the FOV.

the sum of the squares of the errors between the model function defined by equation (3.16) and the data points acquired experimentally. This minimisation is done through a sequence of well-chosen updates on the values of the model parameters. With such an algorithm, the choice of the initial guess is crucial to allow the minimisation to converge towards the right solution. As the resonance shifts are small across the FOV, computing the median of the ODMR spectra

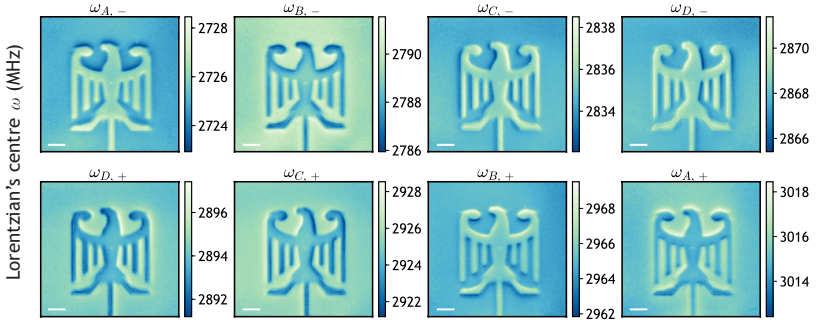

Figure 3.16: **Fitted Lorentzian centre parameter for each pixel over the FOV.** Scale bars are 10 µm wide.

over all the pixels and taking the returned fitting parameters is sufficient to set the initial guess for each pixel.

Finally, from the returned fit parameters of each pixel, the centre frequencies of each experimental resonance transition $\{\omega_{i,\pm}^{\text{exp}}\}_{i=A \text{ to } D}$ are extracted. The resulting resonance transitions are shown in figure 3.16 when the current runs through the eagle-shaped microstructure.

The resulting frequencies $\{\omega_{\pm,i}\}_{i=1 \text{ to } 4}$ are then used to infer the Hamiltonian parameters (denoted here as the vector $\vec{p}$) by using the l-BFGS-b solver to minimise the root-mean-square error function, also called cost function and given by:

$$\chi = \sum \left[\omega_{i,j}^{\text{exp}} - \omega\left(\vec{B}, D_{\text{gs}} + \delta, \alpha, \beta\right)\right]^2. \tag{3.17}$$

In equation (3.17), $\omega\left(\vec{B}, D_{\text{gs}} + \delta, \alpha, \beta\right)$ is calculated using the ground state Hamiltonian $\mathcal{H}_{NVi}$ for each NV axis, as given by equation (3.2). The overall optimisation process is summarised in figure 3.17.

The initial guess to minimise the cost function given by equation (3.17) is determined by using the knowledge of the background magnetic field. To visu-

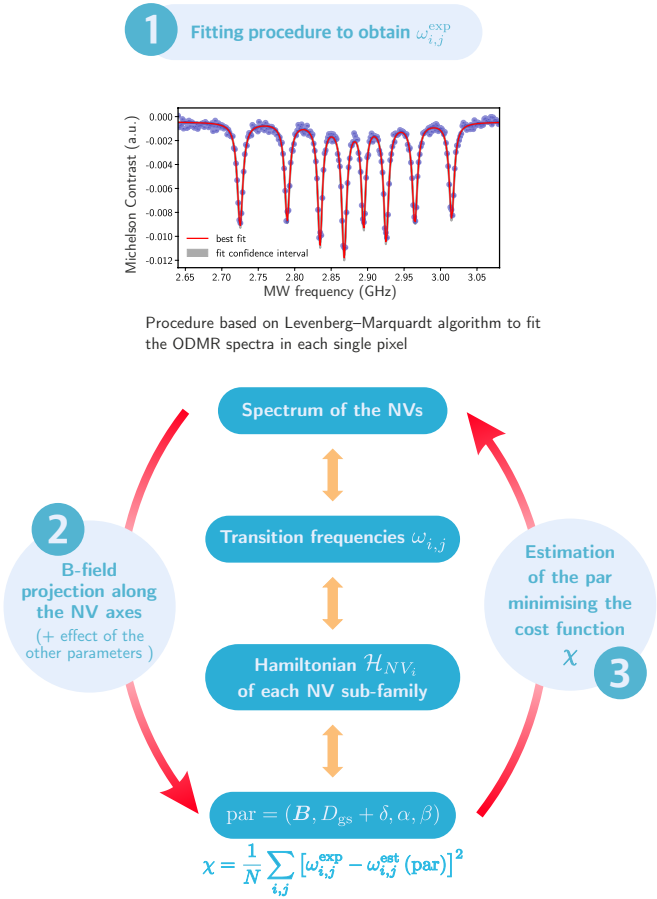

Figure 3.17: **Optimisation overall process.** 1) ODMR spectra are fitted for each pixel over the FOV, and the experimental resonance frequencies are extracted. 2-3) The parameters par $= \left(\vec{B}, D_{\text{gs}} + \delta, \alpha, \beta\right)$ are estimated by iteration until minimising the cost function χ. B-field represents the magnetic field.

alise the minimisation process, spherical coordinates, as shown in figure 3.18, are used to represent the cost function χ, with only the angles θ and φ as free parameters. The resulting representation is given by figure 3.19. The choice of the background magnetic field defines the boundaries of the problem for which there is a unique solution.

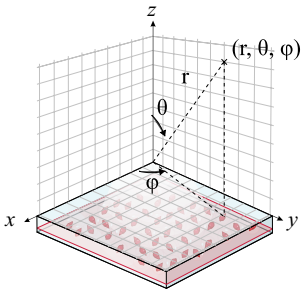

Figure 3.18: **Lab frame spatial coordinates.** The Cartesian coordinates are given by (x, y, z) and the spherical coordinates are given by (r, θ, φ).

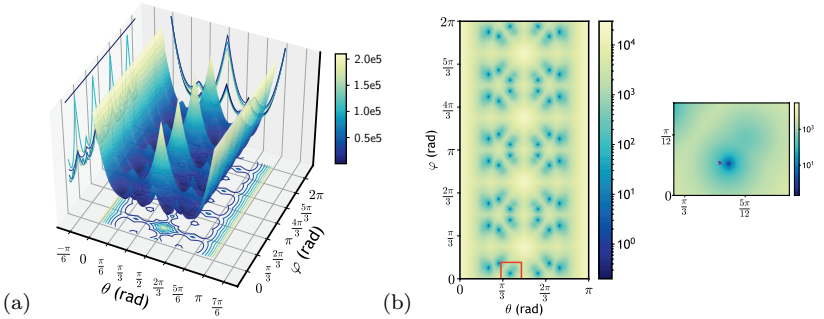

Figure 3.19: **Cost function χ with free parameters θ and φ.** The red square represents the boundaries chosen according to the background magnetic field, and the purple cross represents the initial guess.

Finally, the data are fully processed with all the parameters free. In order to account for the Oersted field created by the closed-circuit only, the magnetic field sensed by the NV centres is measured twice: with current ON and then with current OFF. The difference between the magnetic field obtained with a closed-circuit and the magnetic field obtained with an open-circuit are given in figure 3.20. The maps clearly reflect the features of the eagle, such as sharp edges and smooth features. Besides, the magnetic field magnitude corresponds to the expected magnitude given by equation (3.14) when taking into account the geometry of the system and the current amplitude sent to the microstructure. Thus, the optimisation process successfully reconstructed the Oersted fields created by the structure in the lab frame.

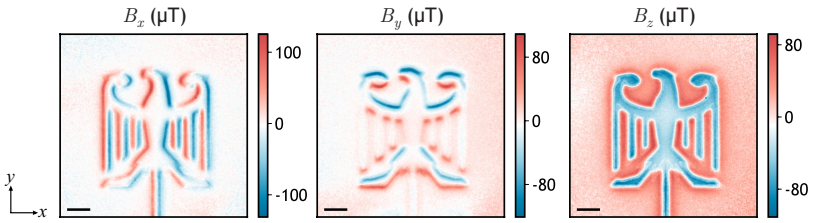

Figure 3.20: **Oersted fields induced by the current flowing through the Eagle-shaped microstructure.** The maps are represented in the lab frame with Cartesian coordinates (x, y, z). The scale bars are 10 µm wide.

In addition, the maps resulting from the parameters D_{gs} are shown in figure 3.21. Dependence on temperature is observed, with the maps showing an average temperature increase of about 4 °C (an increase in temperature shifts the frequency to lower values). This can be used to observe an abnormal temperature rise in circuits and locate defects.

Finally, as predicted in section 3.2.2, for such fields α and β show similar behaviour. In order to image vector strain/electric fields, the fields must be large enough to induce a few tens of MHz shifts. Alternatively, the background mag-

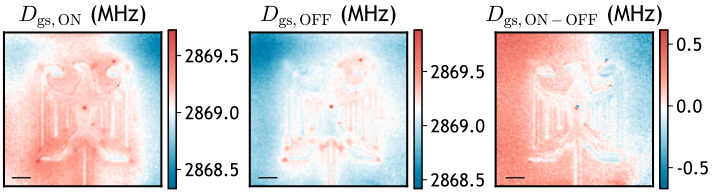

Figure 3.21: **Resulting D_{gs} parameter.** $D_{gs,ON}$ represents the D_{gs} when current is running through the circuit and $D_{gs,OFF}$ represents the D_{gs} with the background magnetic field only. The scale bars are 10 µm wide.

netic field must be carefully engineered to enhance the NV centre's sensitivity to such fields.

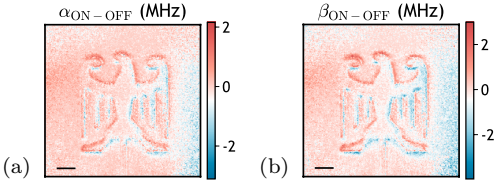

Figure 3.22: **Resulting α and β parameters.** α_{ON-OFF} and $\beta_mathrmON - OFF$ represent the resulting α, β when current is running through the circuit and the background magnetic field is retrieved. The scale bars are 10 µm wide.

3.4 Conclusions and outlook

This chapter discussed a robust method to reconstruct the magnetic fields in the lab frame without prior knowledge about the sample. Such a technique is crucial for imaging current distributions or magnetisation. As NV centres do not rely on cryogenic temperatures like SQUID magnetometers and can be designed in nanoscale sizes, they can be brought into close vicinity to the sample of interest, thus making them ideal for sub-micro imaging application.

The ODMR signal is rich, and further information can be extracted from the spectra. The parameters $\{\omega_{i,\pm}^{\text{exp}}\}_{i=A \text{ to } D}$ are sufficient to reconstruct the vector magnetic field, as shown in section 3.3.3. However, it is worth noting that the remaining parameters, such as the Lorentzian amplitude and linewidth shown in figures 3.23 and 3.24, respectively, can help to find more information about the device and the experimental conditions.

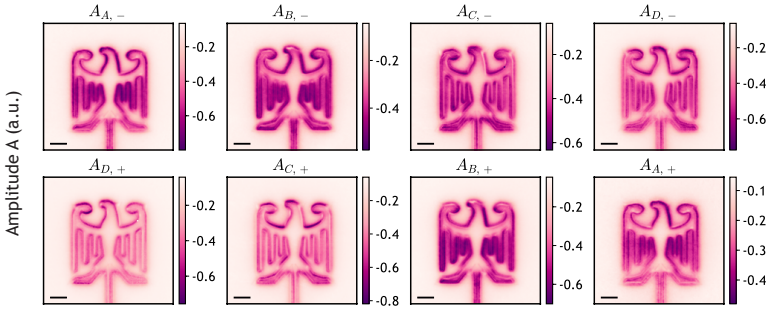

Figure 3.23: **Fitted Lorentzian amplitude parameter.** Scale bars are 10 µm wide.

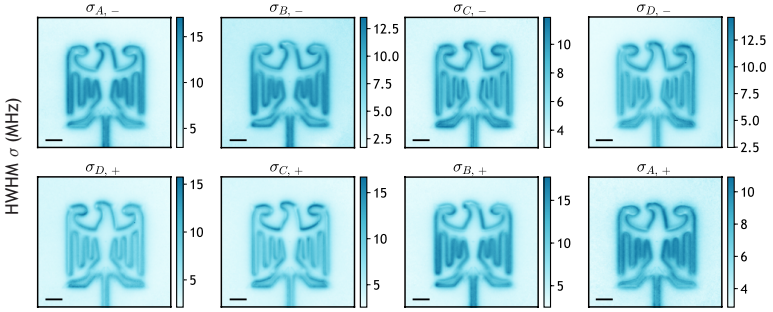

Figure 3.24: **Fitted Lorentzian linewidth parameter.** Scale bars are 10 µm wide.

In particular, the linewidth of the Lorentzian function depends on the MW power, as derived in [37, 109]. The half width at half maximum (hwhm) pa-

rameters can be used to observe MW effects on the device, such as potential cross-talks. Alternatively, the hwhm can be used to sense fields in the GHz regime using ODMR measurements. The amplitude can also help to determine the control fields of the NV centres (such as the optical field intensity). The resulting maps are shown in figure 3.24 for the hwhm and figure 3.23 for the amplitude, where clear effects of the control fields on the eagle can be seen. Thus, with the ODMR measurement alone, many experimental parameters can be determined, and future developments in this direction would lead to a practical and compact NV microscope.

In addition, the method has been designed to extract a large number of parameters, allowing simultaneous mapping of the vector magnetic field, D_{gs}, α and β. This is particularly relevant for experiments where multiple parameters must be tracked, such as observing transition phase phenomena. Future developments incorporating a dynamic background magnetic field optimised to track specific parameters can be envisioned to perform multiple experiments on a sample.

Finally, mapping Oersted fields is not always sufficient to capture all the physics behind current distributions. Therefore, it is important to generate current maps. Thus, current distributions, as shown in figure 3.25, can be reconstructed using Oersted field maps. The procedure is described in the next chapter.

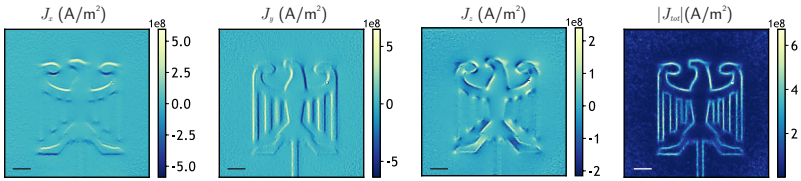

Figure 3.25: **Reconstructed current distribution map of the eagle-shaped microstructure.** The maps are represented in the lab frame with Cartesian coordinates (x, y, z). The scale bars are 10 µm wide.

Chapter 4

Current reconstruction: the magnetic inverse problem

Stray magnetic fields contain significant information about the electronic and magnetic properties of a source system. Retrieving these properties is crucial for a wide range of applications in various fields of science and technology, including condensed matter physics [42, 141], earth sciences [215], medicine [216, 217] and for the development of integrated circuits, as described in chapter 5. The conversion of the magnetic field into the desired source quantity, such as current density or magnetisation, is known as the *magnetic inverse problem*. The reconstruction of two-dimensional magnetisation patterns using NV centres is described in [42, 218].

This chapter discusses the non-invasive detection of currents, which is possible through the detection of long-range Oersted fields created by moving charges, according to the Biot-Savart law. Although mapping Oersted fields does not provide a direct picture of the current flow, the current density can be accurately reconstructed for some geometries. The methods for reconstructing the current density using Maxwell's equations and the Fourier formalism are discussed in this chapter.

The chapter is structured as follows:

(1) Section 4.1 gives an introduction to the inverse problem by means of a case study, used throughout the chapter.

(2) Section 4.2 gives insights into how to interpret magnetic field patterns according to Maxwell's equations and discusses the quantitative information that can be retrieved.

(3) Section 4.3 describes the method for reconstructing current density patterns based on the deconvolution method using the Fourier filter formalism. The process is applied to planar 2D structures, 2.5D slab structures, and 3D designs.

(4) Finally, in section 4.4, the conclusions and outlook of the chapter are discussed.

4.1 Introduction to the inverse problem using a case study

4.1.1 Maxwell's equations

Electromagnetic waves can be expressed using classical and quantum descriptions.

In the quantum description, the field appears as a collection of photons and is of relevance in processes involving a discrete number of light particles, such as two-photon microscopy [219, 220].

In the classical approach, electromagnetic waves are the association of an electric field $\boldsymbol{E}$ with an orthogonal magnetic field $\boldsymbol{B}$. They can be described mathematically by the Maxwell's equations summarised in the table 4.1. In this work, the classical formalism is adopted.

Gauss' electric law	$\nabla \cdot \mathbf{E} = \frac{\rho}{\varepsilon_0}$	(4.1)
Gauss' magnetic law	$\nabla \cdot \mathbf{B} = 0$	(4.2)
Faraday's law of induction	$\nabla \times \mathbf{E} = -\frac{\partial \mathbf{B}}{\partial t}$	(4.3)
Ampère's circuital law	$\nabla \times \mathbf{B} = \mu_0 \left(\mathbf{J} + \varepsilon_0 \frac{\partial \mathbf{E}}{\partial t} \right)$	(4.4)

Table 4.1: **Maxwell's equations in the SI units system.**

4.1.2 The inverse problem

A planar U-shaped microstructure, as depicted in figure 4.1, is considered.

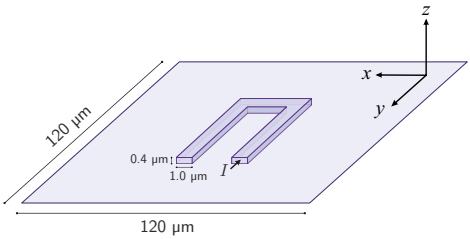

Figure 4.1: **Geometry of the U-shaped current-carrying wire** with lab-frame coordinates xyz.

A current of amplitude $I = 10\,\mathrm{mA}$ runs through the structure, resulting in the current distribution shown in figure 4.2. The Biot-Savart law given by equation (3.14) describes how magnetic fields are generated at a given distance from a current source. However, as illustrated in figure 4.3, the inverse operation is not straightforward and is known as the *magnetic inverse problem* [221].

Solving the magnetic inverse problem can be a difficult task because magnetic fields decrease and spread rapidly with distance from the source, as shown in

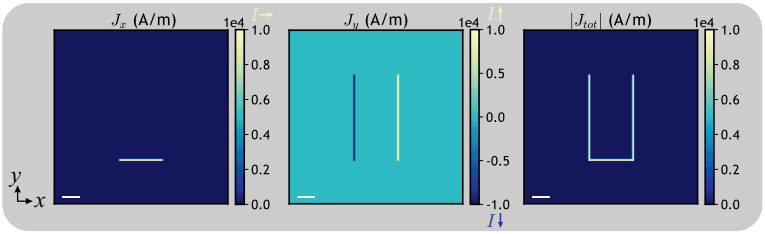

Figure 4.2: **Current distribution simulation.** A current of amplitude $I = 10\,\text{mA}$ runs through a 1 µm-wide planar structure, resulting in the current distributions J_x, J_y and thus, $|J_{tot}| = \sqrt{J_x^2 + J_y^2}$. The scale bars are 10 µm wide.

figure 4.4. Thus, originally separate sources can produce magnetic fields that either blend or cancel each other out. Such an evolution leads to magnetic patterns in which the geometry of the source is lost after only a few µm. Therefore, minimising the distance between the source and the magnetic field sensor is a crucial parameter to consider when designing the sensing experiment.

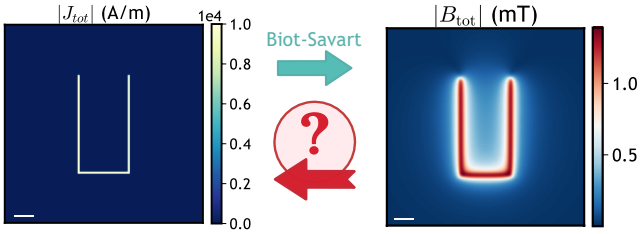

Figure 4.3: **Current distribution: the inverse problem.** Deriving the magnetic field distribution from knowledge of the current source can be done using Biot-Savart law. The inverse procedure is not a straightforward problem to solve. The scale bars are 10 µm wide.

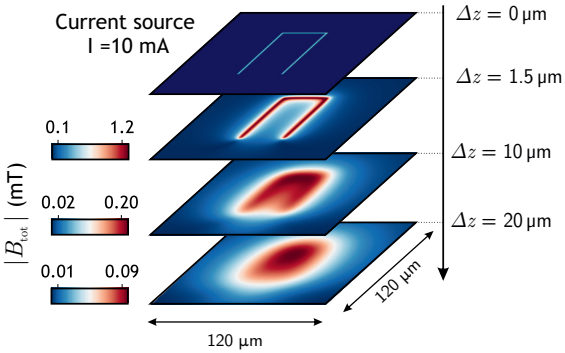

Figure 4.4: **Current distribution and induced Oersted fields over the distance.** As described by Biot-Savart law given by equation (3.14), a magnetic field produced by a current source spreads over the distance of observation.

In the following, methods for reconstructing the current density distribution and techniques for retrieving information about the magnetic field sources, such as the current amplitude or the position of the wires, are described. To this end, the Oersted fields generated by the U-shaped microstructure are simulated and serve as a data basis. The Oersted fields are simulated for a reasonable distance from the source, i.e. for a realistic realisation with the NV-based widefield microscope, here for a distance of $\Delta z = 1.5\,\mu m$ from the wire, as shown in figure 4.5.

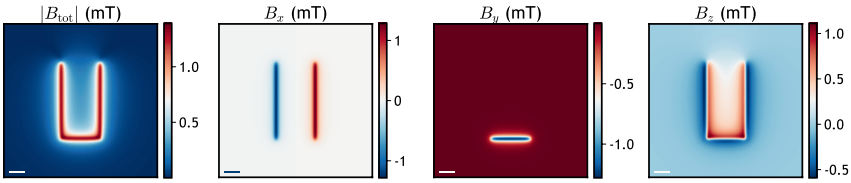

Figure 4.5: **Oersted fields at a distance** 1.5 µm **from the source plane.** The scale bars are 10 µm wide.

4.2 Interpretation of magnetic fields patterns according to Maxwell's equations

4.2.1 A qualitative approach for solving the inverse problem

If no information can be obtained about the geometry of the experimental environment, e.g. the distance between the sensor and the source, using the Ampère's circuital law given by the equation (4.4), can be sufficient to reconstruct the global pattern of the current density. To do this, the curl of the vector field $\boldsymbol{B}$ must be calculated, and thus the data must obey the Nyquist-Shannon sampling theorem [222].

For a planar source of stationary current $\mathbf{J} = (J_x, J_y, 0)^\intercal$, $\mathbf{J}$ is given by:

$$\mathbf{J}(x,y) = \frac{1}{\mu_0} \begin{pmatrix} \frac{\partial B_z}{\partial y} \\ -\frac{\partial B_z}{\partial x} \\ 0 \end{pmatrix}. \tag{4.5}$$

Applying Ampère's circuital law to the magnetic field map B_z obtained in figure 4.5 results in figure 4.6a.

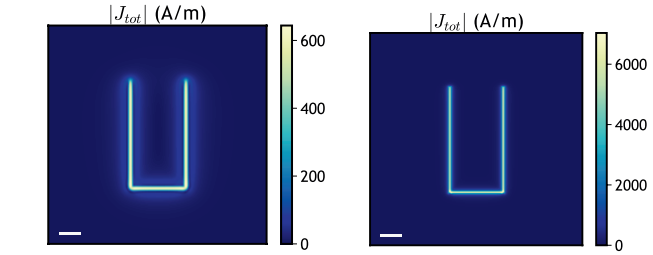

Figure 4.6: **Current density reconstructed using Ampère's law.** a) Current distribution reconstructed using B_z acquired at $z = 1.5\,\mu m$. b) Current distribution reconstructed using B_z acquired at the surface of the lead, i.e. $z = 0.2\,\mu m$. Scale bars are $10\,\mu m$ wide.

Spreading of the current distribution over the edge of the structure can be observed. Since the Ampère's law describes the current distribution in the source plane, it is unsuitable for measurements away from the source. However, this method is relevant for measurements near contact with the source, such as in figure 4.6b. Although this method is not well suited to the widefield microscope, it can be well adapted to scanning probe devices that can collect enough data points across microstructures and measure the field nearly at the contact with the sample.

4.2.2 Quantifying the current amplitude in the leads

Quantifying the current amplitude in the leads can be done with the Stokes theorem or the infinite wire approximation. Both methods are discussed in the following.

4.2.2.1 Using Stokes theorem

Stokes' theorem states that the line integral of a vector field over a loop equals the flux of its curl through the enclosed surface. The theorem implies that one can determine the current amplitude if the cross-section of the magnetic field signal is fully integrated over a line. Stokes' theorem, applied to the Ampère's law, is thus defined as:

$$I_x = \frac{\mu_0}{2} \int B_y dy, \tag{4.6}$$

$$I_y = \frac{\mu_0}{2} \int B_x dx, \tag{4.7}$$

where I_x is the current amplitude in a lead along the $x-$axis and I_y is the current amplitude in a lead along the $x-$axis.

Integrating the signal $|B_x(x, y = 50\,\mu\text{m})|$, as depicted in figure 4.7, according to equation (4.6) yields a current amplitude $|I| = 9.13(5)\,\text{mA}$ in each lead. The method is slightly more accurate when a single lead is simulated separately,

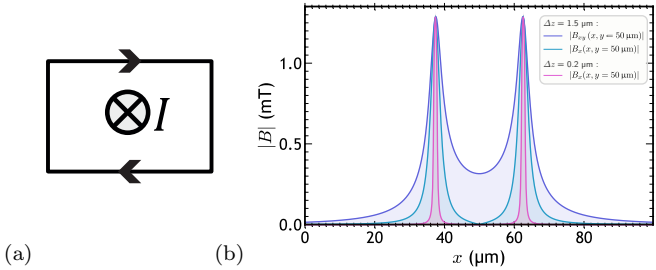

Figure 4.7: **Current amplitude estimated using Ampère's law and Stokes' theorem.** a) Schematic representation of Stokes' theorem. b) The blue curves represent the intersections of the lines along x for $|B_x|$ and $|B_{xy}|$ at $y = 50\,\mu\text{m}$ and $\Delta z = 1.5\,\mu\text{m}$. The pink curve represents the line intersection along x for $|B_x|$ at $y = 50\,\mu\text{m}$ and $\Delta z = 0.2\,\mu\text{m}$.

as it returns a current amplitude $|I| = 9.56(5)\,\text{mA}$ in the lead. If only B_{xy} is available in an experiment (e.g. for a single NV centre or SQUID), the signal is then integrated over $|B_{xy}(x, y = 50\,\mu\text{m})|$, and equation (4.6) provides a current amplitude $|I| = 20.2(2)\,\text{mA}$ in each lead. Therefore, the contributions of B_y completely distort the results and the method should only be used for well-separated wire contributions. Finally, this method becomes very accurate when the signal is measured in close proximity to the source since it yields $|I| = 9.92(5)\,\text{mA}$ in each lead when $\Delta z = 0.2\,\mu\text{m}$.

Thus, using Stokes' theorem for simple circuits in a widefield setup can be a simple and quick method to evaluate current amplitudes. For better accuracy, the data should be fitted with the infinite wire approximation, as described in the next section.

4.2.2.2 Using the infinite wire approximation

As mentioned earlier, the cross sections can be fitted according to the Biot-Savart model given by the equation (3.14) and using the infinite wire approximation as follows:

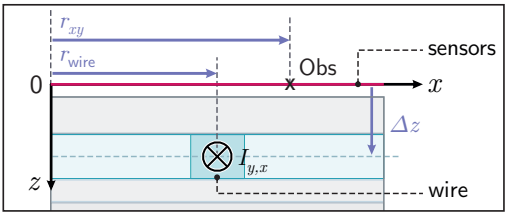

Figure 4.8: **Schematic view of the $xz-$plane of a typical experiment.** The variables used to fit the data using equation (4.8) are labelled according to an arbitrarily chosen observation point Obs.

$$B_{x,y} = \frac{\mu_0 I_{y,x} \Delta z}{2\pi[|r_{xy} - r_{\text{wire}}|^2 + \Delta z^2]} + o, \tag{4.8}$$

where $I_{y,x}$ is the lateral current amplitude, r_{xy} is the observation position on the xy-plane, r_{wire} is the position of the current source on the xy-plane, Δz is the distance between the current source and the observation position on the vertical axis z and o is a constant offset. For better representation, the parameters are shown in figure 4.8.

Fitting the signal $B_x(x, y = 50\,\mu\text{m})$ at $\Delta z = 1.5\,\mu\text{m}$, with the infinite wire model and keeping the parameters I and Δz free results in figure 4.9. The fitting parameters result in a current amplitude $|I| = 10.07(1)\,\text{mA}$ in each lead and a distance $z = 1.550(2)\,\mu\text{m}$.

Mainly, the fit gives information about the total current amplitude in the leads and the localisation of the current sources with respect to the observation position in Cartesian coordinates $\{x, y, z\}$. Additionally, such fit can help in investigating multi-layered devices, as further explored in chapter 5. The next section discusses how to image the current distributions using their associated magnetic field images.

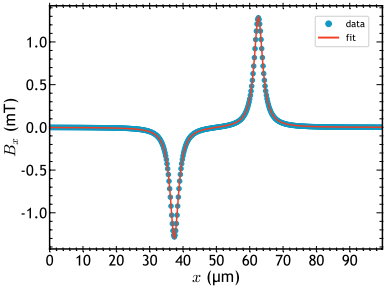

Figure 4.9: **Curve fit with infinite wire approximation.** Line intersection of B_x along x at $y = 50\,\mu\text{m}$ and $\Delta z = 1.5\,\mu\text{m}$, where the blue dots represent the data and the red line represents the fit using the equation (4.8) as a model.

4.3 Reverse propagation

The procedure follows the method described in [223, 224], where the components of the magnetic field are used to numerically invert the Biot-Savart law given by the equation (3.14).

To reconstruct the lateral current density J_{xy}, the integral equation of the Biot-Savart law must be solved with J_x, J_y as unknown elements. To solve the equations, the Biot-Savart law can be rewritten as a convolution, such as:

$$\mathbf{B}(\mathbf{r}) = \frac{\mu_0}{4\pi}\boldsymbol{J}(\mathbf{r}') * \boldsymbol{G}(\mathbf{r} - \mathbf{r}'), \tag{4.9}$$

where $\mathbf{B}(\mathbf{r})$ is the magnetic field observed at the observation position $\mathbf{r}$, $\boldsymbol{J}(\mathbf{r}')$ is the current distribution at the source plane, and $\boldsymbol{G}(\mathbf{r} - \mathbf{r}')$ is a green function describing the spreading of the magnetic field over the distance from the current source. For better interpretation, the convolution is illustrated in figure 4.10.

To extract the $\boldsymbol{J}(\mathbf{r}')$ term, equation (4.9) is deconvoluted [225] using the Fourier formalism, which has been introduced in chapter 2. This method is powerful since it can partially compensate for the loss of spatial resolution due

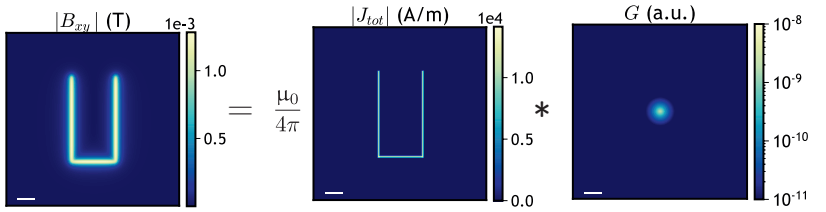

Figure 4.10: **Convolution of the current density at the source plane $\boldsymbol{J}(\mathbf{r}')$ with the green function $\boldsymbol{G}(\mathbf{r}-\mathbf{r}')$.** As described in equation (4.9), the Oersted field observed at the position $\mathbf{r}$ can be considered as the result of a convolution between the current distribution at the source plane and a green function describing the spreading of the magnetic field over the distance from the source. The scale bars are 10 µm wide.

to field propagation. However, a major drawback is that the method amplifies the high-frequency components of the Fourier domain and, hence, noise. In order to compensate for the noise amplification effect, the procedure requires spatial filtering to dampen the high-frequency components. However, filtering tends, in turn, to smooth out the fine features of the image. Consequently, the magnetic field's signal-to-noise ratio must be optimised to obtain the most accurate current density mapping to limit the use of filters. In this work, this is achieved by considering a precise NV Hamiltonian when determining the magnetic field contribution described in section 3.1.3.

The Fourier transforms of the magnetic fields generated by the U-shaped microstructure are given by b_x, b_y and b_z, as shown in figure 4.11. The U-shaped structure is simple and noise-free, so the Fourier transform pattern is easy to understand since the wires contribute to the signal with sinus cardinal (sinc) functions. On the Fourier images, we can see that b_x results from the combination of two sinc functions on the k_x-axis while b_y corresponds to a single sinc function on the k_y-axis. Besides, we can see that b_z is the combination of b_x and b_y. Thus, having access to b_z only to determine the lateral current density

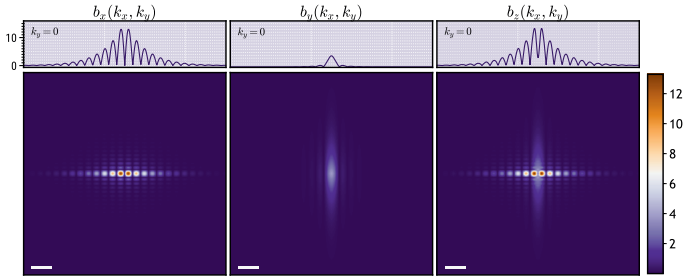

Figure 4.11: **Magnetic field in the Fourier plane**, with zp = 5. The upper curves show the trace at $k_y = 0$. The scale bars = 10*zp units.

inherently causes singularities since the frequencies on $k_x = 0$ and $k_y = 0$ cannot be correlated.

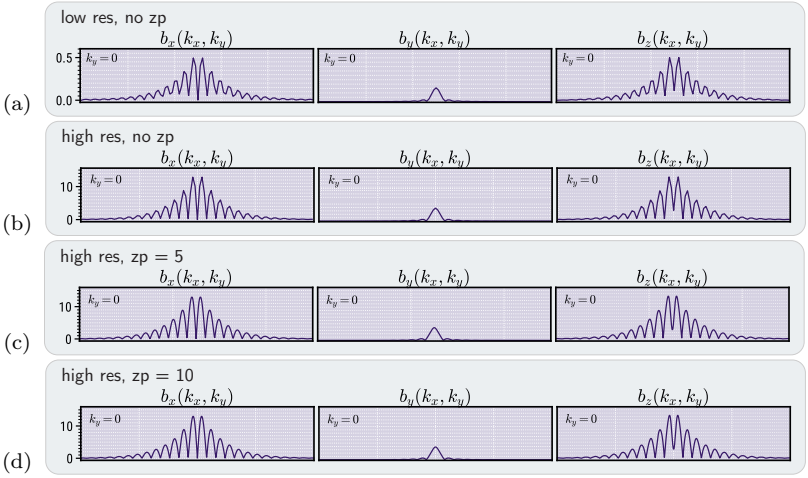

Figure 4.12: **Effect of spatial resolution and zp on the Fourier signal.** Low resolution (res) is defined as 1 pixel = 1 µm in real space while high resolution is defined as 1 pixel = 0.2 µm.

It is important to note that with discretised field maps, undersampling can lead to loss of information. Therefore, to avoid undersampling of the spectrum by the fast Fourier transformation (FFT) algorithm, zero padding (zp)[1] was used. The effects of zp on the Fourier signal are shown in figure 4.12.

Using the Fourier transforms of the magnetic field b_x, b_y and b_z, the Biot-Savart law can now be deconvoluted. In the following, different geometrical dimensions are considered.

4.3.1 Two-dimensional current reconstruction

When a current is confined in a 2D structure lying in the xy-plane (i.e. $z = 0$), $\boldsymbol{J}$ can be redefined as a lineal current density expressed in units of A/m that depends only on the planar coordinates (x, y). The integral equation (3.14) becomes a 2D integral over (x', y'). With $\boldsymbol{J}^{\mathrm{T}} = (J_x \; J_y \; 0)$, the components of the magnetic field can therefore be expressed as follows:

$$B_x(x,y,z) = \frac{\mu_0 z}{4\pi} \iint_{-\infty}^{+\infty} \frac{J_y(x',y')}{\left[(x-x')^2 + (y-y')^2 + z^2\right]^{3/2}} dx'dy', \tag{4.10}$$

$$B_y(x,y,z) = \frac{\mu_0 z}{4\pi} \iint_{-\infty}^{+\infty} \frac{-J_x(x',y')}{\left[(x-x')^2 + (y-y')^2 + z^2\right]^{3/2}} dx'dy', \tag{4.11}$$

$$B_z(x,y,z) = \frac{\mu_0}{4\pi} \iint_{-\infty}^{+\infty} \frac{J_x(x',y')(y-y') - J_y(x',y')(x-x')}{\left[(x-x')^2 + (y-y')^2 + z^2\right]^{3/2}} dx'dy'. \tag{4.12}$$

When the 2D current runs in a slab delimited by the planes $z = z_1$ and $z = z_2$, the dimensions are considered as 2.5D, and the current density is expressed in units of A/m^2. The equations can be rewritten as follows:

[1] i.e. adding additional zeros to extend the frame of the original data to obtain finer frequency bins in the Fourier frame.

$$B_x(x,y,z) = \frac{\mu_0 z}{4\pi} \iint_{-\infty}^{+\infty} \int_{z_1}^{z_2} \frac{J_y(x',y')}{\left[\Delta x^2 + \Delta y^2 + \Delta z^2\right]^{3/2}} dx'dy'dz', \tag{4.13}$$

$$B_y(x,y,z) = \frac{\mu_0 z}{4\pi} \iint_{-\infty}^{+\infty} \int_{z_1}^{z_2} \frac{-J_x(x',y')}{\left[\Delta x^2 + \Delta y^2 + \Delta z^2\right]^{3/2}} dx'dy'dz', \tag{4.14}$$

$$B_z(x,y,z) = \frac{\mu_0}{4\pi} \iint_{-\infty}^{+\infty} \int_{z_1}^{z_2} \frac{J_x(x',y')\Delta y - J_y(x',y')\Delta x}{\left[\Delta x^2 + \Delta y^2 + \Delta z^2\right]^{3/2}} dx'dy'dz', \tag{4.15}$$

where:

$$\Delta x = (x - x'),$$
$$\Delta y = (y - y'),$$
$$\Delta z = (z - z').$$

Additionally, the continuity condition for the current can be added:

$$\nabla \cdot \boldsymbol{J} = 0. \tag{4.16}$$

Using the Fourier transform defined by:

$$f(k_x, k_y, z) = \int_{-\infty}^{+\infty} \int_{-\infty}^{+\infty} F(x,y,z) e^{k_x x + k_y y} dxdy, \tag{4.17}$$

the set of equations can be rewritten in the Fourier space $\{k_x, k_y\}$, such as:

$$\begin{pmatrix} b_x \\ b_y \\ b_z \\ 0 \end{pmatrix} = \frac{\mu_0}{4\pi} \begin{pmatrix} 0 & g_z \\ -g_z & 0 \\ g_y & -g_x \\ ik_x & ik_y \end{pmatrix} \cdot \begin{pmatrix} j_x \\ j_y \end{pmatrix}$$

where $\{b_x, b_y, b_z\}$, $\{j_x, j_y, 0\}$, $\{g_x, g_y, g_z\}$ are respectively the Fourier components of the magnetic field $\boldsymbol{B}$, the current density $\boldsymbol{J}$, and the green function

$\boldsymbol{G}$. The difference between the 2D and the 2.5D system lies in the expression of the green function, which can be found in [226].

With two unknowns and four equations, it is an overdetermined system. The system can be solved as it is but because the use of B_z introduces a singularity and tends to produce artefacts, the system is reduced to a determined system:

$$\begin{pmatrix} b_x \\ b_y \end{pmatrix} = \frac{\mu_0}{4\pi} \begin{pmatrix} 0 & g_z \\ -g_z & 0 \end{pmatrix} \cdot \begin{pmatrix} j_x \\ j_y \end{pmatrix}$$

To solve this system, where the Fourier components $\{j_x, j_y, 0\}$ are the unknown parameters, the QR decomposition method [227] is used and a brief description can be found in the appendix C. Since the data for these simulations are noise-free, no additional filter is required and the inverse Fourier transform of j_x and j_y can be computed. The results are given in figure 4.13 for a 2D structure and in figure 4.14 for a 2.5D structure of total thickness = 0.4 µm.

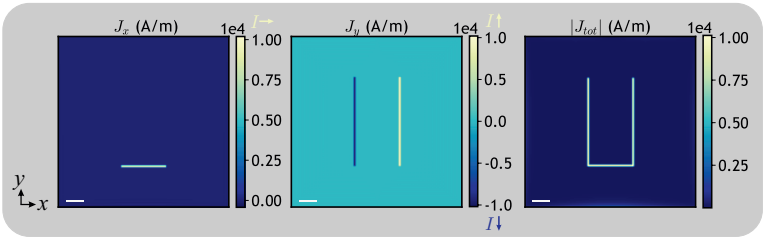

Figure 4.13: **Current distribution reconstructed using the 2D lineal model.** The scale bar are 10 µm wide.

When dealing with real data, as in chapter 5, a Hanning window (see chapter 2) is used on j_x and j_y to smooth out high-frequency components that tend to exacerbate noise. Thus, the QR decomposition method is used to solve the

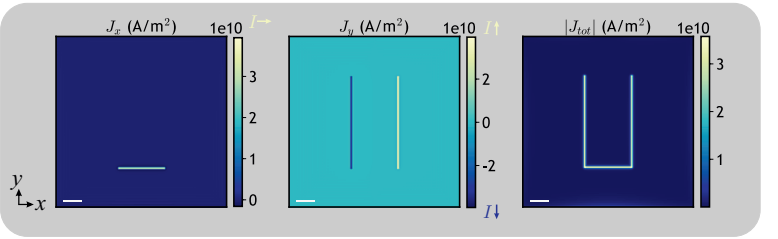

Figure 4.14: **Current distribution reconstructed using the 2D model in a slab.** Scale bar are 10 µm wide.

problem and an inverse Fourier transform is calculated on the returned parameters j_x and j_y. Finally, total variation denoising is applied to the data using the Chambolle's algorithm [228].

As described in [218], using the lateral components B_x and B_y shows better performance for the current reconstruction than using the vertical component B_z. As already discussed, one reason for this is that B_z introduces a singularity into the deconvolution process. Furthermore, B_z has an intrinsic longer-range behaviour compared to the lateral components B_x and B_y, which leads to artefacts in the current reconstruction procedure. In addition, it is important to note that the clear separation between B_x and B_y provides better readability of the signal than seeking B_z only, e.g. as given with SQUIDs. Finally, this ability to distinguish B_x from B_y is crucial in multilayered chips where orthogonal signals may overlap at the observation position.

4.3.2 Three-dimensional current reconstruction

Knowing B_x, B_y grants us access to a fully determined system when the three-dimensional components of the current density are unknown parameters. The equations are rewritten as follows:

$$B_x(x,y,z) = \frac{\mu_0}{4\pi} \iint_{-\infty}^{+\infty} \int_{z_1}^{z_2} \frac{J_y(x',y',z')\Delta z - J_z(x',y',z')\Delta y}{\left[\Delta x^2 + \Delta y^2 + \Delta z^2\right]^{3/2}} dx'dy'dz' \tag{4.18}$$

$$B_y(x,y,z) = \frac{\mu_0}{4\pi} \iint_{-\infty}^{+\infty} \int_{z_1}^{z_2} \frac{J_z(x',y',z')\Delta x - J_x(x',y',z')\Delta z}{\left[\Delta x^2 + \Delta y^2 + \Delta z^2\right]^{3/2}} dx'dy'dz' \tag{4.19}$$

$$B_x(x,y,z) = \frac{\mu_0}{4\pi} \iint_{-\infty}^{+\infty} \int_{z_1}^{z_2} \frac{J_x(x',y',z')\Delta y - J_y(x',y',z')\Delta x}{\left[\Delta x^2 + \Delta y^2 + \Delta z^2\right]^{3/2}} dx'dy'dz' \tag{4.20}$$

In the Fourier space, this translates to:

$$\begin{pmatrix} b_x \\ b_y \\ b_z \\ 0 \end{pmatrix} = \frac{\mu_0}{4\pi} \begin{pmatrix} 0 & g_z & -i\frac{g_z k_y}{k} \\ -g_z & 0 & i\frac{g_z k_x}{k} \\ i\frac{g_z k_y}{k} & -i\frac{g_z k_x}{k} & 0 \\ -i\frac{k_x}{k} & -i\frac{k_y}{k} & \frac{\partial j_z}{\partial z} \end{pmatrix} \cdot \begin{pmatrix} j_x \\ j_y \\ j_z \end{pmatrix}$$

Again, the contribution from b_z is left out and the system is reduced as follows:

$$\begin{pmatrix} b_x \\ b_y \\ 0 \end{pmatrix} = \frac{\mu_0}{4\pi} \begin{pmatrix} 0 & g_z & -i\frac{g_z k_y}{k} \\ -g_z & 0 & i\frac{g_z k_x}{k} \\ -i\frac{k_x}{k} & -i\frac{k_y}{k} & \frac{\partial j_z}{\partial z} \end{pmatrix} \cdot \begin{pmatrix} j_x \\ j_y \\ j_z \end{pmatrix}$$

As for the 2D case, a QR decomposition method (see appendix C) is used to solve the system and a Hanning window is applied on j_x, j_y and j_z to filter high-frequency components on real data, as used in chapter 5. Finally, an inverse Fourier transform followed by a Chambolle denoising algorithm is applied to the returned parameters, resulting in J_x, J_y, J_z maps shown in chapter 3 and 5.

4.4 Conclusions and outlook

This chapter discussed different approaches to solving the magnetic inverse problem to reconstruct the current distributions.

First, a qualitative method for interpreting magnetic field patterns using the Ampére's law was presented. The equation is valid in the plane of the source, whereas measurements are usually acquired away from the source plane. Therefore, this method is only a good approximation if the measurements are taken close enough to the source (e.g., at the surface of the conductor). The advantage of this method is to avoid singularities in uniaxial sensors (e.g. a single NV centre). However, the signal must be highly resolved to process the curl of the vector (i.e. the signal's rise due to the current must obey the Nyquist-Shannon sampling theorem). Therefore, the method can be helpful for scanning probe devices where a single NV centre is employed.

Secondly, two methods were introduced to quantify the current amplitude in the leads. The first method uses the Stokes' theorem. It is simple to implement, but the technique is only accurate if the signal of each wire is clearly defined. In addition, the signal must be fully integrated (i.e. the FOV must be large enough for the signal to vanish towards zero or be fully interpolated) and background-free. The second method fits the data with the infinite wire approximation. This time, the procedure is more accurate (less than 1 % error estimate), can handle multiple wires contribution and gives information about the circuit's geometry.

At last, a powerful method for converting Oersted fields to the desired quantity is the deconvolution-based method presented in section 4.3. This technique reconstructs the current distribution in the source plane by deconvoluting the signal from a green function containing the propagation information of the signal. For noise-free images, it perfectly matches the expected values. With real data, the method can amplify high-frequency noise, and it is important to apply filters to mitigate this effect. Finally, the method unfolds its full potential when used with multi-axis sensors. Firstly, because single-axis sensors only provide B_z when measuring the Oersted fields, the deconvolution process is prone to singularities in the components of the Fourier transform, for which $k_x = 0$ and $k_y = 0$. In contrast, sensors with multiple axes provide all magnetic field components and avoid these singularities, which can cause errors, artefacts and

further amplify noise. Furthermore, the ability of NV centres to capture the full vector information of the magnetic fields can be used to derive three-dimensional current distributions, as the systems of equations involved in the deconvolution process can be fully determined. This capability is crucial for assessing modern electronics, such as 3D integrated circuits, and is applied in chapter 5.

Chapter 5

Application to three-dimensional integrated circuit's activity imaging

The rapid growth and downscaling of silicon integrated circuits (ICs) have ushered in an unprecedented revolution in many areas of today's society [229–232]. For example, ICs enabled access to high-speed internet [233], in-car navigation [234] and the development of medical devices such as leadless pacemakers [235]. However, if the semiconductor community has underpinned *Moore's law* [236] for over 50 years by shrinking the size of electronic components, the scaling roadmap is nearing its end [229, 237]. Hence, next-generation technologies like self-autonomous driving devices [238] or the recently unveiled quantum processor *Eagle* [239] rely on a new strategy: adopting compact three-dimensional chip architectures [240–242].

In this regard, **device development, optimisation and failure analysis are severely challenged due to the absence of methods for direct visualisation of three-dimensional charge flow.** This particularly concerns multi-layer chips with sub-micron feature sizes, and **future advances in modern technologies critically depend on our ability to analyse such complex structures reliably**.

The use of NV centres for mapping vector currents in ICs is promising because it combines key features to investigate micro- and nano-electronic devices:

the method is non-destructive, highly sensitive and presents high spatial resolution in all three-dimensional directions. Pioneering work with NV centres has successfully demonstrated IC activity imaging [183, 243] but was limited to a two-dimensional investigation. In this chapter, prior-free imaging of vector currents in a state-of-the-art three-dimensional integrated circuit is demonstrated. This work is part of a publication available in [173].

This chapter is organised as follows:

(1) Section 5.1 introduces the particularities of three-dimensional circuit architectures. Historical technology advancements leading to this design and challenges to image electric currents in such structures are briefly reviewed.

(2) Section 5.2 demonstrates IC's activity imaging using NV centres. The current amplitude and temperature gradients of a faulty chip are compared to those of an operational one.

(3) Section 5.3 presents simulations of Oersted fields generated by multi-layered ICs comprising vertical interconnects. Procedures to differentiate signals in such complex structures are discussed.

(4) In section 5.4, reconstructed images of the three-dimensional components of the current density within the operational chip are presented.

(5) Finally, in section 5.5, the conclusions and outlook of the chapter are discussed.

5.1 Three-dimensional integrated circuit architecture

5.1.1 More than Moore

The invention of the first programmable, electric computers (Z1 [244], ENIAC [245], and Colossus [246]) marked the first time in human history where high-level human thought processes were offloaded to machines that offered better

execution. A couple of years later, in 1958, the first electronic integrated system[1] was elaborated [248, 249]. The idea of a technology roadmap for semiconductors emerged, leading to *Moore's law* in 1965 [236]. In a few words, *Moore's law* is defined as the ability to integrate twice as many transistors into a chip every two years, at a fixed cost. Following this trend, advances in silicon lithography [250–252] have enabled such exponential miniaturisation of electronics that has ushered in the modern technologies surrounding us.

However, as elementary electronic components such as transistors reach atomic scale [253, 254] and high-density electronics inherently leads to excessive heat [237], *Moore's law* is expected to flatten out by 2025 [255]. Solutions involving new materials [256, 257], device architectures [241, 242] and switching mechanisms [258, 259] have emerged to drive technology developments further. These new strategies, also known as the *More than Moore* trend, outline a new semiconductor roadmap [260]. Future advances still depend on system integration, and one dominant approach is to move from lateral to vertical scaling, i.e. to a three-dimensional chip architecture as summarised in figure 5.1.

5.1.2 Three-dimensional chip architecture

Three-dimensional integration of micro and nano-systems has become essential for advancing semiconductor technologies [261]. Vertical scaling dramatically enhances chip performances by further improving the functionality of IC technology and reducing the design's complexity.

An integrated three-dimensional circuit (3D-IC) consists of two or more layers of vertically stacked active electronic components, interconnected with vertical elements such as through-silicon vias (TSVs) [262]. Such structure improves bandwidth between chips, leading to faster data exchange and overall system energy savings through reduced communication ways. Finally, the 3D design increases integration densities and facilitates heterogeneous materials, devices, and signals co-integration, as shown in figure 5.2. Hence, such a design enhances performance and range of capability. For example, heterogeneity allows image

[1] This invention led to the 2000 Nobel Prize in Physics [247].

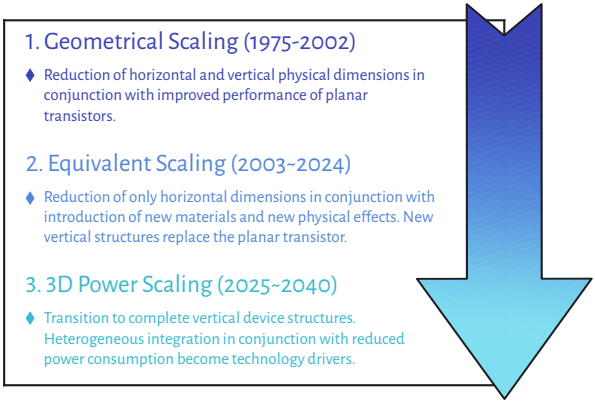

Figure 5.1: **The different ages of scaling.** The three eras of transistor scaling highlighted by NTRS[a], ITRS[b], ITRS 2.0, IRDS[c]. Adapted from [260].

[a]National Technology Roadmap for Semiconductors
[b]International Technology Roadmap for Semiconductors
[c]International Roadmap for Devices and Systems

sensors to be integrated with processors and can significantly impact future computer vision systems [263].

Overall, 3D-IC devices promise to offer multiple advantages over conventional 2D-IC devices. However, three-dimensional integration requires a better understanding of the many overlapping and vertically interconnecting systems. For this, adapted sensors are required.

5.1.3 Probing three-dimensional chip's activity

5.1.3.1 IC failure analysis

The design of a new electronic chip involves several stages, of which failure analysis serves to predict and determine the root cause of a malfunction. The design process typically requires a 12-18 month phase of iterative debugging, and failure analysis is frequently required at other times during the development

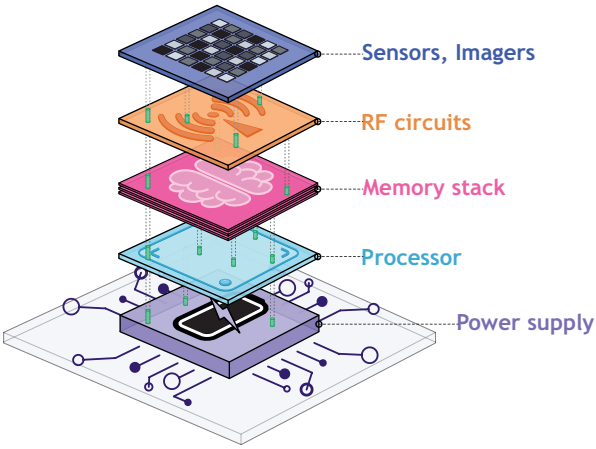

Figure 5.2: **Compact heterogeneous 3D-IC architecture.** Each active 3D-IC layer contains functional units such as processor cores and memories and heterogeneous devices such as analogue radiofrequency (RF) circuits and sensors. TSVs are integrated into the 3D-IC to generate signal, power or ground between different levels and allow communication between different layers of equipment.

process [264]. Early life failure analysis is critical as it helps to validate a functional design at an early stage of the semiconductor chain, as shown in figure 5.3, and thus steer the manufacturing process adequately.

Several aspects need to be investigated, which can fall into three categories: physical failure analysis, electrical failure analysis and data failure analysis. Physical examination is primarily used to inspect manufacturing defects, electrical investigation is used to pinpoint failure sites and data analysis is used to predict the behaviour of a chip. These techniques and tools have evolved alongside the chip designs over the past few decades [265]. In physical failure analysis, for example, the process has developed from standard microscopy to scanning electron microscopy (SEM) [266, 267], which makes it possible to detect local material anomalies on the chip surface. In electrical analysis, hot spots in the functioning device can be investigated with infrared (IR) imaging

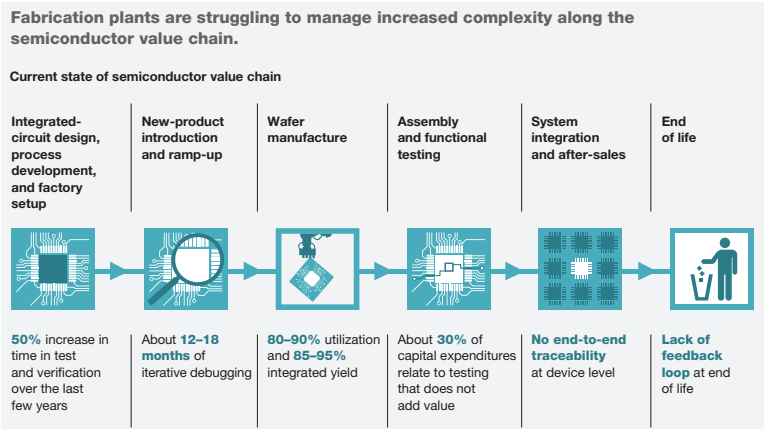

Figure 5.3: **Current state of the semiconductor value chain.** Failure analysis is an important process in manufacturing an electronic chip. Powerful and reliable analysis techniques are required to reduce overall costs. Reprinted from [264].

[268, 269], but the method is insufficient to locate a fault in a complex chip. Therefore, sophisticated SQUID-based microscopes have been developed that allow imaging of the current distribution and reveal anomalous chip behaviour with high precision [270]. Finally, several techniques can be combined in a single device to perform a complete and efficient failure analysis [271].

Although failure analysis tools are very sophisticated, 3D chip architecture addresses new challenges: planar investigations are no longer sufficient. To this end, a method based on ptychographic X-ray laminography has been recently developed and allows the analysis of geometric features with a spatial resolution of only a few nanometres [272, 273]. However, the lack of 3D electrical information limits the reliability of failure analysis on 3D-ICs.

In this context, a new strategy that enables three-dimensional current imaging on the nanoscale is investigated in the next sections.

5.1.3.2 Carrier transport in semiconductors

Current in an electronic circuit conveys information from one system part to another. Hence, the ability to detect the current's magnitude and direction is crucial for design verification, and failure analysis of anomalous currents such as leakages [274].

In thermal equilibrium, mobile electrons in the conduction band of a semiconductor move with an average velocity of 10^7 cm/s [275]. Such thermal motion of electrons is stochastic and does not result in a net current flow in the material. However, two processes can be responsible for a net current flow, under an applied bias:

(1) the presence of an electric field $\boldsymbol{E}$;

(2) the presence of a carrier concentration gradient in the material.

The first mechanism, called electron drift, induces the electrons to flow in the opposite direction of $\boldsymbol{E}$, creating a net current through the material. The second mechanism induces carriers' diffusion away from the higher concentration region to the lower concentration one, creating a net current flow in the semiconductor.

Both mechanisms can be measured using NV centres in diamond, but the following sections will discuss electron drift exclusively.

5.1.3.3 Measuring IC's activity

A natural choice to image charge transport in semiconductor devices is to sense its associated magnetic field, which passes unaffected and unobstructed through most if not all, materials used in such devices. This approach is known as the magnetic current imaging (MCI) method. Subsequently, the current distribution can be retrieved following the procedure discussed in chapter 4. Yet, the Oersted fields need to be measured and several approaches are possible.

One solution consists of delayering the chip to probe the field with a microneedle, ensuring a high spatial resolution of the magnetic field, but the method is destructive [276]. Non-destructive alternatives are based on SQUID and giant

magneto-resistance (GMR) microscopes. At room temperature, SQUID-based microscopes demonstrate excellent magnetic field sensitivity but only achieve a spatial resolution of about a few tens of micrometres due to an inherent stand-off distance [277]. Conversely, GMR microscopes can achieve sub-micron spatial resolution but demonstrate lower sensitivities [278, 279]. Furthermore, SQUID and GMR microscopes are only sensitive to a single magnetic field component, limiting reliable current imaging to the two-dimensional realm.

NV centres have the unique property to probe all three vectorial components of a magnetic field simultaneously and non-destructively on the nanoscale [21, 168]. As discussed in chapter 4, this property gives insights into the three-dimensional current distribution.

5.2 Investigating operational and faulty electronic chips

5.2.1 Experimental configuration and presentation of the test 3D-IC

The NV-based widefield microscope, described in chapter 2 and depicted in figure 5.4a, is used to synchronously map vectorial magnetic fields produced by an electronic device over a region of about 90 µm × 90 µm. MW drive was carried through a 50 µm-thick copper wire with a MW power of approximately 30 dBm. For all the measurements reported in this chapter, the total continuous-wave laser power at the back aperture of the objective was about 90 mW. The camera settings were set to 2 × 2 pixel-binning. All measurements were performed in an ambient environment at room temperature, under a bias magnetic field $|B_0|$ (with a magnitude of ≈ 5.8 mT) generated using a permanent magnet thermally stabilised at a temperature of ≈ 37 °C.

The chip investigated here is a microchip, shown in figure 5.4b, used as an mm-wave test circuit for automotive radar applications. The chip design relies on the mm-wave back-end-of-line (BEOL) technology described in [280], where interconnections between stacked layers are essential to ensure high performances of the chip [281]. Observing the device with bright-field microscopy

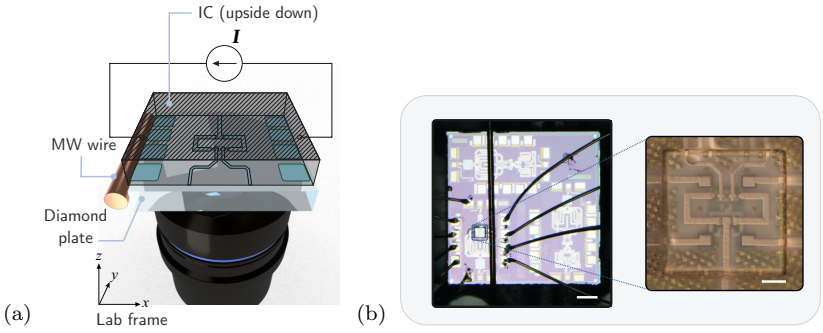

Figure 5.4: **Setup configuration and photograph of the IC.**
a) Schematic of the experiment. A microfabricated diamond plate containing a layer of near-surface NV centres is glued to the integrated circuit. The sample is mounted to an inverted microscope where laser and MW radiations excite the NV centres. A CCD camera records the emitted photoluminescence (PL) as described in section 2.2.2. b) Photograph of the IC microchip. The left-hand side picture shows the overall chip with different circuit designs. The diamond plate is glued to a region of interest outlined by a blue square. A copper wire carrying MWs is placed next to the diamond, and wire bonds connect the chip to a power supply. The right-hand side picture shows a zoom-in on the diamond plate. The scale bars are 200 µm for the left-hand side photograph and 20 µm for the right-hand side one.

at different focuses reveals two planes with conductive wires and the backplane of the chip (see figure 5.5). The IC chip was wire bonded to a printed circuit board (PCB) with 20 µm-thick gold wires. The PCB was electrically connected to a power supply (Hameg, Rhode&Schwarz) generating 3.3 V of supply voltage needed to run the chip and an additional 2 V bias signal was used to vary the total current sent to the main circuit. All the experiments were conducted without prior information about the chip, i.e. where the current should flow.

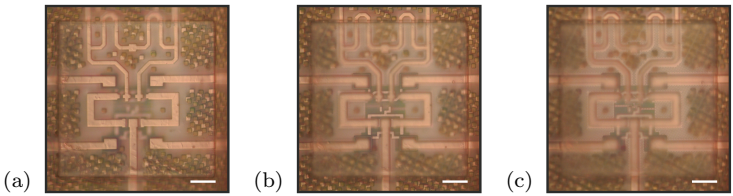

Figure 5.5: **Bright-light microscopy images of the 3D-IC with different focuses.** a) Focus on the upward plane of the electronic chip. b) Focus on the middle plane of the electronic chip. c) Focus on the backplane of the chip. All photographs are taken with x 50 magnification and the scale bars are 20 µm wide.

The aim of this section is to compare the signal produced by an operational device with a faulty one and reveal anomalous behaviour with faulty chips, otherwise indistinguishable by physical inspection.

5.2.2 Probing the perturbed NV Hamiltonian

The principle of the experiment is described in chapter 3. A diamond plate homogeneously implanted with near-surface NV centres (see appendix A) is placed in the vicinity of the current flow, at a distance of only a few hundred nanometres from the surface of the IC. A total current $I = 19.8\,\mathrm{mA}$ is injected into the circuit, which splits into several subpaths, creating distinct local Zeeman interactions with the proximal NV centres.

The experiment is performed on two distinct chips: an operational device and a defective one. Investigating both samples using bright-light microscopy reveals no difference (see figure 5.6). On the contrary, observing the Oersted fields exposes the failure immediately. ODMR spectrum taken near a wire in the operational device (figure 5.7) and in the defective one (figure 5.8) show significantly different Zeemaan shifts induced by the current. To further quantify the fields, the spectrum is fitted to extract the eight resonance frequencies for each pixel of the image. Finally, the extracted resonance frequencies are compared

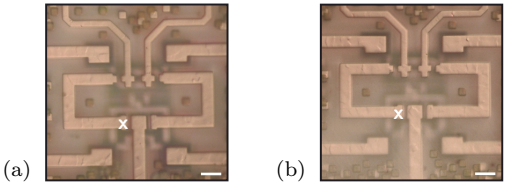

Figure 5.6: **Optical images of the operational and the defective ICs.** a) Optical image of the operational IC within the ROI chosen for the experiment. b) Optical image of the defective IC within the ROI chosen for the experiment. The scale bars are 10 µm wide.

to the ground state NV spin Hamiltonian, including the ZFS, the Zeeman and the Stark effects as defined in equations {(3.2a), (3.2b), (3.2c)}.

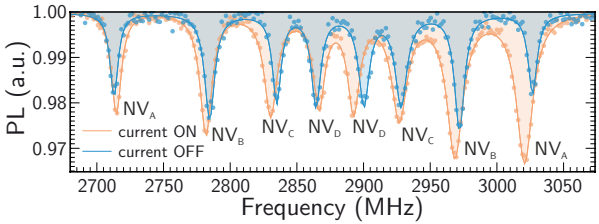

Figure 5.7: **ODMR spectra from a single-pixel near the edge of a semiconductor stripe in the operational device.** The spectra are taken at the white cross position in figure 5.6(a). The blue spectrum is obtained with a bias magnetic field B_0 of $\approx 5.8\,\mathrm{mT}$ used to split the eight resonances lines of the NV ensemble. The orange spectrum is acquired when current flows in the IC, creating a shift in the resonances due to the Zeeman interaction of the NV centres with the Oersted field. Solid lines are multiple-Lorentzian fits. Each resonance is labelled according to the corresponding NV orientation, as defined in figure 3.3.

The resulting magnetic fields extracted from the Zeeman interaction are shown in figure 5.9 for the operational device and in figure 5.10 for the defective one.

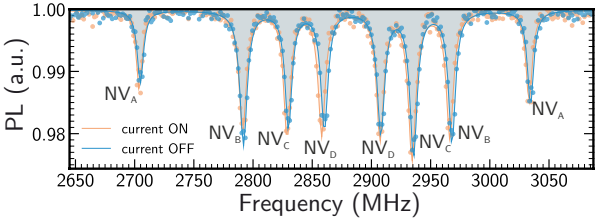

Figure 5.8: **ODMR spectra from a single-pixel near the edge of a semiconductor stripe in the faulty device.** The spectra are taken at the white cross position in figure 5.6(b). The blue spectrum is obtained with a bias magnetic field B_0 of $\approx 6.0\,\mathrm{mT}$ used to split the eight resonances lines of the NV ensemble. The orange spectrum is acquired when current flows in the IC, creating a shift in the resonances due to the Zeeman interaction of the NV centres with the Oersted field. Solid lines are multiple-Lorentzian fits. Each resonance is labelled according to the corresponding NV orientation, as defined in figure 3.3.

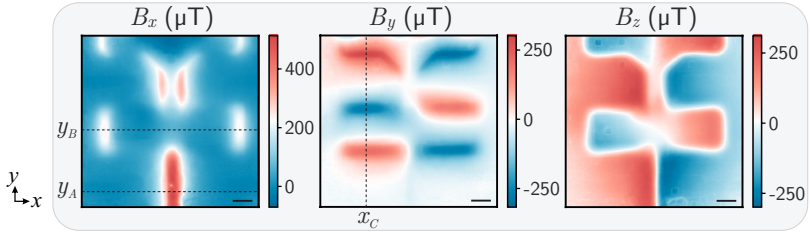

Figure 5.9: **Vectorial Magnetic field produced by the current-carrying wires in the operational device.** Mapping of the three vectorial magnetic field components B_x, B_y, B_z produced by the operational IC. The sign gives the direction of the field. Linecuts at y_A, y_B and at x_C are shown in figure 5.15-(a) for deeper analysis. The scale bars are 10 μm wide.

With the operational device, Oesterd fields clearly reflect the geometry of the underlying structure. The defective device produces nearly one order of magnitude lower magnetic fields (maximum amplitude of $|B_x| = 513(6)\,\mu\mathrm{T}$ compared

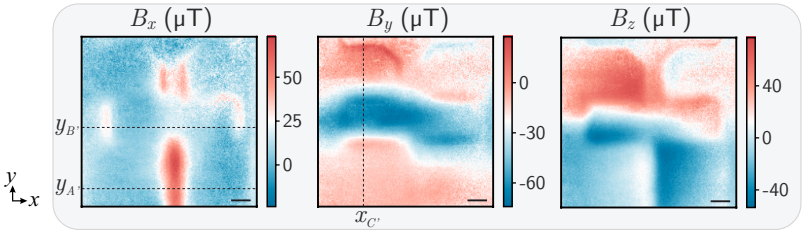

Figure 5.10: **Vectorial Magnetic field produced by the current-carrying wires in the defective device.** Mapping of the three vectorial magnetic field components B_x, B_y, B_z produced by the defective IC. The sign gives the direction of the field. Linecuts at $y_{A'}, y_{B'}$ and at $x_{C'}$ are shown in figure 5.15-(b) for deeper analysis. The scale bars are 10 μm wide.

to 73(5) μT). Furthermore, the magnetic field maps B_y and B_z produced by the defective chip show a different unstructured pattern. Further information can be extracted from the remaining parameters and are discussed below.

The ZFS has a dependence with the temperature T such as $\partial D_{\text{gs}}/\partial T \approx -75\,\text{kHz/K}$ at room temperature [195]. With no further information about the strain inside the crystal or prior information about the temperature distribution, the terms D_{gs} and the Stark term δ cannot be decorrelated. Hence, the resulting map $D_{\text{gs}} + \delta$ are shown together in figure 5.11. In figure 5.11a (operational device), the main effective parameter seems to be the temperature. The temperature is higher in the centre of the FOV and colder at the edges. This temperature rise can be explained by the presence of transistors at the centre of the map (underneath the surface), which produce heat expelled with the contact of the diamond's surface. The difference between both maps shows an averaged rise of $\approx 30K$ with closed circuits. In figure 5.11b (defective device), a singularity is present in open and closed-circuit. If attributed to temperature effects, the singularity would translate to a constant drop of $\approx 12\,K$ in this region, which is not likely to happen. The singularity can be instead associated with strain, which reduces the band gap in semiconductors and then enhances

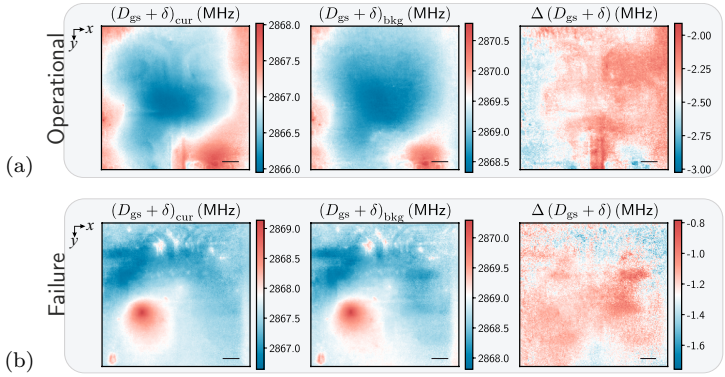

Figure 5.11: $D_{gs}+\delta$ **parameters for the operational and defective devices.** a) $D_{gs}+\delta$ parameters for the operational device, with closed-circuit $(D_{gs}+\delta)_{cur}$, open-circuit $(D_{gs}+\delta)_{bkg}$ and the difference $\Delta\,(D_{gs}+\delta) = (D_{gs}+\delta)_{cur} - (D_{gs}+\delta)_{bkg}$. b) Same as a) but for the faulty device.

leakage. Strain might be present outside the FOV as well, and the induced current leakage can explain the reduced Oersted fields generated by the defective device.

NV centres for which $\vec{B_0}$ is minimal along their quantisation axis (here NV centres along with the $\hat{u}_{NVC}$ and $\hat{u}_{NVD}$ axes) show a better sensitivity to the Stark effect [36, 53]. Such property can be exploited to seek electric field and strain effects simultaneously with the magnetic field and the ZFS, through the α and β terms, which are here mapped in figures 5.12 and 5.13 respectively. In figures 5.12 and 5.13, when the current is switched off, the spectral shifts can be unambiguously associated with internal strain inside the diamond. Additionally, the overall spectral shifts associated with strain yield similar ones to those previously reported for diamond plates [282]. However, completing the experiment with spectroscopy measurements to confirm the internal strain of the crystal would provide more robust solutions to further conclude on electric and strain effects. Furthermore, in order to reach a better sensitivity to seek

the electric fields used in this experiment via the Stark effect, ^{12}C-enriched diamonds where NV centres show narrower spectral lines should be used. Still, it is worth noting that considering α and β as part of the free parameters in the optimisation process enhances the magnetic field maps' SNR by approximately 1 % and gives insights that α, β. Even if no conclusion can be drawn about the direct observation of electric fields, this value is important in the next part, where the robustness of the current reconstruction relies on low-noise magnetic field images.

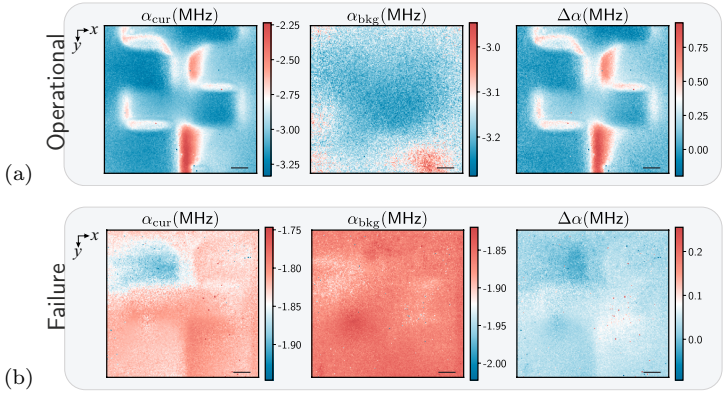

Figure 5.12: α **parameter for the operational and defective devices.** a) α parameters for the operational chip, with closed-circuit α_{cur}, open-circuit α_{bkg} and the difference $\Delta\alpha = \alpha_{\mathrm{cur}} - \alpha_{\mathrm{bkg}}$. b) Same as a) but for the faulty device.

Probing the NV centres' Hamiltonian is promising to simultaneously monitor temperature rises, strain, and currents. Such measurement is advantageous for IC analysis, where peak temperatures can go up to about 400 K. To unleash the full potential of this method, further investigation and measurements to decorrelate all the effects need to be further investigated. The following sections will focus on extracting information from the magnetic field maps.

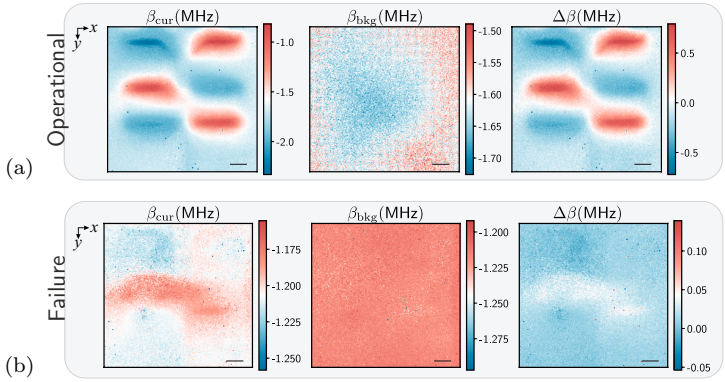

Figure 5.13: β **parameter for the operational and defective devices.** a) β parameters for the operational device, with closed-circuit β_{cur}, open-circuit β_{bkg} and the difference $\Delta\beta = \beta_{\text{cur}} - \beta_{\text{bkg}}$. b) Same as a) but for the faulty device.

5.2.3 Lateral current distribution inside the device.

To better understand the current distribution producing the Oersted field patterns (figure 5.9 and figure 5.10), the lateral current density J_{xy} is reconstructed, following the procedure described in chapter 4. The resulting current density distributions are displayed in figure 5.14. The maps show the lateral current density amplitude $|J_{xy}|$ integrated over the vertical axis z. In the operational device (figure 5.14a), the current paths follow the shape of the structure visible in figure 5.6a. A closer look at the central part of the map reveals a weak current contribution with wide lateral spreading, indicating the presence of underneath currents. Finally, the flow appears significantly weaker in some parts of the circuit, like at the sharp corners. In the defective device (figure 5.14b), several current sources produce fields of similar intensity and observing $|J_{xy}|$ alone is insufficient to comprehend the anomalies in the current path.

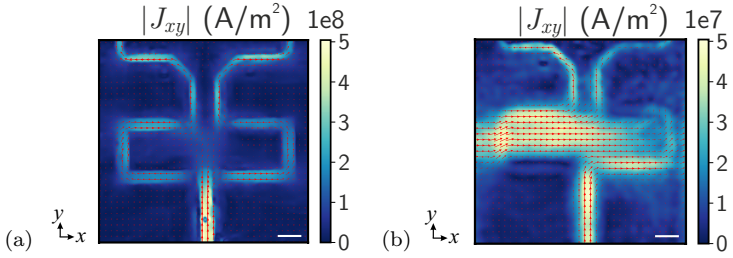

Figure 5.14: **Current distributions in the operational and the defective ICs.** a-b) In-plane current density map reconstructed from B_x and B_y in figure 5.9 and figure 5.10, respectively. Red arrows represent the flux lines of the current densities. The scale bars are 10 µm wide.

To further understand the current distribution, the different layer contributions are investigated to locate the flow within the device and seek the third dimension of the current density, J_z.

5.2.4 Localisation of currents inside the multi-layered device

The Biot-Savart law (equation (3.14)) describes the evolution of the magnetic field generated by a current source over the distance of observation. Therefore, currents can be localised in space by investigating the source-sensor distance dependence of the law. Thus, to resolve the signal in the vertical direction z, linecuts in the magnetic field maps B_x and B_y (figure 5.9 and figure 5.10) are investigated. The linecuts in B_x at positions $y = y_A$, $y = y_B$ for the operational device are shown in figure 5.15a and linecuts at positions $y = y_{A'}$, $y = y_{B'}$ for the defective device are shown in figure 5.15b. Finally, linecuts in B_y at positions $x = x_c$ for the operational chip and at $x = x_{c'}$ for the defective chip are shown in figure 5.16.

The linecuts are fitted according to the Biot-Savart model (equation (3.14)), using the infinite wire approximation given by the equation (4.8), defined in section 4.2.2.2. At first, the parameters I_{xy}, r_{wire}, dz, and o are considered as

free parameters. The fitting reveals a contribution from two layers: the first at $\Delta z_1 = 4.5(5)\,\mu\text{m}$ away from the layer of NV centres, and the second at $\Delta z_2 = 8.5(8)\,\mu\text{m}$. The fitting procedure is repeated a second time, considering only the two vertical positions mentioned above. The results are shown in figure 5.15 and figure 5.16. The returned parameters are given in tables 5.1, 5.2 and 5.3.

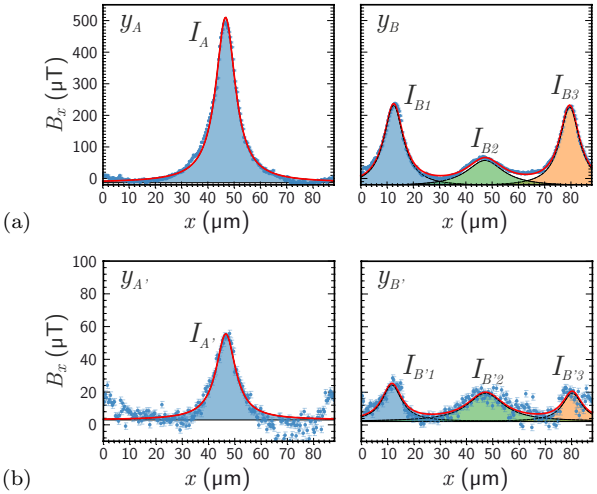

Figure 5.15: **Experimental contributions of Oersted fields originating from different layers.** a) Linecuts of experimental data (blue dots) outlined in figure 5.9 along the x-axis at the vertical position y_A (left panel) and at the vertical position y_B (right panel). b) Linecuts of experimental data (blue dots) outlined in figure 5.10 along the x-axis at the vertical position $y_{A'}$ (left panel) and at the vertical position $y_{B'}$ (right panel). The fit (solid red line) of each curve returns the parameters given in tables 5.1 and 5.2. Plain colours underline the contribution of each single wire.

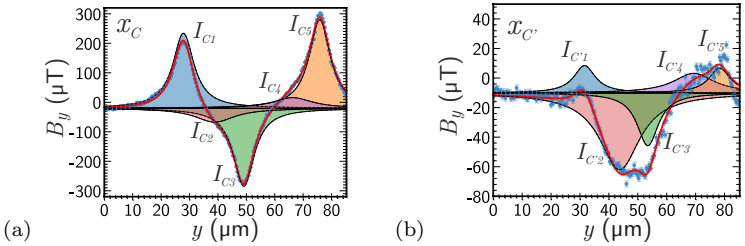

Figure 5.16: **Current distributions in the operational and the defective ICs.** a) Linecut along y at the position $x = x_C$ for the operational device. The curve is fitted with a 5-wire model (red solid line), and the returned current amplitudes are displayed in table 5.3. b) Same as a) but for the defective device, i.e. at $x = x_{C'}$.

In the operational (failure) case scenario, a current of amplitude I_A ($I_{A'}$) is identified in the main lead, which divides into currents of amplitude I_{B1} ($I_{B'1}$) and I_{B3} ($I_{B'3}$) in the split branches (figure 5.15a,b). Comparing the results of the defective device with those of the operational one, one can observe that most of the loss occurs in the outer layer (at Δz_1) where the current amplitude is one order of magnitude lower. In contrast, the deeper layer (at Δz_2) shows less loss. Analysis of the line profiles along y at positions $x = x_c$ and $x = x_{c'}$ reveals another current contribution at Δz_2 present in the operational and defective devices, in both cases without any obvious anomaly, with $I_{C2} \simeq I_{C'2}$. From these observations, the fault seems to take place in the layer at Δz_2 and then affects the outer layer by propagation.

Overall, the simple model with infinite wire approximation already shows excellent agreement with the experimental data. To check the consistency of the procedure, the values for different biases are compared with those given by the manufacturer in section 5.2.5. In addition, a simulation of the Oersted fields generated by a multilayer chip is performed in section 5.3.

	Linecut along x, at $y = y_A$	Linecut along x, at $y = y_{A'}$
$\Delta z = \Delta z_1$ $\hookrightarrow 4.5\,\mu m$	$I_A = 11.77(6)\,mA$	$I_{A'} = 1.18(4)\,mA$

Table 5.1: **Fit results of the experimental data linecuts at $y = y_A$ and $y = y_{A'}$.** Fit using a single-wire model. The linecut along x, at $y = y_A$ is taken from the operational device's data and the linecut at $y = y_{A'}$ is taken from the defective device's data

	Linecut along x, at $y = y_B$	Linecut along x, at $y = y_{B'}$
$\Delta z = \Delta z_1$ $\hookrightarrow 4.5\,\mu m$	$I_{B1} = 5.64(5)\,mA$	$I_{B'1} = 0.50(3)\,mA$
	$I_{B3} = 5.76(5)\,mA$	$I_{B'3} = 0.39(3)\,mA$
$\Delta z = \Delta z_2$ $\hookrightarrow 8.5\,\mu m$	$I_{B2} = 3.49(8)\,mA$	$I_{B'2} = 0.73(5)\,mA$

Table 5.2: **Fit results of the experimental data linecuts at $y = y_B$ and $y = y_{B'}$.** Fit using a single-wire model. The linecut along x, at $y = y_B$ is taken from the operational device's data and the linecut at $y = y_{B'}$ is taken from the defective device's data

	Linecut along y, at $x = x_C$	Linecut along y, at $x = x_{C'}$
$\Delta z = \Delta z_1$ $\hookrightarrow 4.5\,\mu m$	$I_{C1} = 5.73(5)\,mA$	$I_{C'1} = 0.42(3)\,mA$
	$I_{C3} = -5.94(6)\,mA$	$I_{C'3} = -0.80(4)\,mA$
	$I_{C5} = -6.76(6)\,mA$	$I_{C'5} = 0.38(5)\,mA$
$\Delta z = \Delta z_2$ $\hookrightarrow 8.5\,\mu m$	$I_{C2} = -1.99(8)\,mA$	$I_{C'2} = -2.20(5)\,mA$
	$I_{C4} = 1.54(8)\,mA$	$I_{C'4} = 0.56(6)\,mA$

Table 5.3: **Fit results of the experimental data linecuts at $x = x_C$ and $x = x_{C'}$.** Fit using a single-wire model. The linecut along y, at $x = x_C$ is taken from the operational device's data and the linecut at $x = x_{C'}$ is taken from the defective device's data

5.2.5 Comparison with manufacturer's values

In order to assess the validity of the experimental results and confirm the operation of the device, the values obtained experimentally are compared with the

actual geometry of the device and the expected current amplitudes given by the manufacturer.

As mentioned above, the multi-layered BEOL technology was developed and described by the manufacturer in [280] and a capping layer of about 2.3 µm protects the conductive layers. The Areal confocal 3D probe (NanoFocus AG) was used to measure the sample's height profile, enabling to estimate the thickness of the glue to 0.8(1) µm. Thus, the distance of the active layers to the NV centres can be estimated to $\Delta z_{1,\mathrm{true}} = 4.5(1)\,\mu\mathrm{m}$ and $\Delta z_{2,\mathrm{true}} = 7.9(1)\,\mu\mathrm{m}$. As such, the experimentally determined values of Δz_1 and Δz_2 are confirmed with the actual geometry of the device.

The current amplitudes determined experimentally for the operational device are now compared to the expected values of direct current in the main lead and the split branches given by the manufacturer. The values depend on an applied bias voltage and are summarised in table 5.4.

Bias Voltage	Resulting current for main lead	Resulting current for split branches
no bias	$I_A = 10.0\,\mathrm{mA}$	$I_{B1,3} = 5.0\,\mathrm{mA}$
0.5 V	$I_A = 8.2\,\mathrm{mA}$	$I_{B1,3} = 4.1\,\mathrm{mA}$
1.0 V	$I_A = 10.0\,\mathrm{mA}$	$I_{B1,3} = 5.0\,\mathrm{mA}$
2.0 V	$I_A = 13.8\,\mathrm{mA}$	$I_{B1,3} = 6.9\,\mathrm{mA}$
3.0 V	$I_A = 17.6\,\mathrm{mA}$	$I_{B1,3} = 8.8\,\mathrm{mA}$

Table 5.4: **Bias voltage dependence of current, given by the manufacturer.**

The Oersted field is acquired for each bias using the same procedure as in section 5.2.2, resulting in the B_x maps shown in figure 5.17. The linecuts along the x-axis at positions y_A and y_B are shown in figure 5.18. The linecuts are fitted according to the equation (3.14) and the resulting current amplitudes in the main lead and the split branches are summarised in the table 5.5. Taking into account the losses due to the in-house settings, such as the gold wire bonding, the values follow the same tendency as expected. This confirms the good functioning of the device labelled so far as the *operational* device.

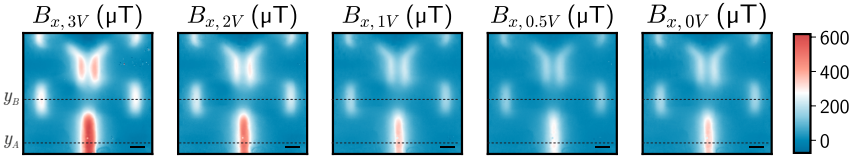

Figure 5.17: B_x **maps produced by various bias voltages.** From left to right: the bias voltage has been set to the following values: 3.0 V, 2.0 V, 1.0 V, 0.5 V, no bias; resulting in Oersted fields of different magnitude. Linecuts along the x-axis, at y_A and y_B are shown in figure 5.18. Note that the dataset for the bias voltage 2.0 V is a different dataset than shown in figure 5.9. The scale bars are 10 μm wide.

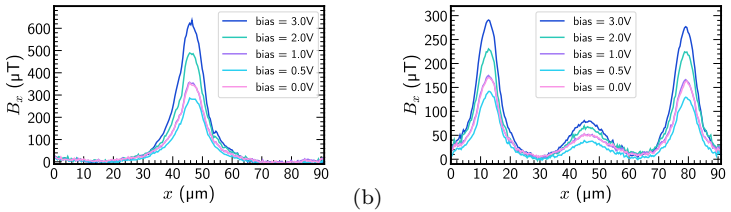

Figure 5.18: B_x **profiles for various bias voltages.** a) Linecut of B_x along x at a position $y = y_A$, showing the Oersted field produced by the main lead for various bias voltages. b) Linecut of B_x along x at a position $y = y_B$, showing the Oersted field produced by the split branches for various bias voltages.

Bias Voltage	Resulting current for main lead	Resulting current for split branches
no bias	$I_A = 8.49(5)$ mA	$I_{B1} = 3.95(3)$ mA, $I_{B3} = 4.21(3)$ mA
0.5 V	$I_A = 7.14(5)$ mA	$I_{B1} = 3.29(3)$ mA, $I_{B3} = 3.59(3)$ mA
1.0 V	$I_A = 8.58(5)$ mA	$I_{B1} = 4.04(3)$ mA, $I_{B3} = 4.27(3)$ mA
2.0 V	$I_A = 11.79(6)$ mA	$I_{B1} = 5.66(5)$ mA, $I_{B3} = 5.71(5)$ mA
3.0 V	$I_A = 15.6(1)$ mA	$I_{B1} = 7.07(4)$ mA, $I_{B3} = 7.44(4)$ mA

Table 5.5: **Bias voltage dependence of current, extracted experimentally.**

5.3 Simulation of Oersted fields generated by a 3D device

5.3.1 Signal generated by a 3D device

In this section, all the magnetic field simulations were made using Python software. The simulation reproduces the layering of the chip, which consists of the BEOL technology made of SiGe described in [280], and some of the apparent geometric features for guidance only. The total thickness of the simulated structure is 11.8 µm and combines twelve stacked layers, as depicted in figure 5.19. As shown in figure 5.20, two layers across the structure are electrically active and designated as 1st and 2nd active layers (ALs). TSVs connect the 1st AL to the bottom layer of the structure.

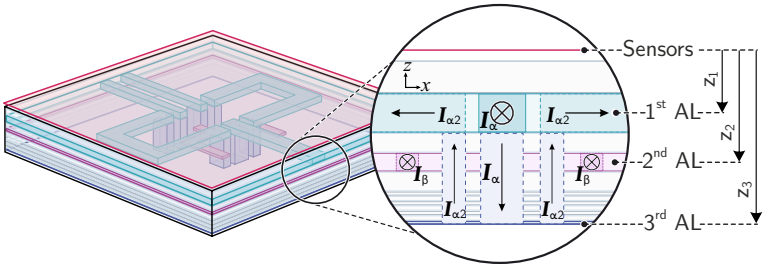

Figure 5.19: **Geometry of the simulated structure.** A layer of NV centres is separated from the chip by 0.8 µm. The structure consists of twelve layers comprising the two ALs and TSVs. A current of amplitude $I_\alpha = 11.8\,\text{mA}$ flows into the main branch of the 1st AL, flows down to the bottom layer of the structure where it splits into two subpaths of amplitude $I_{\alpha 2} = \frac{I_\alpha}{2}$ and flows back to the 1st AL. In the second AL, a current of amplitude $I_\beta = 2\,\text{mA}$ is injected into each of the two branches, which then combine into one.

The magnetic fields generated by this structure are simulated, resulting in patterns at the position of the sensors shown in figure 5.21. Similar to the experimental observations (figure 5.9), the contribution of the 1st AL is well-defined and clearly related to the shape of the structure. The contribution of the 2nd AL shows a pronounced lateral dispersion, and the signal arising from

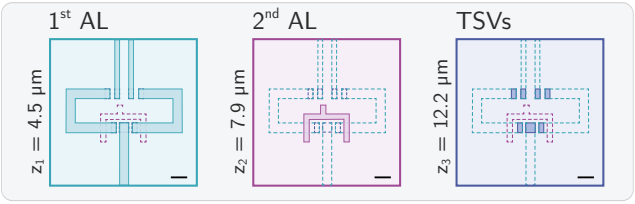

Figure 5.20: **Top view of the individual AL and TSVs that make up the simulated structure.** The 1st, 2nd AL and the bottom layer of the structure are located at $z_1 = 4.5\,\mu m$, $z_2 = 7.9\,\mu m$ and $z_3 = 12.2\,\mu m$ from the sensors. The scale bars are 10 µm wide.

two different wires starts to blur. Finally, the vertical current's contribution is weak due to the observation position and the presence of counterpropagating currents that average the contributions of the magnetic field out. Nevertheless, a current propagating vertically has a non-zero contribution in B_{xy} contrary to its contribution in B_z.

Figure 5.22 shows the simulated Oersted fields generated by each AL and the TSVs at the sensor position. The complexity in non-destructively mapping the activity of such devices is that the signal blurs with distance, and signals originating from different parts can blend into each other and create complex patterns. For these reasons, recognising and distinguishing patterns is a crucial feature that needs further development in the current reconstruction. This section discusses how the contributions of the different parameters differ and how they can, therefore, be used with pattern recognition algorithms.

5.3.2 Signal generated by TSVs

An essential aspect of this simulation is the Oersted fields generated by the TSVs. A striking feature is that the TSVs do not generate a signal in B_z since the current only flows along the vertical axis z. Accordingly, methods based solely on the measurement of B_z (e.g. standard microscopes based on SQUIDs)

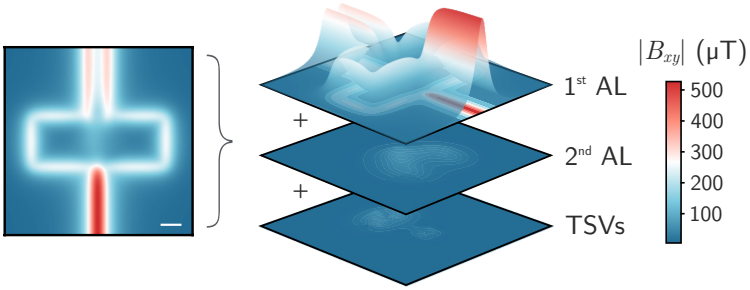

Figure 5.21: **Oersted field contributions emanating from different layers in the simulated structure.** The Left-hand side panel shows the Oersted field in the xy-plane generated by all active components at the sensor layer position. The right-hand side panel shows the separate contribution from each AL, where the vertical axis represents the lateral magnetic field amplitude $|B_{xy}|$. The scale bar is 10 µm wide.

are not sufficient to map the activity generated by TSVs. Therefore, it is worth mentioning that NV-based imaging provides, as of today, the best alternative to map the activity of TSVs with high spatial resolution.

Three critical factors influence the magnetic pattern produced by TSVs: the number of wires contributing to the pattern, the length l_z of each wire, and the current amplitude I in a wire and its direction. Here, the influence of each of these parameters on the simulated structure is investigated.

Figure 5.23 shows the amplitude patterns of the magnetic field $|B_{xy}| = \sqrt{B_x^2 + B_y^2}$ and the flux lines generated by each TSV in the simulated circuit. First, the contributions of the elements propagating in opposite directions are separated, leading to figures 5.23a-b. The pattern produced by a single wire is simple: the magnetic field is zero at the centre of the wire and has a radial symmetry around the axis of the wire. Downstream currents produce clockwise flux lines, while upstream currents produce counterclockwise ones. Compared to a single wire, the pattern created by two co-propagating wires close together

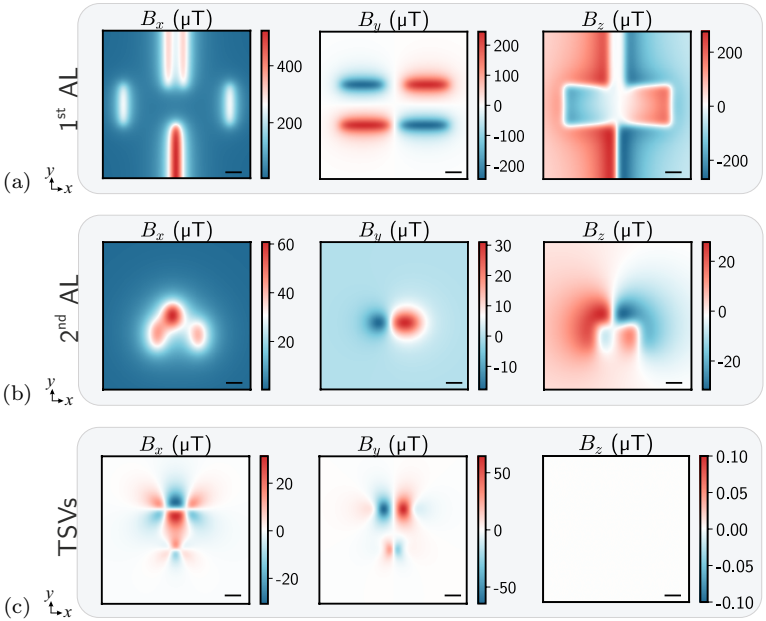

Figure 5.22: **Top view of the Oersted fields generated by the active element of the simulated structure.** a) B_x, B_y, B_z patterns generated by the 1st AL at the position of the sensors. b) B_x, B_y, B_z patterns generated by the 2nd AL at the position of the sensors. c) B_x, B_y, B_z patterns generated by the TSVs at the position of the sensors. The scale bars are 10 µm wide.

is slightly different. The magnetic field is zero when the flux lines of each wire cancel out, and the pattern of magnetic amplitude depends on the distance between the two wires. Finally, when the contributions of all the wires are combined (including opposing currents), the pattern becomes more complex, as shown in figure 5.23c. The total magnetic field magnitude becomes smaller, making it difficult to determine the number of wires from the magnetic amplitude pattern alone. However, observation of the magnetic flux lines provides additional information: three significant loops corresponding to the number of

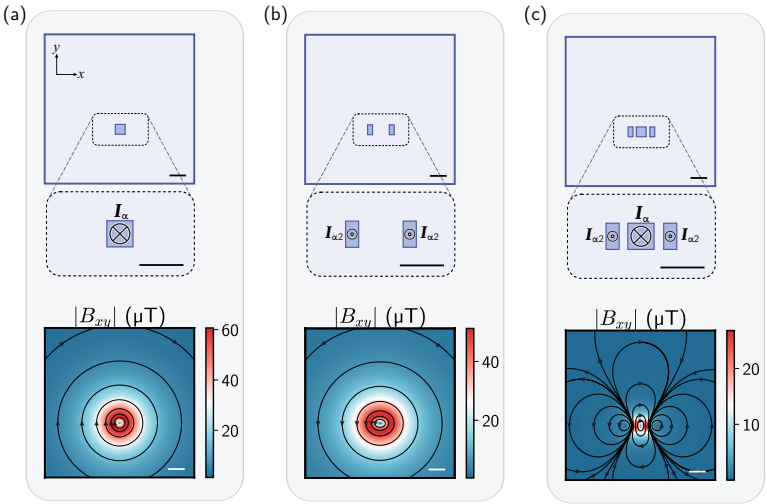

Figure 5.23: **Top view of the Oersted fields generated by the TSVs.** a) *Top*: Schematic of the simulated structure with a close-up around the lead in which a current of amplitude I_α flows from the 1$^{\text{st}}$ AL to the bottom layer of the chip. *Bottom*: Corresponding $|B_{xy}|$ pattern generated by the simulated TSV at the position of the sensors. b) *Top*: Schematic of the simulated structure with a close-up around the leads, in which a current of amplitude $I_{\alpha 2} = \frac{I_\alpha}{2}$ flows from the bottom layer of the chip to the 1$^{\text{st}}$ AL. *Bottom*: Corresponding $|B_{xy}|$ pattern generated by the simulated TSVs at the position of the sensors. c) *Top*: Schematic of the simulated structure with a close-up around the leads combining the current distributions from (a) and (b). *Bottom*: Corresponding $|B_{xy}|$ pattern generated by the simulated TSVs at the position of the sensors. The solid black lines with arrows represent the magnetic field flux. The scale bars are 10 μm wide.

wires can be observed. Therefore, observing the magnetic flux lines in conjunction with the amplitude pattern is an important tool to consider for determining the number of wires in magnetic field analysis.

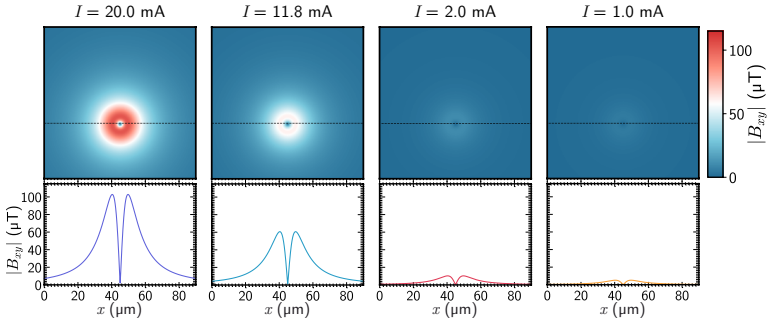

Figure 5.24: **Magnetic field pattern for a vertical wire with different current amplitude I.** Field observed at a distance $z = 4.5\,\mu\text{m}$ for a single wire of length $l_z = 7.7\,\mu\text{m}$. *Top*: Magnetic field patterns. *Bottom*: Magnetic field profile taken along the dashed black line drawn on each magnetic field map. The second panel from the left shows the parameters used for the central TSV in the simulated structure.

In figure 5.25, the impact of the total amplitude I in a single TSV on the resulting magnetic field pattern is considered. Various amplitudes I are considered while all the other parameters are kept constant, and a linear relationship between the total current I in a wire and the Oersted field amplitude can be observed. The higher the total current I in a wire, the higher the Oersted field amplitude and the wider the resulting magnetic field pattern.

Finally, in figure 5.24, the influence of the length l_z of a single TSV on the magnetic field pattern is considered. The Oersted field produced by a wire of length l_z results from the contributions of infinitesimals integrated over l_z. The greater the length l_z of the wire, the greater the amplitude of the Oersted field. Here, too, the resulting magnetic field pattern expands with l_z.

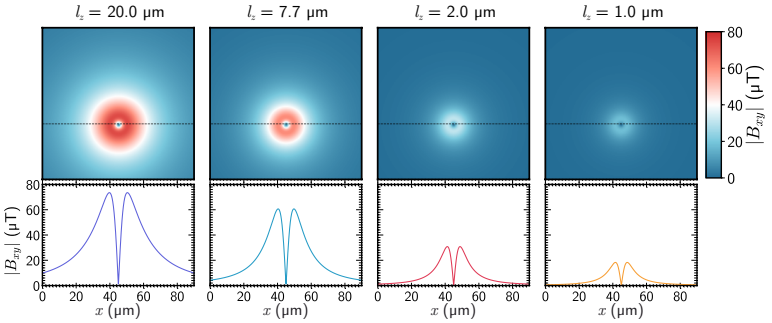

Figure 5.25: **Magnetic field pattern for a vertical wire with different length l_z.** Field observed at a distance $z = 4.5\,\mu\text{m}$ for a single wire of length l_z. The total current amplitude is $I_\alpha = 11.8\,\text{mA}$. *Top*: Magnetic field patterns. *Bottom*: Magnetic field profile along the dashed black line on each magnetic field map. The second panel from the left shows the parameters used for the central TSV in the simulated structure.

However, figure 5.26 shows that the influence of the parameters I and l_z scales differently. The total current amplitude I has a stronger effect on the total amplitude $|B_{xy}|$ than the length l_z. On the other hand, the lateral spreading of the magnetic pattern is more pronounced with the length l_z than with the total amplitude I. Therefore, the dependence of $|B_{xy}|$ on these parameters can be differentiated.

Furthermore, additional measurements can be made in an experiment. For example, $|B_{xy}|$ can be measured by varying the magnitude I or by performing scans over the vertical distance z above the sample. Finally, since multiple wires in all directions create a more complex pattern, the information given by $(B_{xy} - B_z)$ can be used to isolate the contributions of the TSVs only. Exploring these features for developing pattern recognition algorithms using machine learning is extremely promising for the analysis of complex chip designs.

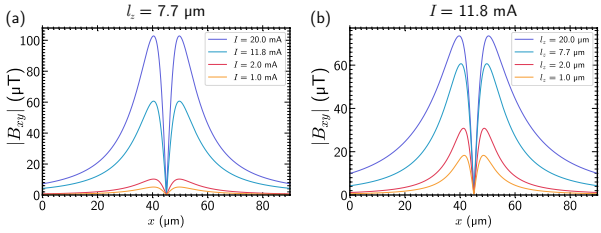

Figure 5.26: **Magnetic field profiles for a vertical wire with different parameters.** a) Field observed at a distance $z = 4.5\,\mu\text{m}$ for a single wire of length $l_z = 7.7\,\mu\text{m}$ and with varying current amplitude I. b) Field observed at a distance $z = 4.5\,\mu\text{m}$ for a single wire of varying length l_z. The total current amplitude is $I_\alpha = 11.8\,\text{mA}$.

5.3.3 Signal generated by overlapping wires

Finally, another aspect to consider in multi-layered devices is the contribution of overlapping wires. Several case studies are discussed in this section.

First, two overlapping wires with different dimensions are considered, as shown in figure 5.27a. A current I_α flows along the y-axis in a single wire located in the 1$^{\text{st}}$ AL and in a second wire located in the 2$^{\text{nd}}$ AL, producing the Oersted fields shown in figure 5.27b. As the magnetic pattern spreads over the distance z, there is an apparent distortion of the pattern: a local increase in intensity due to the wire in the 2$^{\text{nd}}$ AL can be observed. A complementary way to assess the presence of the underlying wire is to look at the profile of B_x along the current direction (i.e. the y-axis) as shown in figure 5.27c. The Oersted field generated by the wire in the 2$^{\text{nd}}$ AL adds a bell-shaped pattern to the otherwise almost flat B_x profile. Therefore, local rises in the Oersted field maps and profiles along the current direction can help identify the wires' contributions from different layers. It is important to note that inspection of B_x along the y-axis is only possible because the NV centres resolve the three components B_x, B_y, B_z separately, as opposed to methods that detect B_z only.

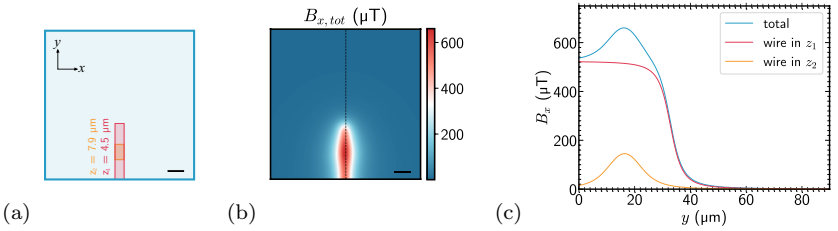

(a) (b) (c)

Figure 5.27: **Top view of Oersted fields created by overlapping wires of different dimensions.** a) Schematic top view of the overlapping wires. b) $B_{x,tot}$ pattern generated by the combined contributions of a current I_α in the overlapping leads, at the sensor position. c) B_x profile along the dashed line in (b). The blue line represents the combined contribution of both wires; the red line shows the contribution of the wire in the 1st AL (i.e. $z = z1$), and the orange line shows the contribution of the wire in the 2nd AL (i.e. $z = z2$). The scale bars in (a)-(b) are 10 µm wide.

Secondly, overlapping wires with identical dimensions are considered with two scenarios: wires with partial overlap as in figure 5.28a and wires with perfect overlap as in figure 5.29a. Again, a current I_α flows along the y-axis in a wire in the 1st AL and in a second wire in the 2nd AL. The resulting Oersted fields are shown in figure 5.28b-d and figure 5.29b-d. A linecut along the orthogonal axis of the wire (i.e., the x-axis) is shown in figure 5.30. In the case of partially overlapping wires, the lateral shift between the wires results in an asymmetric magnetic pattern. This asymmetry undoubtedly underlines the contribution of the different wires and helps to determine them. Finding evidence of multi-wire contributions is more challenging in the case of completely overlapping wires. The depths of the wires must be known so that the wings of the magnetic field profile (vanishing sides) can help determine the contribution of the wires.

In both cases, fitting a single profile line with no prior information is insufficient to determine the number of wires, depth, and current contribution. Assuming the Oersted field is measured through a larger area where the paths

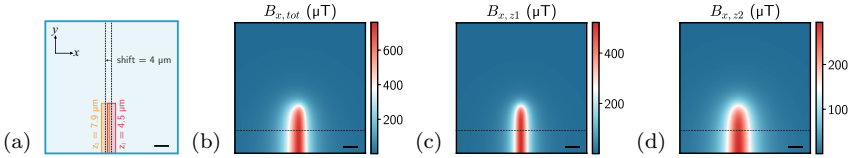

Figure 5.28: **Top view of Oersted fields created by partially overlapping wires.** a) Schematic top view of the partially overlapping wires. b) B_x pattern generated by the combined contributions of the main leads in the 1st AL and the 2nd AL, at the sensor position. c) B_x pattern generated by the contribution of the main lead in the 1st AL, at the position of the sensor. d) B_x pattern generated by the contribution of the main leads in the 2nd AL, at the position of the sensor. The scale bars are 10 µm wide.

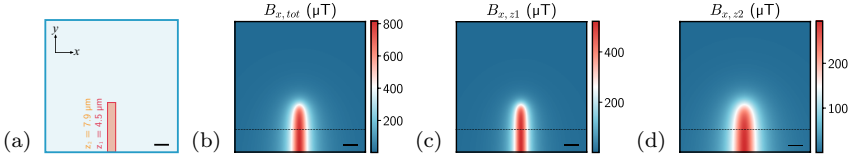

Figure 5.29: **Top view of the Oersted fields generated by perfectly overlapping wires.** a) Schematic top view of the overlapping wires. b) B_x pattern generated by the combined contributions of the main leads in the 1st AL and the 2nd AL, at the position of the sensor. c) B_x pattern generated by the contribution of the main lead in the 1st AL, at the position of the sensor. d) B_x pattern generated by the contribution of the main leads in the 2nd AL, at the position of the sensor. The scale bars are 10 µm wide.

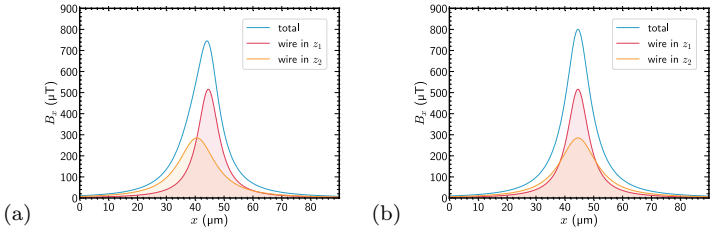

Figure 5.30: **Magnetic field profiles generated by overlapping wires.** a) B_x profile generated by the partially overlapping wires, along the dashed line shown in figure 5.28. b) B_x profile generated by the perfectly overlapping wires, along the dashed line shown in figure 5.29. In (a) and (b), blue lines represent the combined contribution from both wires; red lines show the contribution from the wire in the 1$^{\text{st}}$ AL (i.e. $z = z1$) and orange lines show the contribution from the wire in the 2$^{\text{nd}}$ AL (i.e. $z = z2$).

differentiate, optimisation of the fitting procedure over the overall circuit can lead to robust results. This procedure is valid when the device is not too complex (i.e. single wires are distinguishable on some parts of the circuit). Otherwise, the device's geometry must be first determined by other means, such as X-ray imaging.

Finally, in the last scenario, crossing wires are considered. This time, a current I_α runs along with the y-axis in a wire in the 1$^{\text{st}}$ AL and along with the x-axis in a wire in the 2$^{\text{nd}}$ AL as shown in figure 5.31a. These currents generate orthogonal Oersted fields, as shown in figure 5.31b-d. The currents are unambiguously distinguishable as NV centres separately image the three magnetic field components.

From this analysis, it is clear that the NV centres offer several advantages for mapping currents in a three-dimensional device. The unique ability to image B_x, B_y, and B_z separately on the nanoscale grants access to all components of current density in microdevices. Furthermore, it enables the search for in-depth information, especially with crossing wires for which the B_x map can be

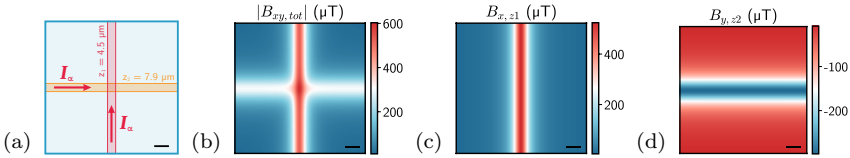

Figure 5.31: **Top view of Oersted fields generated by the crossing overlapping wires.** a) Schematic top view of the overlapping wires. b) B_x pattern generated by the combined contributions of the main leads in the 1st AL and the 2nd AL, at the sensor position. c) B_x pattern generated by the contribution of the main lead in the 1st AL, at the position of the sensor. d) B_x pattern generated by the contribution of the main leads in the 2nd AL, at the position of the sensor. The scale bars are 10 µm wide.

decorrelated from the B_y map. Finally, these fields can be measured with the highest resolution known for the MCI method, as discussed in section 2.1.2.

Finally, to observe vertical currents, information about the third component of the current density J_z is inferred in section 5.4.

5.4 Three-dimensional current imaging with sub-micron resolution

5.4.1 Experimental results

The current-carrying wires have a non-negligible thickness of a few hundred nanometres, leading to a possible contribution of the current's z component. In order to evaluate the total current density reliably, a component $J_z \neq 0$ in equation (3.14) is now considered, following the procedure described in chapter 4. The resulting maps are shown in figure 5.32, and as for the current density images in figure 5.16, they show an integrated signal over the vertical axis z. Using the fitting algorithm employed in figure 5.15 over the entire map would enable the selection of the signal from each layer separately. However, the layout must be known for several microns-thick devices to reconstruct the current density

reliably over the entire chip, since the magnetic field spreading from the deep layers is too prominent. Thus, in figure 5.33, the current in the outer lead only is represented (data out of the leads are not displayed for representation only).

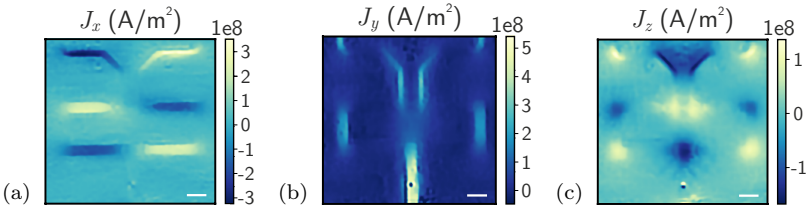

Figure 5.32: **Current density maps.** a-c) Images of the three vectorial components of the current density J_x, J_y, J_z for the operational device. The scale bars are 10 µm wide.

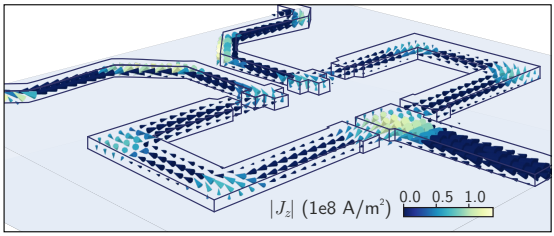

Figure 5.33: **Three-dimensional representation of the current flow in the outer layer of the IC.** The thickness of the arrow scales with the total current density magnitude, and the colour scales with the magnitude of J_z.

A non-negligible current flow in the z-direction at the edges and the corners of the leads can be observed in figure 5.32c and figure 5.33. Such observation implies that using a two-dimensional model for a three-dimensional device can lead to locally underestimating the current amplitude. For example, a weaker current density was observed at the corners of the split branches when considering a lateral flow only, such as in figure 5.16. This information can be crucial for evaluating current crowding at corners in interconnect structures, which plays

an essential role in nucleating voids and hence failure of ICs [283–285]. Substantially, having access to the full-vector information of the current density helps quantify and understand current flow through different stacks in layered materials. For instance, in the outer layer, a prominent J_z contribution at the edge of the main branch can be observed. As for the simulation (figure 5.21), this contribution is the result of counter-propagating currents. The current in the main lead flows down to a deeper layer, where it splits into two paths and goes back to the outer layer. As the component B_z does not carry information about J_z and B_{xy} shows a specific pattern with the presence of counter-propagating fields, one can develop an algorithm using $(B_{xy} - B_z)$ with pattern recognition techniques [286] to identify the contribution from each current sources.

5.4.2 Spatial resolution limitations

Resolving currents from different sources across the structure also depends on the spatial resolution of the imaging technique. NV centres offer the closest sensor-sample proximity known so far, but the geometry and capping layers of microelectronic devices themselves limit the spatial resolution of magnetic field maps to a few micrometres. This section discusses the limitations related to the spatial resolution of the imaging technique.

5.4.2.1 Spatial resolution of the optical imaging instrument

According to Rayleigh's criterion [163] and with the optical setup configuration used in this work (see section 2.2.2), the optical lateral spatial resolution xy is about 450 nm. Such a high spatial resolution is required here to avoid restricting the spatial resolution of the magnetic field images. For situations where an even higher spatial resolution is needed, techniques to image beyond the diffraction limit can be applied to the NV-based microscope [3, 100].

5.4.2.2 Spatial resolution of the magnetic field images

One crucial aspect of any magnetic field detection technique is that the resolution is ultimately limited by the sensor-source distance or the sensor size. As an

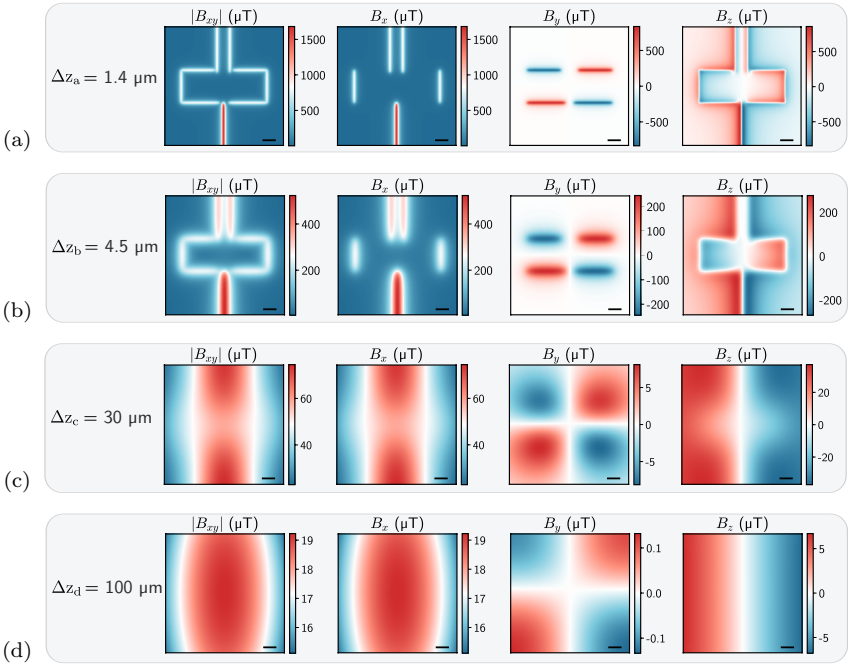

Figure 5.34: **Magnetic field patterns produced by the 1st simulated AL at different distances of observation.** a) Magnetic patterns at $\Delta z_a = 1.4\,\mu m$, i.e. right at the surface of the leads. b) Magnetic pattern at $\Delta z_b = 4.5\,\mu m$, i.e. at a distance set by the geometry of the chip plus the $0.8\,\mu m$ stand-off distance of the NV centres with the sample. c) Magnetic pattern at $\Delta z_c = 30\,\mu m$. d) Magnetic pattern at $\Delta z_d = 100\,\mu m$, i.e. at the standard required stand-off distance with SQUID-based imagers.

NV centre is an atom-like system, the limiting factor for the spatial resolution here is naturally the sensor-source distance. It is then essential to ensure the closest proximity between the NV centres and the sample. For this reason, the sensor was placed at only $< 1\,\mu m$ from the sample's surface. The spatial resolution of the magnetic field images is then mainly limited by the architecture of the chip itself and is about a few µm for the magnetic field maps shown in figure 5.9 and 5.10. An extra distance between the sensor and the current source dramatically reduces the spatial resolution of the magnetic field images. In figure 5.34, the effect of several micrometres on the magnetic field pattern produced by the 1^{st} AL is illustrated. At the surface of the leads (figure 5.34a), the magnetic features are sharp, and the pattern unambiguously reflects the geometry of the circuit. A few µm away, at the position of the sensors as simulated in figure 5.19, the magnetic field slightly broadens, but no information is lost (figure 5.34b). Finally, at greater distances, as shown in figure 5.34c,d, the magnetic field features broaden such that the main pattern is lost. Additionally, the magnetic field amplitude is severely affected: nearly two orders of magnitude are lost between the magnetic field observed at $\Delta z_a = 1.4\,\mu m$ and $\Delta z_d = 100\,\mu m$.

5.4.2.3 Spatial resolution of the current density images.

Finally, many parameters affect the spatial resolution of the current density image. Namely, the spatial resolution of the magnetic field, the SNR of the magnetic field images and the filters used during the current reconstruction procedure affect the spatial resolution of the current density image. As the method relies on an inverse propagation process, it is possible to partially recover the loss of resolution due to the sensor-source distance. To quantify it, in figure 5.35, a linecut perpendicular to the main lead in the experimental data is evaluated.

Here, the spatial resolution Δx is defined by the rise of the current density function across a step edge according to Sparrow's resolution criterion [287]. Δx is determined as the distance over which the current density rises from

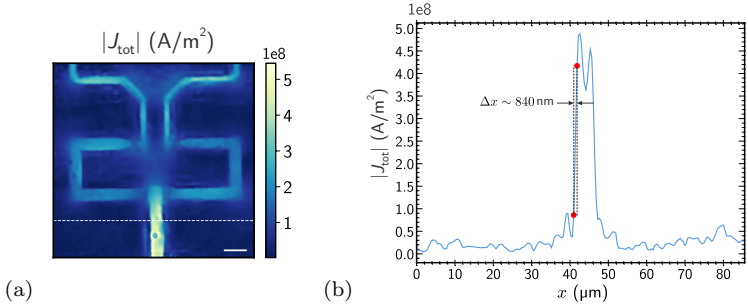

Figure 5.35: **Current density spatial resolution.** a) Total current density amplitude map $|J_{\mathrm{tot}}|$ with $|J_{\mathrm{tot}}| = \sqrt{J_x^2 + Jy^2 + J_z^2}$. b) Linecut of the current density amplitude map along the white dashed line shown in (a). The bottom red dot represents 15 % of the value of the function's rise and the top red dot represents 85 % of the rising value. The distance between the red dots defines the spatial resolution.

15% to 85% between its baseline and its maximum value [37, 288]. The spatial resolution Δx is about 840 nm. This way, a sub-micron resolution is ensured and can be further enhanced using additional regularisation methods during the current reconstruction procedure [224].

5.5 Conclusions and Outlook

Prior-free imaging of the three-dimensional current density in a multilayer integrated circuit using NV centres in diamond was established in this work. First, the current flow in a functional chip was compared with the current flow in a defective chip. Using the high dynamic range of the NV centre, an order of magnitude lower current amplitude was observed in the defective chip. To better understand the failure, the currents originating from different leads were localised, and, in particular, the decorrelation of the signal originating from multiple stacked layers was revealed. The challenges of mapping three-dimensional current densities were addressed through several simulations. Finally, imaging of

the three vector components of the current density was demonstrated. Although the out-of-plane component of the current density J_z is generally neglected in current density imaging techniques, a significant out-of-plane contribution of J_z was revealed close to sharp edges. In order to non-destructively resolve each layer with higher resolution, the current distribution at the source plane should be interpolated using additional layout information. The structure's layout information can be obtained using circuit designs when available or using ptychographic X-ray laminography techniques [273] when the sample is unknown. Thus, combining NV-based imaging to X-ray imaging [289] would allow us to infer the complete information of nanoscale three-dimensional current-carrying structures with no prior information.

As such, the use of NV centres during the development process of an IC can be envisioned as a systematic procedure, as depicted in figure 5.36.

Finally, it is worth noting that the sensing scheme of Oersted fields can be further developed to enable the detection of current sources in the nA range [147, 290–292], and to tune signal acquisition to other ranges such as GHz [55, 293–295]. Such a capability would make it possible to resolve even weak current density fluctuations and potentially provide new insights into the local conductivity of materials in condensed matter physics.

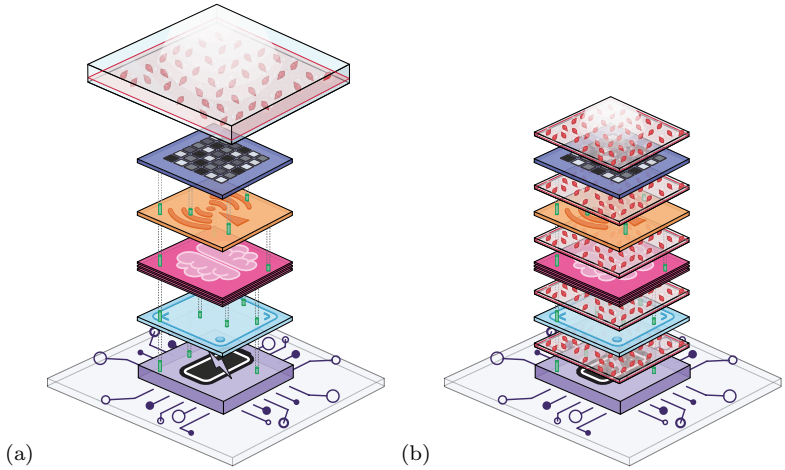

Figure 5.36: **Outlook: Integration of NV-based imaging into the development steps of 3D-ICs.** a) *External sensors.* Configuration used in this work: a layer of sensors outside the IC is brought close to the device, where all the contributions are sensed simultaneously. b) *Built-in sensors.* Alternatively, during the development phase, defect centres can be integrated into the dielectric layers that serve as heat dissipators in the device. Engineering light to access each defect layer would provide a high-resolution three-dimensional map of the current density.

Part III

Probing life

Biological systems comprise complex environments with a vast range of physiological variables, such as free radicals, concentrations of ions, pH, temperature, and forces. Quantifying and localising the involved parameters in biophysical and biochemical processes in such environments is challenging, yet, essential for answering key questions in cellular biology and biomedicine [296]. To date, our understanding of biological processes such as cell signalling or cancer metastasis is limited because it requires bio-compatible sensors combining high sensitivity, selectivity, and spatiotemporal resolution. Therefore, developing new sensors to monitor biological events at the single cell level and under physiological conditions is essential to further understanding life processes.

In this regard, the chemically inert diamond host material, combined with the versatility and wide working range of the NV centre, makes it an ideal candidate for biomedical applications [17, 297–300]. Embedded in nanodiamonds, NV centres can be used as biomarkers for fluorescence imaging and keep track of temperature gradients in cells [60] or to sense free radicals released by oxidative stress in cells [301]. In bulk diamond, NV centres can be used to detect magnetically labelled cancer cells [302] or to measure magnetic fields produced by neuronal action potentials [303]. Modifying the diamond surface enables to probe localised chemical events such as local modification of pH [145, 304].

In part III of this manuscript, NV centres are used as external sensors to probe life at the single cell level and assess water oxygen levels. Chapter 6 examines the mechanocommunication channels of a cell, which are not yet well understood, although they are involved in many life processes. Chapter 7 is dedicated to inferring the dissolved oxygen levels in water, which has the potential to identify the harm that humankind's activities present to the ocean.

Chapter 6

NV-based force sensor for cell adhesion study

Cells communicate by receiving, processing and transmitting chemical, electrical and mechanical signals [305–308]. Over the last two decades, interest in mechanical forces generated by cells has grown due to their involvement in regulating cell function, signalling, and cell adhesion for the development and formation of tissues [309]. These signalling processes involve exchange with the extracellular matrix (ECM), a complex three-dimensional macromolecular network that orchestrates cell coordination [310, 311]. It is also believed that cancer cell invasion through the ECM depends on the ability of cells to generate traction forces [312]. Despite their importance, research on these mechanisms is challenging due to the complexity of living systems, particularly at the single-cell level. The well-established techniques to measure these forces are either invasive, enable measurement on ensembles of cells only, or are limited by low dimensionality [313]. In order to quantify the role of cell traction in dense 3D matrices, novel sensors enabling force measurements in the pN-range on sub-cellular scales are being investigated. Among them, DNA-based sensors, known as *DNA hairpin*, emerged, enabling the first quantifications of such forces at the single molecule level [314, 315]. However, the toxicity of gold nanoparticles used with such techniques is under debate [316, 317] and may alter the cell behaviour. Additionally, the method covers a narrow working range of a few

pN only [315]. Thus, combining DNA hairpin with the NV-based sensor is a promising way to leverage these limitations and hence, enable further studies.

This chapter investigates the binding mechanics of cells with their environment using DNA hairpin-like methods with NV centres. The chapter is organised as follows:

(1) Section 6.1 introduces the importance of cell-matrix interactions for tissue homeostasis.

(2) Section 6.2 discusses preliminary experiments to evaluate the sensing capabilities of the NV-based force-sensing device. In this section, NV centres' interaction with spin labels is investigated.

(3) Section 6.3 discusses first experiments employing NV centres to measure fibroblasts[1] traction forces mediated by a functionalised diamond, which mimics the cell environment.

(4) Finally, section 6.4 discusses the conclusions and outlook of the chapter.

6.1 Introduction to cells and their environment

6.1.1 The eukaryotic cell: a complex and active entity

The cell is the smallest structural and functional unit of living organisms, which can exist independently [319]. It constitutes a very complex system, as depicted in figure 6.1. An essential part of the cell, yet not well understood, is the cell membrane. It is a highly active region where all the interactions with the environment happen: it protects the cell from its surroundings and regulates substances transport across the cell [320–322]. The cell membrane is also an important site of cell-matrix and cell-cell communications [309, 323]. As such, a large variety of protein receptors and identification proteins are present on the surface of the membrane [324]. Functions of membrane proteins include

[1] Fibroblasts are biological cells synthesising the structural framework for animal tissues and playing a critical role in wound healing [318].

surface recognition [325], cell-cell contact [326], signalling [327], enzymatic activity [328], or transporting substances across the membrane [329]. Among these receptors, the integrin plays a fundamental role in activating cell surface composites by mediating cell-cell and cell-matrix mechanical interactions [330]. These mechanical interactions mediated by integrins are the focus of this chapter and are investigated in section 6.3.

6.1.2 The extracellular matrix: a substrate for life modelled by fibroblasts

The ECM is a three-dimensional, non-cellular structure present in all tissues and essential for life. The ECM is composed of a dynamic and complex network of proteins[2], growth factors, and polysaccharides that provide physical structure to the cellular microenvironment [311, 331]. The ECM components are produced by surrounding cells, and secreted into the ECM via exocytosis [332]. In turn, the ECM guarantees the structural integrity of tissues and organs and modulates cell function processes. To this end, the ECM provides cues via chemical and mechanical signalling routes to enable cell interactions, migration, proliferation, and differentiation for healthy tissue formation [333, 334]. Hence, this dynamic interplay between a cell and its surrounding ECM determines the cell fate and tissue homeostasis [310].

A central cell that synthesises ECM is the fibroblast, depicted in figure 6.1. Since fibroblasts are easy to grow in culture, they are often used for biological studies and serve as the main subject of the experiment described in section 6.3. Fibroblasts are not only undemanding but they are also extensively studied for their role in tissue repair and related diseases. The ability to synthesise ECM makes fibroblasts a leading figure in the wound healing process in response to tissue injury [335, 336]. At the end of an inflammatory phase [337], the first fibroblasts infiltrate the wound where proliferation and differentiation are activated (24-48 hours after injury) [338]. In this phase, the fibroblasts remodel the

[2]Among the proteins present in the ECM, collagen is the most abundant.

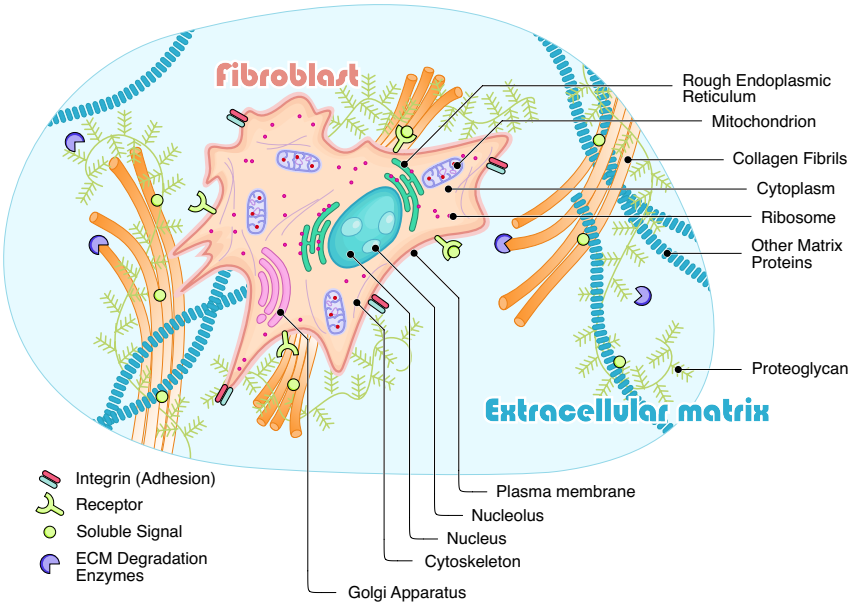

Figure 6.1: **Schematic of a fibroblast cell in the ECM.** The fibroblast is a eukaryotic cell, i.e. a complex structure containing multiple organelles which perform various functions within the cell. One of the fibroblast's functions is to produce ECM components such as collagen, giving structure to interstitial tissues. Other elements of the ECM constantly interact with cells by serving as ligands for cell receptors such as integrins, thereby transmitting mechanical signals that regulate the cell behaviour.

ECM by releasing degradative enzymes to cleave the damaged ECM components and by producing new elements [339, 340].

With anomalous fibroblasts such as cancer-associated fibroblasts [341, 342], the renewal of the ECM is altered, leading to dysregulation of the ECM composition, structure and abundance and leading to a stiffer ECM substrate. Such remodelling of the ECM creates a microenvironment that promotes tumourigenesis and metastasis [343–345]: cancerous cells generate greater forces than healthy cells, enabling them to invade the ECM and then the blood vessels aggressively. The communication channels that allow cellular motility[3] and the stiffness of the ECM are thus closely linked to tumour progression. Further studies on cell-matrix communication can therefore lead to the development of new therapeutics.

6.1.3 Cell-matrix communication mediated by integrins

As discussed in section 6.1.2, cell communication is essential to maintain tissue homeostasis, mount an effective immune response and promote tissue repair. Among the communication channels, it is widely recognised that mechanical forces underpin many molecular processes that maintain life. The integrin proteins are one of the main force-transducing receptors in cells [330, 347]. It provides a mechanical bridge linking the ECM to the cytoskeleton[4] of the cell and transduces cues from the ECM to initiate biochemical signalling that stimulates cellular motility [349].

6.2 Measuring biomarkers and NV centres interactions: preliminary experiments

The experiment to measure cell adhesion forces using NV centres in diamond is described in detail in section 6.3.1. The experimental concept is to observe how a

[3] Cellular motility is the spontaneous movement of a cell from one place to another through energy consumption [346].

[4] The cytoskeleton is composed of an assembly of protein filaments and is responsible for cell shaping and migration [348].

cell deforms an elastic medium by tracking spin labels: gadolinium (Gd^{3+}) ions. This section describes preliminary experiments to estimate the sensitivity of NV centres to Gd ions in order to establish an optimal and realistic configuration for the cell experiment.

6.2.1 Relaxation induced by external ion fluctuations

Spin labelling of molecules with paramagnetic ions is a widely used technique to determine molecular structures and study their dynamics [350, 351]. Relaxometry with NV centres makes use of the dipole-dipole interaction between the NV centre and a paramagnetic species to determine the relative position (see chapter 1). A key property in the choice of the paramagnetic species, i.e. the spin label, is the spin magnetic moment. The higher the magnetic moment, the stronger the interaction between the label and the probe. For this reason, the gadolinium species [352, 353], chelated in DOTA [354] to avoid toxicity, was chosen for the experiments presented in this chapter. Gadolinium is also commonly used as a contrast agent for MRI, where it is used for labelling tissues [355, 356]. Gadolinium is a rare earth metal that most commonly occurs as a trivalent Gd^{3+} ion. The existence of seven unpaired electrons in its 4f-orbital leads to a large electronic spin of $S = 7/2$. However, the net magnetic moment created by Gd^{3+} ions is the result of purely random fluctuations causing a large distribution of magnetic frequencies with a mean amplitude of $\langle B \rangle \simeq 0$ [122]. The standard schemes used for the detection of DC and AC fields cannot be applied. However, a transient polarisation of the spins occurs within the noise and induces changes in the longitudinal spin relaxation time T_1 of the NV centre.

As described in section 1.3.5, the relaxation rate of the NV centre T_1^{-1} is the combination of an intrinsic diamond $T_{1,int}^{-1}$ and environmentally $T_{1,env}^{-1}$ induced relaxation rates. In the case of relaxation induced by Gd ions, the $T_{1,env}^{-1}$ term is mainly influenced by the dipolar coupling between the NV centre and the Gd^{3+} ion. The $T_{1,env}^{-1}$ term is thus given by the integrated product of the normalised resonance line of the spin transition with the power spectrum of the spin noise.

Consequently, it is dependent on the distance r that separates the Gd ion from the NV centre, as described by equation (6.1)[122]:

$$T_{1,env}^{-1}(r) \simeq 2\frac{\mathrm{f_{Gd}} * B_{\mathrm{rms}}^2(r)}{\mathrm{f_{Gd}^2} + D_{\mathrm{gs}}^2}, \tag{6.1}$$

where f_{Gd} expresses Gd^{3+} fluctuation rate and corresponds to 1.75 GHz in DOTA [357], $B_{\mathrm{rms}} = \sqrt{\langle B^2 \rangle}$ is the magnetic dipolar term rising from the $NV - Gd^{3+}$ interaction, given in units of frequency. The expression of B_{rms} depends on the geometry of the experiment and is given in [122, 123].

6.2.2 Gd-loaded beads measurements

In this experiment, modified silica beads with a diameter of 3.9(1) µm are investigated. The surface of the silica beads was modified with Gd^{3+} DOTA complexes. The beads were deposited on the surface of a diamond with shallow implanted NV centres (see appendix A), as depicted in figure 6.2. Thus, T_1 was measured according to the protocol described in chapter 1. The resulting curves are fitted according to the model described in appendix D.

Figure 6.3 shows the deposited beads under bright illumination, and figure 6.4 shows the corresponding T_1 map resulting from the experimental data fit. At the contact point between the beads and the diamond surface, a sharp decrease in the T_1 values can be observed. Since the microbeads have a curved profile, as depicted in figure 6.2b, only the Gd^{3+} in the immediate vicinity of the NV centres contribute to the signal.

Figure 6.3b and figure 6.4b show close-ups of an arbitrarily chosen bead to further investigate its effect on T_1 and a reference signal to determine $T_{1,int}$ and thus extract $T_{1,env}$. The T_1 profile along the dashed line shown in figure 6.4b is represented in figure 6.5. A clear decrease of T_1 by a few hundred nanometres can be observed. Since the neighbouring Gd^{3+}-loaded beads are 3.9(1) µm wide, they do not contribute to this signal.

On a small scale, the distribution of Gd^{3+} can be approximated by a 2D layer of ions above the NV centres. Considering this approximation and the

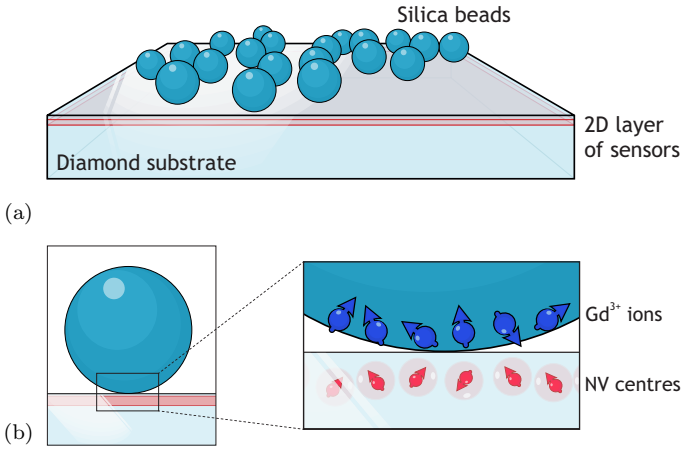

Figure 6.2: **Gd-loaded beads on a diamond membrane.** a) Schematic of the overall view of the experiment. b) Close-up on a single bead. Only the Gd^{3+} ions in the interaction range of the NV centre contribute to the signal.

experimental values of $T_{1,int}$ and $T_{1,env}$, simulations of the T_1 signal were performed with respect to the NV-Gd^{3+} distance and for different Gd^{3+} ion densities. The results are shown in figure 6.6. Considering NV centres with a mean depth of about 7 nm, the resulting Gd^{3+} ion density is given by about $\sigma = 5000\,Gd^{3+}/\mu m^2$. Although previous experiments have shown the detection of Gd^{3+} ions with NV centres on a microscope [122], the samples were large compared to the experimental design required in the next section. Here, sensitivity down to a few ions per NV centre was demonstrated since the NV centre showed a strong response for about $120\,Gd^{3+}$ ions within the diffraction-limited spot. Finally, although smaller densities can be detected, since experiments with living cells require short averaging times and therefore lead to poor SNR, densities of $\sigma = 5000\,Gd^{3+}/\mu m^2$ and above should be used for the next part.

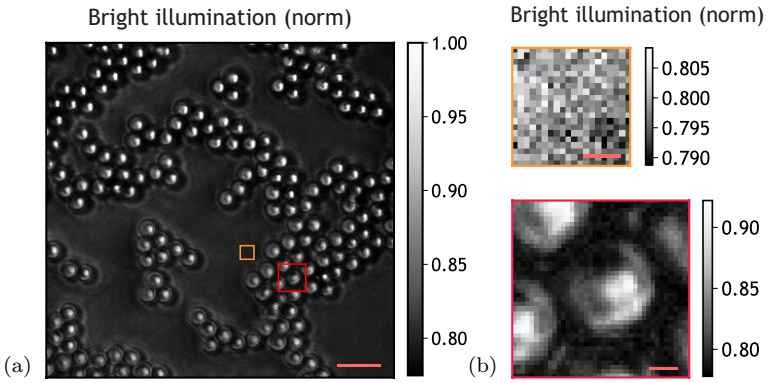

Figure 6.3: **Gd-loaded beads under bright illumination.** a) Full map. The scale bar is 10 µm wide. b) *Top:* Enlarged area with no beads, taken as reference. *Bottom:* Enlarged area enclosing the bead to investigate. Scale bars are 1 µm wide.

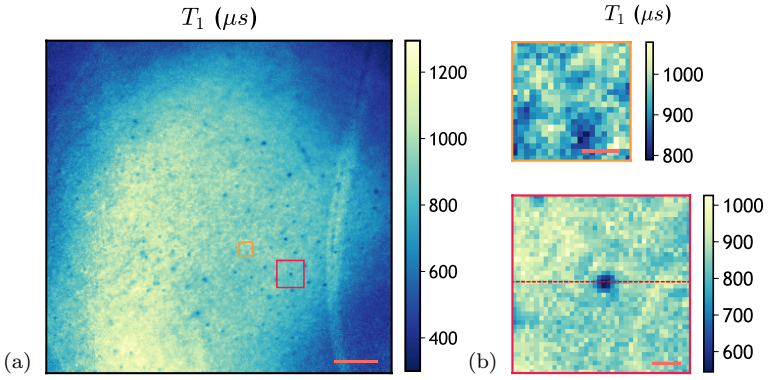

Figure 6.4: **T_1-maps generated by Gd-loaded beads.** a) Full map. The scale bar is 10 µm wide. b) *Top:* Enlarged area with no beads, taken as reference, to determine $T_{1,\text{int}}$. *Bottom:* Enlarged area enclosing the bead to investigate. Scale bars are 1 µm wide.

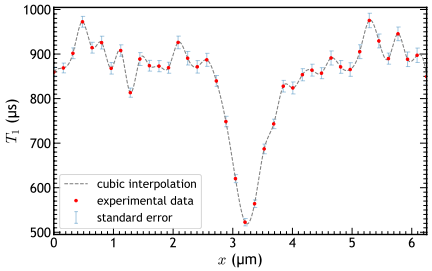

Figure 6.5: T_1**-profile generated by a single Gd-loaded bead.** Only the surface close enough to the NV centres leads to Gd^{3+} − NVs interactions. The red dots represent experimental data, and the dashed line is a cubic interpolation.

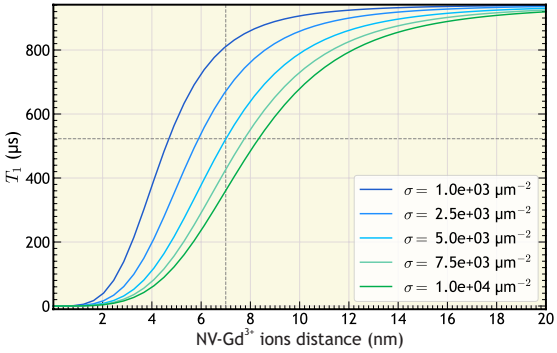

Figure 6.6: T_1 **induced changes with NV-**Gd^{3+} **distance.** For a proximal NV centre located at 7 nm distance from the surface (i.e. from the Gd^{3+} ions), the decrease in T_1 observed in figure 6.5 is induced by an ion density $\sigma = 5000\,Gd^{3+}/\mu m^2$.

6.3 Measuring forces exerted by a single cell

6.3.1 Apparatus design

The aim of the experiment is to measure forces applied by fibroblasts while communicating with the ECM through integrin receptors. To this end, the surface of a diamond with shallow implanted NV centres (sample C, see appendix A) was modified to mimic the ECM, as depicted in figure 6.7. The structure is as follows:

- A 2 nm layer of SiO_2 grafted with polyethylene glycol (PEG) chains of length $L_0 = 5.1$ nm covers the diamond surface;
- Each PEG chain is annexed with two specific terminations:
  - a DOTA complex, which is a chelator that can capture a metallic ion and thus be loaded with a Gd^{3+} ion before the experiment;
  - an Arg-Gly-Asp (RGD) ligand, a short peptide present in the ECM that can bind to the integrin present on the cell surface [358].

The PEG chain is a molecular structure composed of repeating ethylene glycol units, giving the chain elasticity. Therefore, it can be compressed or stretched out when a force is applied to its extremity. By relaxometry, the distance r separating the NV centre to the chelated Gd^{3+} ion can be determined. Hence, the deformation induced by a cell binding to the RGD receptors can be deduced by comparison with the length of the chain at rest.

6.3.2 Protocol for measuring pN-range forces

In this section, the procedure for measuring forces by tracking spin labels is discussed.

The first step is to measure T_1 with a cell generating traction forces. The experiment is repeated without the cell to obtain a reference measurement. The experimental values denoted $T_{1,\mathrm{cell}}$ and $T_{1,\mathrm{ref}}$ for the measurement with the cell and the reference, respectively, are extracted using the fitting procedure

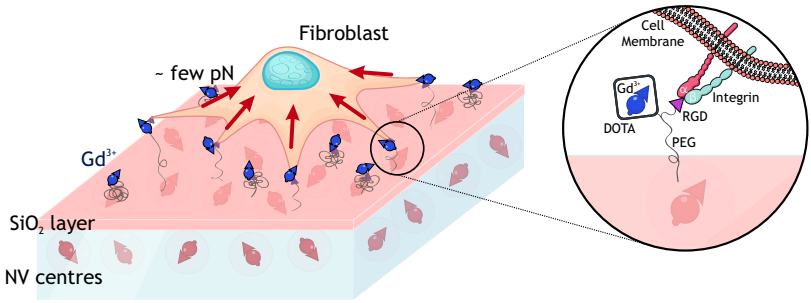

Figure 6.7: **Cell experiment configuration.** A diamond surface is modified to mimic the fibroblast natural environment and labelled with spin markers (here, Gd^{3+} ions). A living fibroblast binds to the PEG chains through the RGD ligands and exerts traction force on them. As the chain is pulled away, the distance r between the NV centre and the Gd^{3+} becomes larger and the NV-Gd^{3+} coupling weaker. PEG chains are spaced by 10 nm.

described in the appendix D and shown in figure 6.8. Thus, $\Delta T_1 = T_{1,\text{cell}} - T_{1,\text{ref}}$ can be extracted to estimate the effects caused by the forces generated by the cell.

As in the experiment discussed in section 6.2.2, the second step is to evaluate the interaction between the NV centres and the Gd^{3+} ions to infer the distance r separating the spins. A two-dimensional layer of Gd^{3+} spins of density $\sigma = 10\,000\,Gd^{3+}/\mu m^2$ overlying the NV centres is considered to estimate the magnetic dipolar term arising from the $NV - Gd^{3+}$ interaction, described by the Hamiltonian 1.18. Using the equations (1.16) and (6.1), the experimentally determined value of T_1 can be related to the distance r, as shown in figure 6.9. In this way, the deformation of the chain caused by the traction force can be determined.

Finally, the third step is to calculate the corresponding force that causes the deformation $\Delta\delta$ using the so-called worm-like chain (WLC) model. The WLC model is an analytical solution derived by C. Bustamante and co-workers in

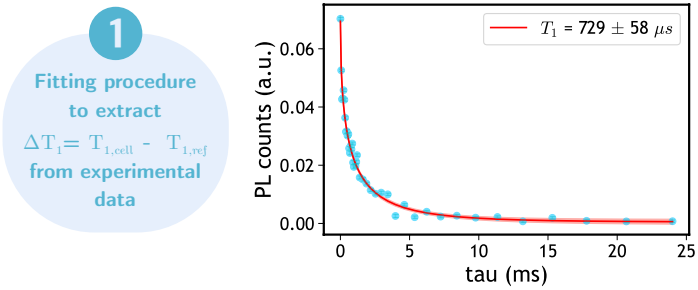

Figure 6.8: **Force estimation step 1: fitting the data to extract ΔT_1.** Each pixel in the map contains a curve fitted with a stretched exponential. The fitting returns the relaxation time T_1. The data are first collected with the cell on top, returning $T_{1,\mathrm{cell}}$, and then collected after removing the cell, returning $T_{1,\mathrm{ref}}$.

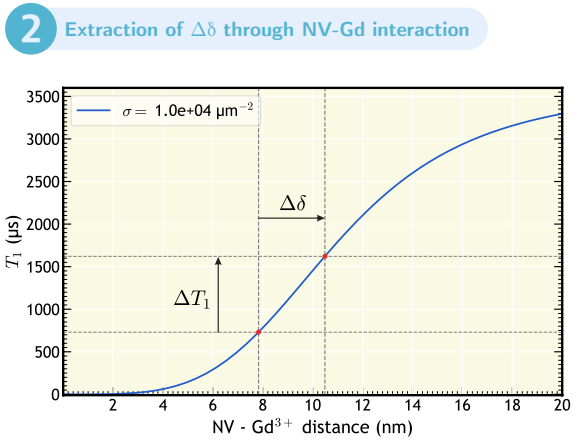

Figure 6.9: **Force estimation step 2: estimation of $\Delta\delta$ using ΔT_1 and the magnetic dipolar term resulting from the $\mathrm{NV} - \mathrm{Gd}^{3+}$ interaction.**

[359] and was initially developed to fit the force-extension diagram of a DNA dimer. As experiments became more rigorous with advancing technology, the model was refined five years later by C. Bouchiat *et al.*. Corrective terms were added by comparing the first WLC model with the exact numerical solution, resulting in the equation (6.2) [360].

The force F causing a deformation $\Delta\delta$ is thus given by:

$$F = \frac{k_B T}{L_p}\left[\frac{1}{4\left(1-\frac{\Delta\delta}{L_0}\right)^2} - \frac{1}{4} + \frac{\Delta\delta}{L_0} + \sum_{i=2}^{i\leq 7}\alpha_i\left(\frac{\Delta\delta}{L_0}\right)^i\right], \tag{6.2}$$

where k_B is the Boltzmann constant, T is the temperature, L_0 is the contour length of the molecule, L_p is its persistence length and α_i are the correction terms given in [360]. The length of the polymer depends on the number of glycol units forming the chain and the surrounding media. In the following, the values are calculated for the cell culture medium [361].

The model is computed for two PEG chains with different contour lengths L_0, and the results are shown in figure 6.10. A long PEG chain with 3400 glycol units, denoted PEG_{3400}, shows a slowly varying linear progression of the force-deformation relationship. Although this configuration is advantageous as it shows a large deformation of about 1 nm for 1 pN applied force, this configuration is not suitable for the experiment performed here. For such PEG chains, an applied force of only a few pN leads to a deformation of several nanometres, and the interaction NV-Gd becomes out of range. Therefore, a shorter polymer chain with 800 glycol units, referred to as PEG_{800}, was chosen for this work. This time, the polymer length matches the dynamic range of the NV-Gd relationship since Gd^{3+} can affect T_1 for each conformation.

In summary, the procedure is as follows:

(1) The experiment is performed twice: first with the cell binding to the functionalised diamond and a second time after cleaving the adhesion between the cell and the substrate. Thus $\Delta T_1 = T_{1,\text{cell}} - T_{1,\text{ref}}$ is determine for each pixel of the map.

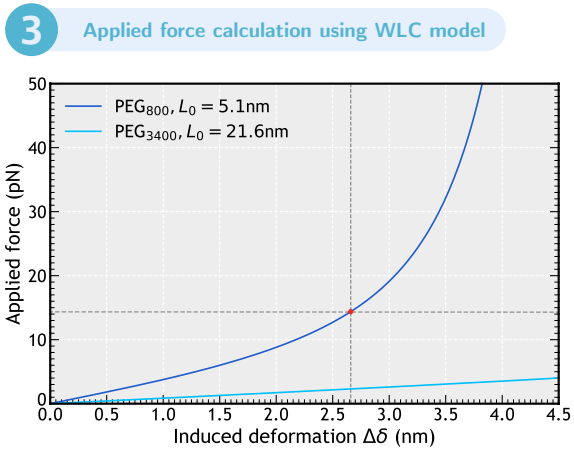

Figure 6.10: **Force estimation step 3: calculation of the force according to the WLC model.**

(2) The deformation of the PEG chain $\Delta\delta$ is estimated by calculating the dipolar interaction between the NV centres and the Gd^{3+} ions.

(3) Finally, the force is estimated using the WLC model.

6.3.3 Experimental results

At the frontier between physics and biology, where advanced experimental protocols involve laser and microwave radiations on a living subject, it is crucial to ensure the right conditions to maintain the perenniality of the subject during an experiment. To this end, the NV-pumping laser was used at an angle corresponding to total internal reflection (TIR) conditions [161]. In this way, the light exposure of the sample was kept minimal to prevent phototoxicity [362] of the bio-sample. In addition, the signal was acquired and averaged over 3 cycles to keep the total acquisition time minimal, and a carbonated bath solution was used to allow the sample to survive despite external stimulation [298].

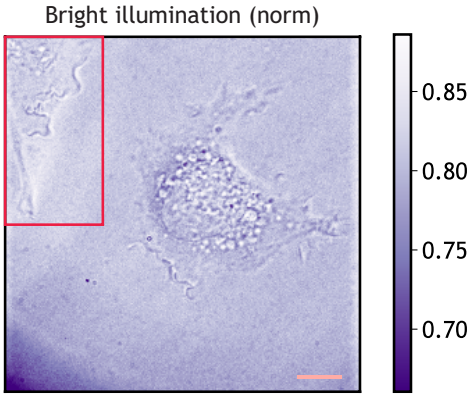

Figure 6.11: **Cell under bright illumination.** Scale bar is 10 µm wide.

Finally, the experiment was conducted at 37 °C using an incubator on the stage to provide optimal conditions for the cell culture.

Fibroblast cell cultures were incubated on the modified diamond surface for approximately three hours. This time was needed to ensure that the cells adhere and bound properly to the surface[5]. Good adhesion is determined by observing the shape of the cells: when the cell binds properly to the ligands, it spreads over a large surface [364]. Therefore, T_1 measurements were performed on a single cell attached to the diamond as shown in figure 6.11. Thenceforth, the cell was removed from the diamond surface using trypsin to cleave the bonds between the cell and the PEG chains. Finally, a phosphate-buffered saline (PBS) buffer was used to clean the diamond surface from the cell culture medium. The T_1 measurement was performed a second time on the same site and under the same conditions (with a clean cell culture medium on the surface, at 37 °C) to complete the reference measurements.

[5]The adhesion process is directly related to the ligand density [363], so it is important to consider enough RGD receptors such that the cell can adhere correctly.

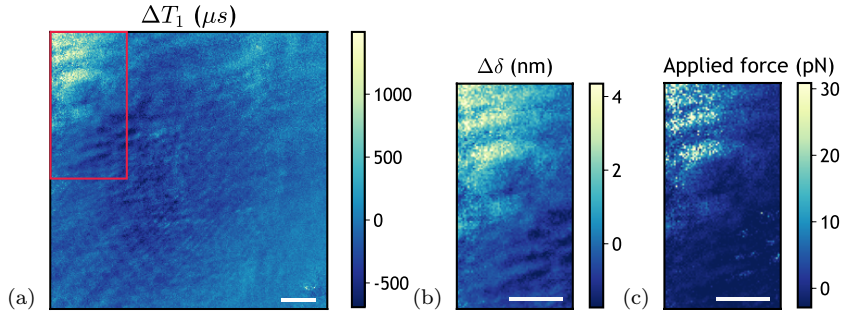

Figure 6.12: **Force exerted by a living cell.** a) Full ΔT_1 map. b) ROI showing the deformation $\Delta\delta$ deduced from the NV-Gd^{3+} interaction. c) Corresponding force map computed using the equation (6.2). Scale bars are 10 µm wide

The difference between $T_{1,\text{cell}}$ measured with the cell on the diamond and $T_{1,\text{ref}}$ obtained from the reference measurement results in the ΔT_1 map shown in figure 6.12a. Although the experiment was intended to measure the forces exerted by the cell in the centre of the frame, there is no clear signal at this site. Instead, a strong signal emanates from the upper left corner, where a cell that is partially visible in figure 6.11 is located. The TIR condition, which was at the limiting angle due to the limited space using illumination through the objective, was most likely causing the middle cell not to produce a signal. Since the cells have a different refractive index than the cell culture medium and the organelles are also different from the membrane itself, the TIR condition was not met for the entire sample. Since the laser beam is Gaussian, the repetitive laser pulse locally transmitted placed considerable demands on the biological sample, and the central cell did not keep adherence over time.

Thus, the focus now is on the upper left corner, where the optical field is much lower. Figures 6.12b,c show the deformation of the PEG chains and the induced traction forces calculated using the equation (6.2), respectively. The deformation of the PEG layer follows the shape of the cell, although it is blurred

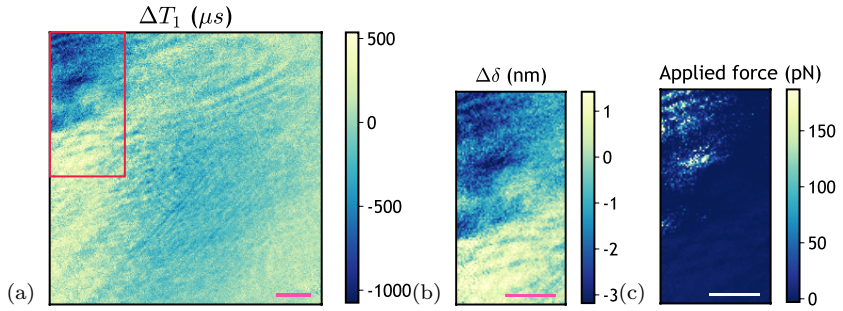

Figure 6.13: **Force exerted by a cell under stress.** a) Full map of ΔT_1. b) ROI showing the deformation $\Delta\delta$ deduced from the NV-Gd^{3+} interaction. c) Corresponding force map, given for reference only. Scale bars are 10 µm wide

because of the long acquisition time of the measurement. Additionally, the deformation is in adequacy with the PEG length. Analysis of figure 6.12c shows an average force per ligand of about a few pN. As reported in literature [365], the forces are in the pN-range, and the maximum integrin tension typically appears near the centre of the rod-shaped elongated structure. Thus, these measurements demonstrate a promising use of the NV centres to measure forces exerted by cells. Improvements to elaborate a non-invasive technique are discussed in section 6.4.

However, it is interesting to show that the signal changes over time. Figure 6.13 shows a subsequent measurement where the cell appears to push against the substrate. Such behaviour emphasises that the cell is subjected to stress [366, 367], most likely caused by the MW pulses that were used to obtain good signal contrast. The most significant deformations caused by the cell, shown by the $\Delta\delta$ map in figure 6.13b, indicate that the Gd ions are pushed to the bottom of the PEG chain. This situation can be caused by shear stress pushing the PEG chain to the side. The force map shown in figure 6.13c is, therefore, given for reference only. The stress caused to the cell can be observed directly under

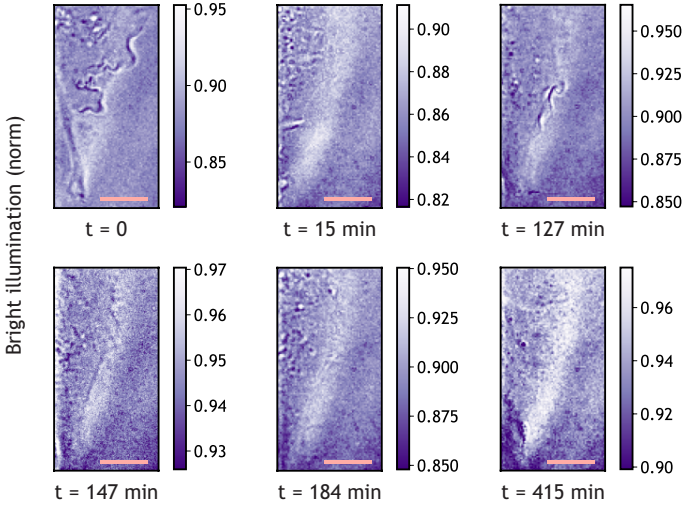

Figure 6.14: **Cell under bright illumination at different time scales.** Over time, the cell death can be observed [368]. At t=0, the cell spreads well to the side while it retracts with time. The measurements shown in figure 6.12 were made between $t = 15\,\text{min}$ and $t = 127\,\text{min}$, when the cell was still alive. The scale bars are 10 µm wide

the microscope with bright illumination, as shown in figure 6.14. Before the measurement, the cell spreads out over a large area, showing excellent adhesion to the substrate. However, over time, the cell retracts itself, making it difficult to distinguish the features after a few hours of measurements. Since the cell was positioned where the laser intensity was low (at the tail of the Gaussian beam), it is most likely the MW radiation that caused this stress. Therefore, future measurements should include an all-optical scheme.

These experiments show that the forces induced by a single cell can be measured with NV centres in diamond, regardless of whether it exerts tensile forces or compressive forces against the substrate. The resolution is about 300 recep-

tors within the diffraction-limited spot and could be scaled down to measure a single receptor, as further discussed in section 6.4.

6.4 Conclusions and outlook

Nanomechanical sensors based on NV centres have been developed in the past [63], but the method and the reported sensitivity do not allow the detection of a mechanical signal induced through the receptors of a cell. The strategy adopted here was to functionalise the diamond surface to measure cell-induced forces. Polymer chains, acting as springs, were grafted onto the diamond surface and given a specific termination enabling RGD-integrin binding tracking. The termination included Gd^{3+} ions that interact with NV centres, and that can be detected with relaxometry.

To ensure an optimal device design, a first experiment was performed with Gd^{3+} ions bound to microspheres. A clear signal was generated with about 120 Gd^{3+} ions within the diffraction-limited spot.

In this way, first experiments with cell cultures of fibroblasts could be performed. The results are very encouraging as they showed the detection of cell-induced forces in the pN range and with subcellular resolution. The main features of the geometry of the fibroblasts were identifiable and showed traction forces where the maximum tension occurred near the centre of the typical rod-like elongated structure of the cell, as reported in the literature [365]. However, the long measurement duration shows that external stimulations by MW alter the behaviour of the cell, which is under stress. Thus, the conditions to keep the cell alive were not optimal and the experiment needs to be redesigned to be non-invasive to the cell. To this end, an all-optical scheme is proposed in chapter 8, optimised to maximise the contrast of the signal on the widefield microscope.

Providing the experiment is redesigned, the NV-based device can be used to study the dynamics of the cell [369] since both traction and compressive forces have been detected. In this context, single-tau experiments [122] can

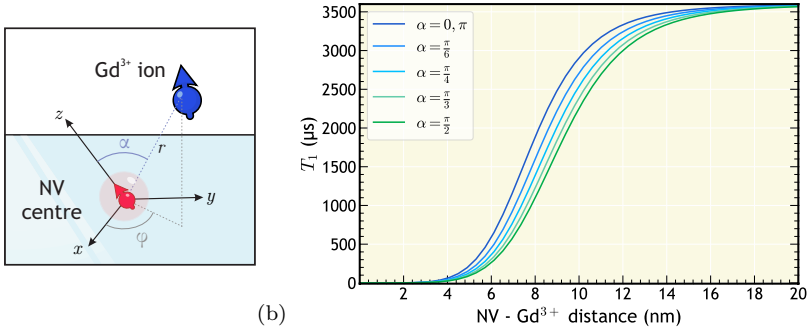

(a) (b)

Figure 6.15: **Outlook: using single pairs of NV-Gd^{3+} for 3D quantification.** Since the dipolar coupling term with the Gd^{3+} has an angular dependence between the two spins, vectorial information can be retrieved.

be performed with a well-calibrated system to enable the visualisation of such forces with high video frame-rates acquisition.

Finally, this experiment measured the averaged values of the traction forces where the vertical component dominates. Access to scalar information is a sufficient approach to obtain information about the system. However, to investigate the effects of stress on the cell, a three-dimensional characterisation is needed. This can be realised with a single NV centre for which the dipolar coupling term with the Gd^{3+} has an angular dependence between the two spins, as shown in figure 6.15. Therefore, further development using prior identification of the orientation of the NV centres, e.g. using polarised light, will lead to three-dimensional force detection. This will allow quantification of both lateral and azimuthal traction at the level of a single receptor, leading to new insights in the field of cell-matrix communication.

Chapter 7

Sensing dissolved oxygen in water

Oxygen, O_2, also known as molecular oxygen, constitutes 20.95% of the volume of the Earth's atmosphere and is essential for many metabolic processes, including human life. It oxidises sugars to produce energy via adenosine triphosphate (ATP) and it is a key substrate for numerous intracellular biochemical reactions [370]. O_2 deprivation, known as hypoxia, causes stress in organisms by triggering complex adaptive responses to balance the supply of O_2 with metabolic and bioenergetic demand. In particular, hypoxia in tissues is the fundamental cause of degenerative diseases and ultimately leads to death if the concentration of O_2 remains low for too long. Therefore, maintenance of O_2 homeostasis is essential for the survival of most prokaryotic and eukaryotic species. Accordingly, measuring O_2 is one way to study life on Earth [371].

The ocean, also known as the "lungs of the Earth", is the main source of oxygen on Earth since it produces more than half of the world's oxygen consumption. In addition, the ocean plays a key role in maintaining the global ecosystem by acting as a carbon sink and regulating heat transport. However, human activities threaten this balance and signs of ocean deoxygenation have been observed. An important parameter to monitor on a global scale is, therefore, the dissolved oxygen (DO) in water [372, 373]. Despite this importance, there is a lack of practical and accurate sensors that can be used on board ships. This chapter explores the NV-based system as a potential practical, accurate and portable sensor for DO.

This chapter is organised as follows:

(1) Section 7.1 describes how to measure DO variations using NV centres in diamond.

(2) Section 7.2 presents and discusses preliminary experiments using commercial O2-meters.

(3) Section 7.3 demonstrates first experimental results using NV centres to sense DO.

(4) Finally, conclusions are discussed in section 7.4, and an outlook to further develop DO sensing using NV centres is presented.

7.1 Measuring dissolved oxygen (DO) in water

The ocean is one of the greatest support of life on Earth, where physical and biogeochemical processes govern oxygen dynamics in the ocean. The ocean gains oxygen in the upper layer through the photosynthesis of autotrophic organisms and through oxygen from the atmosphere, which dissolves in the undersaturated waters. Conversely, the ocean loses oxygen throughout the water column: at the surface through outgassing of oxygen to the atmosphere in over-saturated waters and from the surface to the depths through the respiration of aerobic organisms and oxidation of reduced chemical species. Therefore, the oxygen levels in the ocean are highly dynamic, and sensors combining precision, real-time, stability and portability need to be developed. In particular, sensors that measure DO with an accuracy of about 0.02 mg/l are required to measure the variations caused by the respiration of organisms in the dark ocean [374]. These conditions set the figure of merit that the NV-based sensor should achieve.

7.1.1 Measuring DO using available tools

Conventional methods to determine the DO content in water include iodometric titration (Winkler method), electrochemical detection (Clark method), and optical detection (fluorescence quenching method), which are described in [375].

In short, the Winkler method has a very high determination accuracy but a cumbersome detection procedure and long response times that prevent continuous online detection. The most widely used method is the Clark method, which is also precise and easier to handle. Its detection speed is high, but it consumes oxygen and has a long response time because the electrode has to be polarised, preventing long-term measurements. Finally, the optical sensor of the fluorescence quenching method has many advantages. It does not consume oxygen and is not easily influenced. It also allows remote detection and processing and performs continuous online detection. However, a significant disadvantage so far is its low detection accuracy [375].

Overall, the accuracy and real-time performance of these devices cannot meet the requirements of both in situ and long-term online measurements.

7.1.2 Working principle of the DO sensing based on NV centres

The working principle of the O_2 sensing measurement with NV centres is based on the paramagnetic property of the molecular oxygen.

Molecular oxygen occurs naturally in several forms [376]. The most stable and hence abundant form is the triplet $^3O_2$ formed with the stable isotope of oxygen ^{16}O. A possible Lewis representation[1] is given by :

where the two unpaired electrons are highlighted. The triplet ground state of the $^3O_2$ molecule, thus, forms a diradical.

Since the O_2 molecules are paramagnetic, the interaction with NV centres can be measured via relaxometry. In order to account for the influence of the O_2 molecules alone, the signal must be compared to a signal obtained with a water sample with a zero-oxygen level.

[1] Various Lewis representations are accepted, although they do not accurately represent the bonds that form the $^3O_2$ molecule. For an accurate representation, the energy diagram found in [376] should be drawn instead.

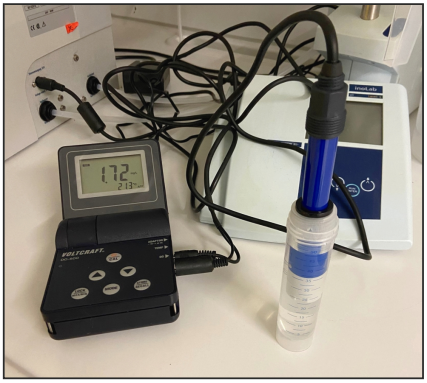

Figure 7.1: **Picture of the O_2-meter used for the preliminary experiments.** One can see the device on the left-hand side of the picture, displaying the DO content measured by the electrode inserted in the tube containing the water sample.

7.2 Preliminary experiments

In this section, a conventional O_2-meter, based on the Clark method, was used to conduct initial experiments to establish reference measurements. The device is shown in figure 7.1 while displaying the oxygen content of a water solution with reduced oxygen. The device is capable of measuring dissolved oxygen in a range from 0 mg/l to 20 mg/l in liquid water and at temperatures between $\sim$ 0 °C and 50 °C. The precision of the instrument can reach 0.07 mg/l for 10 min acquisition, although the accuracy is strongly influenced by the calibration of the device.

7.2.1 Preparation of the zero-oxygen sample

In order to control the DO content in water, two approaches are investigated in this section.

The first approach is to degas oxygen from water. For this, the choice of the gas is essential, as it must neither react with other components nor interact with NV centres. Therefore, the argon gas is chosen because it is a noble gas (i.e. chemically inert), and the atoms are heavy enough to push the oxygen out. For about two hours, argon gas was run through water. Measuring the oxygen content immediately after degassing gives a value of 0.4(2) mg/l, but within ten minutes, the amount of oxygen rises again to 0.64(7) mg/l. The process of degassing water is, therefore, not convincing enough to prepare a water sample with zero-oxygen content.

Since it is not possible to remove all the DO from water by physical means, the second approach involves a chemical reaction that consumes oxygen. Such a reaction is commonly used in the industry where oxygen scavengers are used to preserve items from oxidation. For example, sulfites can be used to prevent the rusting of pipes in wastewater systems [377] or to control the oxidation of foods [378].

In this section, sodium sulfite is used to react with oxygen to form sodium sulfate. The reaction, described in [379], proceeds as follows:

$$Na_2SO_3 + \frac{1}{2}O_2 \rightarrow Na_2SO_4. \tag{7.1}$$

When the reaction is total, all of the DO is consumed.

In order to find the optimum amount of sodium sulfite to produce the zero-oxygen water sample, several solutions containing different concentrations of sodium sulfite in water were prepared. First, a molar solution of Na_2SO_3-H_2O was prepared, of which 12.5 µl, 15 µl, 50 µl, 100 µl and 200 µl were added to 40 ml water. The resulting amounts of sodium sulfite per unit of 1 ml of water correspond to 39.38 µg, 78.75 µg, 0.16 mg, 0.32 mg and 0.63 mg.

On this basis, two series of measurements were carried out with these samples. After the preparation of the solutions, the oxygen content of all the samples was measured at room temperature. Since the reaction of the sodium sulfite with the O2 molecule is slow, the oxygen concentration in the samples was

measured again after a few hours. The resulting curves are shown in figure 7.2 where the measurements after a few hours result in lower O_2 content. Finally, measurements over time are carried out for the solutions with 320 mg/l and 630 mg/l sodium sulfite, resulting in the curves shown in figure 7.3.

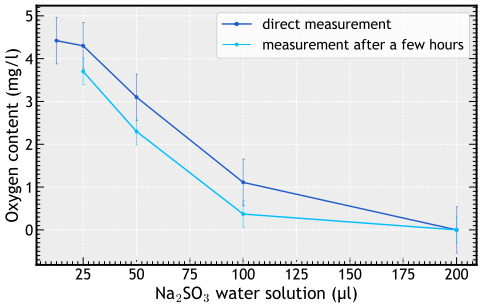

Figure 7.2: **Oxygen content in Na_2SO_3-H_2O solutions.** The amounts of Na_2SO_3 water solution correspond to the amount added to 40 ml water. The measurements were performed at room temperature.

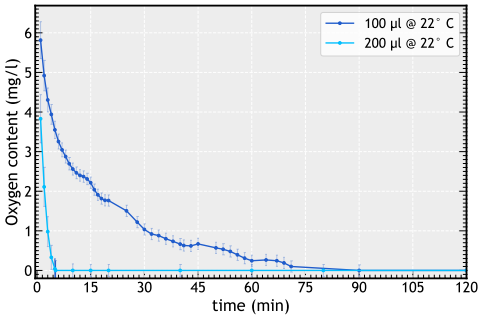

Figure 7.3: **Reaction time of the O_2 consumption in an Na_2SO_3-H_2O solution at room temperature.** The curves represent measurements done with 100 µl and 200 µl, corresponding to solutions with 320 mg/l and 630 mg/l of sodium sulfite.

In order to obtain a rapid and long-lasting reaction, a solution with sodium sulfite in excess is preferred. Therefore, aqueous solutions with 630 mg/l sodium sulfite and more can be used to prepare the solution with zero-oxygen content. The use of sodium sulfite in excess also ensures that O_2 does not dissolve again over time.

7.2.2 Temperature dependence of the oxygen levels

The oxygen absorbing capacity of water depends on external conditions such as temperature and pressure [380]. Examples of oxygen concentrations at ambient conditions are referenced in [381]. In order to vary the amount of O_2 in a controlled manner, experiments were conducted to assess the dependence of DO with temperature.

Starting at room temperature, a sample of ultrapure water was heated in a water bath until reaching about 40 °C and the DO content was measured simultaneously. The measurement was repeated twice, and the results are shown in figure 7.4. A downward trend can be seen, but is unstable with large fluctuations. Since the values given in [381] are larger, another measurement was conducted.

This time, a sample of ultrapure water was gassed with O_2 for about 30 seconds, and the sample was placed in a water bath at a regulated temperature. The experiment was carried out for three different temperatures: 22 °C, 31 °C and 36.5 °C. The O_2 content was monitored over time, and the results are shown in figure 7.5. The data were fitted to the stretched exponential model given by the equation (D.1), where the resulting offsets are $y_{0,22°C} = 8.6(2)$ mg/l, $y_{0,31°C} = 7.3(1)$ mg/l, $y_{0,36.5°C} = 6.2(2)$ mg/l for the temperatures 22 °C, 31 °C and 36.5 °C, respectively. These values indicate the degree of saturation of DO in water and are consistent with the values given in [381]. Since the curves show a clear temperature dependence and vary slowly after about 180 min, samples with different amounts of O_2 are prepared in this way for the experiments with NV centres described in section 7.3.3.

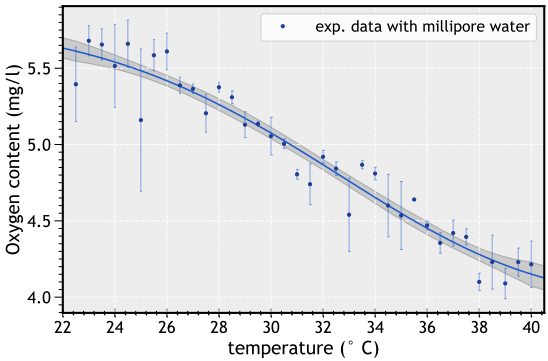

Figure 7.4: **Temperature dependence of O_2 content in water.** Millipore water refers to ultrapure water.

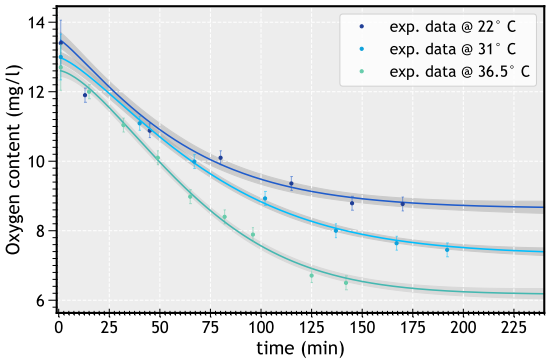

Figure 7.5: **Temperature dependence of O_2 content in saturated water over time.** Dots represent experimental data taken at temperatures 22 °C, 31 °C and 36.5 °C and the solid lines represent the fit to a stretched exponential. The grey halos surrounding the fit lines represent the confidence range of the fit.

7.3 Sensing DO with NV centres

7.3.1 Experimental settings

To conduct the sensing experiments with NV centres, a diamond membrane is mounted on an Ω-shaped coil grown by lithography on a coverslip, as shown in figure 7.6. The omega loop has an inner diameter of about 800 µm and provides a homogeneous field for the NV centres. The coverslip is attached to a PCB to transmit the MW radiations.

To perform experiments with solution flows in direct contact with the diamond surface, a microfluidic device was fabricated in-house, using polydimethylsiloxane (PDMS) [382]. The flow cell was thus mounted on the coverslip with the microcoil and diamond and is shown in figure 7.6b. Needles were attached to the inlet and outlet parts to fill the channel with solutions and drain it. A syringe can be used to inject the liquids into the flow cell and suck them out again. Since PDMS does not react to water and various solvents, the cell can be used for several weeks with the sulfite solutions and water needed for the experiment [383].

(a) 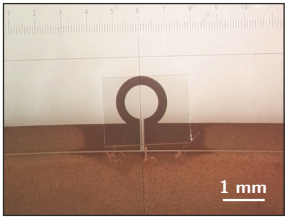

(b) 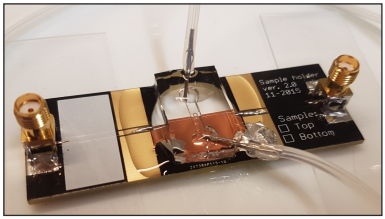

Figure 7.6: **Photos of the flow cell and MW antenna used for the experiment.** a) Image of the microcoil fabricated by in-house lithography on a glass coverslip. The diamond membrane is glued on top of the microcoil. b) A flow cell made with PDMS is mounted on the coverslip glued to the diamond membrane.

7.3.2 Cleaning the diamond surface

Adsorbates, including O_2, can contaminate the diamond surface, resulting in reduced T_1 times. Therefore, it is primordial to clean the diamond surface before starting the experiment. Here, the sample D described in appendix A was employed. The diamond was first cleaned using Piranha and acid boiling as described in appendix A.

The sample was placed on the NV-based widefield microscope and illuminated with a 532 nm-laser beam, resulting in the fluorescence pattern shown in figure 7.7. As the NVs ensemble is irradiated with a Gaussian laser beam, the NV centres fluorescence pattern follows this shape, and bright and dark areas appear in the image. Thus, a ROI is selected to encompass the areas where the laser light is strong and homogeneous enough.

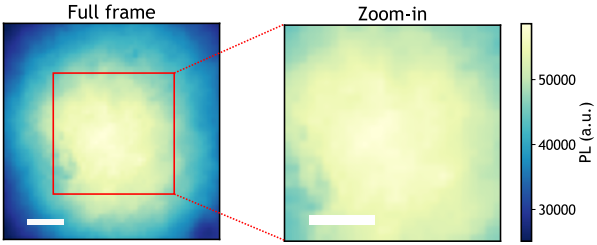

Figure 7.7: **PL intensity frame.** Full frame PL intensity as recorded by the CCD camera and the selected ROI is delimited by a red square. The scale bars are 10 µm.

A T_1 measurement is performed, and the resulting map is evaluated with the averaged signal in the ROI. The resulting curve was fitted to the stretched exponential function given in appendix D and the returned T_1 parameter was much shorter than expected with $T_1 = 99(1)$ µs.

Following this experiment, different dosages of a sodium sulfite-water solution were tested on the diamond D to see if O_2 adsorbates affected the NV centres due to the air composition. The flow cell was rinsed with three different sodium

sulfite-water concentrations, and the solution was left in the cell after rinsing. The number of millilitres of solution used for each rinse and the resulting averaged relaxation time are given in figure 7.8. The results reveal that rinsing the diamond surface with sodium sulfite significantly increases T_1. Observation of the signal over time, as shown in figure 7.9, indicates that there is an optimal time for which the sodium sulfite solution should remain in the flow cell. Overall, and as summarised in figure 7.10, the final wash step resulted in $T_1 = 918(36)\,\mu s$, i.e., one order of magnitude increase in T_1.

These observations were repeated in several experiments and then evaluated on another diamond sample, sample E (see appendix A). This time, only one washing step was performed with a high concentration of sodium sulfite (1133 mg/l). As can be seen in figure 7.11, this wash step again resulted in a significant increase in T_1, which evolved from $T_1 = 499(20)\,\mu s$ to $T_1 = 1655(53)\,\mu s$. This diamond sample was then chosen to perform the experiment with DO sensing, presented in the next section.

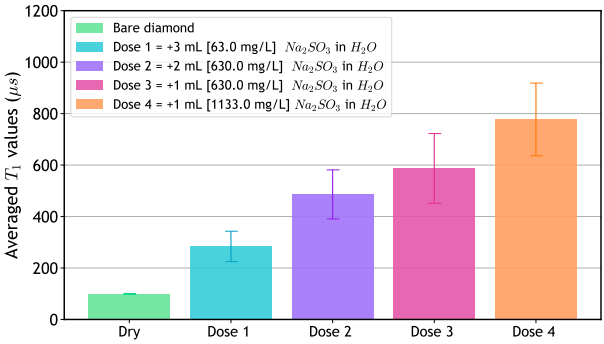

Figure 7.8: **Washing steps using sodium sulfite solutions.** Averaged T_1 evolution after distinct washing steps using sodium sulfite in water.

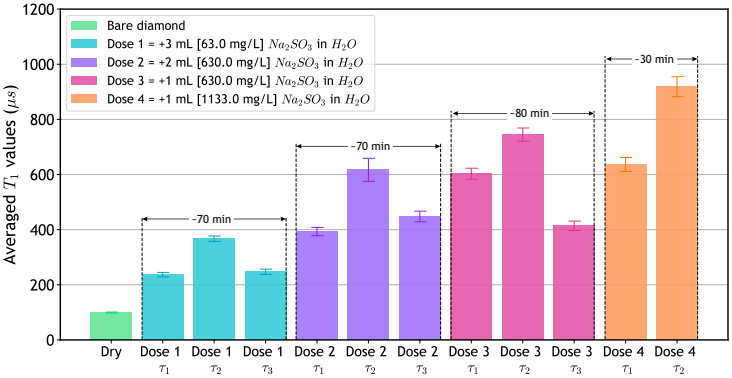

Figure 7.9: T_1 **recovery using sodium sulfite in water.** Observing T_1 evolution over time within a washing step reveals optimal times at which the solution should be changed.

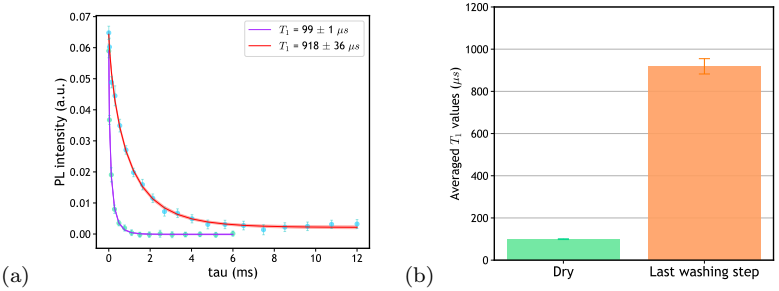

Figure 7.10: **Sample D:** T_1 **comparison before and after wash.** Comparison of T_1 before washing with sodium sulfite and after last washing step. a) Relaxometry curves, dots represent experimental data points, error bars represent the standard deviation, and solid lines correspond to the line fits. b) Histogram showing the T_1 values extracted from (a). One can observe nearly one order of magnitude difference.

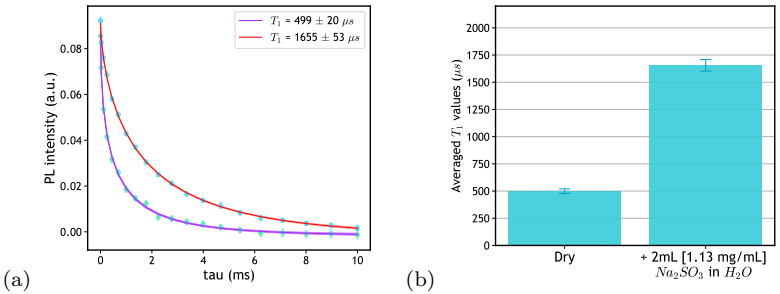

Figure 7.11: **Sample E: T_1 comparison before and after wash.** Comparison of T_1 before washing with sodium sulfite and after last washing step. a) Relaxometry curves, dots represent experimental data points, error bars represent the standard deviation, and solid lines correspond to the line fit. b) Histogram showing the T_1 values extracted from (a). One can observe nearly one order of magnitude difference.

7.3.3 Dissolved oxygen sensing experiments

The sample E mounted with a flow cell serves now as a probe to investigate the DO content in water, varying with temperature. The temperature of the assembly was controlled by a resistor system that allows raising the temperature on the setup. As in section 7.3.2, the NV centres were illuminated with a 532 nm-laser beam, resulting in the fluorescence map shown in figure 7.12. The signal is examined in the centre of the Gaussian beam bounded by the red square.

The experiment was conducted as follows. First, a control measurement was made at room temperature (about 22 °C), using a sodium sulfite solution with a concentration of 1133 mg/l. After this measurement, a water sample was oxygenated at 40 °C using the procedure described in section 7.2.2, i.e., the sample was gassed with O_2 for about 30 seconds and placed in a water bath at 40 °C for about 180 min. The solution was then transferred to the flow cell, which was already mounted on the setup, stabilised at 40 °C. About 3 ml of

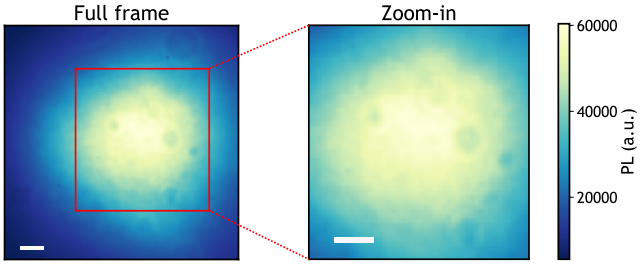

Figure 7.12: **PL intensity frame for the O_2 sensing experiment.** Full frame PL intensity as recorded by the CCD camera and the selected ROI delimited by a red square. The scale bars are 10 µm wide.

the water solution was used to rinse the diamond surface and keep the flow cell filled during the experiment. To avoid high pressure in the cell, the outlet was kept open while the inlet was closed with a syringe. Finally, T_1 measurements were acquired for about 40 min. The procedure was repeated at 30 °C and then at room temperature at about 22 °C.

The results are pixel-wise fitted with the stretched exponential model given in appendix D, resulting in the returned parameters A, b and y_0 shown in figures 7.13, 7.14 and 7.15, respectively. The maps of A and b are examined to control that the ensemble of NV centres in the ROI is homogeneous and homogeneously controlled by optical and MW fields. Finally, the maps of y_0 are used to control that the overall experiment was performed in a similar light environment.

The values obtained for the averaged signal in the ROI are summarised in the tables 7.1, 7.2 and 7.3 and show similar conditions for all experiments.

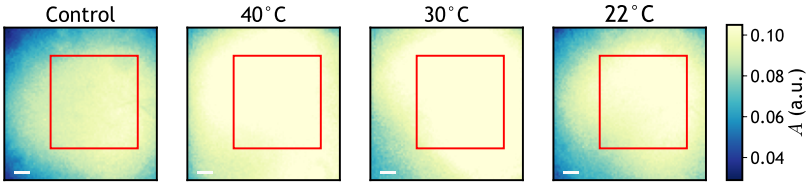

Figure 7.13: **Amplitude parameter A for measurement series with different contents of O_2.** Returned parameters for each pixel of the full frame. The scale bars are 10 µm wide.

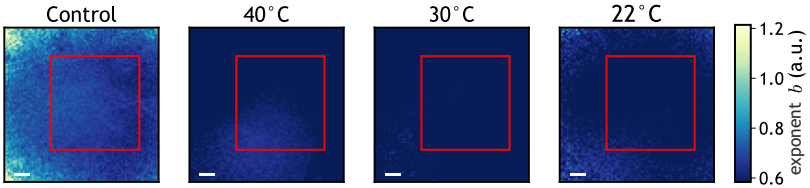

Figure 7.14: **Exponent parameter b for measurement series with different contents of O_2.** Returned parameters for each pixel of the full frame. The scale bars are 10 µm wide.

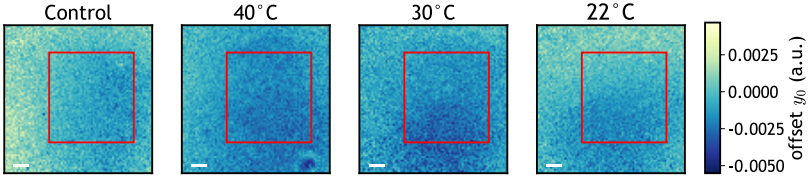

Figure 7.15: **Offset parameter y_0 for measurement series with different contents of O_2.** Returned parameters for each pixel of the full frame. The scale bars are 10 µm wide.

	Control	40 °C	30 °C	22 °C
a (a.u.)	0.094(1)	0.109(2)	0.113(1)	0.102(1)

Table 7.1: The amplitude A of the stretch exponential curve and its standard derivation.

	Control	40 °C	30 °C	22 °C
b (a.u.)	0.68(2)	0.58(2)	0.54(1)	0.57(1)

Table 7.2: The exponent b of the stretch exponential curve and its standard derivation.

	Control	40 °C	30 °C	22 °C
y_0 (a.u.)	−0.0008(7)	−0.002(1)	−0.0020(6)	−0.0010(4)

Table 7.3: The offset y_0 and its standard derivation.

Finally, the value of interest is the longitudinal relaxation time T_1, in figure 7.16. Overall, a clear influence of the DO concentration on the T_1 values can be observed. Interestingly, when looking at the spatially resolved values, a gradient within the ROI can be observed. Since the control is homogeneous in this region, such a gradient may be caused by a gradient of the DO content itself. In fact, the inlet is kept closed while the outlet remains open: such a configuration induces a pressure gradient that affects the O_2 content in the water. The higher the pressure, the higher the O_2 content, which is the tendency observed in the data.

Overall, the data are very encouraging for sensing O_2 in water. A global effect can be assessed from the averaged values for T_1, as shown in figure 7.17. The concentrations of O_2 given in the figure were measured during the experiment with the conventional O_2-meter. Although the same water sample was measured, the values are given for reference only, since the experimental conditions were not exactly the same. From the reported values one can estimate that 1 mg/l reduces T_1 by about 100 µs for O_2 concentrations in the range of 0−8 mg/l. Although the measurement at 22 °C shows no clear difference from that at 30 °C, this can be explained by a local temperature increase due to the use of laser and MW. Therefore, further experiments can be conducted by using the NV centres themselves to measure the in-situ temperature and pressure to obtain a better overview of the local situation.

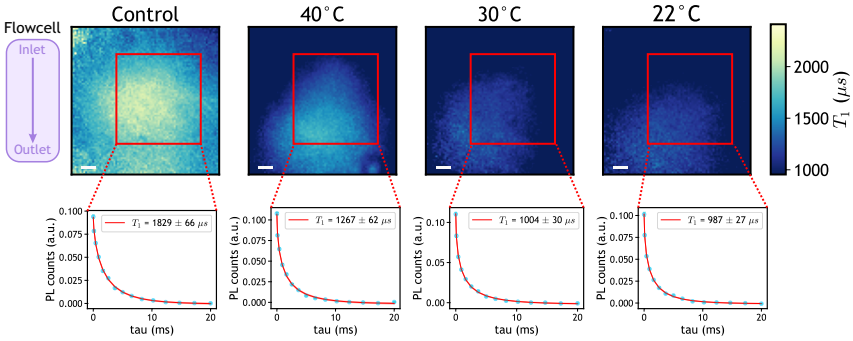

Figure 7.16: T_1 **parameter for measurement series with different contents of O_2.** The flow cell is represented on the left to indicate the position of the inlet and outlet of the flow cell. *Top*: Returned parameters T_1 for each pixel of the full frame. The scale bars are 10 µm wide. *Bottom*: T_1 longitudinal relaxation curves of the NVs ensemble resulting from averaging the signal over the ROI, fitted to a stretch exponential given in appendix D

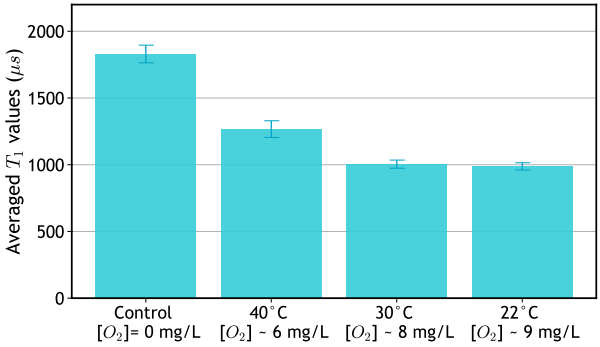

Figure 7.17: **Averaged T_1 values at the different dissolved oxygen concentrations.**

One can conclude from these experiments that the DO content in the water has a clear influence on the T_1 time of the NV centres even on the microscale: the lower the temperature, the higher the DO content and the lower the average T_1 time. The experiment has thus successfully demonstrated that NV centres can be used to detect dissolved oxygen in water. Suggestions for pursuing this project further are discussed in the following section.

7.4 Conclusions and outlook

This chapter established a method for measuring dissolved O_2 in water using NV centres in diamond, and promising results for the development of a highly sensitive device were demonstrated.

The results already showed excellent sensitivity to variations in dissolved O_2 on the microscale, for which 1 mg/l induced about 100 µs change on T_1. Since the signal does not need to be highly resolved in space, the sensitivity can be drastically enhanced by increasing the size of the sensing unit cell. For example, increasing the unit cell size from $\sim 1 \times 1$ µm^2 to $\sim 100 \times 100$ µm^2, will enable the measurement of 0.01 mg/l O_2 fluctuations, as the sensitivity scales with $\frac{1}{\sqrt{N}}$. In addition, the use of large sensor volumes drastically reduces the averaging time, allowing highly dynamic measurements.

The next step is to quantify the concentration of the DO directly using the NV centres. Several routes lead to the quantification of the amount of in situ O_2 molecules in water. First, the dipole interaction between the O_2 molecules and the NV centres can be determined, similarly to the interaction with Gd^{3+} ions shown in chapter 6. The construction of a flow cell with two channels, as shown in [384], would allow the simultaneous measurement of the T_1 intrinsic to the diamond and the T_1 involving the interaction with the O_2 molecules. Alternatively, the isotope $^{17}O_2$ can be measured using NMR protocols. However, the abundance of $^{17}O_2$ is only about 0.037 % [385], which limits the sensitivity of the measurement. Although $^{16}O_2$ has no nuclear spin, it can also be quantified with NMR protocols by studying its influence on the ^{1}H nuclear spin [386]. This

is a promising avenue since ^{1}H-NMR based on NV centres is a well-established technique.

An interesting outcome of the experiments shown in this chapter is that cleaning the diamond surface with sodium sulfite significantly improved the T_1 times of two different diamonds. This is a promising way to define a new systematic cleaning procedure for shallow NV centres before any experiment, as they may suffer from interactions with O_2 adsorbates on the diamond surface.

Finally, by combining the techniques to probe the environment factors with NV centres, such as temperature and pressure, with relaxometry to measure DO, a promising NV-based sensor can be built for environmental research. NV-based probes could be installed in specific areas to monitor the evolution of DO in the oceans online. Alternatively, since the NV centres can be manipulated under extreme conditions, a device can be developed to probe in situ water in the dark ocean.

Part IV

Outlook and Appendices

Chapter 8

Outlook

The common thread running through all the chapters of this dissertation is the endeavour to develop a versatile magneto-optical imager to enable cross-disciplinary applications. To this end, the choice of a widefield microscope is promising for building a compact and practical device with minimal overhead.

Part I in this dissertation presented the widefield imager based on NV centres and its promising properties for developing new technologies. In this regard, part II exploited the particular feature of NV centres to enable multiaxial sensing on the nanoscale, which allows the imaging of magnetic vector fields and, thus, the imaging of three-dimensional current distributions.

Beyond its use for the semiconductor industry to meet the ever-increasing failure analysis needs [387], charge transport in electronic systems is fundamental to many other phenomena and processes in science and technology [230, 388–390]. Therefore, unravelling three-dimensional electronic signals using NV centres in diamond has the potential to leverage progress in many areas. For instance, it can serve neuroimaging to overcome the limits of conventional current density imaging techniques and help to reveal new features [391]. Besides, it can help in understanding fundamental open problems in three-dimensional correlated systems [392, 393]. For example, NV centres can be used to image charge transport in multilayer materials [179, 394, 395], e.g. magnetic tunnel junction on the nanoscale. To this end, a microscope combining the widefield imager with

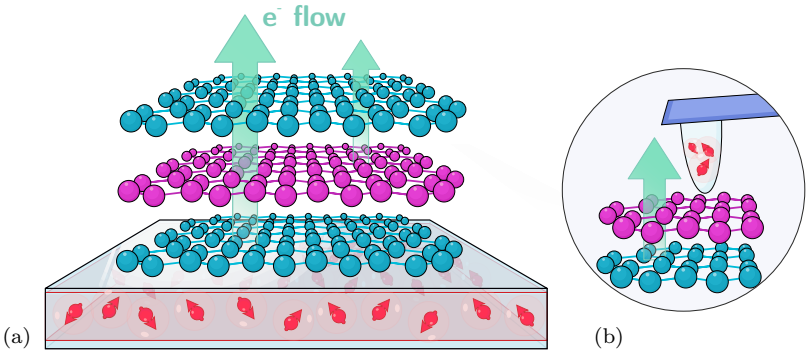

Figure 8.1: **Current flow in multilayer materials at the nanoscale.** NV centres in diamonds can be used to map the magnetisation of atomic layers when no bias voltage is applied. Thus, NV centres can map the orthogonal current flowing through the layers with an additional bias. a) The widefield imager can map large scales of the material. b) The atomic force microscopy (AFM) instrument, using a probe with multiple NV centres, can serve to investigate local events.

an AFM head, as depicted in figure 8.1, would allow imaging of the material at different scales.

Finally, in part III of this manuscript, bio-applications using relaxometry with NV centres were presented. Promising applications have been demonstrated for the study of signals induced by living cells, provided that an all-optical system is used in the future.

Although all-optical schemes are suitable for bio-applications since they avoid invasive MWs, they are not adapted for widefield imaging with a slow detection scheme (e.g. using a CCD camera). All-optical schemes' accumulative background noise and low contrast signal inherently lead to poor SNR if no additional control measurement is executed. The alternative method, not yet explored, is to select the optical transition [396] since the widefield microscope allows a high degree of freedom for shaping the optical excitation. As illustrated in figure 8.2, using a linearly polarised laser beam perpendicular to the NV axis

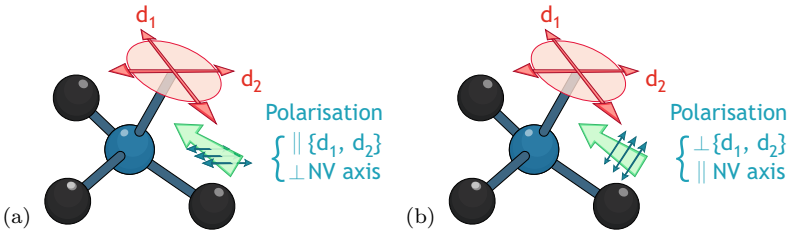

Figure 8.2: **All-optical scheme adapted for widefield imaging.**

maximally excites the NV optical transition in one configuration while ensuring no excitation with the orthogonal polarisation. Switching polarisation in a measurement scheme, e.g. for T_1 measurements, will certainly lead to all-optical widefield imaging with high contrast.

Another application using the NV centres for bio-applications was the development of a method to study dissolved O_2 in water, which is essential for assessing the signs of potential ocean deoxygenation caused by human activities. To this end, NV-based probes could be installed in specific areas to monitor online the evolution of dissolved O_2 in the oceans.

Ultimately, this work has demonstrated the use of the NV-based widefield imager to overcome current challenges in microelectronics and bio-applications. Since most methods rely on robust downstream analysis, the NV-based microscope can be kept simple and thus optimised for users with minimal training. In this way, the widefield imager can be used in a variety of disciplines.

Appendix A

Diamonds samples

Within this work, the diamond surface was treated using common acid boiling (1:1:1 mixture of H_2SO_4:HNO_3:$HClO_4$) to clean the diamond surface [397]. The acid boiling has the advantage of providing oxygen termination at the diamond's surface, stabilising the NV centres in the negatively charged state [151, 398].

A.1 Diamond plates preparation

In this work, diamond plates were prepared using CVD diamonds (electronic grade, Element Six) in which NV centres were created by implantation of nitrogen atoms (cf. A.2 for implantation specificity). An array of diamond plates was fabricated by a combination of electron-beam lithography and reactive ion plasma etching, reducing the thickness of the diamond to a few micrometres only.

Although diamond plates can stick to a sample via *van der Waals* forces, in this manuscript, the diamond plates were glued to the samples to ensure strong binding even with rough surface samples. For this, a tiny drop of ultraviolet (UV)-curable glue is first placed on the sample, and the diamond with the array of plates is brought close to it with the NVs layer facing towards the sample. An individual plate is then broken out of the array using a sharp tungsten tip mounted to a micromanipulator. Optical inspection confirms that the plate has not flipped during this step, which means the NVs layer faces the sample.

Finally, the UV-curable glue is hardened after the plate has been fine-positioned to its final location.

A.2 Diamond substrates used in this dissertation

A.2.1 Samples A - Diamond plates used in chapter 3

NV centres were created by implantation of nitrogen with an energy of 9.8 keV and an implantation dose of 2×10^{12} 1/cm^2 into a 100-oriented CVD diamond (electronic grade, Element Six). After implantation, the diamond was annealed at 960 °C for 2 hours at a pressure of 10^{-7} mbar.

The plates used in chapter 3 are $1 - 2$ µm thick and about 120 µm in size. The resulting NV centres concentration is about 2×10^{10} 1/cm^2 with a depth distribution profile nearly Gaussian, peaking at 15 nm below the surface and with a non-negligible concentration in depth ranging from ≈ 5 to 25 nm.

A.2.2 Samples B - Diamond plates used in chapter 5

Same implantation as sample A. The plates are about 3 µm thick and about 100 µm in size.

A.2.3 Sample C - Diamond membrane used in chapter 6

NV centres were created by implantation of nitrogen with an energy of 2.5 keV and an implantation dose of 1×10^{13} 1/cm^2 into a 100-oriented CVD diamond (electronic grade, Element Six).

A.2.4 Sample D - Diamond membrane used in chapter 7

NV centres were created by implantation of nitrogen with an energy of 2.5 keV and an implantation dose of 4×10^{12} 1/cm^2 into a 100-oriented CVD diamond (electronic grade, Element Six).

A.2.5 Sample E - Diamond membrane used in chapter 7

NV centres were created by implantation of nitrogen with an energy of 4.0 keV and an implantation dose of $2 \times 10^{12}\,1/\mathrm{cm}^2$ into a 100-oriented CVD diamond (electronic grade, Element Six).

All the implantations were done using the nitrogen isotope ^{15}N.

Appendix B

Simplified 7-level model

The full description of magnetic field-dependent photodynamics for a single NV defect can be found in [200].

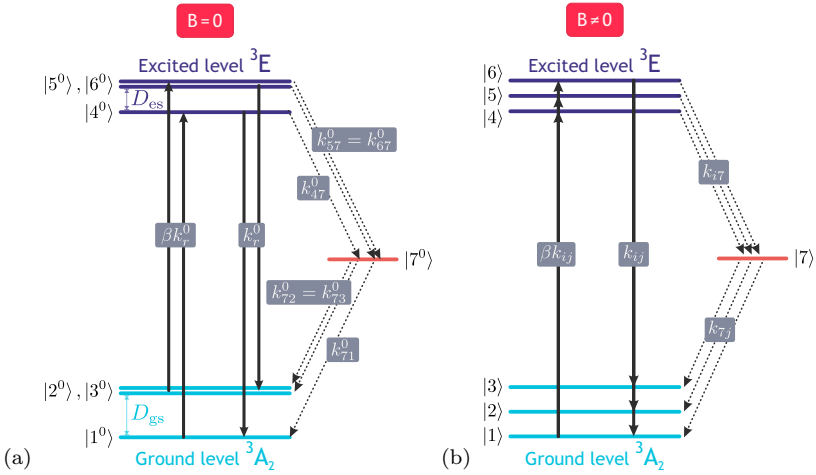

Figure B.1: **Simplified 7-level model.** a) Simplified 7-level model without additional magnetic field. b) Simplified 7-level model with an additional magnetic field $B \neq 0$.

In this manuscript, the photodynamics of the NV centre is described using the simplified 7-level model shown in figure B.1 and with the series of equations (B.1). The equations describe the population evolution of the seven eigenstates labelled $\left\{|i^0\rangle\right\}$ without a magnetic field and $\{|i\rangle\}$ with a magnetic field and where $i \in [1 \text{ to } 7]$.

The rate equations for the system without a magnetic field are given by:

$$\frac{\mathrm{d}n_1}{\mathrm{d}t} = -n_1\beta k_r^0 + n_4 k_r^0 + n_7 k_{71}^0, \tag{B.1a}$$

$$\frac{\mathrm{d}n_2}{\mathrm{d}t} = -n_2\beta k_r^0 + n_5 k_r^0 + n_7 k_{72}^0, \tag{B.1b}$$

$$\frac{\mathrm{d}n_3}{\mathrm{d}t} = -n_3\beta k_r^0 + n_6 k_r^0 + n_7 k_{73}^0, \tag{B.1c}$$

$$\frac{\mathrm{d}n_4}{\mathrm{d}t} = n_1\beta k_r^0 - n_4\left(k_r^0 + k_{47}^0\right), \tag{B.1d}$$

$$\frac{\mathrm{d}n_5}{\mathrm{d}t} = n_2\beta k_r^0 - n_5\left(k_r^0 + k_{57}^0\right), \tag{B.1e}$$

$$\frac{\mathrm{d}n_6}{\mathrm{d}t} = n_3\beta k_r^0 - n_6\left(k_r^0 + k_{67}^0\right), \tag{B.1f}$$

$$\frac{\mathrm{d}n_7}{\mathrm{d}t} = n_6 k_{67}^0 + n_5 k_{57}^0 + n_4 k_{47}^0 - n_7\left(k_{71}^0 + k_{72}^0 + k_{73}^0\right), \tag{B.1g}$$

$$1 = n_1 + n_2 + n_3 + n_4 + n_5 + n_6 + n_7, \tag{B.1h}$$

where the transition rates from $|i^0\rangle$ to $|j^0\rangle$ are given by k_{ij}^0. Assuming that the optical transitions are purely spin-conserving and that the radiative relaxation rate is spin-independent, we have $k_{41}^0 = k_{52}^0 = k_{63}^0 = k_r^0$. In the simulations shown in chapters 1, 2 and 3, the optical pumping parameter is $\beta = 0.5$ ($\ll$ saturation) and the transition rates are given in [200]. The PL emitted by the system is given by:

$$PL \propto n_4 + n_5 + n_6. \tag{B.2}$$

When a static magnetic field $\boldsymbol{B}$ is applied, the seven eigenstates of the system become:

$$|i\rangle = \sum_{j=1}^{7} \alpha_{ij}\left(\boldsymbol{B}\right)|j^0\rangle\,, \tag{B.3}$$

where the coefficients $\alpha_{ij}\left(\boldsymbol{B}\right)$ are calculated numerically using the expressions of the NV ground state Hamiltonian $\mathcal{H}_{\text{gs}}$ and the excited-state Hamiltonian $\mathcal{H}_{\text{es}}$.

The new transition rates $\{k_{ij}\left(\boldsymbol{B}\right)\}$ are given by:

$$k_{ij}\left(\boldsymbol{B}\right) = \sum_{p=1}^{7}\sum_{q=1}^{7} \left|\alpha_{ip}\right|^2 \left|\alpha_{jq}\right|^2 k^0_{pq}. \tag{B.4}$$

For the simulations shown in chapter 3 with an ensemble of NV centres in a (100)-oriented crystal, the Hamiltonians are written in the laboratory spatial coordinates, and each NV axis is considered.

Finally, it is worth noting that the model given by the set of differential equations (B.1) can be further developed considering switching mechanisms between the NV^- and NV^0 states [399], and Rabi driving between the triplet states.

Appendix C

QR decomposition to solve least squares problems

The aim of this appendix is to give a general description of the QR solver and its limitations. A complete and rigorous mathematical description can be found in [400].

C.1 General description of the QR solver

The QR decomposition, also known as QR factorisation, is the decomposition of a matrix A, having linearly independent columns, into the product $A = QR$, where Q is an orthogonal matrix and R is an upper triangular matrix.

Such a method is particularly efficient for solving systems where a sophisticated matrix needs to be inverted. The matrix Q is easy to invert and still preserves the norm and the inner products. This makes the factorisation very suitable for problems where the norm is important and leads to accurate methods for solving least squares problems.

The usual form of the equations system to solve is as follows:

$$Ax = b, \tag{C.1}$$

where A is a m by n matrix, x is the unknown matrix and b is a m dimensional vector. Here, the QR decomposition provides an alternative way of solving the

systems of equations without inverting the matrix A. The Q factor provides orthonormal bases for the span of the columns of A and thus can be particularly relevant in solving non-square linear systems.

When solving least squares problems, we want to minimise:

$$\|Ax - b\|^2 . \tag{C.2}$$

Depending on the number of available linear equations, several case scenarios can be encountered. Here, underdetermined systems and overdetermined systems are briefly described.

C.2 Using the QR solver for underdetermined systems

A system of linear equations is considered underdetermined if there are fewer equations than unknowns. Thus, there are not enough equations to solve the system in a determined manner, and the least-squares minimisation returns the best solution.

C.3 Using the QR solver for overdetermined systems

A system of linear equations is considered overdetermined if there are more equations than unknowns. Solving an overdetermined system can be challenging since multiple inconsistent solutions are possible. In practice, the system $Ax = b$ is such that m is greater than n. In this case, the vector b cannot be expressed as a linear combination of the columns of A. Thus, there is no matrix x that satisfies the problem $Ax = b$ (except in specific cases), but it is possible to determine x so that Ax is as close to b as possible.

It is important to note that using overdetermined systems with experimental data can lead to introducing more noise or artefacts. Thus, the set of data to resolve the problem should be chosen wisely to form a determined system. For example, this was achieved in chapter 5 by excluding the data set corresponding to B_z.

Appendix D

Fitting model for relaxometric curves

The evaluation of the maps resulting from the measurement of T_1 with the widefield setup is done for every pixel. Since a dense ensemble of NV centres was used in this work, each pixel contains the contribution of several NV centres, all of which see slightly different fields. Thus, each trace contained in every pixel results from different contributions and the single exponential fit given by equation 1.17 is not adapted.

Instead, the curves are fitted using the least squares method to a stretched exponential function given by:

$$y(\tau) = A \cdot \exp\left[-\left(\frac{\tau}{T_1}\right)^b\right] + y_0 \tag{D.1}$$

The various parameters describing the behaviour of the curve are as follows:

- The amplitude A gives information about whether the control of the NV centre by laser light and microwaves is homogeneous.
- The exponent b gives information about the NVs ensemble; e.g. if the ensemble is homogeneous.
- Finally, y_0 is the offset resulting from the background noise

Thus, evaluating the above parameters provides T_1 and clues to the experimental conditions.

Bibliography

[1] Robert Hooke, *Micrographia, or some physiological descriptions of minute bodies made by magnifying glasses, with observations and inquiries thereupon.*, London: Printed by Jo. Martyn, and Ja. Allestry, printers to the Royal Society (1665).

[2] R. Won, *Eyes on super-resolution*, Nature Photonics **3**(7), 368–369 (2009).

[3] Editorials, *Beyond the diffraction limit*, Nature Photonics **3**(7), 361–361 (2009).

[4] H. Birch, M. Looi and C. Stuart, *The Big Questions in Science*, Deutsch Andre (2016).

[5] *The Nobel Prize in Physics 2018*, `https://www.nobelprize.org/prizes/physics/2018/press-release/`.

[6] H. Zhang and K.-K. Liu, *Optical tweezers for single cells*, Journal of The Royal Society Interface **5**(24), 671–690 (2008).

[7] K. C. Neuman and A. Nagy, *Single-molecule force spectroscopy: optical tweezers, magnetic tweezers and atomic force microscopy*, Nature Methods **5**(6), 491–505 (2008).

[8] P. Polimeno, A. Magazzù, M. A. Iatì, F. Patti, R. Saija, C. D. Esposti Boschi, M. G. Donato, P. G. Gucciardi, P. H. Jones, G. Volpe and O. M. Maragò, *Optical tweezers and their applications*, Journal of Quantitative Spectroscopy and Radiative Transfer **218**, 131–150 (2018).

[9] C. J. Bustamante, Y. R. Chemla, S. Liu and M. D. Wang, *Optical tweezers in single-molecule biophysics*, Nature Reviews Methods Primers **1**(1), 1–29 (2021).

[10] M. D. Wang, H. Yin, R. Landick, J. Gelles and S. M. Block, *Stretching DNA with optical tweezers*, Biophysical Journal **72**(3), 1335–1346 (1997).

[11] *The Nobel Prize in Physics 2012*, `https://www.nobelprize.org/prizes/physics/2012/summary/`.

[12] G. Wolfowicz, F. J. Heremans, C. P. Anderson, S. Kanai, H. Seo, A. Gali, G. Galli and D. D. Awschalom, *Quantum guidelines for solid-state spin defects*, Nature Reviews Materials **6**(10), 906–925 (2021).

[13] G. Balasubramanian, P. Neumann, D. Twitchen, M. Markham, R. Kolesov, N. Mizuochi, J. Isoya, J. Achard, J. Beck, J. Tissler, V. Jacques, P. R. Hemmer, F. Jelezko and J. Wrachtrup, *Ultralong spin coherence time in isotopically engineered diamond*, Nature Materials **8**(5), 383–387 (2009).

[14] N. Bar-Gill, L. M. Pham, A. Jarmola, D. Budker and R. L. Walsworth, *Solid-state electronic spin coherence time approaching one second*, Nature Communications **4**(1), 1743 (2013).

[15] B. Hensen, H. Bernien, A. E. Dréau, A. Reiserer, N. Kalb, M. S. Blok, J. Ruitenberg, R. F. L. Vermeulen, R. N. Schouten, C. Abellán, W. Amaya, V. Pruneri, M. W. Mitchell, M. Markham, D. J. Twitchen, D. Elkouss, S. Wehner, T. H. Taminiau and R. Hanson, *Loophole-free Bell inequality violation using electron spins separated by 1.3 kilometres*, Nature **526**(7575), 682–686 (2015).

[16] L. Rondin, J.-P. Tetienne, T. Hingant, J.-F. Roch, P. Maletinsky and V. Jacques, *Magnetometry with nitrogen-vacancy defects in diamond*, Reports on Progress in Physics **77**(5), 056503 (2014).

[17] R. Schirhagl, K. Chang, M. Loretz and C. L. Degen, *Nitrogen-Vacancy Centers in Diamond: Nanoscale Sensors for Physics and Biology*, Annual Review of Physical Chemistry **65**(1), 83–105 (2014).

[18] J. Wrachtrup and A. Finkler, *Single spin magnetic resonance*, Journal of Magnetic Resonance **269**, 225–236 (2016).

[19] C. L. Degen, F. Reinhard and P. Cappellaro, *Quantum sensing*, Reviews of Modern Physics **89**(3), 035002 (2017).

[20] E. V. Levine, M. J. Turner, P. Kehayias, C. A. Hart, N. Langellier, R. Trubko, D. R. Glenn, R. R. Fu and R. L. Walsworth, *Principles and techniques of the quantum diamond microscope*, Nanophotonics **8**(11), 1945–1973 (2019).

[21] G. Balasubramanian, I. Y. Chan, R. Kolesov, M. Al-Hmoud, J. Tisler, C. Shin, C. Kim, A. Wojcik, P. R. Hemmer, A. Krueger, T. Hanke, A. Leitenstorfer, R. Bratschitsch, F. Jelezko and J. Wrachtrup, *Nanoscale imaging magnetometry with diamond spins under ambient conditions*, Nature **455**(7213), 648–651 (2008).

[22] C. L. Degen, *Scanning magnetic field microscope with a diamond single-spin sensor*, Applied Physics Letters **92**(24), 243111 (2008).

[23] J. R. Maze, P. L. Stanwix, J. S. Hodges, S. Hong, J. M. Taylor, P. Cappellaro, L. Jiang, M. V. G. Dutt, E. Togan, A. S. Zibrov, A. Yacoby, R. L. Walsworth and M. D. Lukin, *Nanoscale magnetic sensing with an individual electronic spin in diamond*, Nature **455**(7213), 644–647 (2008).

[24] P. Delaney, J. C. Greer and J. A. Larsson, *Spin-Polarization Mechanisms of the Nitrogen-Vacancy Center in Diamond*, Nano Letters **10**(2), 610–614 (2010).

[25] J. R. Maze, A. Gali, E. Togan, Y. Chu, A. Trifonov, E. Kaxiras and M. D. Lukin, *Properties of nitrogen-vacancy centers in diamond: the group theoretic approach*, New Journal of Physics **13**(2), 025025 (2011).

[26] J. Teissier, A. Barfuss, P. Appel, E. Neu and P. Maletinsky, *Strain Coupling of a Nitrogen-Vacancy Center Spin to a Diamond Mechanical Oscillator*, Physical Review Letters **113**(2), 020503 (2014).

[27] A. Barfuss, J. Teissier, E. Neu, A. Nunnenkamp and P. Maletinsky, *Strong mechanical driving of a single electron spin*, Nature Physics **11**(10), 820–824 (2015).

[28] Á. Gali, *Ab initio theory of the nitrogen-vacancy center in diamond*, Nanophotonics **8**(11), 1907–1943 (2019).

[29] B. Naydenov, F. Dolde, L. T. Hall, C. Shin, H. Fedder, L. C. L. Hollenberg, F. Jelezko and J. Wrachtrup, *Dynamical decoupling of a single-electron spin at room temperature*, Physical Review B **83**(8), 081201 (2011).

[30] N. Bar-Gill, L. Pham, C. Belthangady, D. Le Sage, P. Cappellaro, J. Maze, M. Lukin, A. Yacoby and R. Walsworth, *Suppression of spin-bath dynamics for improved coherence of multi-spin-qubit systems*, Nature Communications **3**(1), 858 (2012).

[31] M. Hirose, C. D. Aiello and P. Cappellaro, *Continuous dynamical decoupling magnetometry*, Physical Review A **86**(6), 062320 (2012).

[32] J. F. Barry, J. M. Schloss, E. Bauch, M. J. Turner, C. A. Hart, L. M. Pham and R. L. Walsworth, *Sensitivity optimization for NV-diamond magnetometry*, Reviews of Modern Physics **92**(1), 015004 (2020).

[33] T. Wolf, P. Neumann, K. Nakamura, H. Sumiya, T. Ohshima, J. Isoya and J. Wrachtrup, *Subpicotesla Diamond Magnetometry*, Physical Review X **5**(4), 041001 (2015).

[34] C. Zhang, F. Shagieva, M. Widmann, M. Kübler, V. Vorobyov, P. Kapitanova, E. Nenasheva, R. Corkill, O. Rhrle, K. Nakamura, H. Sumiya, S. Onoda, J. Isoya and J. Wrachtrup, *Diamond Magnetometry and Gradiometry Towards Subpicotesla dc Field Measurement*, Physical Review Applied **15**(6), 064075 (2021).

[35] S. Kolkowitz, A. Safira, A. A. High, R. C. Devlin, S. Choi, Q. P. Unterreithmeier, D. Patterson, A. S. Zibrov, V. E. Manucharyan, H. Park and M. D. Lukin, *Probing Johnson noise and ballistic transport in normal metals with a single-spin qubit*, Science **347**(6226), 1129–1132 (2015).

[36] D. A. Broadway, N. Dontschuk, A. Tsai, S. E. Lillie, C. T.-K. Lew, J. C. McCallum, B. C. Johnson, M. W. Doherty, A. Stacey, L. C. L. Hollenberg and J.-P. Tetienne, *Spatial mapping of band bending in semiconductor devices using in situ quantum sensors*, Nature Electronics **1**(9), 502–507 (2018).

[37] K. Chang, A. Eichler, J. Rhensius, L. Lorenzelli and C. L. Degen, *Nanoscale Imaging of Current Density with a Single-Spin Magnetometer*, Nano Letters **17**(4), 2367–2373 (2017).

[38] D. Kim, M. I. Ibrahim, C. Foy, M. E. Trusheim, R. Han and D. R. Englund, *A CMOS-integrated quantum sensor based on nitrogen–vacancy centres*, Nature Electronics **2**(7), 284–289 (2019).

[39] G. J. Abrahams, S. C. Scholten, A. J. Healey, I. O. Robertson, N. Dontschuk, S. Q. Lim, B. C. Johnson, D. A. Simpson, L. C. L. Hollenberg and J.-P. Tetienne, *An integrated widefield probe for practical diamond nitrogen-vacancy microscopy*, Applied Physics Letters **119**(25), 254002 (2021).

[40] S. C. Scholten, A. J. Healey, I. O. Robertson, G. J. Abrahams, D. A. Broadway and J.-P. Tetienne, *Widefield quantum microscopy with nitrogen-vacancy centers in diamond: strengths, limitations, and prospects*, arXiv:2108.06060 [cond-mat, physics:physics, physics:quant-ph] (2021).

[41] F. Jelezko and J. Wrachtrup, *Single defect centres in diamond: A review*, physica status solidi (a) **203**(13), 3207–3225 (2006).

[42] F. Casola, T. van der Sar and A. Yacoby, *Probing condensed matter physics with magnetometry based on nitrogen-vacancy centres in diamond*, Nature Reviews Materials **3**(1), 17088 (2018).

[43] L. Childress and R. Hanson, *Diamond NV centers for quantum computing and quantum networks*, MRS Bulletin **38**(2), 134–138 (2013).

[44] Y. Chu and M. D. Lukin, *Quantum optics with nitrogen-vacancy centres in diamond*, *Quantum Optics and Nanophotonics*, Oxford University Press (2017).

[45] S. Pezzagna and J. Meijer, *Quantum computer based on color centers in diamond*, Applied Physics Reviews **8**(1), 011308 (2021).

[46] M. S. Grinolds, P. Maletinsky, S. Hong, M. D. Lukin, R. L. Walsworth and A. Yacoby, *Quantum control of proximal spins using nanoscale magnetic resonance imaging*, Nature Physics **7**(9), 687–692 (2011).

[47] F. Ziem, M. Garsi, H. Fedder and J. Wrachtrup, *Quantitative nanoscale MRI with a wide field of view*, Scientific Reports **9**(1), 12166 (2019).

[48] L. T. Hall, C. D. Hill, J. H. Cole, B. Städler, F. Caruso, P. Mulvaney, J. Wrachtrup and L. C. L. Hollenberg, *Monitoring ion-channel function in real time through quantum decoherence*, Proceedings of the National Academy of Sciences **107**(44), 18777–18782 (2010).

[49] A. M. Wojciechowski, M. Karadas, A. Huck, C. Osterkamp, S. Jankuhn, J. Meijer, F. Jelezko and U. L. Andersen, *Contributed Review: Camera-limits for wide-field magnetic resonance imaging with a nitrogen-vacancy spin sensor*, Review of Scientific Instruments **89**(3), 031501 (2018).

[50] J. L. Webb, L. Troise, N. W. Hansen, L. F. Frellsen, C. Osterkamp, F. Jelezko, S. Jankuhn, J. Meijer, K. Berg-Sørensen, J.-F. Perrier, A. Huck and U. L. Andersen, *High-Speed Wide-Field Imaging of Microcircuitry Using Nitrogen Vacancies in Diamond*, Physical Review Applied **17**(6), 064051 (2022).

[51] A. Boretti, L. Rosa, J. Blackledge and S. Castelletto, *Nitrogen-vacancy centers in diamond for nanoscale magnetic resonance imaging applications*, Beilstein Journal of Nanotechnology **10**, 2128–2151 (2019).

[52] E. Bernardi, E. Moreva, P. Traina, G. Petrini, S. Ditalia Tchernij, J. Forneris, Ž. Pastuović, I. P. Degiovanni, P. Olivero and M. Genovese, *A biocompatible technique for magnetic field sensing at (sub)cellular scale using Nitrogen-Vacancy centers*, EPJ Quantum Technology **7**(1), 13 (2020).

[53] F. Dolde, H. Fedder, M. W. Doherty, T. Nöbauer, F. Rempp, G. Balasubramanian, T. Wolf, F. Reinhard, L. C. L. Hollenberg, F. Jelezko and J. Wrachtrup, *Electric-field sensing using single diamond spins*, Nature Physics **7**(6), 459–463 (2011).

[54] J. Michl, J. Steiner, A. Denisenko, A. Bülau, A. Zimmermann, K. Nakamura, H. Sumiya, S. Onoda, P. Neumann, J. Isoya and Jörg Wrachtrup, *Robust and Accurate Electric Field Sensing with Solid State Spin Ensembles*, Nano Letters **19**(8), 4904–4910 (2019).

[55] K. Bian, W. Zheng, X. Zeng, X. Chen, R. Stöhr, A. Denisenko, S. Yang, J. Wrachtrup and Y. Jiang, *Nanoscale electric-field imaging based on a quantum sensor and its charge-state control under ambient condition*, Nature Communications **12**(1), 2457 (2021).

[56] D. M. Toyli, C. F. de las Casas, D. J. Christle, V. V. Dobrovitski and D. D. Awschalom, *Fluorescence thermometry enhanced by the quantum coherence of single spins in diamond*, Proceedings of the National Academy of Sciences **110**(21), 8417–8421 (2013).

[57] P. Neumann, I. Jakobi, F. Dolde, C. Burk, R. Reuter, G. Waldherr, J. Honert, T. Wolf, A. Brunner, J. H. Shim, D. Suter, H. Sumiya, J. Isoya and J. Wrachtrup, *High-Precision Nanoscale Temperature Sensing Using Single Defects in Diamond*, Nano Letters **13**(6), 2738–2742 (2013).

[58] G. Kucsko, P. C. Maurer, N. Y. Yao, M. Kubo, H. J. Noh, P. K. Lo, H. Park and M. D. Lukin, *Nanometre-scale thermometry in a living cell*, Nature **500**(7460), 54–58 (2013).

[59] H. Clevenson, M. E. Trusheim, C. Teale, T. Schröder, D. Braje and D. Englund, *Broadband magnetometry and temperature sensing with a light-trapping diamond waveguide*, Nature Physics **11**(5), 393–397 (2015).

[60] T. Sekiguchi, S. Sotoma and Y. Harada, *Fluorescent nanodiamonds as a robust temperature sensor inside a single cell*, Biophysics and Physicobiology **15**, 229–234 (2018).

[61] P. Konzelmann, T. Rendler, V. Bergholm, A. Zappe, V. Pfannenstill, M. Garsi, F. Ziem, M. Niethammer, M. Widmann, S.-Y. Lee, P. Neumann and J. Wrachtrup, *Robust and efficient quantum optimal control of spin probes in a complex (biological) environment. Towards sensing of fast temperature fluctuations*, New Journal of Physics **20**(12), 123013 (2018).

[62] M. E. Trusheim and D. Englund, *Wide-field strain imaging with preferentially aligned nitrogen-vacancy centers in polycrystalline diamond*, New Journal of Physics **18**(12), 123023 (2016).

[63] M. S. J. Barson, P. Peddibhotla, P. Ovartchaiyapong, K. Ganesan, R. L. Taylor, M. Gebert, Z. Mielens, B. Koslowski, D. A. Simpson, L. P. McGuinness, J. McCallum, S. Prawer, S. Onoda, T. Ohshima, A. C. Bleszynski Jayich, F. Jelezko, N. B. Manson and M. W. Doherty, *Nanomechanical Sensing Using Spins in Diamond*, Nano Letters **17**(3), 1496–1503 (2017).

[64] P. Udvarhelyi, V. O. Shkolnikov, A. Gali, G. Burkard and A. Pályi, *Spin-strain interaction in nitrogen-vacancy centers in diamond*, Physical Review B **98**(7), 075201 (2018).

[65] T. Hom, W. Kiszenik and B. Post, *Accurate lattice constants from multiple reflection measurements. II. Lattice constants of germanium silicon, and diamond*, Journal of Applied Crystallography **8**(4), 457–458 (1975).

[66] L. Pauling, *The nature of the chemical bond. Application of results obtained from the quantum mechanics and from a theory of paramagnetic susceptibility to the structure of molecules*, Journal of the American Chemical Society **53**(4), 1367–1400 (1931).

[67] R. J. Gillespie, *Teaching Molecular Geometry with the VSEPR Model*, Journal of Chemical Education **81**(3), 298 (2004).

[68] C. A. Brookes and E. J. Brookes, *Diamond in perspective: a review of mechanical properties of natural diamond*, Diamond and Related Materials **1**(1), 13–17 (1991).

[69] A. C. Victor, *Heat Capacity of Diamond at High Temperatures*, The Journal of Chemical Physics **36**(7), 1903–1911 (1962).

[70] M. Werner and R. Locher, *Growth and application of undoped and doped diamond films*, Reports on Progress in Physics **61**(12), 1665–1710 (1998).

[71] S. Kasap, C. Koughia, J. Singh, H. Ruda and S. O'Leary, *Optical Properties of Electronic Materials: Fundamentals and Characterization*, S. Kasap and P. Capper, editors, *Springer Handbook of Electronic and Photonic Materials*, Springer Handbooks, 47–77, Boston, MA: Springer US (2007).

[72] A. M. Schrand, H. Huang, C. Carlson, J. J. Schlager, E. Ōsawa, S. M. Hussain and L. Dai, *Are Diamond Nanoparticles Cytotoxic?*, The Journal of Physical Chemistry B **111**(1), 2–7 (2007).

[73] A. Apicella, R. Aversa and F. I. T. Petrescu, *Hybrid Ceramo-Polymeric Nano-Diamond Composites*, American Journal of Engineering and Applied Sciences **11**(2), 766–782 (2018).

[74] C. A. Coulson and M. J. Kearsley, *Colour centres in irradiated diamonds. I*, Proceedings of the Royal Society of London. Series A. Mathematical and Physical Sciences **241**(1227), 433–454 (1957).

[75] J. H. N. Loubser and J. A. v. Wyk, *Electron spin resonance in the study of diamond*, Reports on Progress in Physics **41**(8), 1201–1248 (1978).

[76] J. Walker, *Optical absorption and luminescence in diamond*, Reports on Progress in Physics **42**(10), 1605–1659 (1979).

[77] R. Robertson, J. J. Fox and A. E. Martin, *Two types of diamond*, Philosophical Transactions of the Royal Society of London. Series A, Containing Papers of a Mathematical or Physical Character **232**(707-720), 463–535 (1933).

[78] C. M. Breeding and J. E. Shigley, *The "Type" Classification System of Diamonds and Its Importance in Gemology*, Gems & Gemology **45**(2), 96–111 (2009).

[79] Element Six Technologies US Corporation, *CVD diamond handbook*, © Element Six 2001 - 2022 (2020).

[80] K. M. Itoh and H. Watanabe, *Isotope engineering of silicon and diamond for quantum computing and sensing applications*, MRS Communications **4**(4), 143–157 (2014).

[81] T. Yamamoto, T. Umeda, K. Watanabe, S. Onoda, M. L. Markham, D. J. Twitchen, B. Naydenov, L. P. McGuinness, T. Teraji, S. Koizumi, F. Dolde, H. Fedder, J. Honert, J. Wrachtrup, T. Ohshima, F. Jelezko and J. Isoya, *Extending spin coherence times of diamond qubits by high-temperature annealing*, Physical Review B **88**(7), 075206 (2013).

[82] M. Markham, J. Dodson, G. Scarsbrook, D. Twitchen, G. Balasubramanian, F. Jelezko and J. Wrachtrup, *CVD diamond for spintronics*, Diamond and Related Materials **20**(2), 134–139 (2011).

[83] F. P. Bundy, H. T. Hall, H. M. Strong and R. H. Wentorfjun., *Man-Made Diamonds*, Nature **176**(4471), 51–55 (1955).

[84] G. Davies, M. F. Hamer and W. C. Price, *Optical studies of the 1.945 eV vibronic band in diamond*, Proceedings of the Royal Society of London. A. Mathematical and Physical Sciences **348**(1653), 285–298 (1976).

[85] E. v. Oort, N. B. Manson and M. Glasbeek, *Optically detected spin coherence of the diamond N-V centre in its triplet ground state*, Journal of Physics C: Solid State Physics **21**(23), 4385–4391 (1988).

[86] E. van Oort, P. Stroomer and M. Glasbeek, *Low-field optically detected magnetic resonance of a coupled triplet-doublet defect pair in diamond*, Physical Review B **42**(13), 8605–8608 (1990).

[87] E. Van Oort and M. Glasbeek, *Electric-field-induced modulation of spin echoes of N-V centers in diamond*, Chemical Physics Letters **168**(6), 529–532 (1990).

[88] A. Gruber, A. Dräbenstedt, C. Tietz, L. Fleury, J. Wrachtrup and C. v. Borczyskowski, *Scanning Confocal Optical Microscopy and Magnetic Resonance on Single Defect Centers*, Science **276**(5321), 2012–2014 (1997).

[89] A. Gali, M. Fyta and E. Kaxiras, *Ab initio supercell calculations on nitrogen-vacancy center in diamond: Electronic structure and hyperfine tensors*, Physical Review B **77**(15), 155206 (2008).

[90] C. Schreyvogel, V. Polyakov, S. Burk, H. Fedder, A. Denisenko, F. F. d. Oliveira, R. Wunderlich, J. Meijer, V. Zuerbig, J. Wrachtrup and C. E. Nebel, *Active and fast charge-state switching of single NV centres in diamond by in-plane Al-Schottky junctions*, Beilstein Journal of Nanotechnology **7**(1), 1727–1735 (2016).

[91] M. Pfender, N. Aslam, P. Simon, D. Antonov, G. Thiering, S. Burk, F. Fávaro de Oliveira, A. Denisenko, H. Fedder, J. Meijer, J. A. Garrido, A. Gali, T. Teraji, J. Isoya, M. W. Doherty, A. Alkauskas, A. Gallo, A. Grüneis, P. Neumann and J. Wrachtrup, *Protecting a Diamond Quantum Memory by Charge State Control*, Nano Letters **17**(10), 5931–5937 (2017).

[92] G. Davies, *Dynamic Jahn-Teller distortions at trigonal optical centres in diamond*, Journal of Physics C: Solid State Physics **12**(13), 2551–2566 (1979).

[93] N. B. Manson and J. P. Harrison, *Photo-ionization of the nitrogen-vacancy center in diamond*, Diamond and Related Materials **14**(10), 1705–1710 (2005).

[94] R. J. Epstein, F. M. Mendoza, Y. K. Kato and D. D. Awschalom, *Anisotropic interactions of a single spin and dark-spin spectroscopy in diamond*, Nature Physics **1**(2), 94–98 (2005).

[95] F. M. Hossain, M. W. Doherty, H. F. Wilson and L. C. L. Hollenberg, *Ab Initio Electronic and Optical Properties of the N - V - Center in Diamond*, Physical Review Letters **101**(22), 226403 (2008).

[96] J. Christinck, B. Rodiek, M. López, H. Hofer, H. Georgieva and S. Kück, *Characterization of the angular-dependent emission of nitrogen-vacancy centers in nanodiamond*, Applied Physics B **126**(10), 161 (2020).

[97] E. Bourgeois, A. Jarmola, P. Siyushev, M. Gulka, J. Hruby, F. Jelezko, D. Budker and M. Nesladek, *Photoelectric detection of electron spin resonance of nitrogen-vacancy centres in diamond*, Nature Communications **6**(1), 8577 (2015).

[98] P. Siyushev, M. Nesladek, E. Bourgeois, M. Gulka, J. Hruby, T. Yamamoto, M. Trupke, T. Teraji, J. Isoya and F. Jelezko, *Photoelectrical imaging and coherent spin-state readout of single nitrogen-vacancy centers in diamond*, Science **363**(6428), 728–731 (2019).

[99] L. Razinkovas, M. Maciaszek, F. Reinhard, M. W. Doherty and A. Alkauskas, *Photoionization of negatively charged NV centers in diamond: Theory and ab initio calculations*, Physical Review B **104**(23), 235301 (2021).

[100] M. Pfender, N. Aslam, G. Waldherr, P. Neumann and J. Wrachtrup, *Single-spin stochastic optical reconstruction microscopy*, Proceedings of the National Academy of Sciences **111**(41), 14669–14674 (2014).

[101] O. D. Tucker, M. E. Newton and J. M. Baker, *EPR and ^{14}N electron-nuclear double-resonance measurements on the ionized nearest-neighbor dinitrogen center in diamond*, Physical Review B **50**(21), 15586–15596 (1994).

[102] S. Felton, A. M. Edmonds, M. E. Newton, P. M. Martineau, D. Fisher, D. J. Twitchen and J. M. Baker, *Hyperfine interaction in the ground state of the negatively charged nitrogen vacancy center in diamond*, Physical Review B **79**(7), 075203 (2009).

[103] L. Robledo, H. Bernien, T. van der Sar and R. Hanson, *Spin dynamics in the optical cycle of single nitrogen-vacancy centres in diamond*, New Journal of Physics **13**(2), 025013 (2011).

[104] A. Schweiger and G. Jeschke, *Principles of pulse electron paramagnetic resonance*, Oxford University Press (2001).

[105] I. I. Rabi, *Space Quantization in a Gyrating Magnetic Field*, Physical Review **51**(8), 652–654 (1937).

[106] I. I. Rabi, N. F. Ramsey and J. Schwinger, *Use of Rotating Coordinates in Magnetic Resonance Problems*, Reviews of Modern Physics **26**(2), 167–171 (1954).

[107] N. Atherton, M. Davies and B. Gilbert, *Electron Spin Resonance*, number vol. 14 in Electron spin resonance, Royal Society of Chemistry (1994).

[108] P. G. Baranov, H. J. von Bardeleben, F. Jelezko and J. Wrachtrup, *Magnetic Resonance of Semiconductors and Their Nanostructures: Basic and Advanced Applications*, volume 253 of *Springer Series in Materials Science*, Vienna: Springer Vienna (2017).

[109] A. Dréau, M. Lesik, L. Rondin, P. Spinicelli, O. Arcizet, J.-F. Roch and V. Jacques, *Avoiding power broadening in optically detected magnetic resonance of single NV defects for enhanced dc magnetic field sensitivity*, Physical Review B **84**(19), 195204 (2011).

[110] C. A. Ryan, J. S. Hodges and D. G. Cory, *Robust Decoupling Techniques to Extend Quantum Coherence in Diamond*, Physical Review Letters **105**(20), 200402 (2010).

[111] C. P. Slichter, *Principles of Magnetic Resonance*, Springer Science & Business Media (2013).

[112] Z.-P. Liang and P. C. Lauterbur, *Principles of Magnetic Resonance imaging: a Signal Processing Perspective*, volume PM76, SPIE Optical Engineering Press Bellingham (2000).

[113] K. Wüthrich, *NMR with Proteins and Nucleic Acids*, Europhysics News **17**(1), 11–13 (1986).

[114] T. Staudacher, F. Shi, S. Pezzagna, J. Meijer, J. Du, C. A. Meriles, F. Reinhard and J. Wrachtrup, *Nuclear Magnetic Resonance Spectroscopy on a (5-Nanometer)* ^{3} *Sample Volume*, Science **339**(6119), 561–563 (2013).

[115] H. J. Mamin, M. Kim, M. H. Sherwood, C. T. Rettner, K. Ohno, D. D. Awschalom and D. Rugar, *Nanoscale Nuclear Magnetic Resonance with a Nitrogen-Vacancy Spin Sensor*, Science **339**(6119), 557–560 (2013).

[116] K. S. Cujia, K. Herb, J. Zopes, J. M. Abendroth and C. L. Degen, *Parallel detection and spatial mapping of large nuclear spin clusters*, Nature Communications **13**(1), 1260 (2022).

[117] E. L. Hahn, *Spin Echoes*, Physical Review **80**(4), 580–594 (1950).

[118] P. Peng, X. Huang, C. Yin, L. Joseph, C. Ramanathan and P. Cappellaro, *Deep reinforcement learning for quantum Hamiltonian engineering*, arXiv:2102.13161 [physics, physics:quant-ph] (2021).

[119] K. Jung, M. H. Abobeih, J. Yun, G. Kim, H. Oh, A. Henry, T. H. Taminiau and D. Kim, *Deep learning enhanced individual nuclear-spin detection*, npj Quantum Information **7**(1), 41 (2021).

[120] R. R. Sharp, *Nuclear spin relaxation due to paramagnetic species in solution: Effect of anisotropy in the zero field splitting tensor*, The Journal of Chemical Physics **98**(8), 6092–6101 (1993).

[121] M. Goldman, *Formal Theory of Spin–Lattice Relaxation*, Journal of Magnetic Resonance **149**(2), 160–187 (2001).

[122] S. Steinert, F. Ziem, L. T. Hall, A. Zappe, M. Schweikert, N. Götz, A. Aird, G. Balasubramanian, L. Hollenberg and J. Wrachtrup, *Magnetic spin imaging under ambient conditions with sub-cellular resolution*, Nature Communications **4**(1), 1607 (2013).

[123] F. C. Ziem, N. S. Götz, A. Zappe, S. Steinert and J. Wrachtrup, *Highly Sensitive Detection of Physiological Spins in a Microfluidic Device*, Nano Letters **13**(9), 4093–4098 (2013).

[124] T. Häberle, *Nanoscale Magnetic Resonance Imaging*, Ph.D. thesis, Universität Stuttgart (2017).

[125] A. Batalov, V. Jacques, F. Kaiser, P. Siyushev, P. Neumann, L. J. Rogers, R. L. McMurtrie, N. B. Manson, F. Jelezko and J. Wrachtrup, *Low Temperature Studies of the Excited-State Structure of Negatively Charged Nitrogen-Vacancy Color Centers in Diamond*, Physical Review Letters **102**(19), 195506 (2009).

[126] J. Happacher, D. Broadway, P. Reiser, A. Jiménez, M. A. Tschudin, L. Thiel, D. Rohner, M. l. G. Puigibert, B. Shields, J. R. Maze, V. Jacques and P. Maletinsky, *Low temperature photo-physics of single NV centers in diamond*, arXiv:2105.08075 [cond-mat, physics:quant-ph] (2021).

[127] G.-Q. Liu, X. Feng, N. Wang, Q. Li and R.-B. Liu, *Coherent quantum control of nitrogen-vacancy center spins near 1000 kelvin*, Nature Communications **10**(1), 1344 (2019).

[128] M. Lesik, T. Plisson, L. Toraille, J. Renaud, F. Occelli, M. Schmidt, O. Salord, A. Delobbe, T. Debuisschert, L. Rondin, P. Loubeyre and J.-F. Roch, *Magnetic measurements on micrometer-sized samples under high pressure using designed NV centers*, Science **366**(6471), 1359–1362 (2019).

[129] J. Meijer, T. Vogel, B. Burchard, I. Rangelow, L. Bischoff, J. Wrachtrup, M. Domhan, F. Jelezko, W. Schnitzler, S. Schulz, K. Singer and F. Schmidt-Kaler, *Concept of deterministic single ion doping with sub-nm spatial resolution*, Applied Physics A **83**(2), 321–327 (2006).

[130] D. M. Toyli, C. D. Weis, G. D. Fuchs, T. Schenkel and D. D. Awschalom, *Chip-Scale Nanofabrication of Single Spins and Spin Arrays in Diamond*, Nano Letters **10**(8), 3168–3172 (2010).

[131] J. Martin, R. Wannemacher, J. Teichert, L. Bischoff and B. Köhler, *Generation and detection of fluorescent color centers in diamond with submicron resolution*, Applied Physics Letters **75**(20), 3096–3098 (1999).

[132] V. Borjanović, L. Bistričić, I. Vlasov, K. Furić, I. Zamboni, M. Jakšić and O. Shenderova, *Influence of proton irradiation on the structure and stability of poly(dimethylsiloxane) and poly(dimethylsiloxane)-nanodiamond composite*, Journal of Vacuum Science & Technology B: Microelectronics and Nanometer Structures Processing, Measurement, and Phenomena **27**(6), 2396 (2009).

[133] J. R. Rabeau, A. Stacey, A. Rabeau, S. Prawer, F. Jelezko, I. Mirza and J. Wrachtrup, *Single Nitrogen Vacancy Centers in Chemical Vapor Deposited Diamond Nanocrystals*, Nano Letters **7**(11), 3433–3437 (2007).

[134] K. Ohno, F. Joseph Heremans, L. C. Bassett, B. A. Myers, D. M. Toyli, A. C. Bleszynski Jayich, C. J. Palmstrøm and D. D. Awschalom, *Engineering shallow spins in diamond with nitrogen delta-doping*, Applied Physics Letters **101**(8), 082413 (2012).

[135] B. Naydenov, F. Reinhard, A. Lämmle, V. Richter, R. Kalish, U. F. S. D'Haenens-Johansson, M. Newton, F. Jelezko and J. Wrachtrup, *Increasing the coherence time of single electron spins in diamond by high temperature annealing*, Applied Physics Letters **97**(24), 242511 (2010).

[136] Y.-C. Chen, B. Griffiths, L. Weng, S. S. Nicley, S. N. Ishmael, Y. Lekhai, S. Johnson, C. J. Stephen, B. L. Green, G. W. Morley, M. E. Newton, M. J. Booth, P. S. Salter and J. M. Smith, *Laser writing of individual nitrogen-vacancy defects in diamond with near-unity yield*, Optica **6**(5), 662–667 (2019).

[137] A. Tallaire, J. Achard, A. Boussadi, O. Brinza, A. Gicquel, I. Kupriyanov, Y. Palyanov, G. Sakr and J. Barjon, *High quality thick CVD diamond films homoepitaxially grown on (111)-oriented substrates*, Diamond and Related Materials **41**, 34–40 (2014).

[138] J. Michl, T. Teraji, S. Zaiser, I. Jakobi, G. Waldherr, F. Dolde, P. Neumann, M. W. Doherty, N. B. Manson, J. Isoya and J. Wrachtrup, *Perfect alignment and preferential orientation of nitrogen-vacancy centers during chemical vapor deposition diamond growth on (111) surfaces*, Applied Physics Letters **104**(10), 102407 (2014).

[139] P. Neumann, J. Beck, M. Steiner, F. Rempp, H. Fedder, P. R. Hemmer, J. Wrachtrup and F. Jelezko, *Single-Shot Readout of a Single Nuclear Spin*, Science **329**(5991), 542–544 (2010).

[140] C. Osterkamp, M. Mangold, J. Lang, P. Balasubramanian, T. Teraji, B. Naydenov and F. Jelezko, *Engineering preferentially-aligned nitrogen-vacancy centre ensembles in CVD grown diamond*, Scientific Reports **9**(1), 5786 (2019).

[141] L. Thiel, Z. Wang, M. A. Tschudin, D. Rohner, I. Gutiérrez-Lezama, N. Ubrig, M. Gibertini, E. Giannini, A. F. Morpurgo and P. Maletinsky, *Probing magnetism in 2D materials at the nanoscale with single-spin microscopy*, Science **364**(6444), 973–976 (2019).

[142] F. Jelezko, T. Gaebel, I. Popa, M. Domhan, A. Gruber and J. Wrachtrup, *Observation of Coherent Oscillation of a Single Nuclear Spin and Realization of a Two-Qubit Conditional Quantum Gate*, Physical Review Letters **93**(13), 130501 (2004).

[143] L. P. McGuinness, Y. Yan, A. Stacey, D. A. Simpson, L. T. Hall, D. Maclaurin, S. Prawer, P. Mulvaney, J. Wrachtrup, F. Caruso, R. E. Scholten and L. C. L. Hollenberg, *Quantum measurement and orientation tracking of fluorescent nanodiamonds inside living cells*, Nature Nanotechnology **6**(6), 358–363 (2011).

[144] I. I. Vlasov, A. A. Shiryaev, T. Rendler, S. Steinert, S.-Y. Lee, D. Antonov, M. Vörös, F. Jelezko, A. V. Fisenko, L. F. Semjonova, J. Biskupek, U. Kaiser, O. I. Lebedev, I. Sildos, P. R. Hemmer, V. I. Konov, A. Gali and J. Wrachtrup, *Molecular-sized fluorescent nanodiamonds*, Nature Nanotechnology **9**(1), 54–58 (2014).

[145] T. Rendler, J. Neburkova, O. Zemek, J. Kotek, A. Zappe, Z. Chu, P. Cigler and J. Wrachtrup, *Optical imaging of localized chemical events using programmable diamond quantum nanosensors*, Nature Communications **8**(1), 14701 (2017).

[146] M. H. Alkahtani, F. Alghannam, L. Jiang, A. Almethen, A. A. Rampersaud, R. Brick, C. L. Gomes, M. O. Scully and P. R. Hemmer, *Fluorescent nanodiamonds: past, present, and future*, Nanophotonics **7**(8), 1423–1453 (2018).

[147] D. J. McCloskey, N. Dontschuk, D. A. Broadway, A. Nadarajah, A. Stacey, J.-P. Tetienne, L. C. L. Hollenberg, S. Prawer and D. A. Simpson, *Enhanced Widefield Quantum Sensing with Nitrogen-Vacancy Ensembles Using Diamond Nanopillar Arrays*, ACS Applied Materials & Interfaces **12**(11), 13421–13427 (2020).

[148] S. Pezzagna, D. Wildanger, P. Mazarov, A. D. Wieck, Y. Sarov, I. Rangelow, B. Naydenov, F. Jelezko, S. W. Hell and J. Meijer, *Nanoscale Engineering and Optical Addressing of Single Spins in Diamond*, Small **6**(19), 2117–2121 (2010).

[149] M. Schukraft, J. Zheng, T. Schröder, S. L. Mouradian, M. Walsh, M. E. Trusheim, H. Bakhru and D. R. Englund, *Invited Article: Precision nanoimplantation of nitrogen vacancy centers into diamond photonic crystal cavities and waveguides*, APL Photonics **1**(2), 020801 (2016).

[150] L. Rondin, G. Dantelle, A. Slablab, F. Grosshans, F. Treussart, P. Bergonzo, S. Perruchas, T. Gacoin, M. Chaigneau, H.-C. Chang, V. Jacques and J.-F. Roch, *Surface-induced charge state conversion of nitrogen-vacancy defects in nanodiamonds*, Physical Review B **82**(11), 115449 (2010).

[151] M. V. Hauf, B. Grotz, B. Naydenov, M. Dankerl, S. Pezzagna, J. Meijer, F. Jelezko, J. Wrachtrup, M. Stutzmann, F. Reinhard and J. A. Garrido, *Chemical control of the charge state of nitrogen-vacancy centers in diamond*, Physical Review B **83**(8), 081304 (2011).

[152] J. Hogg and T. West, *The microscope : its history, construction, and application, being a familiar introduction to the use of the instrument and the study of microscopical science*, G. Routledge and Sons, (1871).

[153] W. J. Croft, *Under the Microscope*, World Scientific (2006).

[154] Leica Microsystems, *Science Lab*, available online at `https://www.leica-microsystems.com/science-lab/science-lab-home/`, last accessed on 12.10.2022.

[155] J. Cabello, A. Bailey, I. Kitchen, M. Prydderch, A. Clark, R. Turchetta and K. Wells, *Digital autoradiography using room temperature CCD and CMOS imaging technology*, Physics in Medicine and Biology **52**(16), 4993–5011 (2007).

[156] Y. Liu, C. Ma, Y. Shen and L. V. Wang, *Bit-efficient, sub-millisecond wavefront measurement using a lock-in camera for time-reversal based optical focusing inside scattering media*, Optics Letters **41**(7), 1321 (2016).

[157] G. I. Cancelo, C. Chavez, F. Chierchie, J. Estrada, G. Fernandez-Moroni, E. E. Paolini, M. S. Haro, A. Soto, L. Stefanazzi, J. Tiffenberg, K. Treptow, N. Wilcer and T. J. Zmuda, *Low threshold acquisition controller for Skipper charge-coupled devices*, Journal of Astronomical Telescopes, Instruments, and Systems **7**(1), 015001 (2021).

[158] R. H. Webb, *Confocal optical microscopy*, Reports on Progress in Physics **59**, 427–471 (1996).

[159] J. B. Pawley, *Fundamental Limits in Confocal Microscopy*, J. B. Pawley, editor, *Handbook Of Biological Confocal Microscopy*, 20–42, Boston, MA: Springer US (2006).

[160] J. Icha, M. Weber, J. C. Waters and C. Norden, *Phototoxicity in live fluorescence microscopy, and how to avoid it*, BioEssays **39**(8), 1700003 (2017).

[161] A. L. Mattheyses, S. M. Simon and J. Z. Rappoport, *Imaging with total internal reflection fluorescence microscopy for the cell biologist*, Journal of Cell Science **123**(21), 3621–3628 (2010).

[162] E. Abbe, *Beiträge zur Theorie des Mikroskops und der mikroskopischen Wahrnehmung*, Archiv für Mikroskopische Anatomie **9**(1), 413–468 (1873).

[163] J. W. S. Rayleigh, *XV. On the theory of optical images, with special reference to the microscope*, The London, Edinburgh, and Dublin Philosophical Magazine and Journal of Science **42**(255), 167–195 (1896).

[164] S. W. Hell and J. Wichmann, *Breaking the diffraction resolution limit by stimulated emission: stimulated-emission-depletion fluorescence microscopy*, Optics Letters **19**(11), 780 (1994).

[165] T. A. Klar and S. W. Hell, *Subdiffraction resolution in far-field fluorescence microscopy*, Optics Letters **24**(14), 954 (1999).

[166] M. J. Rust, M. Bates and X. Zhuang, *Sub-diffraction-limit imaging by stochastic optical reconstruction microscopy (STORM)*, Nature Methods **3**(10), 793–796 (2006).

[167] P. Podder, T. Zaman Khan, M. Haque Khan and M. Muktadir Rahman, *Comparative Performance Analysis of Hamming, Hanning and Blackman Window*, International Journal of Computer Applications **96**(18), 1–7 (2014).

[168] S. Steinert, F. Dolde, P. Neumann, A. Aird, B. Naydenov, G. Balasubramanian, F. Jelezko and J. Wrachtrup, *High sensitivity magnetic imaging using an array of spins in diamond*, Review of Scientific Instruments **81**(4), 043705 (2010).

[169] D. Le Sage, K. Arai, D. R. Glenn, S. J. DeVience, L. M. Pham, L. Rahn-Lee, M. D. Lukin, A. Yacoby, A. Komeili and R. L. Walsworth, *Optical magnetic imaging of living cells*, Nature **496**(7446), 486–489 (2013).

[170] J.-P. Tetienne, N. Dontschuk, D. A. Broadway, A. Stacey, D. A. Simpson and L. C. L. Hollenberg, *Quantum imaging of current flow in graphene*, Science Advances **3**(4), e1602429 (2017).

[171] D. A. Broadway, S. C. Scholten, C. Tan, N. Dontschuk, S. E. Lillie, B. C. Johnson, G. Zheng, Z. Wang, A. R. Oganov, S. Tian, C. Li, H. Lei, L. Wang, L. C. L. Hollenberg and J.-P. Tetienne, *Imaging Domain Reversal in an Ultrathin Van der Waals Ferromagnet*, Advanced Materials **32**(39), 2003314 (2020).

[172] J. M. McCoey, M. Matsuoka, R. W. de Gille, L. T. Hall, J. A. Shaw, J.-P. Tetienne, D. Kisailus, L. C. L. Hollenberg and D. A. Simpson, *Quantum Magnetic Imaging of Iron Biomineralization in Teeth of the Chiton Acanthopleura hirtosa*, Small Methods **4**(3), 1900754 (2020).

[173] M. Garsi, R. Stöhr, A. Denisenko, F. Shagieva, N. Trautmann, U. Vogl, B. Sene, F. Kaiser, A. Zappe, R. Reuter and J. Wrachtrup, *Non-invasive imaging of three-dimensional integrated circuit activity using quantum defects in diamond*, arXiv:2112.12242 [cond-mat, physics:physics, physics:quant-ph] (2021).

[174] M. V. Romalis and H. B. Dang, *Atomic magnetometers for materials characterization*, Materials Today **14**(6), 258–262 (2011).

[175] V. M. Acosta, E. Bauch, M. P. Ledbetter, C. Santori, K.-M. C. Fu, P. E. Barclay, R. G. Beausoleil, H. Linget, J. F. Roch, F. Treussart, S. Chemerisov, W. Gawlik and D. Budker, *Diamonds with a high density of nitrogen-vacancy centers for magnetometry applications*, Physical Review B **80**(11), 115202 (2009).

[176] E. Fraczek, V. G. Savitski, M. Dale, B. G. Breeze, P. Diggle, M. Markham, A. Bennett, H. Dhillon, M. E. Newton and A. J. Kemp, *Laser spectroscopy of NV- and NV0 colour centres in synthetic diamond*, Optical Materials Express **7**(7), 2571–2585 (2017).

[177] B. Huang, G. Clark, E. Navarro-Moratalla, D. R. Klein, R. Cheng, K. L. Seyler, D. Zhong, E. Schmidgall, M. A. McGuire, D. H. Cobden, W. Yao, D. Xiao, P. Jarillo-Herrero and X. Xu, *Layer-dependent ferromagnetism in a van der Waals crystal down to the monolayer limit*, Nature **546**(7657), 270–273 (2017).

[178] A. K. Geim and I. V. Grigorieva, *Van der Waals heterostructures*, Nature **499**(7459), 419–425 (2013).

[179] D. R. Klein, D. MacNeill, J. L. Lado, D. Soriano, E. Navarro-Moratalla, K. Watanabe, T. Taniguchi, S. Manni, P. Canfield, J. Fernández-Rossier and P. Jarillo-Herrero, *Probing magnetism in 2D van der Waals crystalline insulators via electron tunneling*, Science **360**(6394), 1218–1222 (2018).

[180] M. L. James and S. S. Gambhir, *A Molecular Imaging Primer: Modalities, Imaging Agents, and Applications*, Physiological Reviews **92**(2), 897–965 (2012).

[181] L. C. Wu, Y. Zhang, G. Steinberg, H. Qu, S. Huang, M. Cheng, T. Bliss, F. Du, J. Rao, G. Song, L. Pisani, T. Doyle, S. Conolly, K. Krishnan, G. Grant and M. Wintermark, *A Review of Magnetic Particle Imaging and Perspectives on Neuroimaging*, American Journal of Neuroradiology **40**(2), 206–212 (2019).

[182] L. Rosa, J. Blackledge and A. Boretti, *Nano-Magnetic Resonance Imaging (Nano-MRI) Gives Personalized Medicine a New Perspective*, Biomedicines **5**(4), 7 (2017).

[183] A. Nowodzinski, M. Chipaux, L. Toraille, V. Jacques, J.-F. Roch and T. Debuisschert, *Nitrogen-Vacancy centers in diamond for current imaging at the redistributive layer level of Integrated Circuits*, Microelectronics Reliability **55**(9-10), 1549–1553 (2015).

[184] Y. Dovzhenko, F. Casola, S. Schlotter, T. X. Zhou, F. Büttner, R. L. Walsworth, G. S. D. Beach and A. Yacoby, *Magnetostatic twists in room-temperature skyrmions explored by nitrogen-vacancy center spin texture reconstruction*, Nature Communications **9**(1), 2712 (2018).

[185] Q.-C. Sun, T. Song, E. Anderson, A. Brunner, J. Förster, T. Shalomayeva, T. Taniguchi, K. Watanabe, J. Gräfe, R. Stöhr, X. Xu and J. Wrachtrup, *Magnetic domains and domain wall pinning in atomically thin CrBr3 revealed by nanoscale imaging*, Nature Communications **12**(1), 1989 (2021).

[186] I. Bertelli, J. J. Carmiggelt, T. Yu, B. G. Simon, C. C. Pothoven, G. E. W. Bauer, Y. M. Blanter, J. Aarts and T. van der Sar, *Magnetic resonance imaging of spin-wave transport and interference in a magnetic insulator*, Science Advances **6**(46), eabd3556 (2020).

[187] R. Dillenschneider, *Quantum discord and quantum phase transition in spin chains*, Physical Review B **78**(22), 224413 (2008).

[188] M. S. Rudner, *Driving toward hot new phases*, Nature Physics **16**(10), 1008–1009 (2020).

[189] S. Ebadi, T. T. Wang, H. Levine, A. Keesling, G. Semeghini, A. Omran, D. Bluvstein, R. Samajdar, H. Pichler, W. W. Ho, S. Choi, S. Sachdev, M. Greiner, V. Vuletić and M. D. Lukin, *Quantum phases of matter on a 256-atom programmable quantum simulator*, Nature **595**(7866), 227–232 (2021).

[190] D. Budker and M. Romalis, *Optical magnetometry*, Nature Physics **3**(4), 227–234 (2007).

[191] M. W. Doherty, N. B. Manson, P. Delaney, F. Jelezko, J. Wrachtrup and L. C. Hollenberg, *The nitrogen-vacancy colour centre in diamond*, Physics Reports **528**(1), 1–45 (2013).

[192] D. M. Toyli, D. J. Christle, A. Alkauskas, B. B. Buckley, C. G. Van de Walle and D. D. Awschalom, *Measurement and Control of Single Nitrogen-Vacancy Center Spins above 600 K*, Physical Review X **2**(3), 031001 (2012).

[193] F. Dolde, H. Fedder, M. W. Doherty, T. Nöbauer, F. Rempp, G. Balasubramanian, T. Wolf, F. Reinhard, L. C. L. Hollenberg, F. Jelezko and J. Wrachtrup, *Electric-field sensing using single diamond spins*, Nature Physics **7**(6), 459–463 (2011).

[194] J. M. Taylor, P. Cappellaro, L. Childress, L. Jiang, D. Budker, P. R. Hemmer, A. Yacoby, R. Walsworth and M. D. Lukin, *High-sensitivity diamond magnetometer with nanoscale resolution*, Nature Physics **4**(10), 810–816 (2008).

[195] V. M. Acosta, E. Bauch, M. P. Ledbetter, A. Waxman, L.-S. Bouchard and D. Budker, *Temperature Dependence of the Nitrogen-Vacancy Magnetic Resonance in Diamond*, Physical Review Letters **104**(7), 070801 (2010).

[196] M. W. Doherty, V. V. Struzhkin, D. A. Simpson, L. P. McGuinness, Y. Meng, A. Stacey, T. J. Karle, R. J. Hemley, N. B. Manson, L. C. Hollenberg and S. Prawer, *Electronic Properties and Metrology Applications of the Diamond NV - Center under Pressure*, Physical Review Letters **112**(4), 047601 (2014).

[197] M. W. Doherty, F. Dolde, H. Fedder, F. Jelezko, J. Wrachtrup, N. B. Manson and L. C. L. Hollenberg, *Theory of the ground-state spin of the NV^- center in diamond*, Physical Review B **85**(20), 205203 (2012).

[198] M. W. Doherty, J. Michl, F. Dolde, I. Jakobi, P. Neumann, N. B. Manson and J. Wrachtrup, *Measuring the defect structure orientation of a single NV^- centre in diamond*, New Journal of Physics **16**(6), 063067 (2014).

[199] M. Chipaux, A. Tallaire, J. Achard, S. Pezzagna, J. Meijer, V. Jacques, J.-F. Roch and T. Debuisschert, *Magnetic imaging with an ensemble of nitrogen-vacancy centers in diamond*, The European Physical Journal D **69**(7), 166 (2015).

[200] J.-P. Tetienne, L. Rondin, P. Spinicelli, M. Chipaux, T. Debuisschert, J.-F. Roch and V. Jacques, *Magnetic-field-dependent photodynamics of single NV defects in diamond: an application to qualitative all-optical magnetic imaging*, New Journal of Physics **14**(10), 103033 (2012).

[201] E. van Oort and M. Glasbeek, *Cross-relaxation dynamics of optically excited N-V centers in diamond*, Physical Review B **40**(10), 6509–6517 (1989).

[202] H.-J. Wang, C. S. Shin, S. J. Seltzer, C. E. Avalos, A. Pines and V. S. Bajaj, *Optically detected cross-relaxation spectroscopy of electron spins in diamond*, Nature Communications **5**(1), 4135 (2014).

[203] M. Mrózek, D. Rudnicki, P. Kehayias, A. Jarmola, D. Budker and W. Gawlik, *Longitudinal spin relaxation in nitrogen-vacancy ensembles in diamond*, EPJ Quantum Technology **2**(1), 22 (2015).

[204] R. Lazda, L. Busaite, A. Berzins, J. Smits, F. Gahbauer, M. Auzinsh, D. Budker and R. Ferber, *Cross-relaxation studies with optically detected magnetic resonances in nitrogen-vacancy centers in diamond in external magnetic field*, Physical Review B **103**(13), 134104 (2021).

[205] M. W. Doherty, V. M. Acosta, A. Jarmola, M. S. J. Barson, N. B. Manson, D. Budker and L. C. L. Hollenberg, *Temperature shifts of the resonances of the NV^- center in diamond*, Physical Review B **90**(4), 041201 (2014).

[206] F. J. Zeleznik, *Quasi- Newton Methods for Nonlinear Equations*, Journal of the ACM **15**(2), 265–271 (1968).

[207] C. G. BROYDEN, *The Convergence of a Class of Double-rank Minimization Algorithms 1. General Considerations*, IMA Journal of Applied Mathematics **6**(1), 76–90 (1970).

[208] R. Fletcher, *A new approach to variable metric algorithms*, The Computer Journal **13**(3), 317–322 (1970).

[209] D. Goldfarb, *A family of variable-metric methods derived by variational means*, Mathematics of Computation **24**(109), 23–26 (1970).

[210] D. F. Shanno, *Conditioning of quasi-Newton methods for function minimization*, Mathematics of Computation **24**(111), 647–656 (1970).

[211] J. C. Oersted, *"Experiments on the effect of a current of electricity on the magnetic needles*, *The Annals of Philosophy*, 273–276, London: Baldwin, Cradock, and Joy (1820).

[212] H. Kukkonen, J. Rovamo, K. Tiippana and R. Näsänen, *Michelson contrast, RMS contrast and energy of various spatial stimuli at threshold*, Vision Research **33**(10), 1431–1436 (1993).

[213] K. Levenberg, *A Method for the Solution of Certain Non-Linear Problems in Least Squares*, Quarterly of Applied Mathematics **2**(2), 164–168 (1944).

[214] D. W. Marquardt, *An Algorithm for Least-Squares Estimation of Nonlinear Parameters*, Journal of the Society for Industrial and Applied Mathematics **11**(2), 431–441 (1963).

[215] E. A. Lima and B. P. Weiss, *Obtaining vector magnetic field maps from single-component measurements of geological samples*, Journal of Geophysical Research **114**(B6), B06102 (2009).

[216] O. Dössel, *Inverse problem of electro-and magnetocardiography: Review and recent progress*, International Journal of Bioelectromagnetism **2**(2), 22 (2000).

[217] J. Nenonen, *Solving the inverse problem in magnetocardiography*, IEEE Engineering in Medicine and Biology Magazine **13**(4), 487–496 (1994).

[218] D. Broadway, S. Lillie, S. Scholten, D. Rohner, N. Dontschuk, P. Maletinsky, J.-P. Tetienne and L. Hollenberg, *Improved Current Density and Magnetization Reconstruction Through Vector Magnetic Field Measurements*, Physical Review Applied **14**(2), 024076 (2020).

[219] P. T. C. So, C. Y. Dong, B. R. Masters and K. M. Berland, *Two-Photon Excitation Fluorescence Microscopy*, Annual Review of Biomedical Engineering **2**(1), 399–429 (2000).

[220] F. Helmchen and W. Denk, *Deep tissue two-photon microscopy*, Nature Methods **2**(12), 932–940 (2005).

[221] E. A. Lima, A. Irimia and J. P. Wikswo, *The Magnetic Inverse Problem*, J. Clarke and A. I. Braginski, editors, *The SQUID Handbook*, volume 2, 139–267, Weinheim, Germany: Wiley-VCH Verlag GmbH & Co. KGaA (2006).

[222] C. Shannon, *Communication in the Presence of Noise*, Proceedings of the IRE **37**(1), 10–21 (1949).

[223] B. J. Roth, N. G. Sepulveda and J. P. Wikswo, *Using a magnetometer to image a two-dimensional current distribution*, Journal of Applied Physics **65**(1), 361–372 (1989).

[224] A. Y. Meltzer, E. Levin and E. Zeldov, *Direct Reconstruction of Two-Dimensional Currents in Thin Films from Magnetic-Field Measurements*, Physical Review Applied **8**(6), 064030 (2017).

[225] E. Karabal, P.-A. Duc, H. Kuntschner, P. Chanial, J.-C. Cuillandre and S. Gwyn, *A deconvolution technique to correct deep images of galaxies from instrumental scattered light*, Astronomy & Astrophysics **601**, A86 (2017).

[226] B. J. Roth, N. G. Sepulveda and J. P. Wikswo, *Using a magnetometer to image a two-dimensional current distribution*, Journal of Applied Physics **65**(1), 361–372 (1989).

[227] C. R. Goodall, *13 Computation using the QR decomposition*, *Handbook of Statistics*, volume 9 of *Computational Statistics*, 467–508, Elsevier (1993).

[228] A. Chambolle, *An Algorithm for Total Variation Minimization and Applications*, Journal of Mathematical Imaging and Vision **20**(1/2), 89–97 (2004).

[229] M. M. Waldrop, *The chips are down for Moore's law*, Nature News **530**(7589), 144 (2016).

[230] Q. Xu, B. Schmidt, S. Pradhan and M. Lipson, *Micrometre-scale silicon electro-optic modulator*, Nature **435**(7040), 325–327 (2005).

[231] H. Iwai and S. Ohmi, *Silicon integrated circuit technology from past to future*, Microelectronics Reliability **42**(4-5), 465–491 (2002).

[232] M. Riordan and L. Hoddeson, *Crystal Fire: The Invention, Development and Impact of the Transistor, Adapted from Chapter 1 of Crystal Fire: The Birth of the Information Age, by Michael Riordan and Lillian Hoddeson, published in 1997 by W. W. Norton & Company.*, IEEE Solid-State Circuits Newsletter **12**(2), 24–29 (2007).

[233] T. Berners-Lee, R. Cailliau, A. Luotonen, H. F. Nielsen and A. Secret, *The World-Wide Web*, Communications of the ACM **37**(8), 76–82 (1994).

[234] I. Skog and P. Handel, *In-Car Positioning and Navigation Technologies—A Survey*, IEEE Transactions on Intelligent Transportation Systems **10**(1), 4–21 (2009).

[235] N. Bhatia and M. El-Chami, *Leadless pacemakers: a contemporary review*, Journal of Geriatric Cardiology : JGC **15**(4), 249–253 (2018).

[236] G. E. Moore, *Cramming more components onto integrated circuits, Reprinted from Electronics, volume 38, number 8, April 19, 1965, pp.114 ff.*, IEEE Solid-State Circuits Society Newsletter **11**(3), 33–35 (2006).

[237] D. Mamaluy and X. Gao, *The fundamental downscaling limit of field effect transistors*, Applied Physics Letters **106**(19), 193503 (2015).

[238] P. Bhargava, T. Kim, C. V. Poulton, J. Notaros, A. Yaacobi, E. Timurdogan, C. Baiocco, N. Fahrenkopf, S. Kruger, T. Ngai, Y. Timalsina, M. R. Watts and V. Stojanovic, *Fully Integrated Coherent LiDAR in 3D-Integrated Silicon Photonics/65nm CMOS*, C262–C263, Kyoto, Japan: IEEE Symposium on VLSI Circuits (2019).

[239] J. Gambetta, *IBM Quantum State of the Union*, IBM Quantum Summit (2021), available online at `https://summit.quantum-computing.ibm.com`, last accessed on 12.10.2022.

[240] S. Salahuddin, K. Ni and S. Datta, *The era of hyper-scaling in electronics*, Nature Electronics **1**(8), 442–450 (2018).

[241] E. P. DeBenedictis, M. Badaroglu, A. Chen, T. M. Conte and P. Gargini, *Sustaining Moore's law with 3D chips*, Computer **50**(8), 69–73 (2017).

[242] A. Lancaster and M. Keswani, *Integrated circuit packaging review with an emphasis on 3D packaging*, Integration **60**, 204–212 (2018).

[243] M. J. Turner, N. Langellier, R. Bainbridge, D. Walters, S. Meesala, T. M. Babinec, P. Kehayias, A. Yacoby, E. Hu, M. Lončar, R. L. Walsworth and E. V. Levine, *Magnetic Field Fingerprinting of Integrated-Circuit Activity with a Quantum Diamond Microscope*, Physical Review Applied **14**(1), 014097 (2020).

[244] *Z1 archives: Der Rechner Z1 - Telekommunikation und Netzwerktechnik*, available online at `http://www.konrad-zuse.net/konrad-zuse/erfindungen/der-rechner-z1/seite01.html`, last accessed on 12.10.2022.

[245] J. Presper Eckert Jr. and J. W. Mauchly, *Electronic numerical integrator and computer* (U.S. Patent 3 120 606, Feb. 1964).

[246] T. Sale, *"General Report on Tunny", The Newmanry History, formatted by Tony Sale* (2001).

[247] *The Nobel Prize in Physics 2000*, `https://www.nobelprize.org/prizes/physics/2000/kilby/facts/`.

[248] J. Kilby, *Invention of the integrated circuit*, IEEE Transactions on Electron Devices **23**(7), 648–654 (1976).

[249] J. Kilby, *The integrated circuit's early history*, Proceedings of the IEEE **88**(1), 109–111 (2000).

[250] J. Kretz, *Lithography for Silicon Nanotechnology*, P. Siffert and E. F. Krimmel, editors, *Silicon: Evolution and Future of a Technology*, 399–414, Berlin, Heidelberg: Springer (2004).

[251] T. Ito and S. Okazaki, *Pushing the limits of lithography*, Nature **406**(6799), 1027–1031 (2000).

[252] C. M. Garner, *Lithography for enabling advances in integrated circuits and devices*, Philosophical Transactions of the Royal Society A: Mathematical, Physical and Engineering Sciences **370**(1973), 4015–4041 (2012).

[253] G. P. Lansbergen, *Transistors arrive at the atomic limit*, Nature Nanotechnology **7**(4), 209–210 (2012).

[254] M. Fuechsle, J. A. Miwa, S. Mahapatra, H. Ryu, S. Lee, O. Warschkow, L. C. L. Hollenberg, G. Klimeck and M. Y. Simmons, *A single-atom transistor*, Nature Nanotechnology **7**(4), 242–246 (2012).

[255] J. Shalf, *The future of computing beyond Moore's Law*, Philosophical Transactions of the Royal Society A: Mathematical, Physical and Engineering Sciences **378**(2166), 20190061 (2020).

[256] V. Coropceanu, J. Cornil, D. A. da Silva Filho, Y. Olivier, R. Silbey and J.-L. Brédas, *Charge Transport in Organic Semiconductors*, Chemical Reviews **107**(4), 926–952 (2007).

[257] F. Schwierz, *Graphene transistors*, Nature Nanotechnology **5**(7), 487–496 (2010).

[258] S. A. Wolf, D. D. Awschalom, R. A. Buhrman, J. M. Daughton, S. von Molnár, M. L. Roukes, A. Y. Chtchelkanova and D. M. Treger, *Spintronics: A Spin-Based Electronics Vision for the Future*, Science **294**(5546), 1488–1495 (2001).

[259] W. Kang, W. Zhao, Z. Wang, J.-O. Klein, Y. Zhang, D. Chabi, Y. Zhang, D. Ravelosona and C. Chappert, *An overview of spin-based integrated circuits*, *2014 19th Asia and South Pacific Design Automation Conference (ASP-DAC)*, 676–683 (2014), iSSN: 2153-697X.

[260] P. Gargini, F. Balestra and Y. Hayashi, *Roadmapping of Nanoelectronics for the New Electronics Industry*, Applied Sciences **12**(1), 308 (2022).

[261] A. W. Topol, D. C. L. Tulipe, L. Shi, D. J. Frank, K. Bernstein, S. E. Steen, A. Kumar, G. U. Singco, A. M. Young, K. W. Guarini and M. Ieong, *Three-dimensional integrated circuits*, IBM Journal of Research and Development **50**(4.5), 491–506 (2006).

[262] Y. Xie, J. Cong and S. Sapatnekar, editors, *Three Dimensional Integrated Circuit Design*, Integrated Circuits and Systems, Boston, MA: Springer US (2010).

[263] A. Elouardi, S. Bouaziz, A. Dupret, L. Lacassagne, J. Klein and R. Reynaud, *Image Processing: towards a System on Chip*, Y.-S. Chen, editor, *Image Processing*, chapter 23, Rijeka: IntechOpen (2009).

[264] O. Burkacky, M. Patel, N. Sergeant and C. Thomas, *Reimagining fabs: Advanced analytics in semiconductor manufacturing*, Copyright© 2017 McKinsey & Company. 7 (2017).

[265] R. Torrance and D. James, *The State-of-the-Art in IC Reverse Engineering*, C. Clavier and K. Gaj, editors, *Cryptographic Hardware and Embedded Systems - CHES 2009*, Lecture Notes in Computer Science, 363–381, Berlin, Heidelberg: Springer (2009).

[266] K. D. Vernon-Parry, *Scanning electron microscopy: an introduction*, III-Vs Review **13**(4), 40–44 (2000).

[267] O. Grosshardt, B. Á. Nagy and A. Laetsch, *Applying microscopic analytic techniques for failure analysis in electronic assemblies*, Applied Microscopy **49**(1), 7 (2019).

[268] *Fault Localization and Functional Testing of ICs by Lock-in Thermography*, volume ISTFA 2002: Conference Proceedings from the 28th International Symposium for Testing and Failure Analysis of *International Symposium for Testing and Failure Analysis* (2002).

[269] G.-Y. Zhuo, H.-C. Su, H.-Y. Wang and M.-C. Chan, *In situ high-resolution thermal microscopy on integrated circuits*, Optics Express **25**(18), 21548 (2017).

[270] L. A. Knauss, A. B. Cawthorne, N. Lettsome, S. Kelly, S. Chatraphorn, E. F. Fleet, F. C. Wellstood and W. E. Vanderlinde, *Scanning SQUID microscopy for current imaging*, Microelectronics Reliability **41**(8), 1211–1229 (2001).

[271] S. Kleindiek, K. Schock, A. Rummel, M. Zschomack, P. Limbecker, A. Meyer and M. Kemmler, *Combining current imaging, EBIC/EBAC, and electrical probing for fast and reliable in situ electrical fault isolation*, 231–234, Reutlingen: IEEE 23rd International Symposium on the Physical and Failure Analysis of Integrated Circuits (IPFA) (2016).

[272] M. Holler, M. Guizar-Sicairos, E. H. R. Tsai, R. Dinapoli, E. Müller, O. Bunk, J. Raabe and G. Aeppli, *High-resolution non-destructive three-dimensional imaging of integrated circuits*, Nature **543**(7645), 402–406 (2017).

[273] M. Holler, M. Odstrcil, M. Guizar-Sicairos, M. Lebugle, E. Müller, S. Finizio, G. Tinti, C. David, J. Zusman, W. Unglaub, O. Bunk, J. Raabe, A. F. J. Levi and G. Aeppli, *Three-dimensional imaging of integrated circuits with macro- to nanoscale zoom*, Nature Electronics **2**(10), 464–470 (2019).

[274] *A Novel Approach to Identifying and Validating Electrical Leakage in Printed Circuit Boards Through Magnetic Current Imaging*, volume ISTFA 2004: Conference Proceedings from the 30th International Symposium for Testing and Failure Analysis of *International Symposium for Testing and Failure Analysis* (2004).

[275] S. K. Saha, *Compact Models for Integrated Circuit Design: Conventional Transistors and Beyond*, CRC Press, 1st edition (2018).

[276] H. Wang, D. Forte, M. M. Tehranipoor and Q. Shi, *Probing Attacks on Integrated Circuits: Challenges and Research Opportunities*, IEEE Design & Test **34**(5), 63–71 (2017).

[277] L. E. Fong, J. R. Holzer, K. K. McBride, E. A. Lima, F. Baudenbacher and M. Radparvar, *High-resolution room-temperature sample scanning superconducting quantum interference device microscope configurable for geological and biomagnetic applications*, Review of Scientific Instruments **76**(5), 053703 (2005).

[278] B. D. Schrag and G. Xiao, *Submicron electrical current density imaging of embedded microstructures*, Applied Physics Letters **82**(19), 3272–3274 (2003).

[279] A. Herrera-May, L. Aguilera-Cortés, P. García-Ramírez and E. Manjarrez, *Resonant Magnetic Field Sensors Based On MEMS Technology*, Sensors **9**(10), 7785–7813 (2009).

[280] J. Böck, K. Aufinger, S. Boguth, C. Dahl, H. Knapp, W. Liebl, D. Manger, T. F. Meister, A. Pribil, J. Wursthorn, R. Lachner, B. Heinemann, H. Rücker, A. Fox, R. Barth, G. Fischer, S. Marschmeyer, D. Schmidt, A. Trusch and C. Wipf, *SiGe HBT and BiCMOS process integration optimization within the DOTSEVEN project*, *2015 IEEE Bipolar/BiCMOS Circuits and Technology Meeting - BCTM*, 121–124 (2015).

[281] J. D. Plummer, M. D. Deal and P. B. Griffin, *Silicon VLSI technology : fundamentals, practice, and modeling*, Upper Saddle River, NJ : Prentice Hall (2000).

[282] Y. Schlussel, T. Lenz, D. Rohner, Y. Bar-Haim, L. Bougas, D. Groswasser, M. Kieschnick, E. Rozenberg, L. Thiel, A. Waxman, J. Meijer, P. Maletinsky, D. Budker and R. Folman, *Wide-Field Imaging of Superconductor Vortices with Electron Spins in Diamond*, Physical Review Applied **10**(3), 034032 (2018).

[283] D. Pierce and P. Brusius, *Electromigration: A review*, Microelectronics Reliability **37**(7), 1053–1072 (1997).

[284] N. Singh, A. F. Bower and S. Shankar, *A three-dimensional model of electromigration and stress induced void nucleation in interconnect structures*, Modelling and Simulation in Materials Science and Engineering **18**(6), 065006 (2010).

[285] H. Ceric and S. Selberherr, *Electromigration in submicron interconnect features of integrated circuits*, Materials Science and Engineering: R: Reports **71**(5-6), 53–86 (2011).

[286] C. M. Bishop, *Pattern Recognition and Machine Learning*, *Pattern Recognition and Machine Learning*, Springer New York (2006).

[287] C. M. Sparrow, *On Spectroscopic Resolving Power*, The Astrophysical Journal **44**, 76 (1916).

[288] T. Yu, H. Liu and W. Cai, *On the quantification of spatial resolution for three-dimensional computed tomography of chemiluminescence*, Optics Express **25**(20), 24093 (2017).

[289] L. Toraille, A. Hilberer, T. Plisson, M. Lesik, M. Chipaux, B. Vindolet, C. Pépin, F. Occelli, M. Schmidt, T. Debuisschert, N. Guignot, J.-P. Itié, P. Loubeyre and J.-F. Roch, *Combined synchrotron x-ray diffraction and NV diamond magnetic microscopy measurements at high pressure*, New Journal of Physics **22**(10), 103063 (2020).

[290] A. M. Edmonds, C. A. Hart, M. J. Turner, P.-O. Colard, J. M. Schloss, K. S. Olsson, R. Trubko, M. L. Markham, A. Rathmill, B. Horne-Smith, W. Lew, A. Manickam, S. Bruce, P. G. Kaup, J. C. Russo, M. J. DiMario, J. T. South, J. T. Hansen, D. J. Twitchen and R. L. Walsworth, *Characterisation of CVD diamond with high concentrations of nitrogen for magnetic-field sensing applications*, Materials for Quantum Technology **1**(2), 025001 (2021).

[291] J.-P. Tetienne, R. W. de Gille, D. A. Broadway, T. Teraji, S. E. Lillie, J. M. McCoey, N. Dontschuk, L. T. Hall, A. Stacey, D. A. Simpson and L. C. L. Hollenberg, *Spin properties of dense near-surface ensembles of nitrogen-vacancy centers in diamond*, Physical Review B **97**(8), 085402 (2018).

[292] J. M. Schloss, J. F. Barry, M. J. Turner and R. L. Walsworth, *Simultaneous Broadband Vector Magnetometry Using Solid-State Spins*, Physical Review Applied **10**(3), 034044 (2018).

[293] J. Zopes, K. Sasaki, K. S. Cujia, J. M. Boss, K. Chang, T. F. Segawa, K. M. Itoh and C. L. Degen, *High-Resolution Quantum Sensing with Shaped Control Pulses*, Physical Review Letters **119**(26), 260501 (2017).

[294] J. Zopes and C. Degen, *Reconstruction-Free Quantum Sensing of Arbitrary Waveforms*, Physical Review Applied **12**(5), 054028 (2019).

[295] K. Mizuno, H. Ishiwata, Y. Masuyama, T. Iwasaki and M. Hatano, *Simultaneous wide-field imaging of phase and magnitude of AC magnetic signal using diamond quantum magnetometry*, Scientific Reports **10**(1), 11611 (2020).

[296] R. Baghban, L. Roshangar, R. Jahanban-Esfahlan, K. Seidi, A. Ebrahimi-Kalan, M. Jaymand, S. Kolahian, T. Javaheri and P. Zare, *Tumor microenvironment complexity and therapeutic implications at a glance*, Cell Communication and Signaling **18**(1), 1–19 (2020).

[297] A. Kuwahata, T. Kitaizumi, K. Saichi, T. Sato, R. Igarashi, T. Ohshima, Y. Masuyama, T. Iwasaki, M. Hatano, F. Jelezko, M. Kusakabe, T. Yatsui and M. Sekino, *Magnetometer with nitrogen-vacancy center in a bulk diamond for detecting magnetic nanoparticles in biomedical applications*, Scientific Reports **10**, 2483 (2020).

[298] J. L. Webb, L. Troise, N. W. Hansen, J. Achard, O. Brinza, R. Staacke, M. Kieschnick, J. Meijer, J.-F. Perrier, K. Berg-Sørensen, A. Huck and U. L. Andersen, *Optimization of a Diamond Nitrogen Vacancy Centre Magnetometer for Sensing of Biological Signals*, Frontiers in Physics **8** (2020).

[299] T. Zhang, G. Pramanik, K. Zhang, M. Gulka, L. Wang, J. Jing, F. Xu, Z. Li, Q. Wei, P. Cigler and Z. Chu, *Toward Quantitative Bio-sensing with Nitrogen–Vacancy Center in Diamond*, ACS Sensors **6**(6), 2077–2107 (2021).

[300] A. Mzyk, Y. Ong, A. R. Ortiz Moreno, S. K. Padamati, Y. Zhang, C. A. Reyes-San-Martin and R. Schirhagl, *Diamond Color Centers in Diamonds for Chemical and Biochemical Analysis and Visualization*, Analytical Chemistry **94**(1), 225–249 (2022).

[301] L. Nie, A. C. Nusantara, V. G. Damle, M. V. Baranov, M. Chipaux, C. Reyes-San-Martin, T. Hamoh, C. P. Epperla, M. Guricova, P. Cigler, G. van den Bogaart and R. Schirhagl, *Quantum Sensing of Free Radicals in Primary Human Dendritic Cells*, Nano Letters **22**(4), 1818–1825 (2022).

[302] D. R. Glenn, K. Lee, H. Park, R. Weissleder, A. Yacoby, M. D. Lukin, H. Lee, R. L. Walsworth and C. B. Connolly, *Single-cell magnetic imaging using a quantum diamond microscope*, Nature Methods **12**(8), 736–738 (2015).

[303] J. F. Barry, M. J. Turner, J. M. Schloss, D. R. Glenn, Y. Song, M. D. Lukin, H. Park and R. L. Walsworth, *Optical magnetic detection of single-neuron action potentials using quantum defects in diamond*, Proceedings of the National Academy of Sciences **113**(49), 14133–14138 (2016).

[304] T. Fujisaku, R. Tanabe, S. Onoda, R. Kubota, T. F. Segawa, F. T.-K. So, T. Ohshima, I. Hamachi, M. Shirakawa and R. Igarashi, *pH Nanosensor Using Electronic Spins in Diamond*, ACS Nano **13**(10), 11726–11732 (2019).

[305] M. R. James Neitzel, *Cell Communication | Learn Science at Scitable*, available online at `https://www.nature.com/scitable/topic/cell-communication-14122659/`, last accessed on 12.10.2022.

[306] B. L. Bassler, *Small talk: cell-to-cell communication in bacteria*, Cell **109**(4), 421–424 (2002).

[307] E. C. Lai, *Notch signaling: control of cell communication and cell fate*, Development **131**(5), 965–973 (2004).

[308] C. M. Waters, B. L. Bassler *et al.*, *Quorum sensing: cell-to-cell communication in bacteria*, Annual review of cell and developmental biology **21**(1), 319–346 (2005).

[309] S.-H. Kim, J. Turnbull and S. Guimond, *Extracellular matrix and cell signalling: the dynamic cooperation of integrin, proteoglycan and growth factor receptor*, The Journal of endocrinology **209**(2), 139—151 (2011).

[310] C. Brownlee, *Role of the extracellular matrix in cell–cell signalling: paracrine paradigms*, Current Opinion in Plant Biology **5**(5), 396–401 (2002).

[311] C. Frantz, K. M. Stewart and V. M. Weaver, *The extracellular matrix at a glance*, Journal of Cell Science **123**(24), 4195–4200 (2010).

[312] T. M. Koch, S. Münster, N. Bonakdar, J. P. Butler and B. Fabry, *3D Traction Forces in Cancer Cell Invasion*, PLoS ONE **7**(3), e33476 (2012).

[313] W. J. Polacheck and C. S. Chen, *Measuring cell-generated forces: a guide to the available tools*, Nature Methods **13**(5), 415–423 (2016).

[314] Y. Zhang, C. Ge, C. Zhu and K. Salaita, *DNA-based digital tension probes reveal integrin forces during early cell adhesion*, Nature Communications **5**(1), 5167 (2014).

[315] V. P.-Y. Ma and K. Salaita, *DNA Nanotechnology as an Emerging Tool to Study Mechanotransduction in Living Systems*, Small **15**(26), 1900961 (2019).

[316] C. J. Murphy, A. M. Gole, J. W. Stone, P. N. Sisco, A. M. Alkilany, E. C. Goldsmith and S. C. Baxter, *Gold Nanoparticles in Biology: Beyond Toxicity to Cellular Imaging*, Accounts of Chemical Research **41**(12), 1721–1730 (2008).

[317] A. Sani, C. Cao and D. Cui, *Toxicity of gold nanoparticles (AuNPs): A review*, Biochemistry and Biophysics Reports **26**, 100991 (2021).

[318] F. Grinnell, *Fibroblast biology in three-dimensional collagen matrices*, Trends in Cell Biology **13**(5), 264–269 (2003).

[319] G. M. Cooper, R. E. Hausman and R. E. Hausman, *The cell: a molecular approach*, volume 4, ASM press Washington, DC (2007).

[320] W. Stein, *The Movement Of Molecules Across Cell Membranes*, Academic Press, Elsevier (1967).

[321] T. Y. Tsong, *Electroporation of Cell Membranes*, E. Neumann, A. E. Sowers and C. A. Jordan, editors, *Electroporation and Electrofusion in Cell Biology*, 149–163, Boston, MA: Springer US (1989).

[322] H. T. McMahon and J. L. Gallop, *Membrane curvature and mechanisms of dynamic cell membrane remodelling*, Nature **438**(7068), 590–596 (2005).

[323] J. Garthwaite, *Glutamate, nitric oxide and cell-cell signalling in the nervous system*, Trends in Neurosciences **14**(2), 60–67 (1991).

[324] B. Geiger, A. Bershadsky, R. Pankov and K. M. Yamada, *Transmembrane crosstalk between the extracellular matrix and the cytoskeleton*, Nature Reviews Molecular Cell Biology **2**(11), 793–805 (2001).

[325] A. F. Williams and A. N. Barclay, *The Immunoglobulin Superfamily—Domains for Cell Surface Recognition*, Annual Review of Immunology **6**(1), 381–405 (1988).

[326] C. S. Chen, J. Tan and J. Tien, *Mechanotransduction at Cell-Matrix and Cell-Cell Contacts*, Annual Review of Biomedical Engineering **6**(1), 275–302 (2004).

[327] L. You, R. S. Cox, R. Weiss and F. H. Arnold, *Programmed population control by cell–cell communication and regulated killing*, Nature **428**(6985), 868–871 (2004).

[328] L. He, G. Yang and X. Geng, *Enzymatic activity and chromatographic characteristics of the cell membrane immobilized on silica surface*, Chinese Science Bulletin **44**(9), 826–831 (1999).

[329] W. D. Stein, *Transport and Diffusion Across Cell Membranes*, Academic Press (1986).

[330] K. Burridge, K. Fath, T. Kelly, G. Nuckolls and C. Turner, *Focal Adhesions: Transmembrane Junctions Between the Extracellular Matrix and the Cytoskeleton*, Annual Review of Cell Biology **4**(1), 487–525 (1988).

[331] R. Mecham, *The Extracellular Matrix: an Overview*, Biology of Extracellular Matrix, Springer Berlin Heidelberg (2011).

[332] A. Morgan, *Exocytosis*, Essays in Biochemistry **30**, 77–95 (1995).

[333] J. D. Humphrey, E. R. Dufresne and M. A. Schwartz, *Mechanotransduction and extracellular matrix homeostasis*, Nature reviews Molecular cell biology **15**(12), 802–812 (2014).

[334] J. F. Hastings, J. N. Skhinas, D. Fey, D. R. Croucher and T. R. Cox, *The extracellular matrix as a key regulator of intracellular signalling networks*, British journal of pharmacology **176**(1), 82–92 (2019).

[335] I. A. Darby, B. Laverdet, F. Bonté and A. Desmoulière, *Fibroblasts and myofibroblasts in wound healing*, Clinical, cosmetic and investigational dermatology **7**, 301 (2014).

[336] K. Y. DeLeon-Pennell, T. H. Barker and M. L. Lindsey, *Fibroblasts: The arbiters of extracellular matrix remodeling*, Matrix Biology **91-92**, 1–7 (2020).

[337] H. N. Wilkinson and M. J. Hardman, *Wound healing: cellular mechanisms and pathological outcomes*, Open Biology **10**(9), 200223 (2020).

[338] B. P., *Wound healing and the role of fibroblasts*, Journal of Wound Care **22**(8), 407–412 (2013).

[339] J. K. Mouw, G. Ou and V. M. Weaver, *Extracellular matrix assembly: a multiscale deconstruction*, Nature reviews Molecular cell biology **15**(12), 771–785 (2014).

[340] M. Xue and C. J. Jackson, *Extracellular matrix reorganization during wound healing and its impact on abnormal scarring*, Advances in wound care **4**(3), 119–136 (2015).

[341] N. Turner and R. Grose, *Fibroblast growth factor signalling: from development to cancer*, Nature Reviews Cancer **10**(2), 116–129 (2010).

[342] A. G. Clark and D. M. Vignjevic, *Modes of cancer cell invasion and the role of the microenvironment*, Current Opinion in Cell Biology **36**, 13–22 (2015).

[343] M. J. Paszek, N. Zahir, K. R. Johnson, J. N. Lakins, G. I. Rozenberg, A. Gefen, C. A. Reinhart-King, S. S. Margulies, M. Dembo, D. Boettiger, D. A. Hammer and V. M. Weaver, *Tensional homeostasis and the malignant phenotype*, Cancer Cell **8**(3), 241–254 (2005).

[344] M. R. Ng and J. S. Brugge, *A Stiff Blow from the Stroma: Collagen Crosslinking Drives Tumor Progression*, Cancer Cell **16**(6), 455–457 (2009).

[345] P. Friedl and S. Alexander, *Cancer invasion and the microenvironment: plasticity and reciprocity*, Cell **147**(5), 992–1009 (2011).

[346] D. Bray, *Cell Movements: From Molecules to Motility*, New York: Garland Science, 2nd edition (2000).

[347] R. O. Hynes, *Integrins: Versatility, modulation, and signaling in cell adhesion*, Cell **69**(1), 11 – 25 (1992).

[348] A. Becchetti and A. Arcangeli, *Integrins and Ion Channels in Cell Migration: Implications for Neuronal Development, Wound Healing and Metastatic Spread*, A. Becchetti and A. Arcangeli, editors, *Integrins and Ion Channels: Molecular Complexes and Signaling*, Advances in Experimental Medicine and Biology, 107–123, New York, NY: Springer (2010).

[349] C. K. Miranti and J. S. Brugge, *Sensing the environment: A historical perspective on integrin signal transduction*, Nature Cell Biology **4**(4), E83–E90 (2002).

[350] W. L. Hubbell, H. S. Mchaourab, C. Altenbach and M. A. Lietzow, *Watching proteins move using site-directed spin labeling*, Structure **4**(7), 779–783 (1996).

[351] J. P. Klare and H.-J. Steinhoff, *Spin labeling EPR*, Photosynthesis research **102**(2), 377–390 (2009).

[352] A. Feintuch, G. Otting and D. Goldfarb, *Gd^{3+} spin labeling for measuring distances in biomacromolecules: why and how?*, *Methods in Enzymology*, volume 563, 415–457, Elsevier (2015).

[353] M. Kaushik, T. Bahrenberg, T. V. Can, M. A. Caporini, R. Silvers, J. Heiliger, A. A. Smith, H. Schwalbe, R. G. Griffin and B. Corzilius, *Gd (III) and Mn (II) complexes for dynamic nuclear polarization: small molecular chelate polarizing agents and applications with site-directed spin labeling of proteins*, Physical Chemistry Chemical Physics **18**(39), 27205–27218 (2016).

[354] P. M. Parizel, H. R. Degryse, J. Gheuens, J. J. Martin, M. Van Vyve, C. De La Porte, P. Selosse, P. Van de Heyning and A. M. De Schepper, *Gadolinium-DOTA enhanced MR imaging of intracranial lesions*, Journal of Computer Assisted Tomography **13**(3), 378–385 (1989).

[355] R. B. Rehr, R. M. Peshock, C. R. Malloy, A. M. Keller, R. W. Parkey, L. M. Buja, R. L. Nunnally and J. T. Willerson, *Improved in vivo magnetic resonance imaging of acute myocardial infarction after intravenous paramagnetic contrast agent administration*, The American Journal of Cardiology **57**(10), 864–868 (1986).

[356] N. C. Silver, C. D. Good, G. J. Barker, D. G. MacManus, A. J. Thompson, I. F. Moseley, W. I. McDonald and D. H. Miller, *Sensitivity of contrast enhanced MRI in multiple sclerosis. Effects of gadolinium dose, magnetization transfer contrast and delayed imaging.*, Brain **120**(7), 1149–1161 (1997).

[357] P. Caravan, J. J. Ellison, T. J. McMurry and R. B. Lauffer, *Gadolinium(III) Chelates as MRI Contrast Agents: Structure, Dynamics, and Applications*, Chemical Reviews **99**(9), 2293–2352 (1999).

[358] E. Ruoslahti, *RGD and other recognition sequences for integrins*, Annual Review of Cell and Developmental Biology **12**, 697–715 (1996).

[359] C. Bustamante, J. F. Marko, E. D. Siggia and S. Smith, *Entropic Elasticity of λ-Phage DNA*, Science **265**(5178), 1599–1600 (1994).

[360] C. Bouchiat, M. Wang, J.-F. Allemand, T. Strick, S. Block and V. Croquette, *Estimating the Persistence Length of a Worm-Like Chain Molecule from Force-Extension Measurements*, Biophysical Journal **76**(1), 409–413 (1999).

[361] N. Backmann, N. Kappeler, T. Braun, F. Huber, H.-P. Lang, C. Gerber and R. Y. H. Lim, *Sensing surface PEGylation with microcantilevers*, Beilstein Journal of Nanotechnology **1**(1), 3–13 (2010).

[362] S. Douthwright and G. Sluder, *Live Cell Imaging: Assessing the Phototoxicity of 488 and 546 nm Light and Methods to Alleviate it*, Journal of Cellular Physiology **232**(9), 2461–2468 (2017).

[363] E. A. Cavalcanti-Adam, T. Volberg, A. Micoulet, H. Kessler, B. Geiger and J. P. Spatz, *Cell Spreading and Focal Adhesion Dynamics Are Regulated by Spacing of Integrin Ligands*, Biophysical Journal **92**(8), 2964–2974 (2007).

[364] J. L. McGrath, *Cell Spreading: The Power to Simplify*, Current Biology **17**(10), R357–R358 (2007).

[365] Y. Liu, R. Medda, Z. Liu, K. Galior, K. Yehl, J. P. Spatz, E. A. Cavalcanti-Adam and K. Salaita, *Nanoparticle Tension Probes Patterned at the Nanoscale: Impact of Integrin Clustering on Force Transmission*, Nano Letters **14**(10), 5539–5546 (2014).

[366] L. Valon and R. Levayer, *Dying under pressure: cellular characterisation and in vivo functions of cell death induced by compaction*, Biology of the Cell **111**(3), 51–66 (2019).

[367] S. Huth, J. W. Blumberg, D. Probst, J. Lammerding, U. S. Schwarz and C. Selhuber-Unkel, *Quantifying force transmission through fibroblasts: changes of traction forces under external shearing*, European Biophysics Journal **51**(2), 157–169 (2022).

[368] S. Fulda, A. M. Gorman, O. Hori and A. Samali, *Cellular Stress Responses: Cell Survival and Cell Death*, International Journal of Cell Biology **2010**, e214074 (2010).

[369] Q. Wei, J. Young, A. Holle, J. Li, K. Bieback, G. Inman, J. P. Spatz and E. A. Cavalcanti-Adam, *Soft Hydrogels for Balancing Cell Proliferation and Differentiation*, ACS Biomaterials Science & Engineering **6**(8), 4687–4701 (2020).

[370] K. E. Lee and M. C. Simon, *SnapShot: Hypoxia-Inducible Factors*, Cell **163**(5), 1288–1288.e1 (2015).

[371] G. L. Semenza, *Life with Oxygen*, Science **318**(5847), 62–64 (2007).

[372] D. Breitburg, L. A. Levin, A. Oschlies, M. Grégoire, F. P. Chavez, D. J. Conley, V. Garçon, D. Gilbert, D. Gutiérrez, K. Isensee, G. S. Jacinto, K. E. Limburg, I. Montes, S. W. A. Naqvi, G. C. Pitcher, N. N. Rabalais, M. R. Roman, K. A. Rose, B. A. Seibel, M. Telszewski, M. Yasuhara and J. Zhang, *Declining oxygen in the global ocean and coastal waters*, Science **359**(6371), eaam7240 (2018).

[373] D. Laffoley and J. Baxter, editors, *Ocean deoxygenation: everyone's problem. Causes, impacts, consequences and solutions*, IUCN, International Union for Conservation of Nature (2019).

[374] J. Arístegui, *Active mesopelagic prokaryotes support high respiration in the subtropical northeast Atlantic Ocean*, Geophysical Research Letters **32**(3), L03608 (2005).

[375] Y. Wei, Y. Jiao, D. An, D. Li, W. Li and Q. Wei, *Review of Dissolved Oxygen Detection Technology: From Laboratory Analysis to Online Intelligent Detection*, Sensors **19**(18), 3995 (2019).

[376] M. Laing, *The three forms of molecular oxygen*, Journal of Chemical Education **66**(6), 453 (1989).

[377] K. H. Rashid and A. A. Khadom, *Sodium sulfite as an oxygen scavenger for the corrosion control of mild steel in petroleum refinery wastewater: optimization, mathematical modeling, surface morphology and reaction kinetics studies*, Reaction Kinetics, Mechanisms and Catalysis **129**(2), 1027–1046 (2020).

[378] W. health organization, *International programme on chemical safety - 932. Preservative: Sulfur dioxide and sulfites (WHO Food Additives Series 42)* (1999), available online at `https://inchem.org/documents/jecfa/jecmono/v042je06.htm`, last accessed on 28.09.2022.

[379] R. D. Srivastava, A. F. Mcmillan and I. J. Harris, *The kinetics of oxidation of sodium sulphite*, The Canadian Journal of Chemical Engineering **46**(3), 181–184 (1968).

[380] G. C. Whipple and M. C. Whipple, *Solubility of Oxygen in sea water.*, Journal of the American Chemical Society **33**(3), 362–365 (1911).

[381] *Oxygen - Solubility in Fresh and Sea Water vs. Temperature*, available online at `https://www.engineeringtoolbox.com/oxygen-solubility-water-d_841.html`, last accessed on 26.10.2022.

[382] J. Friend and L. Yeo, *Fabrication of microfluidic devices using polydimethylsiloxane*, Biomicrofluidics **4**(2), 026502 (2010).

[383] J. C. McDonald, D. C. Duffy, J. R. Anderson, D. T. Chiu, H. Wu, O. J. Schueller and G. M. Whitesides, *Fabrication of microfluidic systems in poly (dimethylsiloxane)*, Electrophoresis: An International Journal **21**(1), 27–40 (2000).

[384] R. D. Allert, F. Bruckmaier, N. R. Neuling, F. A. Freire-Moschovitis, K. S. Liu, C. Schrepel, P. Schätzle, P. Knittel, M. Hermans and D. B. Bucher, *Microfluidic quantum sensing platform for lab-on-a-chip applications*, preprint, Chemistry (2022).

[385] R. Mathur-De Vré, *The NMR studies of water in biological systems*, Progress in Biophysics and Molecular Biology **35**, 103–134 (1980).

[386] K. Livo, M. Prasad and T. R. Graham, *Quantification of dissolved O2 in bulk aqueous solutions and porous media using NMR relaxometry*, Scientific Reports **11**(1), 290 (2021).

[387] I. D. Wolf, *3-D Technology: Failure Analysis Challenges*, Electronic Device Failure Analysis **18**(4), 6 (2016).

[388] A. L. Falk, F. H. L. Koppens, C. L. Yu, K. Kang, N. de Leon Snapp, A. V. Akimov, M.-H. Jo, M. D. Lukin and H. Park, *Near-field electrical detection of optical plasmons and single-plasmon sources*, Nature Physics **5**(7), 475–479 (2009).

[389] B. Weber, S. Mahapatra, H. Ryu, S. Lee, A. Fuhrer, T. C. G. Reusch, D. L. Thompson, W. C. T. Lee, G. Klimeck, L. C. L. Hollenberg and M. Y. Simmons, *Ohm's Law Survives to the Atomic Scale*, Science **335**(6064), 64–67 (2012).

[390] M. Lundstrom, *Applied Physics: Enhanced: Moore's Law Forever?*, Science **299**(5604), 210–211 (2003).

[391] H. H. Eroğlu, O. Puonti, C. Göksu, F. Gregersen, H. R. Siebner, L. G. Hanson and A. Thielscher, *On the reconstruction of magnetic resonance current density images of the human brain: Pitfalls and perspectives*, NeuroImage **243**, 118517 (2021).

[392] B.-J. Yang, E.-G. Moon, H. Isobe and N. Nagaosa, *Quantum criticality of topological phase transitions in three-dimensional interacting electronic systems*, Nature Physics **10**(10), 774–778 (2014).

[393] C. Wang, A. C. Potter and T. Senthil, *Classification of Interacting Electronic Topological Insulators in Three Dimensions*, Science **343**(6171), 629–631 (2014).

[394] L. Esaki, P. J. Stiles and S. v. Molnar, *Magnetointernal Field Emission in Junctions of Magnetic Insulators*, Physical Review Letters **19**(15), 852–854 (1967).

[395] H. J. M. Swagten and P. V. Paluskar, *Magnetic Tunnel Junctions*, K. H. J. Buschow, R. W. Cahn, M. C. Flemings, B. Ilschner, E. J. Kramer, S. Mahajan and P. Veyssière, editors, *Encyclopedia of Materials: Science and Technology*, 1–7, Oxford: Elsevier (2010).

[396] T. P. M. Alegre, C. Santori, G. Medeiros-Ribeiro and R. G. Beausoleil, *Polarization-selective excitation of nitrogen vacancy centers in diamond*, Physical Review B **76**(16), 165205 (2007).

[397] K. J. Brown, E. Chartier, E. M. Sweet, D. A. Hopper and L. C. Bassett, *Cleaning diamond surfaces using boiling acid treatment in a standard laboratory chemical hood*, Journal of Chemical Health and Safety **26**(6), 40–44 (2019).

[398] K.-M. C. Fu, C. Santori, P. E. Barclay and R. G. Beausoleil, *Conversion of neutral nitrogen-vacancy centers to negatively charged nitrogen-vacancy centers through selective oxidation*, Applied Physics Letters **96**(12), 121907 (2010).

[399] S. D. Subedi, V. V. Fedorov, J. Peppers, D. V. Martyshkin, S. B. Mirov, L. Shao and M. Loncar, *Laser spectroscopic characterization of negatively charged nitrogen-vacancy (NV^-) centers in diamond*, Optical Materials Express **9**(5), 2076 (2019).

[400] G. H. Golub and C. F. Van Loan, *Matrix Computations*, JHU Press (1996).

Acknowledgements

Persistence. That's probably what it takes to reach the moment I can finally write these few lines. I met and exchanged with many people along the way of this thesis, which certainly shaped it into its final form. For this, I would like to thank everyone who contributed directly or indirectly to this thesis.

First, I would like to thank Prof. Dr. Jörg Wrachtrup for welcoming me to the 3rd Institute of Physics of Stuttgart. I still remember our first interview where you warned me about the *ungentle* weather of Stuttgart compared to Nice. I still didn't acclimate, but at least I've learned to drink *Sprüdel* to appreciate life in Germany ;). Also, thank you for giving me the freedom to choose my own path and the collaborative opportunities you offered me; they certainly enriched my thesis. Although the route was full of challenges, I learned a lot and now feel able to overcome any upcoming obstacles; I believe that's my biggest takeaway! Finally, Jörg, if you ever happen to read these lines, I invite you for a Tunisian meal or a French cake as a token of my gratitude ;).

For making this thesis happen, I am greatly thankful to Prof. Dr. Stefanie Barz, who took the time to be my second examiner despite her very tight schedule. Along the same line, I am also thankful to Prof. Dr. Christian Holm for chairing my defence.

This thesis wouldn't be the same without all the fruitful collaborations. I am grateful to Dr. Nils Trautmann and Dr. Ulrich Vogl (Carl Zeiss AG) for initiating the IC activity imaging (chapter 5) and their implication throughout the project. This project certainly gave me a liking to working at the edge between the academic world and industry applications, and I hope to continue with such direction in the future. Also, I want to thank everyone from Infineon Technologies AG related to this project, with special thanks to Dr. Herbert Knapp and Dr. Badou Sene, for our exchanges and for providing the chip.

I am grateful to Prof. Dr. Joachim Spatz (Max Planck Institute for Medical Research, University of Heidelberg) and his team for collaborating on the cell

mechano-communication project (chapter 6). It was the first project I worked on in the timeline of my thesis, and it was a fascinating interdisciplinary area to explore.

Although I did not mention my work on nanodiamonds since it was a short phase during my thesis, I would like to thank Dr. Petr Cígler (Institute of Organic Chemistry and Biochemistry, Czech Academy of Sciences) and his team for the interesting collaboration.

Next, I would like to thank the European Commission through the QuSCo project for providing a nurturing network, training and part of the funding that enabled this work. During this project, I had the chance to experience a secondment at the Technische Universität München (TUM). For this, I would like to thank Prof. Dr. Steffen Glaser and his student Amit Devra for welcoming Alastair Marshall and me during this scientific exchange. We certainly learned a lot about quantum optimal control, and it was both a rich and enjoyable experience!

Now comes the time I would like to thank former and present colleagues for their help throughout my thesis, and I hope I won't miss anyone.

Dr. Florestan Ziem, thank you so much for introducing me to the widefield ~~cult~~ legacy and handing it over to me! I remember the day I presented myself during the group meeting, I asked everyone performing sensing to show me their work, and you were by far the most enthusiastic! Was it a pitfall or good luck? I'll keep some mystery around this answer ;). I can say for sure that your enthusiasm undoubtedly affected my final choice, and I don't regret it. Most importantly, I am genuinely thankful for the time you spared for me while you were finishing your own thesis; now I know how precious that time is!

Although we only met once, I thank Dr. Steffen Steinert for starting the widefield legacy in Stuttgart and writing a fantastic thesis. It guided me throughout the years, and now it's with some nostalgia that I will place it back in the library (but I hope to get a copy with your autograph one day!).

Among those who supported me the most, I greatly thank Dr. Rainer Stöhr. You backed me with all my "creative" ideas, whether it was for designing an

eagle (proposing even more ingenious designs I won't speak out here ;)) or to scratch a functioning IC chip (sorry Badou, you probably worked hard to make them work), you were never afraid to try things out. Over the past years, you always offered assistance, discussed with me and helped me put my thoughts in perspective. Finally, for translating my summary into the "Zusammenfassung", many thanks again!

Many thanks also go to Dr. Andrea Zappe for all the warmth, care and assistance with all the biological and chemistry work. It's a chance to have an expert in biology like you in our institute, so thank you a lot for sharing your expertise!

Next, many thanks go to Lena Kühnast. I loved the experience of sharing my expertise with you during your bachelor thesis, and you also brought enthusiasm and fresh energy into the lab, making it a really beneficial experience. I wish you all the best for your future in teaching!

Dr. Andrej Denisenko, for being my diamond provider, sharing your expertise with me and making me discover diamonds before they even appear on the market, thank you a lot!

Dr. Farida Shagieva, thank you for the time spent together, and the discovery of lovely tea smells in our office!

Dr. Rolf Reuter, thank you for your insights and "intransigence" about chemistry; I certainly learned a lot from you!

How would this thesis have been without you, Tanya Shalomayeva? Thank you for the support and all the discussions and lunches we had together; we had many creative topics, and I will undoubtedly miss the lunches with you a lot.

For all the pleasant times together, many thanks go to my QuSColleagues, with particular thoughts to Alastair Marshall. I found a true friend in you. Thank you for the support and all the exchanges about science and Shakespeare literature ;). That was genuinely thrilling me! [1]

Dr. Jonas Meinel, I remember when you first approached me: "I've heard you have no friends, me neither... Let's make some together!" ... And then you

[1] By the way, we should still write a real proposal to detect Axions together!! ;)

know how it ended up; no need to keep proofs here, but thank you for the nice moments together!

Stefan Hirschman, thank you for all the technical support, the lovely moments in Nesselwang and... for handling my MacBook issues despite your allergy to it ;).

Finally, for the lovely time spent together, the scientific tips and the excellent kicker games, I would like to thank many people, namely: Prof. Dr. Roland Nagy (for your cheers-up), Dr. Johannes Greiner (for the fun discussions at the coffee corner), Dr. Torsten Rendler (for your experimental tips and nice time in Berlin), Dr. Dominik Schmid-Lorch (for all kind of "tips" and forever...viva Mexico!), Dr. Vadim Vorobyov (for the "business" exchanges at the kicker table), Matthias Niethammer (because we are "excellent"! ;)), Dr. Roman Kolesov (for the brezel structure and the tips to get gleaming lithography structures), Matthew Joliffe (for training me on understanding Australian accent ;)), Dr. Naoya Morioka (for the okonomiyaki recipe which enlightened my time here), Minsik Kwon (for making me discover the spices from Korea), Santo Santonocito (for the tough kicker training and very positive spirit) and finally, Rouven Maier and Cheng-I "Joey" Ho, who recently joined, I hope you'll take a liking to the widefield cult!

Furthermore, I am thankful to Claudia Unger, Sabrina Jenne, Marion Moll and Dr. Andrea Zappe for taking care of our administration and, therefore, truly running the institute. Also, thanks to Ms Ivanka Spajic for taking care of the institute and making it an enjoyable environment to work in.

Last but not least, Dr. Florian Kaiser, my thesis would have been so different without you, not only for going through the German administration and its rigorous spirit[2] but also for being a source of inspiration. Thank you for everything you shared with me these past few years: frustrations, joys, scientific curiosity, and most importantly: your Röstis; they certainly helped me go through this thesis. Oh, and I almost forgot: thank you for the material in figure 1.1 ;). Ein herzlicher Dank geht an Sabine Kaiser(†2021) und die gesamte Familie Kaiser

[2]How comes a nail in the tire does not get the TÜV? I've made 800 km from Nice with it!

für die Freundlichkeit durch die ich mich in einem fremden Land wie in meiner Heimat fühle.

Finally, regarding my thesis, thanks to all the proofreaders, Rainer, Matthew, Andrea, Andrej, Tanya and Alastair! You certainly helped me to minimise the occurrence of typos and other small mistakes!

To conclude this section, I want to thank my friends and family, who always encouraged me.

Pour l'amitié solide au long des dernières années, merci à Pitchounette et Souad, j'espère que ça durera encore longtemps et que le chapitre de la thèse paraitra n'être qu'un bref instant parmi tant d'autres ;).

Enfin, merci à ma famille pour le soutien sans faille et sans qui tout cela n'aurait pu exister! Merci à Brahim Garsi, mon papa, qui m'a toujours inspiré à travailler dur et à Aïda Garsi, ma maman, pour l'inconditionnel soutien au fil des années! Merci aussi à ma soeur, mon frère, ma belle soeur et mes nieces et neveux pour m'avoir aidé à recharger les batteries lorsque j'en avais besoin. Merci également à mon oncle Mohammed et sa famille pour le soutien ici en Allemagne. Enfin, par de-là les frontières, merci à ma famille et amis en Tunisie pour les encouragements, avec une pensée particulière pour mon oncle Ali!

As a final word, thank you all for everything!